

University of Southampton Research Repository

Copyright © and Moral Rights for this thesis and, where applicable, any accompanying data are retained by the author and/or other copyright owners. A copy can be downloaded for personal non-commercial research or study, without prior permission or charge. This thesis and the accompanying data cannot be reproduced or quoted extensively from without first obtaining permission in writing from the copyright holder/s. The content of the thesis and accompanying research data (where applicable) must not be changed in any way or sold commercially in any format or medium without the formal permission of the copyright holder/s.

When referring to this thesis and any accompanying data, full bibliographic details must be given, e.g.

Thesis: Author (Year of Submission) "Full thesis title", University of Southampton, name of the University Faculty or School or Department, PhD Thesis, pagination.

Data: Author (Year) Title. URI [dataset]

University of Southampton

Faculty of Engineering and Physical Sciences

School of Engineering, Institute of Sound and Vibration Research

Vibroacoustic response of stiffened plates and cylinders for acoustic fatigue application

by

Dong Zhao

ORCID ID 0000-0002-1380-9306

Thesis for the degree of PhD

November, 2021

University of Southampton

Abstract

Faculty of Engineering and Physical Sciences

School of Engineering, Institute of Sound and Vibration Research

Doctor of Philosophy

Vibroacoustic response of stiffened plates and cylinders for acoustic fatigue application

by

Dong Zhao

Vibroacoustic response prediction is a key requirement when one considers acoustic fatigue and sound transmission. Whilst various methods have been developed for vibroacoustic predictions, their applicability and efficiency are limited when applying the methodologies to complex structures and conditions typically present in aerospace applications. The aims of this study are to improve a simplified prediction methodology, so that the effects of stiffeners, curvature, nonlinearity and elevated temperature can be incorporated into a general, efficient and accurate prediction. To achieve this a new framework with some of the existing formulated vibroacoustic quantities is proposed. A linear modal model was developed to predict the vibroacoustic response of stiffened thin plates to incident sound. The model was subsequently extended and applied to stiffened cylinders, where the rigid scattering of the incident sound was included. Subsequently, the surface pressure prediction from the model was experimentally validated for a scaled fuselage structure. Finally, a geometrically nonlinear reduced order model (NLROM) was developed for structures possessing deep stiffeners, high curvature and elevated temperatures. The effects of the nonlinear static characterisation and direct time integration on the predictions were investigated. The effects of vibroacoustic coupling, nonlinearity and elevated temperature for fatigue were quantified.

The key finding was that stiffeners, curvature, nonlinearity and elevated temperature can have significant impacts on the vibroacoustic response and subsequent fatigue life. Firstly, the vibroacoustic coupling is enhanced by stiffeners. Secondly, the presence of curvature can weaken the coincidence and wavelength selectivity as seen in the Joint Acceptance Functions (JAFs). Thirdly, the onset of nonlinear behaviour is initiated at higher excitation levels when there is the presence of stiffeners and curvature. These features, together with a temperature rise, can be captured by the NLROM with appropriate improvement, development and implementation. Finally, the vibroacoustic coupling, nonlinearity and raised temperature are important factors in the estimation of the fatigue life. A significant computational reduction is also achieved and shown using the proposed model, whilst retaining good accuracy compared to existing methodology such as a fully coupled finite element – boundary element model or a fully dynamic nonlinear finite element model solution.

Table of contents

Table of contents.....	I
Table of Tables.....	V
Table of Figures	VII
Research Thesis: Declaration of Authorship	XX
List of Symbols.....	XXI
List of Abbreviations.....	XXIX
Acknowledgements	XXXI
Chapter 1 Introduction.....	1
1.1 A brief overview of acoustic fatigue	1
1.2 Literature review	3
1.2.1 Vibroacoustic response	3
1.2.2 Nonlinear response	11
1.2.3 Acoustic fatigue life prediction.....	13
1.2.4 The thermal loading effect on response and fatigue	14
1.3 Research questions and the original contributions.....	18
1.3.1 Aims and research objectives.....	18
1.3.2 Original contributions.....	20
1.4 Thesis structure	21
Chapter 2 Vibroacoustic response of stiffened thin plates to incident sound.....	23
2.1 A vibroacoustic model for flat plates excited by a sound field	23
2.1.1 The dynamic response for incident plane waves	24
2.1.2 Sound radiation for incident plane waves.....	25
2.1.3 Joint Acceptance Function (JAF) and modal radiation efficiency	25

2.1.4	Vibroacoustic coupling	27
2.1.5	Vibroacoustic response for diffuse field excitation	28
2.1.6	Sound transmission for diffuse field excitation	29
2.2	Structural model	30
2.3	Numerical results of the modal model	35
2.3.1	Dynamic response	35
2.3.2	Sound transmission loss (TL)	43
2.4	Comparison with a coupled FE-BE model	46
2.5	Summary	49
Chapter 3	The acoustic response of stiffened cylinders	50
3.1	Surface pressure descriptions	50
3.1.1	Incident plane wave	51
3.1.2	Incident spherical wave	53
3.2	Modal force and JAF for plane wave excitation	56
3.3	Structural model	58
3.4	Numerical results	61
3.4.1	Joint Acceptance Functions	61
3.4.2	Dynamic response	64
3.4.3	Comparison with a coupled FE-BE model	68
3.5	Summary	70
Chapter 4	Experimental investigation of the acoustic response of a scaled fuselage model	
	72	
4.1	The test structure and modelling	72
4.1.1	The scaled fuselage	72
4.1.2	The normal mode method	74
4.1.3	The FE models	75
4.2	The impact test and results	80

4.2.1	The set-up	80
4.2.2	Test procedures	81
4.2.3	Comparison between measurements and FE results	86
4.3	The acoustic test and results	96
4.3.1	The set-up	96
4.3.2	Preliminary test on the source directivity	98
4.3.3	Acoustic modelling	100
4.3.4	The comparison of the measured pressures	104
4.3.5	The comparison of the vibration response	105
4.4	Summary.....	109
Chapter 5 Numerical investigation of the nonlinear response to high level acoustic excitation		
	111	
5.1	Nonlinear reduced order model.....	111
5.1.1	General formulation	111
5.1.2	Modal basis selection	114
5.1.3	Static loading specification	116
5.1.4	NLROM combined with thermal effects.....	119
5.1.5	Numerical integration schemes.....	123
5.1.6	Damping models and the effects of the solution sample rate	125
5.2	Numerical results.....	127
5.2.1	Example structures and general FE parameters.....	127
5.2.2	NLROM static identification schemes.....	132
5.2.3	The selection of damping and sample rate	143
5.2.4	A comparison between the unstiffened plate, stiffened plate and a stiffened cylinder	149
5.2.5	The effects of elevated temperatures on the nonlinear stiffness contribution	154

5.3	Summary.....	157
Chapter 6	Fatigue life evaluation with the effects of vibroacoustic coupling, nonlinearity and temperature	159
6.1	Methods for the acoustic fatigue life estimation	159
6.1.1	The stress-life approach and the $S-N$ curve.....	159
6.1.2	Palmgren-Miner damage rule and the time domain method	160
6.1.3	Generalised Palmgren-Miner rule and the spectral methods.....	162
6.2	Modal models for the response prediction.....	164
6.2.1	Vibroacoustic coupling and nonlinearity	164
6.2.2	Nonlinear stress and elevated temperature	165
6.3	Numerical results.....	166
6.3.1	Preliminary results.....	167
6.3.2	Comparison of different fatigue estimation methods	169
6.3.3	Comparison of the effects of the different physical conditions and behaviours	175
6.4	Summary.....	177
Chapter 7	Conclusions and future work.....	179
7.1	Conclusions.....	179
7.2	Future work	182
Appendix 1:	Implicit solver description in Abaqus	184
Appendix 2:	Dirlik's method for fatigue estimation	188
List of References	189

Table of Tables

Table 2-1 The structural parameters for the stiffened plates.	32
Table 2-2 The natural frequency and its percentage difference compared to a chosen finely meshed model for the 20 th mode.....	33
Table 2-3 The natural frequency and its difference variation for the 20 th mode	34
Table 3-1 The structural and material parameters for the stiffened cylinders	59
Table 4-1 The structural dimensions of the test structure.....	74
Table 4-2 Details of three FE models for test structure.	76
Table 4-3 The natural frequencies of the first local mode for different mesh size.....	76
Table 4-4 The comparison of the predicted lowest global modes and lowest local mode in FE models A and B with free ends boundary conditions.	78
Table 4-5 A summary of the five sets of impact measurements.....	86
Table 4-6 The peaks to be analysed and their corresponding frequencies and bay positions in the measurement.	90
Table 4-7 The peaks to be analysed and their corresponding frequencies and bay positions in FE models.	91
Table 5-1 Steps of a cold-mode NLROM.....	121
Table 5-2 Steps of a hot-mode NLROM	122
Table 5-3 The relative accuracy and efficiency of three potential numerical integration methods that can be implemented.....	124
Table 5-4 A comparison of the implicit and the explicit schemes in ABAQUS.	124
Table 5-5 Different forms of damping models.	125
Table 5-6 Four different modes sets A – D for stiffened plate. A: Linearly excited flexural modes within the excitation bandwidth. B: All flexural modes within the excitation bandwidth. C: Linearly excited modes within twice the excitation bandwidth. D: All modes within twice the excitation bandwidth.....	133
Table 5-7 The natural frequencies associated with the 34 modes in Table 5-6.....	133
Table 5-8 The convergence for the hot-mode and the cold-mode NLROM with different temperatures and different excitation levels. The tick symbol ‘✓’ means that a converged NLROM solution was guaranteed. The cross symbol ‘✗’ means that the NLROM solution cannot converge for the time integration dynamic solution. The symbol ‘N/A’ means that the nonlinear static tests cannot converge.	143

Table 5-9 The parameters of the excitations and the PSD estimations in the NLRDM predictions.

..... 151

Table of Figures

Figure 1-1 A cracked panel due to acoustic fatigue [1].	1
Figure 1-2 The variation of the JAF for a simply supported rectangular plate excited by a plane wave travelling parallel to two opposite edges and at an angle to the other edge producing the structural-acoustic (trace) wavelength ratio $\lambda_{sx}/\lambda_{tx}$ in the direction of propagation. Circle markers '○': the 1 st mode. Square markers '□': the 2 nd mode. Asterisk markers '*': the 3 rd mode. Plus sign markers '+': the 4 th mode.	4
Figure 1-3 An aircraft fuselage component stiffened by stringers and frames [44].	6
Figure 1-4 The acoustic fatigue facility (AFF) in BAE systems [124].	16
Figure 1-5 The thermal acoustic fatigue apparatus (TAFA) in the Langley Research Centre [119].	17
Figure 1-6 The high intensity acoustic testing facilities in the Wright Laboratory [126]. (a) The random fatigue chamber. (b) The sub-element acoustic chamber. (c) The combined environment acoustic chamber.	17
Figure 1-7 The thermal-acoustic test inside the reverberation chamber in Industrieanlagen-Betriebsgesellschaft MBH (IABG) [127].	18
Figure 2-1 An incident wave (a) onto and a radiated wave (b) from a rectangular plate in an otherwise infinite rigid baffle. k is the wave vector of the incident wave with the incident angle θ and the azimuthal angle ϕ . R is the distance between the observation points for radiated pressure response $p(\theta, \phi, r)$ and transverse displacement response $w(x, y)$.	23
Figure 2-2 Geometry of an orthogonally stiffened, rectangular plates. (a) Stiffener layout: two evenly spaced stiffeners in the x and y directions, respectively; (b) Stiffener detail: I section.	31
Figure 2-3 The comparison of modal properties between a FE model and an analytical model for the lowest 20 modes of stiffened plate. (a) MAC plot; (b) Scatter plot.	34
Figure 2-4 The transverse displacement for different acoustic excitation: diffuse sound field (black solid lines), normal incident plane wave (red dashed lines) and oblique incident plane wave $\theta, \phi = (\pi/4, \pi/4)$ (blue dotted lines). (a) Reference point response of the unstiffened plate. (b) Reference point response of the stiffened plate. (c) Spatial-averaged response of the unstiffened plate including a red solid line calculated from the Liamshev's plane-wave response theory for an oblique incident plane wave and a green solid line calculated from	

doubling of the Liamshev's predictions. (d) Spatial-averaged response of the stiffened plate.	37
Figure 2-5 The mode shapes and natural frequencies of the lowest 12 modes for the unstiffened plate.	39
Figure 2-6 The effect of the vibroacoustic coupling on the transfer function of the transverse displacement. Black solid lines are the fully coupled response and the red solid lines are the uncoupled response. (a) Reference point response of the unstiffened plate. (b) Reference point response of the stiffened plate. (c) Spatially-averaged response of the unstiffened plate. (d) Spatially-averaged response of the stiffened plate.	40
Figure 2-7 Radiation efficiency of the fundamental mode of unstiffened (black solid line) and stiffened (red solid line) plates. The radiation efficiency values are evaluated at the frequencies marked with dashed lines.	41
Figure 2-8 Comparison of vibroacoustic coupling effect for different cases. (a) Four types of plates. Case 1: unstiffened plate; Case 2: plate with 1 x -wise stiffener; Case 3: plate with 1 x -wise and 1 y -wise stiffeners; Case 4: plate with 2 x -wise and 2 y -wise stiffeners. (b) The dB difference of the spatially averaged RMS displacement for different cases using either a full vibroacoustic coupling or an uncoupled (blocked force) model. The bar without shading is for the unstiffened plate. The bars with parallel hatching shading are for the stiffeners with the original height. The bars with cross hatching shading are for the stiffeners with 2/3 of the original height.	42
Figure 2-9 The effect of the modal cross-terms contribution on the transfer function of the displacement response of the reference point on the unstiffened (a) and the stiffened plate (b) excited by a diffuse field. Black solid lines: with modal cross-terms contribution. Red solid line: without the modal cross-terms contribution.	43
Figure 2-10 The effect of acoustic excitation on the TL of the unstiffened (a) and the stiffened (b) plates. Black solid lines: an incident diffuse field. Red dashed lines: a normal incident plane wave. Blue dotted lines: an oblique incident plane wave at an angle $\theta, \phi = (\pi/4, \pi/4)$. Horizontal dash-dotted line: 0 dB line.	44
Figure 2-11 The comparison of TL results between the proposed model and the approximate formulae for the unstiffened plate subjected to a normal incident plane wave and a diffuse field excitation. Red, solid line: the proposed model subjected to normal incident plane wave. Black, solid line: the proposed model subjected to diffuse field. Red, dotted line: the normal incidence mass law. Blue, dash-dotted line: the diffuse field mass law. Blue, dotted line: the	

field incidence mass law. Blue, dashed line: Sewell's simplified formula. Horizontal black, dash-dotted line: 0 dB line.	45
Figure 2-12 The effect of the modal cross-terms contribution on the TL on the unstiffened (a) and the stiffened (b) plate excited by the diffuse field. Black solid lines: include modal cross-terms contribution. Red solid lines: without the modal cross-terms contribution. Horizontal dash-dotted line: 0 dB line.	46
Figure 2-13 A coupled FE-BE COMSOL model for the baffled stiffened plate subjected to diffuse field. (a) The meshed model. (b) The displacement response for the incident diffuse field of amplitude 91 dB at the first resonance frequency of the stiffened plate (62.5 Hz)	48
Figure 2-14 The comparison of the results for the stiffened plate displacement response (a) and the TL (b) for the diffuse field between the proposed modal model (in black, dotted lines) and the coupled FE-BE model (in red, solid lines). Horizontal dash-dotted line: 0 dB line.....	48
Figure 3-1 Diagram of an incident plane wave impinging on a finite cylinder with length of $2L$ and radius of R and with shear diaphragm ends. The plane wave has an acoustic wavenumber vector k with an incident angle of θ_i relative to cylinder axis (z axis) and an azimuthal angle of ϕ_i relative to the positive direction of the x axis.	52
Figure 3-2 Diagrams of a spherical wave impinging on a cylinder from a point source (rs, ϕ_0, z_0) outside the cylinder. The distance between the source and the field point on the cylinder surface is d_{fs} . The distance between the source and the projection of the field point on the cross section plane of the source is dp_{fs}	54
Figure 3-3 A point in two polar coordinate systems.	55
Figure 3-4 Geometry of a cylinder stiffened with stringers and rings.....	58
Figure 3-5 The natural frequencies of the lowest 20 modes for each case of the cylinders, plotted as non-dimensional frequency $\Omega = \omega/\omega_R$ where $\omega_R = 1RE\rho_1 - \nu_2$ is the ring frequency (951 Hz) for a cylindrical plain shell. Circle markers ' \bigcirc ': bare cylinder. Square markers ' \square ': cylinder with only rings. Plus sign markers '+': cylinder with only stringers. Asterisk markers '*': cylinder with both rings and stringers.	60
Figure 3-6 The axial component of the JAF for the first 4 bending modes of cylinder subjected to plane wave excitation. Circle markers ' \bigcirc ': the 1 st mode. Square markers ' \square ': the 2 nd mode. Asterisk markers '*': the 3 rd mode. Plus sign markers '+': the 4 th mode.....	62
Figure 3-7 The circumferential component of the JAF for the 2 nd to the 4 th bending modes of cylinder subjected to plane wave excitation. Square markers ' \square ': the 2 nd mode. Asterisk	

markers ‘*’: the 3 rd mode. Plus sign markers ‘+’: the 4 th mode. The black markers are from the pressure doubling assumption. The red markers are from the blocked pressure assumption	63
Figure 3-8 The circumferential component of the JAF for the first circumferential modes of cylinder subjected to plane wave excitation. The black circled markers ‘○’ are from the pressure doubling assumption. The red circled markers ‘○’ are from the blocked pressure assumption.	64
Figure 3-9 The normalized radial displacement transfer function for the bare cylinder (a), the stiffened cylinder with 9 rings (b), the stiffened cylinder with 8 stringers (c), and the stiffened cylinder with both 9 rings and 8 stringers (d). The responses are for two different surface total pressure assumptions. Solid line: the doubled pressure (twice of the incident pressure). Dotted line: the blocked pressure (the sum of incident pressure and the scattered pressure from rigid cylindrical surface).....	66
Figure 3-10 Orders of the cylinder modes below 1000 Hz for the unstiffened cylinder (a), stiffened cylinder with 9 rings (b), stiffened cylinder with 8 stringers (c) and with both rings and stringers (d). The modes associated with the predominant peaks in corresponding responses are marked by solid circles and are within the bands indicated in grey. Other modes are marked with hollow circles.	67
Figure 3-11 A coupled FE-BE numerical model for the baffled cylinder subjected to an incident plane wave with the incident angle of $\pi/4$ and the SPL of 91 dB at 650 Hz around the highest response peaks. (a) The meshed model. (b) The radial displacement (m) of the cylinder midplane with a scale factor of 1×10^6 and the total acoustic pressure (Pa) on the rigid cylindrical baffle surface.....	68
Figure 3-12 Radial displacement of the reference point for the unstiffened cylinder calculated by different models. Black solid line: analytical model with blocked pressure. Blue dashed line: FE model with blocked pressure. Red dashed line: coupled FE-BE model.....	69
Figure 3-13 Radial displacement of the reference point for the unstiffened cylinder calculated by different models. Black solid line: analytical model with blocked pressure with radiation damping. Red dashed line: coupled FE-BE model.	70
Figure 4-1 The test structure: a quarter scale fuselage model (a) with ring stiffeners (b).	73
Figure 4-2 The drawing of the geometry of the ring-stiffened cylinder test structure.....	73
Figure 4-3 The meshed FE model B in COMSOL.	77

Figure 4-4 The comparison of modal properties between the FE model A and the FE model B for the lowest 8 global modes (mode order 1 - 8) and the lowest local mode (mode order 9) of test structure. (a) MAC plot; (b) Scatter plot.	79
Figure 4-5 The layout of the measurement system used in the impact test.	80
Figure 4-6 The measurement points of the first set of impact tests for the driving point mobility along the axial direction from Bay 7 to Bay 11. 5 measurement positions are on the centres of each bay and are indicated with the red points in the figure, No.1 – 5.....	82
Figure 4-7 The measurement points of the second set of impact tests for the transfer mobility along an axial line on the cylinder's surface. The red point No.36 is for the accelerometer position and the 71 positions equally spaced along the six central bays (Bay 7 – 11) are for the impact points.....	82
Figure 4-8 The measurement positions of the third set of impact tests for the transfer mobility around the circumference of the cylinder in the central bay (Bay 9). The red point No.1 is for the accelerometer position and the 17 impact points are marked around a half of the circumference.....	83
Figure 4-9 The measurement points of the fourth set of impact tests for the transfer mobility around the circumference of the cylinder in Bay 9. The red point is the accelerometer position. The 20 hammer impact points are equally spaced with a separation angle of 1.5°	84
Figure 4-10 The measurement points of the fifth set of impact tests for the transfer mobility around the circumference of the cylinder in Bay 7. The red point is the accelerometer position. The 20 hammer impact points are equally spaced with a separation angle of 1.5°	85
Figure 4-11 The results of the first set of impact tests showing driving-point mobilities (a) and the coherence (b) for the five measurement positions: yellow for position No.1, blue for No.2, black for No.3, green for No.4 and red for No.5.	86
Figure 4-12 The driving-point mobility of the same five positions on the FE model A (a) and the FE model (b) with solid lines with yellow for No.1, blue for No.2, black for No.3, green for No.4 and red for No.5.	87
Figure 4-13 A single bay of the FE model A (a) and the comparison of the driving-point mobilities (b). The red solid line is the FE model A point mobility in No. 1. The blue dotted line is the point mobility of the single bay with SD boundary condition. The green dotted line is the point mobility of the single bay with spring foundation boundary condition.	88
Figure 4-14 Comparison of the point mobility from FE model B with different conditions. Free boundary condition without interior air domain (blue solid line). Free boundary condition with	

interior air domain (blue dotted line). Prestress without interior air domain (red solid line). Prestress with interior air domain (red dotted line).	89
Figure 4-15 The measured and FE driving point mobilities of two bays. (a) Bay 9: black solid for measurement, red solid for FE model A, blue solid for FE model B. (b) Bay 7: yellow solid for measurement, red solid for FE model A, blue solid for FE model B.....	90
Figure 4-16 The measured mode shapes of the first test peak at frequency of 128 Hz. The red asterisk points are the undeformed shape and the blue circle points are the deformed shape. (a) Mode shape from the measurements along the axial direction, extracted from the second set of impact tests. (b) Mode shape from the measurements around the circumferential direction, extracted from the third set of impact tests. The black dashed line is a plot of a sinusoidal function with 2 circumferential wavelengths. The position of the fixed accelerometer is highlighted as the red solid dot.	91
Figure 4-17 The measured mode shapes from the second test peak at frequency of 170 Hz. The red asterisk points are the undeformed shape and the blue circle points are the deformed shape. (a) Mode shape from the measurements along the axial direction, extracted from the second set of impact tests. (b) Mode shape from the measurements around the circumferential direction, extracted from the third set of impact tests. The black dashed line is a plot of a sinusoidal function with 2 circumferential wavelengths. The position of the fixed accelerometer is highlighted as the red solid dot.	92
Figure 4-18 The measured mode shapes from the third test peak at frequency of 434 Hz. The red asterisk points are the undeformed shape and the blue circle points are the deformed shape. (a) Mode shape from the measurements along the axial direction, extracted from the second set of impact tests. (b) Mode shape from the measurements around the circumferential direction, extracted from the fourth set of impact tests. The black dashed line is a plot of a sinusoidal function with 16 circumferential wavelengths. The position of the fixed accelerometer is highlighted as the red solid dot.	93
Figure 4-19 The measured mode shapes of the fourth test peak at frequency of 516 Hz. The red asterisk points are the undeformed shape and the blue circle points are the deformed shape. (a) Mode shape from the measurements along the axial direction, extracted from the second set of impact tests. (b) Mode shape from the measurements around the circumferential direction, extracted from the fourth set of impact tests. The black dashed line is a plot of a sinusoidal function with 17 circumferential wavelengths. The position of the fixed accelerometer is highlighted as the red solid dot.	94

Figure 4-20 The measured mode shapes of the fifth test peak at frequency of 570 Hz. The red asterisk points are the undeformed shape and the blue circle points are the deformed shape. (a) Mode shape from the measurements along the axial direction, extracted from the second set of impact tests. (b) Mode shape from the measurements around the circumferential direction, extracted from the fifth set of impact tests. The black dashed line is a plot of a sinusoidal function with 18 circumferential wavelengths. The position of the fixed accelerometer is highlighted as the red solid dot.	95
Figure 4-21 The acoustic test layout and the measurement system used.	96
Figure 4-22 The acoustic test set up in the anechoic chamber.	97
Figure 4-23 The positions of the reference points.	98
Figure 4-24 The SPLs at the different specified points. (a) Narrow-band measurement with the frequency resolution of 0.625 Hz. (b) One-third octave band spectra. Black lines: measurement points 1 m from the loudspeaker. Red lines: measurement points 2 m from the loudspeaker. Blue lines: measurement points 3 m from the loudspeaker. The results for positions at different angles are represented by different line types. Green dashed line: background noise level at measurement point 1 m from the loudspeaker.	99
Figure 4-25 The estimated source strength in 1/3 octave bands averaged for points over different angles at the same distance from the source. Black lines: measurement points 1 m from the loudspeaker. Red line: measurement points 2 m from the loudspeaker. Blue line: measurement points 3 m from the loudspeaker.	100
Figure 4-26 The meshed BE model (a) and the surface pressure distribution (b) at the frequency of 1000 Hz.	101
Figure 4-27 The comparison of the predicted pressure between the first (the analytical model of spherical wave, in dotted lines) and the second model (BE, in solid lines). The pressure ratios between the three observation points on the cylinder surface and that at the reference point are plotted: the front point (black), the midpoint (red) and the rear point (blue).	102
Figure 4-28 The effect of the cylinder length on the predicted pressure of the points at the median plane wave the cylinder. Solid lines: the front point. Dashed lines: the midpoint. Dotted lines: the rear point. The analytical results for each point are in black. The BE results for different cylinder lengths are in different colours as indicated in the figure legend.	103
Figure 4-29 The comparison of the predicted pressure between the first (the analytical model of spherical wave, in solid lines) and the third (the analytical model of plane wave, in dotted	

lines) model. Black lines: the point at the front of the cylinder. Red lines: the midpoint. Blue lines: the rear point.	104
Figure 4-30 Coherence of the transfer functions between the surface pressure and the reference pressure. Black solid line: the front point. Red solid line: the midpoint. Blue solid line: the rear point.....	104
Figure 4-31 Comparison of the measured pressure ratios (thin, solid lines) with the predicted pressure ratios from the first (analytical) model (thick, solid lines) and from the second (BE) model (dotted lines). Black: the front point. Red: the midpoint. Blue: the rear point.	105
Figure 4-32 Coherence of the transfer functions between the response at the surface points and the reference pressure. Black solid line: the front point. Red solid line: the midpoint. Blue solid line: the rear point. (a) Accelerometer measurement – acceleration response. (b) Laser vibrometer measurement – velocity response.	106
Figure 4-33 The comparison of the measured acceleration (calculated from the measured velocity) and the predicted acceleration in terms of the transfer function to the pressure at the reference point. Black solid lines: measurement. Red solid lines: FE model A with the blocked pressure from the 3 rd analytical model (an approximate plane wave). (a) The front point. (b) The midpoint. (c) The rear point.	107
Figure 4-34 The comparison of the measured acceleration and the predicted acceleration for the front point in terms of the transfer function to the pressure at the reference point. Black solid lines: measurement. Blue solid lines: FE model with fully clamped boundary conditions and the blocked pressure from the 3 rd analytical model (an approximate plane wave).	108
Figure 4-35 The comparison of the acceleration response in terms of the transfer function to the pressure for the front point estimated from the first model (analytical spherical wave excitation in the black solid line) and the third model (analytical plane wave excitation in the black dotted line).....	109
Figure 5-1 A flow chart illustrating the steps of a cold-mode NLROM and a hot-mode NLROM. Two rounded rectangles (dashed line for cold-mode and dotted line for hot-mode) are used for highlighting the different and common steps.	123
Figure 5-2 The meshed FE model of the stiffened plate with shell elements in Abaqus. The expanded the view shows part of one x -wise stiffener joined with the plate.	128
Figure 5-3 The positions of the forcing points, marked in the black solid circles, and the positions of the example response points, marked in the red solid circles, for the stiffened plate (a) and the stiffened cylinder (b).....	130

Figure 5-4 PSD estimations of the normalised displacement for the stiffened plate subjected to the mechanical point force (a) and to the acoustic normal plane wave excitation (b). Cyan dash-dotted lines: linear response predictions. Magenta dotted lines: nonlinear response predictions from the full order FE simulations. Solid lines: nonlinear response predictions from NLROM with mode set A (in blue), mode set B (in red), mode set C (in green) and mode set D (in black).	135
Figure 5-5 Band limited RMS of the normalised displacement of stiffened plate subjected to the mechanical point excitation (a) and to the acoustic plane wave excitation (b). ■■■: linear response predictions. ■■■: NLROM response prediction with mode set A. ■■■: NLROM response prediction with mode set B. ■■■: NLROM response prediction with mode set C. ■■■: NLROM response prediction with mode set D. ■■■: nonlinear response predictions from the full order FE. Three frequency ranges are considered for the responses, i.e. range 1 (0 – 125Hz), range 2 (125 – 250Hz) and range 3 (0 – 250Hz).	136
Figure 5-6 PSD estimations of the nonlinear response for stiffened plate subjected to the point force excitation (a) and to the acoustic plane wave excitation (b). The NLROM results with the nonlinear static identification using the dead loads is in black solid lines and that using the follower loads are in red dashed lines.	137
Figure 5-7 PSD estimations of the normalised nonlinear displacement for the stiffened plate subjected to the point force (a) and to the acoustic plane wave (b) excitations. The NLROM results using the scaling factors corresponding the desired reference displacement of $5h$ are in the blue solid lines, $20h$ are in the green solid lines and $40h$ are in the black solid lines. The full order FE results are in red dotted lines.	139
Figure 5-8 The natural frequencies and mode shapes of the lowest 9 cold modes.	140
Figure 5-9 The natural frequencies and mode shapes of the lowest 9 hot modes with a temperature rise of $50\text{ }^{\circ}\text{C}$	140
Figure 5-10 The natural frequencies and the mode shape of the lowest 9 hot modes with a temperature rise of $100\text{ }^{\circ}\text{C}$	141
Figure 5-11 PSD estimations of the normalised nonlinear displacement for the stiffened plate subjected to the normal plane wave excitation with a temperature rise of $50\text{ }^{\circ}\text{C}$ (a) and $100\text{ }^{\circ}\text{C}$ (b). The cold-mode NLROM predictions are in the black solid lines and the hot-mode NLROM predictions are in the red solid lines. The full order FE predictions are in the blue dotted lines.	142

Figure 5-12 The frequency dependency of the viscous damping ratio for the first 22 modes within the frequency range 0 – 100Hz. ■: stiffness-proportional damping; ■: mass-proportional damping.	145
Figure 5-13 PSD estimations of the normalised displacement for the unstiffened plates with different damping models and subjected to different excitations. (a) Mass-proportional damping. (b) Stiffness-proportional damping. The linear response predictions are in the blue dash-dotted lines. The NLROM response predictions are in the black solid lines. The full order FE predictions are in the red dotted lines.	145
Figure 5-14 PSD estimations of the normalised displacement for the unstiffened plates with the mass-proportional damping model. The sample rate for the full order FE prediction has been increased from 10kHz to 25kHz. The linear response predictions are in the blue dash-dotted lines. The NLROM response predictions are in the black solid lines. The full order FE predictions are in the red dotted lines.	146
Figure 5-15 PSD estimations of the normalised displacement for the unstiffened plates with different damping models and subjected to the plane wave excitation. (a) Mass-proportional damping. (b) Stiffness-proportional damping. The linear response predictions are in the blue dash-dotted lines. The NLROM response predictions are in the black solid lines. The full order FE predictions are in the red dotted lines.	147
Figure 5-16 PSD estimations of the stiffened plate subjected to the point force excitation (a) and to the plane wave excitation (b). The NLROM predictions are in black lines (sample rate 10 kHz). The FEM predictions with the sample rates of 100kHz, 50kHz and 10kHz are in the red dotted lines, the blue dotted lines and the green dotted lines.	148
Figure 5-17 PSD estimations of the normalised displacement for the stiffened plate subjected to the plane wave excitation. Three combinations of sample rate and stiffness-proportional damping level are used: (a) Low sample rate (50kHz) and low damping (1%). (b) High sample rate (100kHz) and low damping (1%). (c) Low sample rate (50kHz) and high damping (2%). The NLROM predictions are in black solid lines. The FEM predictions are in red dotted lines. ..	149
Figure 5-18 The linear predictions of the maximum normalised displacement of the three structures to the point excitation (a) and the plane wave excitation (b). The red bars ■ represent the predictions for the low excitation levels in Table 5-9. The blue bars ■ represent the predictions for the high excitation levels in Table 5-9. The horizontal lines correspond to the value of 1.	151

Figure 5-19 PSD estimations from the NLROM for the three different structures subjected to the point force and plane wave excitations: (a) the unstiffened plate subjected to the point force excitation; (b) the stiffened plate subjected to the point force excitation; (c) the stiffened cylinder subjected to the point force excitation; (d) the unstiffened plate subjected to the plane wave excitation; (e) the stiffened plate subjected to the plane wave excitation; (f) the stiffened cylinder subjected to the plane wave excitation. — · — : the linear response prediction to low level of excitation. — : the nonlinear response prediction to low level of excitation. — · — : the linear response prediction to high level of excitation. — : the nonlinear response prediction to high level of excitation.	152
Figure 5-20 PSD estimations from the full order FE for the stiffened cylinder subjected to the normal plane wave of 174 dB. The black solid line is the linear prediction and the red solid line is the nonlinear prediction.	153
Figure 5-21 The band limited mean square value of the nonlinear displacement for the three structures subjected to the point excitation (a) and to the plane wave excitation (b) outside the excitation. ■ : the results for the low excitation levels in Table 5-9. ■ : the results for the high excitation levels,	154
Figure 5-22 The RFAC of the first 9 modes for the three different temperatures, 0 °C, 50 °C and 100 °C in pairs of the four comparisons: (a) 0 °C - 0 °C. (b) 0 °C - 50 °C. (c) 0 °C - 100 °C. (d) 50 °C - 100 °C.....	156
Figure 5-23 The NLROM estimated PSD of the normalised displacement for the stiffened plates with temperature and subjected to the plane wave excitation. The mode set D (34 modes) is used in NLROM prediction. The three different temperatures, 0 °C, 50 °C and 100 °C are represented by the black, red and blue solid lines.	157
Figure 6-1 A general S-N curve showing different fatigue ranges.....	160
Figure 6-2 An illustration of the rainflow counting method.	161
Figure 6-3 The $S - N$ curve used in the fatigue calculations in the numerical study.....	166
Figure 6-4 The time history (a) and the PDF (b) of the maximum stress in the y direction.	168
Figure 6-5 The PSD of the maximum stress in the y direction.....	168
Figure 6-6 The PDF of the rainflow counting ranges as a histogram in comparison to a theoretical Rayleigh distribution.	169

Figure 6-7 Stress distributions in the y direction (a) and in the x direction (b) when the plate is subjected to the point force excitation. The positions corresponding to the stress maxima are marked by the black circles.	170
Figure 6-8 The PSD estimations of the maximum element normal stress at two directions when the plate is subjected to the point force excitation. The maximum normal stress response in the y direction is in the solid line. The maximum normal stress response in the x direction is in the dotted line.	171
Figure 6-9 Comparison of the fatigue life ratios calculated from three different spectral methods: Rayleigh approach, Factor approach and Dirlik's approach. (a) The fatigue life ratios for the response of the maximum stress in the y direction with one dominating peak. (b) The fatigue life ratios for the response of the maximum stress in the x direction with two comparable dominating peaks.	172
Figure 6-10 The PSD estimations of the maximum element normal stress at y direction when the plate is subjected to the plane wave excitation. The linear prediction is in the solid line and the nonlinear prediction is in the dotted line.	173
Figure 6-11 Comparison of the fatigue life ratios calculated from three different spectral methods: Rayleigh approach, Factor approach and Dirlik's approach. The fatigue life ratio is calculated by normalising the fatigue life calculated from the three spectral methods with that from Rainflow counting method (the horizontal red lines). (a) Fatigue life ratios for the linear response of the maximum stress in the y direction. (b) Fatigue life ratios for the nonlinear response of the maximum stress in the y direction.f	173
Figure 6-12 Stress range PDFs of the linear responses (a) and the nonlinear responses (b). The results calculated from the Rainflow counting method are in the solid lines. The results calculated from the Rayleigh approximation method are in the dotted lines. The results calculated from Dirlik's approach are in the dashed lines.	174
Figure 6-13 Comparison of the rainflow estimated fatigue life calculated for three different configurations. (a) Excitation type: plane wave against point force. (b) Boundary condition: Spring foundation against clamped edges. (c) Elevated temperature: 0 °C, 50 °C and 100 °C. The results of the uncoupled responses are in the blue bars. The results of the coupled responses are in the red bars.	176
Figure 6-14 Comparison of the fatigue life estimated from the responses with and without the nonlinearity and the vibroacoustic coupling and over three different temperature conditions of 0 °C, 50 °C and 100 °C. The results for the linear, uncoupled predictions are in the blue bars.	

The results for the nonlinear, uncoupled predictions are in the red bars. The results for the nonlinear, coupled predictions are in the yellow bars. Two different levels of the plane wave excitations, 146dB in (a) and 149dB in (b), are used..... 177

Research Thesis: Declaration of Authorship

I declare that this thesis and the work presented in it are my own and have been generated by me as results of my own original research.

I confirm that:

1. This work was done wholly or mainly while in candidature for a PhD research degree at this University;
2. Where any part of this thesis has previously been submitted for a degree or any other qualification at this University or any other institution, this has been clearly stated;
3. Where I have consulted the published work of others, this is always clearly attributed;
4. Where I have quoted from the work of others, the source is always given. With the exception of such quotations, this thesis is entirely my own work;
5. I have acknowledged all main sources of help;
6. Where the thesis is based on work done by myself jointly with others, I have made clear exactly what was done by others and what I have contributed myself;
7. Parts of this work have been published (or in press) as:
 - D. Zhao, G. Squicciarini, and N. S. Ferguson, "Vibroacoustic response of stiffened thin plates to incident sound," *Applied Acoustics*, vol. 172, p. 107578, 2021, doi: <https://doi.org/10.1016/j.apacoust.2020.107578>.
 - D. Zhao, G. Squicciarini, and N. S. Ferguson, "Acoustic response of thin-walled, orthogonally stiffened cylinders," *Materials Science and Engineering*, 2019. [Online]. Available: <http://dx.doi.org/10.1088/1742-6596/1264/1/012041>
 - D. Zhao, G. Squicciarini, and N. S. Ferguson, "The acoustic response of stiffened plates," *Journal of Physics: Conference Series*, vol. 1264, p. 012041, 2019, doi: 10.1088/1742-6596/1264/1/012041

Signature:

Date:

List of Symbols

<i>A</i>	1. Coefficients
A_ν	The coefficients of the Hankel function of the second kind of order ν
$A_r^{i,j,k}$	The coefficients of the nonlinear stiffness term for the r^{th} order mode. i, j, k are the order of the modal displacement
<i>C</i>	1. The coherence of transfer functions
$C_{ref,m}$	The coherence of transfer function between the reference point and the measured point
<i>D</i>	1. The total accumulated damage
<i>E</i>	1. Energy
\bar{E}_n	The time averaged vibrational energy associated with the n^{th} mode
	2. Young's modulus
<i>F</i>	1. The static loading in nonlinear static analysis
F_c	Characteristic load
F_r	Reaction force
	2. The expected value of the occurrence rate
F_p	The expected value of the peak occurrence rate
F_{zc}	The expected value of the zero cross occurrence rate
<i>H</i>	1. Hankel function
$H_\nu^{(2)}$	The Hankel function of the second kind of order ν
<i>I</i>	1. Function $I_m(x) = \int_{-L}^L \sin \frac{m\pi(z+L)}{2L} e^{-ixz} dz$
<i>J</i>	1. The Bessel function of the first kind
J_ν	The Bessel function of the first kind of order ν
<i>K</i>	1. Stiffness matrix
K	Linear stiffness matrix
K_1	Quadratic nonlinear stiffness matrix
K_2	Cubic nonlinear stiffness matrix
	2. Constant parameter for fatigue law
<i>L</i>	1. Cylinder length

M	1. Mass matrix
N	1. The number of modes used in modal summation
	N_l The number of modes used in the linear modal summation
	N_{nl} The number of modes used in the nonlinear static characterisation
	2. The number of cycles to failure
P	1. The static loading in nonlinear static analysis
	P_c Characteristic pressure
Q	1. Source strength
R	1. Cylinder radius
S	1. The total number of plane waves to represent a diffuse field
	2. Power spectral density
	S_x The power spectral density of the x process
	3. Stress
	S_a The stress amplitude
	S_{rms} The root mean square (RMS) value of the stress
T	1. Transfer matrix
	T_p The pressure to force transfer matrix
	2. Temperature
	3. The finite length of a period
W	1. Power
	W_n The acoustic power radiated by the n^{th} order mode
X	1. Fourier transform of the x process
Z	1. Dynamic stiffness
	Z_n The dynamic stiffness for the n^{th} order mode
a	1. Plate length
	2. Acceleration
	3. Scaling factor
	a_n The scaling factors for the n^{th} order mode
	a_m The scaling factors for the m^{th} order mode
b	1. Plate width
	2. Constant parameter for fatigue law

c	1. The sound speed in air
	2. Damping
	c_n The viscous (Rayleigh) damping rate for the n^{th} order mode
d	c_{n0} The critical damping coefficient for the n^{th} order mode
	1. Distance
	d_{fs} The distance between the point sound source and the field point
	d_{pfs} The distance between the point sound source and the projection of the field point on the cross section plane of source
	2. Depth
e	d_s The depth of the cross section of the stiffener
	1. Base of natural logarithms
f	1. Force
	f Nodal force vector
	f_d Damping force
	2. Frequency
	f_s Sampling frequency (rate)
i	1. $\sqrt{-1}$
	2. Order of modal displacement in nonlinear stiffness coefficient
j	1. Joint Acceptance Function (JAF)
	j_A The axial component of the JAF
	j_C The circumferential component of the JAF
	j_n The JAF for the n^{th} order mode
	$j_{n,s}$ The JAF for the n^{th} order mode due to the s^{th} plane wave
	2. The order of modal displacement in nonlinear stiffness coefficient
k	1. Wavenumber
	k_p The underlying free bending wavenumber of the plate material
	\vec{k} Wavenumber vector
	k_{tc} The acoustic trace wavenumber around the cylinder circumferential direction
	2. The order of modal displacement in nonlinear stiffness coefficient
	3. Stiffness

	k_n	The modal stiffness for the n^{th} order mode
	$k_{\Delta T}$	The linear modal stiffness change to the temperature change of ΔT
	$k_{n\Delta T_0}$	The linear modal stiffness at a temperature rise of ΔT_0
	k'_n	The modal stiffness for the n^{th} order hot mode
l	1. Modal force	
	l_{mn}	The modal force for the $(m,n)^{\text{th}}$ order mode
	l_n	The modal force for the n^{th} order mode
	$l_{n\Delta T}$	The modal force for the n^{th} order mode due to the thermal loading
	2. Length	
	l_c	Cylinder length
	3. Force	
	l_o	The overall force due to a uniform pressure field $2p_0$ over the cylinder surface
m	1. Mass	
	m_A	Mass per unit area
	m_n	The modal mass for the n^{th} order mode
	m_1^r	The added mass of the air for the first mode of the plate
	m'_n	The modal mass for the n^{th} order hot mode
	2. Mode order	
n	1. Mode order	
p	1. Sound pressure	
	p_0	A doubling of the amplitude of sound pressure
	p_{total}	Total sound pressure
	$p_{incidnet}$	Incident sound pressure
	$p_{reflected}$	Reflected sound pressure
	$p_{radiated}$	Radiated sound pressure
	$p_{blocked}$	Blocked sound pressure
	$p_{radiated,ex}$	External radiated sound pressure
	$p_{radiated,in}$	Internal radiated sound pressure
	2. Probability density function (PDF)	

	p_{rfr}	The PDF for the rainflow stress cycle ranges
q	1. Modal displacement	
	q_n	The modal displacement of the n^{th} order mode
	q'_n	The modal displacement of the n^{th} order hot mode
	q_{nT}	The static modal displacement due to the thermal loading for the n^{th} order mode
r	1. Spherical coordinate – the radial component	
	r_s	The radial coordinate of the point source
	2. Radius	
	r_e	Equivalent radius of the piston
	r_c	Cylinder radius (for numerical simulation)
t	1. time	
	2. Shell thickness	
	t_c	The thickness of the cylindrical shell
	t_s	The thickness of the stiffener wall
u	1. Mode order	
	2. The axial displacement of the middle surface of the cylindrical shell	
	\bar{u}_{mn}	The modal displacement of the symmetric circumferential modes
	\bar{u}'_{mn}	The modal displacement of the antisymmetric circumferential modes
v	1. Velocity	
	$\langle \overline{v_n^2} \rangle$	The spatial-averaged mean-square velocity for n^{th} order mode
	2. Circumferential displacement of the middle surface of the cylindrical shell	
	\bar{v}_{mn}	The modal displacement of the symmetric circumferential modes
	\bar{v}'_{mn}	The modal displacement of the antisymmetric circumferential modes
w	1. Nodal displacement	
	\ddot{w}	Nodal acceleration
w	1. Transverse displacement response	

	w_s	The displacement response to each plane wave s
	$\overline{w^2}$	Mean square value of the displacement response
	2.	Radial displacement of the middle surface of the cylindrical shell
	w_p	The desired displacement at position p
	\bar{w}_{mn}	The modal displacement of the symmetric circumferential modes
	\bar{w}'_{mn}	The modal displacement of the antisymmetric circumferential modes
	3.	Width
	w_s	The width of the cross section of the stiffener
x	1.	Spatial coordinate
	2.	Displacement
	3.	Time history of the x process
y	1.	Spatial coordinate
z	1.	Spatial coordinate
	z_s	The axial coordinate of the point source (in cylindrical coordinate system)
Γ	1.	Gamma function, for integers $\Gamma(n) = n! = n(n-1)(n-2) \dots 1$
Δ	1.	Incremental quantity
Φ	1.	Velocity potential
α	1.	Factor
	α_n	The factor of modal mass for the mass-proportional damping for the n^{th} order mode
β	1.	Factor
	β_n	The factor of modal stiffness for the stiffness-proportional damping for the n^{th} order mode
ϵ	1.	Phase
η	1.	Loss factor
	η_n^r	The radiation damping loss factor for the n^{th} order mode
θ	1.	Spherical coordinate – the incident angle component
	θ_i	The incident angle of the incident wave
	1.	Vector function for nonlinear stiffness

	θ'	The ector function for nonlinear stiffness using hot modes
λ	1. wavelength	
	λ_{sx}	The structural wavelength along the x direction
	λ_{tx}	The acoustic trace wavelength along the x direction
	λ_m	The structural wavelength along the cylinder axial direction
	λ_n	The structural wavelength around the cylinder circumferential direction
	λ_{tA}	The acoustic trace wavelength along the cylinder axial direction
	λ_{tC}	The acoustic trace wavelength around the cylinder circumferential direction
	λ_p	The bending wavelength for an infinite plate
ν	1. Poisson's ratio	
	2. The order for Bessel and Hankel functions	
ξ	1. Viscous damping ratio	
	ξ_n	The viscous damping ratio for the n^{th} order mode
π	1. 3.14...	
ρ	1. Density	
	ρ_0	Air density
σ	1. Radiation efficiency	
	σ_n	The radiation efficiency for the n^{th} mode
τ	1. Sound transmission coefficient	
	τ_d	The sound transmission coefficient of a diffuse field
	2. Dummy variable for integral	
ϕ	1. Spherical coordinate – the azimuthal angle component	
	ϕ_i	The azimuthal angle of the incident wave
	ϕ_s	The azimuthal coordinate of the point source (in cylindrical coordinate system)
ψ	1. Mode shape	
	ψ_n	The mode shape of the n^{th} order mode
	ψ_m	The mode shape of the m^{th} order mode
	ψ_{nP}	The entry of mode shape of the n^{th} order mode at the position P

ω

1. Radian frequency

ω_n The natural frequency for the n^{th} order mode

ω'_1 The fluid loaded natural frequency for the first mode

List of Abbreviations

AFF	Acoustic Fatigue Facility
BEM	Boundary Element Method
BW	Band Width
DOF	Degree of Freedom
ESA	European Space Agency
ESDU	Engineering Science Data Unit
FEM	Finite Element Method
FRF	Frequency Response Function
IC	Implicit Condensation
IFT	Inverse Fourier Transform
JAF	Joint Acceptance Function
MAC	Modal Assurance Criterion
NLROM	Nonlinear Reduced Order Model
PDF	Probability Density Function
POD	Proper Orthogonal Decomposition
POM	Proper Orthogonal Mode
POV	Proper Orthogonal Value
PSD	Power Spectral Density
PWT	Progressive Wave Tube
RFAC	Restoring Force Assurance Criterion
RMS	Root Mean Square
SD	Shear Diaphragm
SEA	Statistical Energy Analysis
SPL	Sound Pressure Level
TAFA	Thermal Acoustic Fatigue Apparatus
TBL	Turbulent Boundary Layer
TL	Transmission Loss
V/STOL	Vertical/Short Take-Off and Landing
WFE	Wave Finite Element

Acknowledgements

I am very thankful for a great deal of supports and help I have received from various people and organisations. Without them I can never complete this thesis.

I am immensely thankful to my supervisor Neil Ferguson. He has been constantly supporting me with his knowledge and wisdom. He faithfully dedicated in guiding me throughout my PhD journey. It is my true honour to be his student.

I give my sincere thanks to my supervisor Giacomo Squicciarini. His zeal, integrity and patience have motivated and encouraged me so much in my study. His expertise in experiment and modelling has indispensably benefited my research.

I would like to acknowledge my sponsor, Beijing Institute of Structure and Environment Engineering, for its financial support. I am grateful for the studentship which covered my study and living fees for more than three years.

I give my sincere thanks to the many academics and colleagues who have supported my thesis: Lorenzo Dozio and Serkan Guler have generously shared their research outcomes with me; David Thompson and Jordan Cheer have provided insightful and inspiring suggestions for my work; Christopher Knuth, Xiaowan Liu, Wenjing Sun, Boniface Hima and Sorawit Limthongkul and other PhD students in my research group all offered me practical help in my research. Thank you!

I would like to acknowledge the High Performance Computing facility and services in University of Southampton, which are essential for me to produce the numerical results in this thesis.

Finally, I want to thank my beloved wife, son and parents. They have made many sacrifices in order that I could pursue my PhD degree. Thank you!

Chapter 1 Introduction

1.1 A brief overview of acoustic fatigue

The purpose of this research is to improve the prediction methodology for the structural response and the subsequent fatigue life due to acoustic excitation. Particular attention will be devoted to the vibroacoustic response of thin-walled structures. Immediate applications of this study are in acoustic fatigue for aerospace applications, where plate-like and cylindrical components are utilized in aircraft or spacecraft fuselage and wings or control surfaces and are typically acoustically excited by either jet or rocket noise respectively. A brief introduction and overview of the key features of acoustic fatigue follows.

Acoustic fatigue is dynamic structural fatigue due to the behaviour possessing high frequency stress reversals due to acoustic excitation. A sound pressure level (SPL) of above 100 dB is usually assumed and the structural response may range from remaining linear to behaving in a nonlinear manner. These stresses/strains may have relatively small amplitudes compared to those caused by other types of loads, but they usually occur at high frequencies, so the fatigue damage can accumulate and happen in a relatively short period of the operational service. An extreme example of a skin panel that was damaged by acoustic fatigue is shown in Figure 1-1, which is taken from an acoustic fatigue test [1]. Acoustic fatigue prediction typically determines how long the structures can survive in an acoustic environment. The prediction process may sequentially cover the modelling of the acoustic excitation, the estimation of the structural vibration and the estimation of the fatigue life. Temperature or thermal loading is also a necessary input parameter in the application to launch vehicles or high-performance aircraft.



Figure 1-1 A cracked panel due to acoustic fatigue [1].

In the late 1950's, acoustic fatigue failures were first reported in aircraft structures exposed to sound pressure fluctuation produced from the jet engines. The fatigue failure due to the random loading was first investigated and idealised by a single degree of freedom modal response system by Miles [2]. He applied the Palmgren - Miner hypothesis of cumulative fatigue damage in the subsequent fatigue life estimation [3]. This work was subsequently extended to accommodate the full multi-modal response of a continuous system by Powell [4]. The Joint Acceptance Function (JAF) was then also introduced to describe the spatial coupling between the pressure loading and the structural modes. In the light of practical aerospace structures, such as flat plates, control surfaces and stiffened plates, Clarkson simplified the prediction by assuming a predominant fundamental modal response and in-phase pressure over the structure surface [5], which gave a conservative estimate of the stress. Up to the mid 1970's, with considerable work being done [6, 7] to develop applicable techniques from interdisciplinary research, the acoustic fatigue problems became mature enough to be addressed in design guidelines [5, 8-10] and generally became less of an issue.

Renewed emphasis returned to theoretical study of acoustic fatigue in the mid 1980's, when the new generation of aircraft/spacecraft with hypersonic or 'vertical/short take-off and landing' (V/STOL) configurations were being considered. Nonlinear response problem, appeared due to the increased acoustic loads [11] and higher performance requirements. A wide range of early studies were conducted to pursue analytical solutions [12-17], but the most feasible numerical approaches, finite element methods (FEM) [18-23] and the Monte Carlo simulation [24], became prevalent in the early 1990's. The subsequent fatigue life estimation methods were also developed for the nonlinear response [25-30]. New structural configurations such as composite structures were also considered [18, 31, 32]. The new interests promoted a research collaboration at a European level with a Brite Euram project, ACOUFAT [33]. It considered constructions with advanced materials and structural arrangements. Over the next decade, many attempts were made to overcome the computational challenges and improve predictions for modern design configurations, concerning the nonlinear effects coupled with the thermal and aerodynamic loads [1, 34].

A literature review is given in the following section. It is structured over four main corresponding aspects including vibroacoustic response, nonlinear vibration, fatigue life estimation and thermal loading.

1.2 Literature review

1.2.1 Vibroacoustic response

Structures characterised by high stiffness and low mass are typically required in aerospace applications; examples include launch vehicle fairings and aircraft fuselages. Stiffened, thin plates or cylindrical shells are often used in this context. These structures are most likely to be excited by high intensity sound fields and their vibroacoustic responses can subsequently lead to major concerns for acoustic fatigue and sound transmission. In addition, thin structures can exhibit important vibroacoustic coupling phenomena that on some occasions need to be taken into account.

This section reviews a few of the methods that have been developed and used to predict vibroacoustic structural response. The structural and the acoustic models, either separately or coupled, have all typically been linear. When the acoustic excitation levels are very high, the structural response becomes geometrically nonlinear, which cannot be predicted accurately by the linear models. This will be addressed in the Section 1.2.2.

1.2.1.1 Joint Acceptance Function (JAF)

The structural response to acoustic excitation can be calculated by making use of the Joint Acceptance Function (JAF) in a modal approach. The JAF is a spatial coupling factor between the structural mode shape and the surface pressure distribution. Mathematically it is defined as the ratio between the modal force due to a specific sound field and the overall static force due to a uniform pressure field [4].

For example, the JAF for a sound field acting on a rectangular plate can be written as [35]

$$j_n(\omega) = \frac{\int_0^b \int_0^a \psi_n(x, y) p(x, y, \omega) dx dy}{p_0 ab}, \quad \text{Eq.(1-1)}$$

where $j_n(\omega)$ is the JAF for the n^{th} mode at the angular frequency of ω , $\psi_n(x, y)$ is the mode shape of the n^{th} mode, a and b are the dimensions of the plate, and p_0 is an equivalent uniform pressure field. In the case of baffled plates, p_0 corresponds to a doubling of the pressure amplitude of the incident field ignoring the re-radiation. JAF indicates how efficiently the n^{th} mode can be excited when subjected to the particular sound field $p(x, y, \omega)$ in comparison to a uniform excitation.

Figure 1-2 shows the JAF for the first 4 modes of a rectangular plate calculated using Eq.(1-1). The four edges of the plate are simply supported, so that the mode shapes as well as the

structural bending wavelength have exact analytical expressions but other boundary conditions have been considered. In the calculation, a plane wave with an incident angle of $\pi/4$ to the x direction and normal to the y direction is assumed. The edge along the x direction is set to be 0.8m and that along the y direction is 0.3m. As here, the JAFs can and are often plotted against the ratio of the structural wavelength to the acoustic trace wavelength, so that they are independent of the incident angle and the structural dimensions. In this example, this wavelength ratio along the ordinate axis is zero, as the acoustic trace wavelength is infinite in that direction. The wavelength ratio, given along the abscissa axis, is proportional to frequency for each mode with a given structural wavelength.

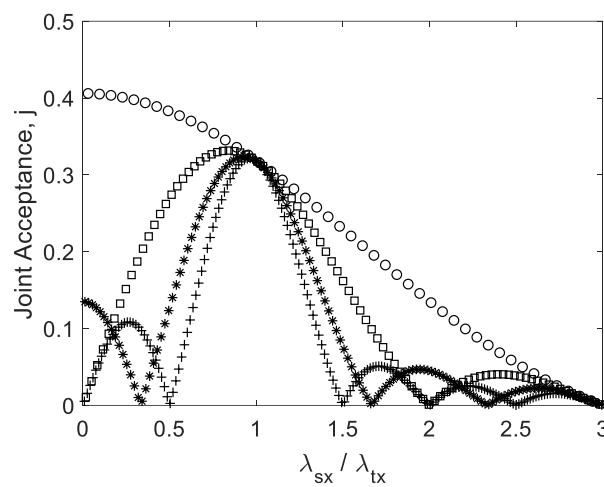


Figure 1-2 The variation of the JAF for a simply supported rectangular plate excited by a plane wave travelling parallel to two opposite edges and at an angle to the other edge producing the structural-acoustic (trace) wavelength ratio $\lambda_{sx}/\lambda_{tx}$ in the direction of propagation. Circle markers 'o': the 1st mode. Square markers '□': the 2nd mode. Asterisk markers '*': the 3rd mode. Plus sign markers '+': the 4th mode.

The result demonstrates some apparent behaviour of the JAF. Firstly, the JAF, being a non-dimensional factor, measures the effectiveness of the sound pressure for exciting modes in its variation over different modes and different structural-acoustic wavelength ratios. Secondly, when the acoustic trace wavelength matches the structural wavelength at the coincidence frequency $\frac{\lambda_{sx}}{\lambda_{tx}} = 1$, a maximum appears in the corresponding JAF for all but the 1st mode, which is the coincidence effect. Thirdly, the remaining wavelength ratio domain for the JAF consists of harmonic peaks and valleys. This is the acoustic wavelength selectivity of the JAF due to the cancellation of wavelength harmonics in the modal force distributions [36].

The JAF can apply to any types of sound fields, which can be random in time and space, such as random diffuse fields and turbulent boundary layer (TBL). In these cases, instead of using the exact description of the pressure distribution, the spatial correlation of the pressure field

is used to evaluate the JAF [4]. One numerical example of this was presented by Wallace in [37]. The correlation coefficients were used to calculate the JAF for a random plane wave excitation. The calculation was also extended to the random diffuse field by averaging the JAF over all spatial incident field directions in the half-space above the plate.

The pressure correlation also affects the JAF behaviour. The work of Bozich [36] shows that the mode shapes lose their acoustic wavelength selectivity as the pressure correlation decreases. The JAFs for different modes coalesce at high frequencies. Some approximations of particular pressure fields can be made to simplify the calculation of JAF. The in-phase pressure was firstly assumed for jet noise by Clarkson [5]. Together with the assumption of a predominant modal response at the fundamental frequency, the mean square stress at any point on a panel is given by a simplified equation which can be readily applied in flat plates, control surfaces and integrally stiffened panels. The estimated stress levels were within a factor of twice the measured values despite the coarse simplifications. One consequence of the in-phase pressure assumption is that the response of all of the antisymmetric modes is lost, which is not the case for other sound fields like TBL. Blevins [38] later approximated the surface pressure distribution by the mass-weighted mode shapes, which effectively makes the JAF equal to unity and avoids the numerical integration. This approximation provides a conservative estimation and over predicts the subsequent structural response.

In the aforementioned literature the JAF is used to describe the coupling from the pressure field to the vibration (structural modes), but not vice versa. It means that the JAF method effectively leads to an uncoupled solution, without including the re-radiated pressure caused by the structural vibration. Generally, because of the low density of air compared to the structural material, this re-radiated pressure is small enough to have a negligible effect on the structural vibration. However, the vibroacoustic coupling might play a significant role for lightweight stiff structures such as spacecraft antenna [39]. As an attempt to move the current state of the art forward, the JAF has also been included in the calculation of the radiation quantities and consequently used to describe a fully vibroacoustic coupled model in this research.

The JAF can also be applied to curved structures. The JAFs for rings and cylinders subjected to reverberant fields and TBL have been listed in an ESA manual [40]. Coyette [41] extended the calculation to include truncated conical geometry and provided an efficient method of evaluating the JAF for a diffuse field excitation by using an alternative form of the spatial correlation function. However, the scattering effect of the sound is not included in the analysis.

Wenzel [42] derived the pressure correlation for an infinite cylinder in a diffuse sound field taking into account the rigid scattering effect. His numerical result shows that the rigid scattering effect significantly influences the spatial correlation around the circumference, whilst it has little effect along the axial direction. He also demonstrated the different asymptotic behaviours of the JAF between the flat plate and the cylinder [43].

To explore the sound scattering effect in a wider context, this research investigates the acoustic response of cylinders subjected to both incident plane and spherical waves. The effects of the stiffeners and vibroacoustic coupling are also investigated.

1.2.1.2 Structural modelling

The most typical structure used in aerospace vehicles are curved shells stiffened by longitudinal stringers and circumferential frames, as shown in Figure 1-3 for an example of an aircraft fuselage component.

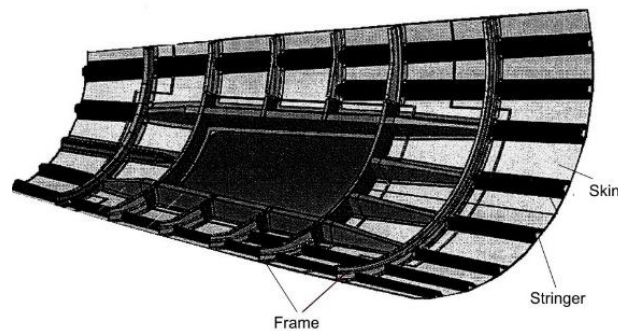


Figure 1-3 An aircraft fuselage component stiffened by stringers and frames [44].

If the curvature is low (shallow), these structures can be considered as stiffened plates. Clarkson [5] presented an approximate model of stiffened plates based on the Rayleigh-Ritz energy method. A panel made up of many plates was used to take into account the bending effect of stiffeners. A more detailed and complete analysis can be achieved by considering the compatibility conditions. In an example of a four-plate box structure, Abrahamson [45] applied the continuity condition (displacement and rotation) and the moment equilibrium at the plate intersections, which yield four independent sets of equations. They were then solved by the Newton-Raphson iteration. The assumed-modes approach have been used [46, 47] for structures with light stiffeners; usually the in-plane motion of the plate is neglected and the plate-stiffener interface is treated as a line.

Another common type of structure is the stiffened cylinder where the curvature effect cannot be neglected. The current methods for the modelling of stiffened cylinders are classified as

the discrete approach [48] and the 'smeared' stiffness approach [49]. For orthogonally stiffened cylinders, a design guideline for the estimation of the lower natural frequencies and mode shapes, of either the flexural or the torsional vibrations, is provided by ESDU [50]. Rosen and Singer [51] derived three sets of equilibrium equations and boundary conditions from Donnell [52] and Flügge [53] theories for stiffened cylinders. A good agreement was achieved for the natural frequencies and mode shapes between the theory and corresponding test results. Wang et al. [54] extended the Rayleigh - Ritz method for solving the free vibration problem of cylindrical shells with varying ring-stiffener distributions.

In comparison with stiffened plates, the stiffeners may produce different effects on the modal characteristics of the cylindrical shells due to the coupling of extension and bending motion around the circumference. The influences of the eccentricity, in addition to the in-plane and the rotary inertias of the stiffeners, were investigated with reference to an unstiffened cylinder by Parthan and Johns [55]. The effects of the number, location and material distribution of the stiffeners on the natural frequencies were examined by Wang et al. [54]. Bageri and Jafari [56] discussed the effects of the nonuniformity of the stiffener distribution on the dynamic characteristics of stiffened shells. They performed modal testing to obtain the modal characteristics of these cylindrical shells. The results provide reference data for non-uniform stiffened cylinders.

For more complex structures, it is generally not possible to derive analytical expressions. In this case, the finite element method (FEM) is usually used. With the structural dimensions, boundary conditions, material parameters and mesh dimensions, a free vibration analysis can be performed in the FE model to obtain the mode shapes and natural frequencies [57]. FEM can generally provide more accurate results as it usually involves less simplifications than an analytical model representation.

The current structural modelling techniques are mostly very mature and various tools/methods can be used depending on the specific application. To investigate the effects of stiffeners and curvatures on the vibroacoustic response, the strength and weakness of the structural modelling methods (analytical, semi-analytical and FEM) need to be explored, so that appropriate methods can be selected. In this research, this process has been applied to the examples of stiffened plates and cylinders, and in the experimental work for a scaled fuselage structure.

1.2.1.3 Vibroacoustic coupling

Numerical methods are commonly used to address the vibroacoustic coupling. They include either the finite element method (FEM) or the boundary element method (BEM). The structure is normally modelled by a FE model. The acoustic domain can be modelled by either the FEM [58] or the BEM [59] [60] [61]. Then both the vibration response and the radiated sound can be calculated by either a coupled FE-FE or a coupled FE-BE solution.

For these solutions, the compatibility and equilibrium conditions at the common surface between the structure and the acoustic domains are considered. This approach is particularly useful for in addressing the complex geometry in both structural and acoustic domains, which might not be conveniently modelled by analytical approaches. Whist this approach offers a great level of accuracy at low frequencies, it suffers from a very heavy computational cost due to the fine mesh required as the frequency increases [57]. The cost can even be prohibitively high for subsequent Monte Carlo simulations, which are required to numerically produce an ensemble of diffuse fields [62].

Various methods are available for reducing the computational cost. Starting from the early work of Mead in the periodic structures [63], the wave finite element (WFE) methodology proved to drastically reduce the problem size in terms of degrees of freedom compared to FE models [64]. Generally a small segment/periodic cell of the structure is modelled in WFE and the periodicity conditions are applied. The eigenvalue problems can be solved for the free structural wavenumbers by postprocessing the mass and stiffness matrices using the periodic structure theory. The state vectors (displacement and forces) are represented by a series of wave mode vectors. The amplitude of these wave modes under forced excitation can be obtained by using a Fourier transform and contour integration. Then the response at any point of the structure can be determined. Renno [65] applied this method to predict the forced response of a waveguide subjected to a convected harmonic pressure. This method was also applied to two-dimensional plane and curved thin-walled structures [66]. The properties of the structures can also vary through the thickness (e.g. laminated plates, sandwich panels, etc.). Numerical issues using the WFE will arise at high frequencies. The finite element discretisation errors become large if the size of the element is too large; round-off errors can occur if the element is too small. In addition, the spatial discretisation will also cause aliasing effects. These issues have been discussed by Mace [66]. For the sound radiation and transmission problems, the 2.5D FE/BE approach [67] can be adopted and is widely used in the prediction of railway noise [68]. Some analytical methods can be applied in the analysis of

the vibrations of the one-dimensional or the quasi-one-dimensional systems. They include methods based on: transfer matrices [69, 70], direct solutions [71], the space-harmonic method [72, 73] and phased array receptance functions [74]. The theory has also been developed to analyse the vibration of general two-dimensional periodic systems [75]. Particular features of the structures might be required, such as having constant cross-sections and being periodic along one direction.

Alternatively, a modal approach can be used in a coupled solution, where the total surface pressure, including the re-radiated pressure, is incorporated. Fahy [76] presented an analytical approach that included the vibroacoustic coupling for an infinite strip subjected to an incident plane wave. The total surface pressure was decomposed into two parts: the blocked pressure including the incident sound and the reflected sound from an infinitely rigid surface, and the radiated pressure due to the structural vibration. He demonstrated that, compared to a non-coupled solution, the effect of vibroacoustic coupling resulted mostly in adding damping for thin plates in air. Mejdı [47] extended this analysis to stiffened plates by using a modal expansion technique together with the full radiation impedance matrix. The spatial-averaged mean square velocity and radiated power due to a point source excitation were predicted and compared with FEM and BEM simulations to examine the effect of cross-modal contributions. The response to a diffuse field was also evaluated by using the field incidence approximation [77] and compared with measurements.

The radiated sound from the vibrating structure can also be represented in terms of modal radiation efficiencies, which indicates how effectively the vibration of one mode can radiate sound power in comparison to a vibrating piston with the same mean square average velocity. The modal radiation efficiency σ_n is defined as [78]

$$\sigma_n(\omega) = \frac{W_n}{\rho_0 c a b \langle \overline{v_n^2} \rangle}, \quad \text{Eq.(1-2)}$$

where W_n is the acoustic power radiated by the n^{th} mode and $\langle \overline{v_n^2} \rangle$ is the spatial-averaged mean-square normal velocity of the plate for the n^{th} mode. ρ_0 is the air density and c is the sound speed in air.

Compared with the JAF, which describes the coupling from the pressure field to the vibration (structural modes), the modal radiation efficiency describes the coupling from the structural modes to the radiated sound field. Hence, the radiation efficiencies are typically used to predict the sound radiation due to external forces.

Herein, a relationship between the JAF and the modal radiation efficiency has been derived. This allows a prediction to be made using a direct calculation for the vibroacoustic response and the sound transmission loss in the presence of a diffuse field whilst still accounting for full vibroacoustic coupling.

1.2.1.4 Statistical Energy Analysis (SEA) and a hybrid alternative

It is difficult to accurately predict the vibroacoustic responses of structures by the aforementioned methods at high frequencies, when the vibration modes cannot be well separated and the structural wavelength is short. A detailed representation of the model requires a large number of degrees of freedom in deterministic approaches such as the JAF and the FEM. Furthermore, the prediction accuracy becomes less reliable and is sensitive to the small details of the structure which might not be precisely determined because of uncertainty.

SEA provides an alternative method to predict the high frequency response in terms of energy levels. In SEA, broad-band excitation is assumed and the response energy is averaged in space and frequency. The whole system is divided into a set of subsystems, each of which is allocated a single degree of freedom representing the stored vibration energy. Then a power balance equation for each of them is formulated with the parameters such as modal density and the coupling loss factors in addition to the dissipation loss factors. The literature regarding SEA is extensive [79-81]. A typical aerospace application of this method to a structure was considered by Irvine [82]. He calculated the mean square, space-time averaged response of a cylindrical shell subjected to a diffuse, broadband sound field. The results were compared with an empirical method (the Franken method [83]). A good agreement was achieved above 600 Hz where the assumptions of SEA were valid.

However, the SEA method is not accurate in the low to middle frequency range. More recent hybrid methods [84, 85] exist, which couple low modal density systems, such as beams, stiffeners and frames, in a FEM model sense, with an SEA model for the high modal density parts of coupled structure (such as the plates, skin, etc.). Larko and Cotoni [39] considered the vibroacoustic response of a spacecraft antenna to launch acoustic excitation. In their analysis, the SEA method was used to estimate the high frequency response and a hybrid finite element-statistical energy (hybrid FE-SEA) model for the low to mid-frequency responses. The results were compared to the test measurement data and to a FE-BEM model. Both the hybrid FE-SEA method and the FE-BEM method agree well with the test results, but the computation time was significantly reduced in the former approach.

The SEA and a hybrid alternative are not directly relevant to the thesis. This is because they are formulated on the basis of power flow between coupled systems and the result is a frequency band average of the total vibrational energy in each system. This is not an ideal way to predict the stress response at critical points whilst the normal modes methods are applicable [86].

1.2.2 Nonlinear response

When subjected to high levels of acoustic excitation, the structural vibration response may become nonlinear, because of the geometric nonlinearity caused by the large deflection. For an example of the two-dimensional straight beam with clamped ends, the nonlinear strain-displacement equation is [87]

$$\varepsilon_x = \frac{du}{dx} + \frac{1}{2} \left\{ \frac{dw}{dx} \right\}^2$$

where u is the displacement in the in-plane x direction, w is the transverse displacement in the out of plane z direction. ε_x is the longitudinal strain. The first term in the right hand side is linearly dependent on the longitudinal displacement. The second term is nonlinearly dependent on the bending displacement and for large amplitude flexural displacements produces non-negligible membrane strains and stresses.

The nonlinearity could affect the frequency content, the amplitude and the response statistics. However, the linear prediction methods mentioned in Section 1.2.1 do not account for these nonlinear effects. The two commonly used approaches, the nonlinear finite element model (FEM) and nonlinear reduced order model (NLROM), are reviewed briefly in the following sections. A more detailed description with further relevant literature is given in Chapter 5.

1.2.2.1 Nonlinear finite element model

Nonlinear FEM has become the most feasible numerical approach since the mid 1980's [11] [18-23] when the nonlinear finite element codes became available. The codes are based on the FE equation of motion including geometric nonlinearity [87]

$$\mathbf{M}\ddot{\mathbf{w}} + [\mathbf{K} + \mathbf{K}_1(\mathbf{w}) + \mathbf{K}_2(\mathbf{w}, \mathbf{w})]\mathbf{w} = \mathbf{f}(t) \quad \text{Eq.(1-3)}$$

where \mathbf{w} is the nodal displacement and \mathbf{f} is the nodal force. \mathbf{M} and \mathbf{K} are the linear mass and stiffness matrices. \mathbf{K}_1 is the quadratic nonlinear stiffness matrix (a linear function of \mathbf{w}) and \mathbf{K}_2 is the cubic nonlinear stiffness matrix (a quadratic function of \mathbf{w}).

The nonlinear finite element codes have been implemented in commercial FE software such as Abaqus. By building the structural model, defining the acoustic loadings and selecting an appropriate numerical integration scheme [88], the nonlinear response (displacement and stress) can be obtained in a converged nonlinear solution. However, the computational cost of using nonlinear FEM for a complex structure subjected to random acoustic loading is very high. This is because the nonlinear stiffness matrices, \mathbf{K}_1 and \mathbf{K}_2 in Eq.(1-3), that usually possess many thousands of degrees of freedom, must be instantaneously updated within the time step t that should be small enough to resolve the highest frequency of interests. Industrial users have supercomputers that are able to solve the high dimension nonlinear FE models, but it still takes huge computational memory space and long solution time for complex structures and extended time histories. In an example which will be given in Chapter 5, a memory storage of 48 GB and a solution time of 600 hours are required for a stiffened plate with 64062 DOFs using the Iridis High Performance Computing (HPC). This computational cost, even for a supercomputer, is currently prohibitive for the nonlinear FE modelling to be used in an early design stage or trade-off study.

1.2.2.2 Nonlinear Reduced Order Model (NLROM)

The nonlinear reduced order model (NLROM) has been established and rapidly developed over the past few decades [87, 89]. It is essentially a FE-based modal approach, which has proven to be much more efficient than a full order nonlinear FEM. The large number of the physical DOFs in Eq.(1-3) can be reduced to just a few modal DOFs by using the modal transformation and truncation. Meanwhile, the nonlinear stiffnesses \mathbf{K}_1 and \mathbf{K}_2 can be approximated by a few polynomial terms with constant coefficients; the latter can be evaluated via a one-off static nonlinear characterisation.

NLROM has been successful applied to simple structures such as straight beams and flat plates [1, 90] and the effects of the modal basis and static identifications [34, 91, 92] have been widely discussed. For those structures, the bending modes and membrane modes are linearly independent and only nonlinearly coupled. The application has also been extended to structures possessing the linear coupling of the in-plane and out-of-plane motions, such as for a moderately stiffened plate [90], shallow curved beams [93] and shallow curved panels [87].

However, the implementation of NLROM has rarely been examined for structures with deep stiffeners and/or high curvature such as stiffened cylinders. For these structures, apart from the linear and nonlinear coupling between the bending and the membrane modes, the complex structural configurations might have significant effects on the nonlinear static and

dynamic response of the structures as well as on the statically applied loadings. Therefore, the implementation of NLROM, its wider structural geometry application and its comparison with a full order FE model for these structures should be studied. In addition, the thermal effect on the implementation of the NLROM should also be examined.

1.2.3 Acoustic fatigue life prediction

Acoustic fatigue is a safety concern for structures with high levels of acoustic introduced vibration [94]. The amplitudes of the vibration are typically still within the elastic deformation range of the structural material, although the loading can be high enough to exercise the geometric nonlinearity of the structure. So acoustic fatigue failure normally occurs over many cycles of higher frequency vibration. However, the structures are still at risk of failure in a relatively short period of time, as high frequency components are usually contained within the acoustic excitation and the subsequent responses.

The inputs for the fatigue life calculation include the information on the fatigue failure of the material, usually provided by an experimentally obtained curve (S - N curve, that is the stress (S) to the number of cycles (N) to failure), and the response data. Different methods for the estimation the acoustic fatigue life have been developed and are well documented [95-97]. Given the $S - N$ curve, the accuracy of the estimated fatigue life is dependent on whether an appropriate method is used and whether the response data is accurate.

Depending on the required type of the response data, the methods can be categorized as either time domain methods [96] or spectral methods [97]. Miles [98] reviewed different methods for estimating the fatigue life due to random loading. Benasciutti et al. [99] reviewed the frequency domain methods for multi-axial fatigue analysis. Bishop and Sherratt [100] reviewed the traditional statistical tools available for the fatigue life calculation from power spectral density data.

1.2.3.1 Time domain methods

The idea of the time domain methods is to count the stress cycles in the response time histories; the latter are often obtained from FEM simulations. Different cycle counting algorithms can be implemented, such as the level-crossing counting [101], the peak counting [101, 102] and the rainflow counting methods [103-107]. Among them, the rainflow cycle counting methodology [103-105] is considered as the most accurate technique. A detailed introduction of the latter can be found in the design guidance of ESDU [50].

One limitation of the time domain approach is the high computation cost, increasing with the number of sample points, especially when processing the random time histories of finely meshed 3-D FE models [108].

1.2.3.2 Frequency domain methods

The early spectral methods, outlined in [94], are applied to the vibration responses assuming stationary, Gaussian and narrow band random processes. Typically, the latter assumptions are applicable for the response of lightly damped, single degree of freedom (SDOF) systems subjected to broadband random excitation. In this latter case, analytical expressions in the form of the Rayleigh distribution exist for the rainflow cycle stress range probability density function (PDF). An essential part of the method is the estimation of the lowest resonance frequency in bending or flexure of different structures, including plates, cylinders and box structures.

However, multi-modal random responses are generally expected for structures with continuous mass and stiffness distributions and one cannot represent the response as being dominated by the fundamental mode. In this sense, a damage correction factor can be introduced into the Rayleigh approximation to represent the wideband process with an equivalent narrowband process, i.e. the Rainflow damage factor method [109]. A semi-empirical method, namely Dirlik's method [110], was developed and is mostly widely used as a spectral method to accommodate the multi-modal response. In this method the PDFs for the stress ranges of the rainflow cycles are postulated as a function of the spectral parameters or statistical moments. A Gaussian process is assumed in Dirlik's simulation to perform the Inverse Fourier Transform. However, this assumption is usually not valid for the response of nonlinear systems to the excitation with a Gaussian distribution. The nonlinear response probability distribution may be non-Gaussian [87, 111].

1.2.4 The thermal loading effect on response and fatigue

Temperature changes in constrained structures introduce thermal stresses [112]. The thermal stresses in simple structures such as plates, cylindrical shells and spherical shells have been investigated by Timoshenko [113]. The thermal stresses consequently influence the dynamic properties of structures and affect the vibration response to acoustic excitation and the subsequent fatigue life.

1.2.4.1 Analytical and numerical methods

Different types of thermal loading distribution introduce different effects on the vibrational behaviour of structures. For simple temperature distributions, a number of representative examples of thermal stresses estimations were summarised in the textbook 'Roark's Formulas for Stress and Strain' [114]. Sundara Raja Iyengar and Chandrashekhara [115] developed a Fourier series based method to determine the thermal stresses in a flat plate with arbitrary in-plane temperature distribution. Lee [116] investigated the dynamic response of plates and shells at elevated temperatures. The thermal effects of the global expansion due to uniform temperature, the local expansion due to temperature variation and the thermal moment due to temperature gradient across the plate thickness were examined using the single-mode model of Galerkin's method. Mei et al. [23, 117] presented an efficient finite element method for the prediction of the nonlinear response of composite panels at elevated temperatures.

The thermal stress may also cause snap-through buckling [118]. Snap-through buckling is a mode of instability where the excited structures may pass from an equilibrium state to a non-adjacent equilibrium configuration. An experimental investigation of the acoustically excited random motion of a plate which is buckled due to thermal stress was made by Ng and Clevenson [119]. The results indicated that the effects of the snap-through behaviour on fatigue damage may only occur when a plate or a shallow shell is fully clamped. Lin and Yeh [120] conducted an analytical and experimental study on the buckling behaviour of cylindrical shells. It was found that the ratio of the length to radius and the boundary conditions had little influence on the buckling loads, but they caused a variety of post-buckling behaviours.

The thermal stress may also influence the fatigue life of structures. The fatigue life estimations for panels, subjected to acoustic excitation and exhibiting a snap through behaviour under compressive loads possibly due to thermal loading, have been investigated [121, 122]. Ge et al. [123] developed a plane model based on shear strain to predict the fatigue life of metallic structures under combined thermal-acoustic loading. A comparison with the uniaxial Goodman model showed that this model is conservative, indicating thermal loading can significantly reduce the fatigue life. A reduced order model based on the FEM was presented by Radu et al. [26] to predict the response to thermal-acoustic loading and subsequent fatigue life on panels. An improved computational efficiency was achieved to generate a long time history for the stresses that were subsequently used for the fatigue life estimation.

1.2.4.2 Test facilities for thermal-acoustic test

Experimental test facilities are indispensable tools for validating acoustic response/fatigue predictions subjected to thermal-acoustic loadings during their operational life. Figure 1-4 shows the acoustic fatigue facility (AFF) at BAE systems in the UK [124]. It was designed to provide capabilities for high levels of acoustic excitation in conjunction with thermal loading and static in-plane loading for the development of V/STOL aircraft. The sound source can produce controlled sound in the frequency range 30Hz – 500Hz with sound pressure levels (SPL) up to 175dB. The thermal loading up to 800°C can be applied to the specimen by an in-house heating system, with rise/cooling rates between 20°C and 700°C in 30 seconds. Static in-plane loadings of up to 70 tonnes can be applied to the specimen. Test specimens with various shape and sizes (up to 1.2m×2.5m) can be tested with different acoustic field and loading conditions.



Figure 1-4 The acoustic fatigue facility (AFF) in BAE systems [124].

Figure 1-5 shows the thermal acoustic fatigue apparatus (TAFA) in the Langley Research Centre in the US [119, 125]. It can simulate a grazing incident sound field with SPL up to 168dB and the frequency range 40Hz – 500Hz for both harmonic and random acoustic loadings. It has a heating capability of 1093°C.

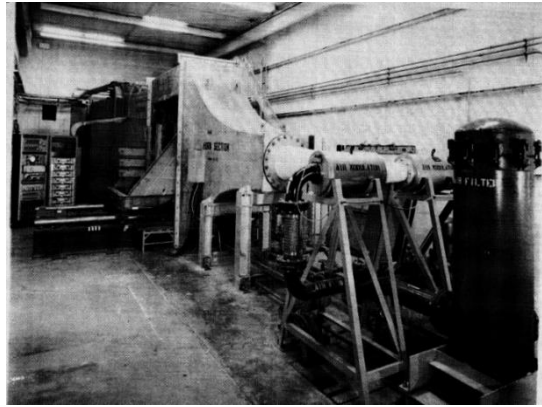


Figure 1-5 The thermal acoustic fatigue apparatus (TAFA) in the Langley Research Centre [119].

Figure 1-6(a) - Figure 1-6 (c) show the high intensity acoustic testing facilities in the Wright Laboratory in the US [126].

Figure 1-6 (a) shows the random fatigue chamber. It provides a random force output up to the root mean square (RMS) value of 89,000 N. The chamber is coupled with an environmental chamber operating from -157°C to 1427°C . It can be used to determine the influence of temperature and pressure on materials for hypersonic structures.

Figure 1-6 (b) shows the sub-element chamber. The progressive wave tube (PWT) can provide acoustic loadings of SPL up to 180dB. The maximum temperature is 1371°C . The size of the testing structure is up to $0.3\text{m} \times 0.6\text{m}$.

Figure 1-6 (c) shows the combined environment acoustic chamber. It was designed for the testing of structures at temperatures up to 1648°C and SPL up to 180dB.

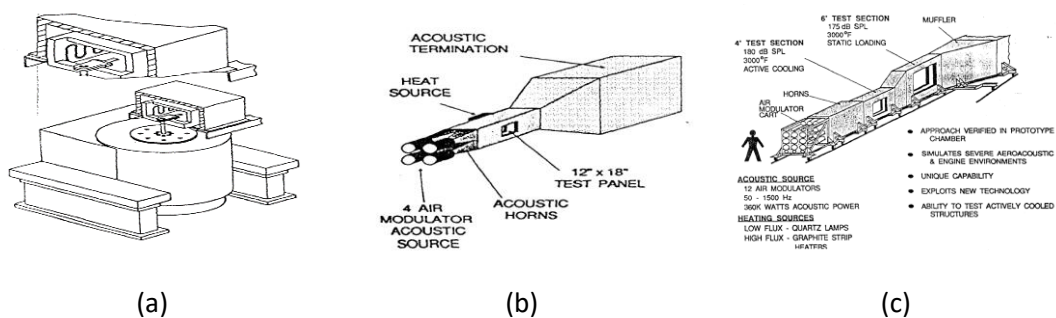


Figure 1-6 The high intensity acoustic testing facilities in the Wright Laboratory [126]. (a) The random fatigue chamber. (b) The sub-element acoustic chamber. (c) The combined environment acoustic chamber.

Figure 1-7 shows the thermal-acoustic test inside the reverberation chamber in Industrieanlagen-Betriebsgesellschaft MBH (IABG) in Germany [127]. It was developed to satisfy the test requirements relating to reusable spacecraft, hypersonic vehicles and advanced launchers. A flaming heating system providing temperatures up to 1300°C is mounted in a reverberation chamber or installed in a PWT. The former can provide controlled

noise in the frequency range 100Hz – 10kHz at SPLs up to 155dB, while the latter can provide noise in the frequency range 50Hz – 10kHz at SPLs up to 160dB for a test section of size 0.8m×1.2m. The test structure in Figure 1-7 is the tank structure of the European launcher ARIANE 5 [127].

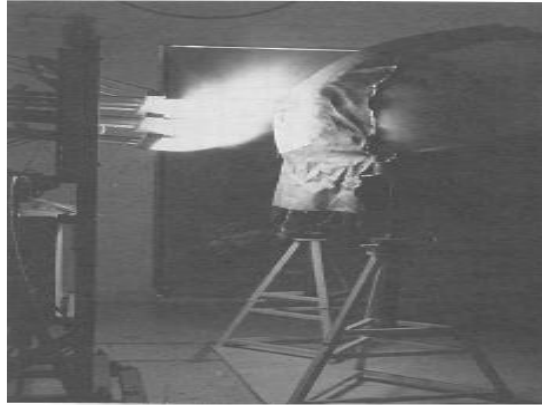


Figure 1-7 The thermal-acoustic test inside the reverberation chamber in Industrieanlagen-Betriebsgesellschaft MBH (IABG) [127].

The description of thermal-acoustic testing is brief and not directly relevant to the thesis. This is because such testing requires dedicated facilities, which were not available during the timescales of this study.

1.3 Research questions and the original contributions

1.3.1 Aims and research objectives

As presented earlier, various methods have been developed for vibroacoustic predictions and a few of them have been reviewed in Section 1.2.1. However, for complex structures and loading conditions typically present in aerospace applications and especially for a coupled vibroacoustic analysis, the numerical methods suffer from high computational costs and poor physical interpretation, while the applicability of the analytical methods is limited to simple cases. It is clear that an efficient and accurate framework with concise formulations that capture the behaviour of the main quantities is necessary for evaluating the vibroacoustic responses.

The majority of the previous investigations comprised flat panels being excited acoustically with few works relating to curvature. It was not until the early 2000s [128-133] that the response of curved shells under acoustic excitation was addressed more systematically. Even then, the same assumption of a single fundamental mode being dominant in the response was not changed, which was typically restricted to the shallow shell assumption [38, 134-139].

High curvature in structures such as cylinders significantly affects either the structural dynamics or the way acoustic loads excite the structure. Further investigation of the acoustic response of cylinders is necessary.

Many methods have also been developed to address the nonlinear effects such as the nonlinear reduced order model (NLROM). The efficiency and accuracy of NLROM have been well proven over a full order finite element model (FEM) for structures such as moderately stiffened plates and shallow curved panels. However, the application of NLROM has rarely been examined for more complex structures, such as those with deep stiffeners and/or high curvatures. These structural features may pose challenges in the implementation procedures of NLROM such as nonlinear characterisation and numerical integrations. In addition, the thermal effect should also be examined.

The overall aims are thus to improve the vibroacoustic prediction methodologies for acoustic fatigue applications, by development of efficient and accurate methodologies that are capable of handling complex structural arrangements (e.g. curvature and stiffening) in addition to nonlinear response (due to high excitation levels) and high temperature effects.

In particular, the detailed objectives of this PhD work are to investigate four research questions:

- Research question 1: How to improve or reformulate the existing simplified methodology for estimating the vibroacoustic response of stiffened plates? (Chapter 2)
- Research question 2: Can the prediction method be extended to analyse and predict the behaviour of cylindrical, orthogonally stiffened cylinders? If it can be extended, then produce the required formulation. (Chapter 3 and Chapter 4)
- Research question 3: How to incorporate the effects of the nonlinear response and elevated temperature into a general, efficient and accurate structural response prediction? (Chapter 5)
- Research question 4: What are the consequences of vibroacoustic coupling, geometric structural nonlinearity and elevated temperature on the subsequent acoustic fatigue life? (Chapter 6)

All of these questions, when addressed, will require validation either experimentally or numerically via simulations using accepted existing typically numerical methodologies for comparison.

1.3.2 Original contributions

The overall aims and objectives have been achieved by the original contributions from the three research questions.

For research question 1, a new framework for evaluating the coupled vibroacoustic response of flat plates, stiffened or not, to incident sound in terms of some of the existing formulated vibroacoustic quantities, namely modal radiation efficiency and/or Joint Acceptance Functions has been produced. Compared to similar studies ([76] [47]), the proposed approach gives a concise step by step formulation which only requires the in-vacuo modal parameters and extends the applicability to finite, stiffened plates with arbitrary boundary conditions subjected to either plane wave or diffuse field excitation. In addition, a significant computational reduction is achieved whilst retaining good accuracy compared to a fully coupled, numerical FE-BE solution. This work has been included in a conference paper [140] and a journal paper [141].

For research question 2, the modal model is extended and applied to stiffened cylinders subjected to both spherical wave and plane wave sound fields. Within this model, different excitation assumptions, including the blocked pressure and the doubling of the incident pressure can be compared, and the full vibroacoustic coupling can be accounted for by including radiation damping. A set of tests and measurement on a ring-stiffened, thin-walled aircraft fuselage model have been carried out to investigate the predictions of the surface pressures and the subsequent vibration responses for the stiffened cylinder in the context of a practical structure. Part of this work has been included in a conference paper [142].

For research question 3, the linear analysis for a stiffened plate and cylinder from research questions 1 and 2 has been extended to include a nonlinear analysis by applying a geometrically nonlinear reduced order model (NLROM). The effects of the nonlinear characterisations and the time integrations have been investigated and the thermal loading is incorporated in NLROM by introducing a suitable representative boundary conditions at the elevated temperature.

For research question 4, use was made of the vibroacoustic model (developed in Chapter 2) and the NLROM (extended in Chapter 4) for the stiffened plate to produce the response data with different physical and environmental conditions. The consequences of using the proposed model for fatigue life estimation have been investigated in terms of the sensitivity to the vibroacoustic coupling, the nonlinearity and the elevated temperature on the fatigue

life prediction. It is planned to work toward a journal publication for the research undertaken in this area.

One can envisage that the procedure presented in the remainder of this work can be used in the early stage design and optimisation of aerospace structures operating in harsh environmental (temperature and acoustic) conditions.

1.4 Thesis structure

The rest of this thesis is divided into the following chapters.

Chapter 2 presents a linear modal model that predicts the vibration response and sound transmission through stiffened thin plates excited by different forms of incident sound field. Firstly, a detailed description of the model is given. The model is then applied to an example stiffened plate. The numerical results are produced for the structural model, dynamic response and sound transmission. Results from simple formulae from earlier literature are also reported for reference. Finally, a comparison between the modal and a fully coupled FE-BE solution implemented in a commercial software is presented.

Chapter 3 presents a linear modal model that predicts the surface pressure and vibration response of stiffened cylinders subjected to both plane wave and spherical wave excitations. Firstly, the total surface blocked pressure for the plane wave and the spherical wave excitation are revisited. The Joint Acceptance Functions (JAFs) based on both the blocked pressure and the doubling in pressure for the plane wave excitation are then derived for an unstiffened cylinder with shear diaphragm end boundary conditions. The numerical results for the dynamic responses are then given for cylinders with different stiffener configurations and surface pressure assumptions, including the doubled pressure and the blocked pressure with rigid scattering from the structure surface. Finally, the response of the unstiffened cylinder subjected to the blocked pressure are also compared with that from a coupled FE-BE model.

Chapter 4 describes and reports on tests and measurements on a ring-stiffened, thin-walled aircraft fuselage scale model. The aim is to investigate the predictions of the surface pressure and the subsequent vibration responses for the stiffened cylinder in the context of a practical structure. The finite element method, instead of the normal mode method, is used for the complex test structure. First, the mobility of the test structure was measured by an instrumented impact test and was compared with the results from several different FE models. Then the acoustic test was performed in the anechoic chamber to examine both the excitation and the response models for the cylinder subjected to a spherical wave.

Chapter 5 investigates the nonlinear response of stiffened plates and cylinders subjected to high level acoustic excitations based on the nonlinear reduced order model (NLROM). Firstly, the effects of the modal basis selections, the static loading scheme, the time integration and the thermal loading for the nonlinear characterisation and the subsequent response predictions are examined. Then the two example structures studied in Chapters 2 and 4 are revisited to illustrate the effects of different NLROM configurations as well as the effects of stiffeners, curvature and elevated temperatures.

Chapter 6 investigates the consequences of the NLROM predictions on the fatigue life estimation. Firstly, available published spectral methods are compared with the time domain rainflow counting approach, highlighting the effect of the multi-modal response. Then, the assumptions inherent for the vibroacoustic coupling, nonlinearity and elevated temperatures are applied to a numerical model of a stiffened plate. The vibration response for the latter is then investigated for the fatigue damage using the rainflow counting approach. The nonlinear reduced order model (NLROM) is used in parallel for the dynamic response prediction. The estimated fatigue life is also compared using the NLROM response predictions with those coming from a full order FE model simulation.

Conclusions and recommendations for future work are briefly summarised in Chapter 7. There is scope for future studies, including improvements to the NLROM methodology, solving potential limitations, as well as some experimental validation.

Chapter 2 Vibroacoustic response of stiffened thin plates to incident sound

This chapter proposes a linear modal model for prediction of the vibration response and sound transmission through stiffened thin plates excited by different forms of incident sound field. Vibroacoustic coupling is maintained in the solution by deriving relationships between the modal radiation efficiency and Joint Acceptance Functions (JAF) for baffled stiffened plates. The response for different structural configurations, plane versus diffuse acoustic excitation and modelling approximations are discussed to present a systematic quantification of the factors influencing the vibroacoustic response.

2.1 A vibroacoustic model for flat plates excited by a sound field

Figure 2-1 (a) shows a generic set-up and convention for a rectangular plate excited by an incident harmonic acoustic plane wave. Figure 2-1 (b) shows the set-up and convention for the re-radiated sound. An infinite rigid baffle is assumed elsewhere in the x - y plane. The structure is analysed in the rectangular coordinate system (x, y, z) and the pressure field is analysed in the spherical coordinate system (r, θ, ϕ) . The origins of the two coordinate systems are the same, i.e. at the corner of the midplane of the plate as shown in Figure 2-1. The boundary conditions at the plate edges are assumed to be arbitrary in the formulation.

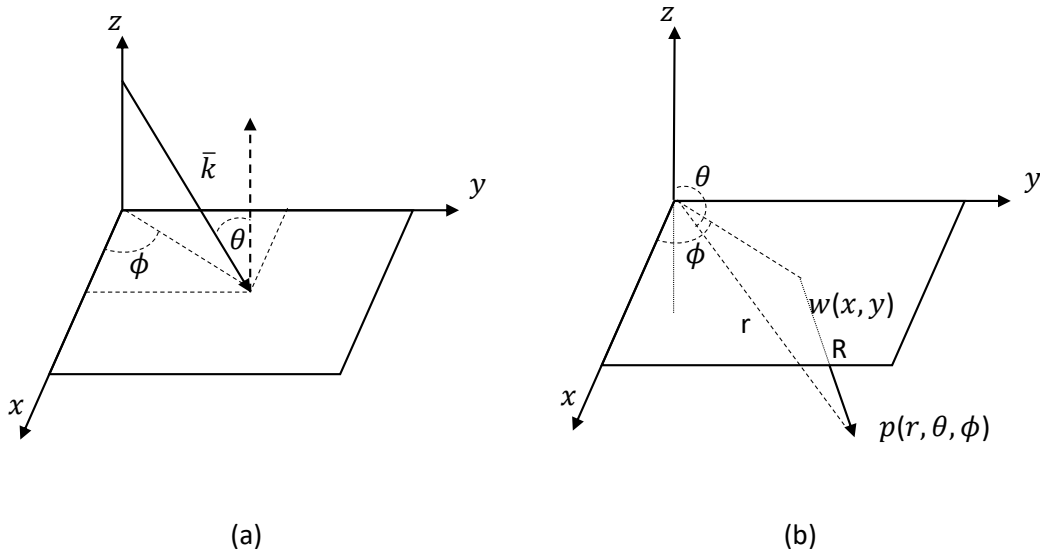


Figure 2-1 An incident wave (a) onto and a radiated wave (b) from a rectangular plate in an otherwise infinite rigid baffle. \bar{k} is the wave vector of the incident wave with the incident angle θ and the azimuthal angle ϕ . R is the distance between the observation points for radiated pressure response $p(\theta, \phi, r)$ and transverse displacement response $w(x, y)$.

2.1.1 The dynamic response for incident plane waves

Using the expansion theorem [143], the displacement response of the plate can be written as a superposition of the normal modes $\psi_{n(x,y)}$ multiplied by the corresponding time-dependent modal displacement $q_n(t)$. The displacement response of the plate is governed by the equation of motion

$$D\nabla^4 w + \rho h \frac{\partial^2 w}{\partial t^2} = p, \quad \text{Eq.(2-1)}$$

where $D = Eh^3/12(1 - \nu^2)$ is the plate flexural rigidity, ∇^4 is the biharmonic operator, ρh is the mass per unit area of the plate, ν is the Poisson's ratio, p is the transverse force per unit area, i.e. pressure. Eq.(2-1) is based on the following assumptions:

- The displacement w is small compared to the plate thickness h ;
- The normal stresses in the direction transverse to the plate can be neglected;
- Any straight line normal to the middle plane before deformation remains a straight line normal to that plane during deformation.

The displacement w can be expressed in the form of normal modes as

$$w(x, y, t) = \sum_{n=1}^{\infty} \psi_n(x, y) q_n(t). \quad \text{Eq.(2-2)}$$

where the normal modes $\psi_n(x, y)$ satisfy the Eq.(2-1) for $p = 0$ and for the boundary conditions of the plate.

In the frequency domain, Eq.(2-2) can be written as

$$w(x, y, \omega) = \sum_{n=1}^{\infty} \psi_n(x, y) q_n(\omega). \quad \text{Eq.(2-3)}$$

The time harmonic dependency $e^{i\omega t}$ and the symbol for real part Re are neglected throughout the thesis. The modal displacement $q_n(\omega)$ is a complex amplitude for the n^{th} mode and depends on the excitation on that mode.

When the plate is excited by an incoming plane wave, the pressure field can be expressed as

$$p(x, y, \omega) = p_A e^{-ik(x \cos \phi \sin \theta + y \sin \phi \sin \theta)} \quad \text{Eq.(2-4)}$$

where p_A and k are the amplitude and the wavenumber of the sound field.

Substituting Eq.(2-3) and Eq.(2-4) into Eq.(2-1) and applying the orthogonality of normal modes, the modal displacement is expressed as

$$q_n(\omega) = \frac{p_0 ab j_n(\omega)}{Z_n(\omega)}, \quad \text{Eq.(2-5)}$$

where $Z_n(\omega)$ is the dynamic stiffness of the structure. It is equal to $m_n[-\omega^2 + \omega_n^2 + i\eta\omega_n^2]$, where m_n is the modal mass, ω_n is the natural frequency and η is the loss factor. p_0 is an equivalent uniform pressure field. In the case of baffled flat plates, p_0 corresponds to a doubling of the pressure amplitude of the incident field ($2p_A$), ignoring the re-radiation. j_n is the Joint Acceptance Functions (JAF) and can be evaluated from Eq.(1-1) as

$$j_n(\omega) = \frac{1}{ab} \int_0^b \int_0^a \psi_n(x, y) e^{-ik(x \cos \phi \sin \theta + y \sin \phi \sin \theta)} dx dy, \quad \text{Eq.(2-6)}$$

2.1.2 Sound radiation for incident plane waves

The sound power re-radiated from the rear side of the plate can be obtained by integrating the far-field acoustic intensity over a hemisphere with radius r .

For harmonic motion, it can be written as

$$W(\omega) = \frac{r^2}{2\rho_0 c} \int_0^{2\pi} \int_0^{\frac{\pi}{2}} |p(r, \theta, \phi, \omega)|^2 \sin \theta d\theta d\phi, \quad \text{Eq.(2-7)}$$

where ρ_0 is the air density and c is the sound speed in air. For a baffled plate coupled with the rear acoustic domain, this is equal to the transmitted sound power.

The incident sound power from the plane wave is

$$W^i(\theta, \phi) = \frac{ab p_0^2 \cos \theta}{2\rho_0 c}. \quad \text{Eq.(2-8)}$$

The sound power transmission coefficient τ is defined as the ratio of transmitted to incident sound power [76]. Hence,

$$\tau(\theta, \phi) = \frac{r^2}{ab p_0^2 \cos \theta} \int_0^{2\pi} \int_0^{\frac{\pi}{2}} |p(\theta, \phi, r, \omega)|^2 \sin \theta d\theta d\phi. \quad \text{Eq.(2-9)}$$

2.1.3 Joint Acceptance Function (JAF) and modal radiation efficiency

In order to obtain expressions for the radiation damping and for the vibroacoustic response of plates in a diffuse sound field, it is convenient to relate the JAF with the modal radiation efficiency.

The radiated pressure can be calculated for the baffled plate using the Rayleigh integral [144]

$$p(r, \theta, \phi, \omega) = \frac{-\omega^2 \rho_0}{2\pi R} \int_0^b \int_0^a w(x, y, \omega) e^{-ikR} dx dy. \quad \text{Eq.(2-10)}$$

R is the distance between the observation point and the plate surface element with displacement $w(x, y)$ in Figure 2-1 (b).

Two assumptions are made regarding the amplitude and phase terms using an approximation for R , assuming that the observation point is in the far field. In this cases, R may be approximated by r , considering $R \gg a$ and $R \gg b$. For the term e^{-ikR} , the phase is much more sensitive to the change of the distance R , so R is approximated by the geometric relation of $r - (x \cos \phi + y \sin \phi) \sin \theta$.

Applying these approximations and replacing the displacement w using Eq.(2-2), then

$$p(r, \theta, \phi, \omega) \approx -\frac{\omega^2 \rho_0 e^{-ikr}}{2\pi r} \sum_{n=1}^{\infty} q_n \int_0^b \int_0^a \psi_n(x, y) e^{ik(x \cos \phi \sin \theta + y \sin \phi \sin \theta)} dx dy. \quad \text{Eq.(2-11)}$$

The double integral in Eq.(2-11) can be related to the complex conjugate of the JAF in Eq.(2-6). Hence the radiated pressure due to the n^{th} mode can be written as

$$p_n(r, \theta, \phi, \omega) = -\frac{\omega^2 \rho_0 a b e^{-ikr}}{2\pi r} q_n j_n^*(\theta, \phi, \omega). \quad \text{Eq.(2-12)}$$

Substituting Eq.(2-12) into Eq.(2-11) and Eq.(2-7), the total sound power radiated from one side of the plate can then be expressed as

$$W(\omega) = \frac{\omega^4 \rho_0 a^2 b^2}{8\pi^2 c} \left(\sum_{n=1}^{\infty} |q_n|^2 \int_0^{2\pi} \int_0^{\pi/2} |j_n|^2 \sin \theta d\theta d\phi \right. \\ \left. + \sum_{\substack{n=1 \\ u=1 \\ u \neq n}}^{\infty} q_n q_u^* \int_0^{2\pi} \int_0^{\pi/2} j_n j_u^* \sin \theta d\theta d\phi \right). \quad \text{Eq.(2-13)}$$

The first summation inside the brackets gives the radiated power associated with each individual normal mode. The second summation represents the modal cross terms. The modal cross terms have been included in this work, but the effects of neglecting them on the dynamic response and the sound transmission loss (TL) have been discussed in Section 2.3.1.3 and Section 2.3.2.2. If these modal cross terms are neglected, the acoustic power radiated by the n^{th} mode can be obtained by substituting Eq.(2-12) into Eq.(2-7), i.e.

$$W_n(\omega) = \frac{\omega^4 \rho_0 a^2 b^2}{8\pi^2 c} |q_n|^2 b \int_0^{2\pi} \int_0^{\pi/2} |j_n(\theta, \phi, \omega)|^2 \sin \theta d\theta d\phi. \quad \text{Eq.(2-14)}$$

The time averaged and spatial-averaged mean square normal velocity $\langle \overline{v_n^2} \rangle$ due to n^{th} mode can be expressed as

$$\langle \overline{v_n^2} \rangle = \frac{\omega^2 |q_n|^2}{2ab} \int_0^b \int_0^a \psi_n^2(x, y) dx dy, \quad \text{Eq.(2-15)}$$

where the mode shapes are real-valued.

Use is made of modal representation of the averaged mean square normal velocity and the radiated power to develop a novel relationship between the JAF and the radiation efficiency. Substituting Eq.(2-14) and Eq.(2-15) into Eq.(1-2), this relationship can be obtained as

$$\sigma_n(\omega) = \left(\frac{kab}{2\pi} \right)^2 \frac{\int_0^{2\pi} \int_0^\pi |j_n|^2 \sin \theta d\theta d\phi}{\int_0^b \int_0^a \psi_n^2(x, y) dx dy}. \quad \text{Eq.(2-16)}$$

The double integral in the numerator of the above expression has been evaluated for a simply supported rectangular plate by Wallace [78]. A numerical solution is required when dealing with other boundary conditions or stiffened plates.

2.1.4 Vibroacoustic coupling

The modal radiation damping and the added mass of the air should be considered when a fully coupled response is to be calculated.

The radiation damping loss factor for the n^{th} mode is defined as [76]

$$\eta_n^r(\omega) = \frac{W_n(\omega)}{\omega_n \bar{E}_n}, \quad \text{Eq.(2-17)}$$

where \bar{E}_n is the time averaged vibrational energy associated with the n^{th} mode, i.e. for a rectangular non-uniform plate

$$\bar{E}_n = \int_0^b \int_0^a m_A(x, y) \overline{v_n^2} dx dy, \quad \text{Eq.(2-18)}$$

where $m_A(x, y)$ is the mass distribution over the plate surface and has units of kgm^{-2} .

A new step is made to evaluate the radiation damping by using the relationship between the JAF and radiation efficiency in Eq.(2-16). Substituting Eq.(2-14) and Eq.(2-18) into Eq.(2-17), the modal radiation damping loss factor can be expressed as

$$\eta_n^r = \frac{\rho_0 c}{\omega_n m_n} \sigma_n \int_0^b \int_0^a \psi_n^2(x, y) dx dy, \quad \text{Eq.(2-19)}$$

where m_n is the modal mass given by $\int_0^b \int_0^a m_A(x, y) \psi_n^2(x, y) dx dy$.

The added-mass effect of the surrounding fluid is generally very small in the case of air. This can be neglected for all modes except the fundamental one, for which it can be approximated from the reactance of the radiation impedance of a piston which vibrates with an equivalent volume velocity [76], i.e.

$$ab\langle \overline{v_1^2} \rangle = \pi r_e^2 \overline{v_1^2}, \quad \text{Eq.(2-20)}$$

where r_e is the equivalent radius of the piston. Here the subscript 1 is used instead of n to indicate that Eq.(2-20) is only valid for the fundamental mode.

The added mass of the air for a piston is $\frac{8}{3}\rho_0 r_e^3$ [76]. The added mass of the air for the first vibration mode of the plate is then expressed as

$$m_1^r = \frac{8}{3}\rho_0 \left(\frac{\int_0^b \int_0^a \psi_1^2(x,y) dx dy}{\pi} \right)^{\frac{3}{2}}. \quad \text{Eq.(2-21)}$$

As the modal stiffness remains the same, the first natural frequency is modified as

$$\omega'_1 = \omega_1 \sqrt{\frac{m_1}{m_1 + m_1^r}} \quad \text{Eq.(2-22)}$$

where m_1 is the modal mass of the fundamental plate mode.

By making use of Eq.(2-19) and Eq.(2-21), the evaluation of the fully coupled response is simplified. Only the in-vacuo modal parameters and the existing formulated vibroacoustic quantities are required.

For the higher order modes, the added mass can be approximated by $\frac{\rho_0}{k_p}$ for the case of $k_p \gg k$, where k_p is the underlying free bending wavenumber of the plate material[76]. However, this is neglected in the present formulation.

2.1.5 Vibroacoustic response for diffuse field excitation

A diffuse sound field can be regarded as a superposition of harmonic plane waves with random phases and with equal amplitude p_0 . These are incident on the baffled plate from all possible directions over one side, i.e. $\theta \in (0, \frac{\pi}{2})$, $\phi \in (0, 2\pi)$ [145].

The linear displacement response $w(x, y, \omega)$ on the plate surface to the diffuse field excitation can then be obtained by summing the response $w_s(x, y, \omega)$ to each plane wave s . As these plane waves have random phases relative to each other, the individual displacements

$w_1, w_2, \dots, w_S \dots$ are uncorrelated and the total mean square response $\overline{w^2}$ is found by adding up the mean square values of the individual responses:

$$\overline{w^2} = (2abp_0)^2 \lim_{S \rightarrow \infty} \frac{1}{S} \sum_{s=1}^S \left(\sum_{n=1}^{\infty} \frac{\psi_n^2 |j_{n,s}|^2}{Z_n^2} + \sum_{\substack{n=1 \\ u=1 \\ u \neq n}}^{\infty} \frac{\psi_n \psi_u j_{n,s} j_{u,s}^*}{Z_n Z_u^*} \right), \quad \text{Eq.(2-23)}$$

where S is the total number of plane waves used to represent a diffuse field and $Z_n = m_n^2 [-\omega^2 + \omega_n^2 + i(\eta + \eta_n^r)\omega_n^2]$ is the modal dynamic stiffness of the plate. The first summation inside the brackets gives the sum of the mean square response in the individual normal modes, i.e. the direct mean square response. The second summation represents the cross terms.

If the cross term contribution in Eq.(2-23) is neglected, the value of the summation outside the brackets can be evaluated by using the hemispherical model [145]. The area element of an infinitesimal segment for the hemisphere is $r^2 \sin \theta \Delta \phi \Delta \theta$. The number of plane waves per unit area of the hemisphere is $\frac{S}{2\pi r^2}$. So the number of plane waves passing through an infinitesimal segment can be approximated as $\left(\frac{S}{2\pi r^2}\right) r^2 \sin \theta \Delta \phi \Delta \theta$, each of which is associated with the squared JAF value of $|j_{n,s}(\theta, \phi, \omega)|^2$.

Therefore, Eq.(2-23) can be simplified as

$$\overline{w^2} \approx (2abp_0)^2 \sum_{n=1}^{\infty} \frac{\psi_n^2(x, y)}{Z_n^2(\omega)} \left(\frac{1}{2\pi} \int_0^{2\pi} \int_0^{\frac{\pi}{2}} |j_n|^2 \sin \theta \, d\phi d\theta \right). \quad \text{Eq.(2-24)}$$

This equation replaces a discrete but infinite summation over S in Eq.(2-23) by a finite integral of incident and azimuthal angles.

A new step can also be taken from Eq.(2-24) by recognising the same integral in the relationship between JAF and radiation efficiency in Eq.(2-16). Substituting Eq.(2-16) into Eq.(2-24), the (direct) mean square response to the diffuse sound field can be related directly to the modal radiation efficiency σ_n as,

$$\overline{w^2} \approx 8p_0^2 \frac{\pi c^2}{\omega^2} \sum_{n=1}^{\infty} \frac{\psi_n^2(x, y)}{Z_n^2(\omega)} \sigma_n(\omega) \int_0^b \int_0^a \psi_n^2(x, y) dx dy. \quad \text{Eq.(2-25)}$$

2.1.6 Sound transmission for diffuse field excitation

The sound transmission coefficient for a diffuse field is [47]

$$\tau_d = \frac{\int_0^{2\pi} \int_0^{\frac{\pi}{2}} \tau(\theta, \phi) \sin \theta \cos \theta d\theta d\phi}{\int_0^{2\pi} \int_0^{\frac{\pi}{2}} \sin \theta \cos \theta d\theta d\phi}. \quad \text{Eq.(2-26)}$$

Again the relationship between the JAF and radiation efficiency can be used to obtain a new formula to evaluate Eq.(2-26). Substituting Eq.(2-9) and Eq.(2-16) into Eq.(2-26), this can be expressed as

$$\tau_d = \frac{16\pi\rho_0^2 c^4}{ab} \sum_{n=1}^{\infty} \frac{\sigma_n^2}{Z_n^2} \int_0^b \int_0^a \psi_n^2(x, y) dx dy. \quad \text{Eq.(2-27)}$$

This is often presented in the form of the sound Transmission Loss (TL): $TL = 10 \log_{10} \left(\frac{1}{\tau_d} \right)$.

The expressions for the plate's displacement response Eq.(2-25) and the sound transmission coefficient Eq.(2-27) show that the fully coupled vibroacoustic response of structure to a diffuse field can be simplified and evaluated by knowing the mode shapes, the natural frequencies, the damping and the modal radiation efficiency. The first two quantities can be obtained from a free vibration analysis by using either analytical or numerical approaches, while the modal radiation efficiencies can be evaluated from Eq.(2-26). The pointwise vibroacoustic responses for diffuse field excitation are approximated only by the modal parameters, which are not confined to specific boundary conditions or structural configurations.

2.2 Structural model

The vibroacoustic model presented in Section 2.1 relies on knowing the modal properties of the plate. Different approaches exist to evaluate the free vibration of stiffened plates.

Analytical models, such as the assumed-modes approach, have been presented [46, 47] and they are valid within the assumption of light stiffeners; usually the in-plane motion of the plate is neglected and the plate-stiffener interface is treated as a line.

Alternatively, a structural in vacuo FE model can provide more accurate results as it usually involves less simplification than an analytical model representation. For example, the in-plane motion of the plate is retained using shell elements, or laminate shell elements for composite plates, with the stiffeners being modelled as beam, shell or solid elements depending on the configuration and geometry (i.e. straight or curvilinear). This may result in an increased computational cost compared to an analytical one, but the free vibration analysis of the FE model can still be solved within a reasonable time to cover the modes up to a certain

frequency range of interest. Subsequently, the integral expressions for the vibroacoustic response can be evaluated using a numerical discretisation of the integrals over the structural domains.

Figure 2-2 shows the geometry of the orthogonally stiffened, rectangular plate adopted as an example in this chapter. The plate is ribbed orthogonally by two stiffeners parallel to the y -axis and two stiffeners parallel to the x -axis, as illustrated in Figure 2-2 (a). The cross-section of the stiffeners is depicted in Figure 2-2 (b).

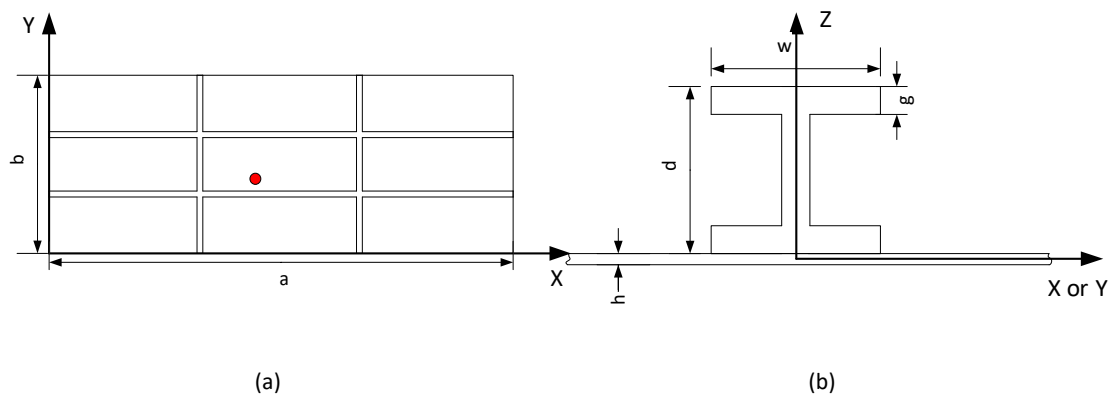


Figure 2-2 Geometry of an orthogonally stiffened, rectangular plates. (a) Stiffener layout: two evenly spaced stiffeners in the x and y directions, respectively; (b) Stiffener detail: I section.

The red point in Figure 2-2 (a) is a reference point where the displacement response is predicted and its coordinate is (1.06,0.38) m. This point is selected at an arbitrary position. However, the conclusions are not affected by the exact point location. This is because although there is variation of the modal response depending on the position, the acoustic response of stiffened plates is always dominated by the fundamental mode [140]. All points on the plate exhibit this fundamental mode.

Table 2-1 lists the geometry and the material properties of the stiffened plate. Damping ratios of aircraft panels are adopted and these are usually in the range of 0.5% - 2% [58]. Therefore, a constant value of structural damping loss factor of 1% is assumed in this chapter. Simply supported boundary conditions are adopted in this chapter, but these could be changed in the structural model as required.

Table 2-1 The structural parameters for the stiffened plates.

Plate (unit: mm)		Stiffener (unit: mm)		Material (aluminium)	
a , length	2400	w , width	30	E , Young's modulus (GPa)	71
b , width	900	d , depth	30	ρ , density (kg/m^3)	2700
h , thickness	2	g , thickness	5	ν , Poisson's ratio	0.3
				η , damping loss factor	1%

It can be seen from the structural dimensions that the thickness of the plate is 15 times smaller than the height of the stiffeners. This may result in a significant coupling between the out-of-plane and in-plane displacements of the plates for the bending motion, which is not necessarily included in some analytical models available in the literature. The emphasis of the current research is on the vibroacoustic behaviour of stiffened plate and the generic configurations of the stiffeners may not necessarily meet the full assumptions of light stiffeners required in analytical models [20].

In order to evaluate possible approaches to predict the free vibration of stiffened plates, the mode shapes and natural frequencies calculated from an analytical and a finite element model are compared.

The analytical model is the one given and detailed by Dozio [46]. The MATLAB code¹ was implemented with the number of trial functions selected by verification of the solution's convergence. The criterion is by inspection of the percentage difference in the natural frequency for the 20th mode, as given in Table 2-2. In the convergence study, the number of trial functions increases in each direction in increments of 5 additional functions. The natural frequency of the 20th mode for each study was calculated and the percentage difference compared to the results using the highest number of trial functions implemented (70 for x direction and 50 for y direction) was given. The criterion of no greater than 0.2% in the frequency difference is chosen. So the final selected trial function numbers are 60 in the x direction and 40 in the y direction. A free vibration analysis shows that there are 420 modes present at the frequency range up to 1500 Hz.

¹ The MATLAB code for the analytical mode was provided by Dozio [46].

Table 2-2 The natural frequency and its percentage difference compared to a chosen finely meshed model for the 20th mode.

Number of trial functions(N_x, N_y)	Natural frequency of 20 th mode (Hz)	Percentage difference to finest mesh results (%)
(40,20)	151.06	1.43
(45,25)	150.21	0.86
(50,30)	149.75	0.55
(55,35)	149.42	0.33
(60,40)	149.19	0.17
(65,45)	149.03	0.07
(70,50)	148.93	0

The Finite Element (FE) model was developed in the 'Structural mechanics' module of COMSOL software [146]. The plate was represented with quadratic shell elements and the stiffeners with cubic beam elements with 'I-profile' cross-section. The beams were then coupled to the plate in the setting of 'Shell-Beam Connection' in the 'Multiphysics' module. The mesh size was selected by verification of the solution's convergence. The criterion is the percentage difference in the natural frequency for the 20th mode given in Table 2-3. In the convergence study, the mesh size of the shell element reduces from 0.114 m to 0.02 m. The natural frequency of the 20th mode for each study was calculated and the percentage difference compared to the finest mesh (0.02 m) was given. The result shows that for the mesh size of 0.029 m, the frequency difference is 0.02% to the results for the finest mesh. So the mesh size of 0.029 m was chosen and the corresponding FE model has 2520 shell elements. A free vibration analysis shows that there are 431 modes present at the frequency range up to 1500 Hz.

Table 2-3 The natural frequency and its difference variation for the 20th mode

Mesh size (m)	Natural frequency of 20 th mode (Hz)	Percentage difference to finest mesh results (%)
0.114	151.11	2.32
0.057	147.99	0.20
0.038	147.78	0.06
0.029	147.72	0.02
0.023	147.70	0.01
0.020	147.69	0

Figure 2-3 shows the comparison of the modal properties in terms of the Modal Assurance Criterion [147], for the mode shapes, and the scatter plots for the first 20 natural frequencies.

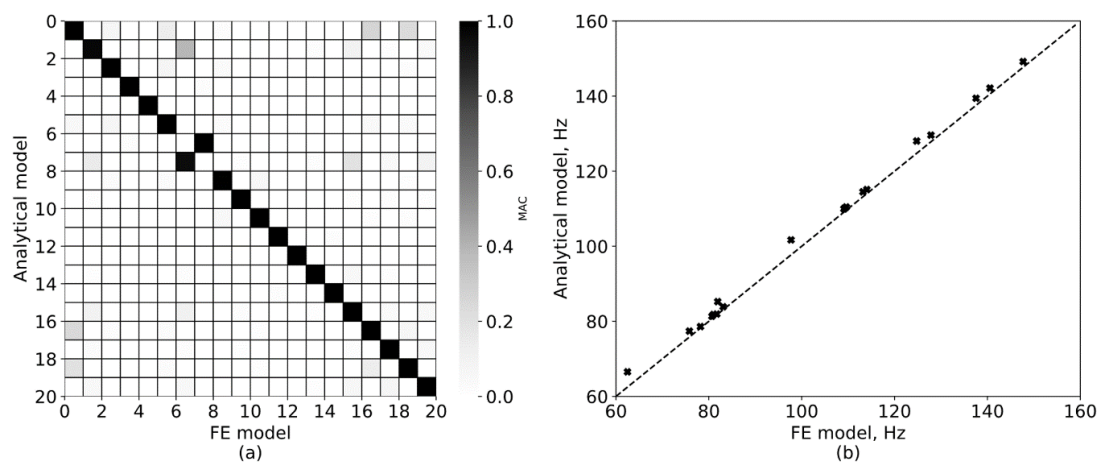


Figure 2-3 The comparison of modal properties between a FE model and an analytical model for the lowest 20 modes of stiffened plate. (a) MAC plot; (b) Scatter plot.

The analytical model provides a good prediction for the natural frequencies and mode shapes for the first 20 modes. However, the natural frequencies predicted by the analytical model tend to be higher than those calculated by FE and this may be due to neglecting the deformation and hence strain energy associated with the in-plane motion of the plate. This also applies to the first mode, which is known to be typically the major contributor to the response of a flat plate subjected to an acoustic excitation [140]. Although the mode shape agreement for the two models of this mode is high as seen in the MAC value, the difference in the fundamental natural frequency, shown as the first point in the scatter plot Figure 2-3 (b), leads to a shift in the corresponding resonance. In addition, the MAC for higher frequency

modes show larger but still acceptable difference between the analytical and the numerical results.

For the purpose of performing a parametric study, the analytical model is initially used to generate the modal basis behind the calculations reported in Section 2.3. In Section 2.4, the FE model is used, coupled with an acoustic domain, to validate the vibroacoustic calculations introduced in Section 2.1. In order to align the modal basis used as an input in the proposed modal model with the numerical model, the modal basis obtained from the FE model is in this latter part preferred to the analytical one, although the modes are generally still in good agreement.

2.3 Numerical results of the modal model

2.3.1 Dynamic response

The dynamic responses of the plate subjected to acoustic excitations are given in terms of the transverse displacement at an arbitrary reference point. The point is at position (1.06,0.38) m and it is highlighted in Figure 2-2 (a). In addition, the spatially-averaged displacement is also evaluated.

The sound pressure level (SPL) of the incident sound field is 91 dB for all the cases evaluated. The diffuse field is constructed by 603 incident waves above the plate surface. The method for calculating the direction of these waves is taken directly from reference [62]. The amplitude of each individual plane wave is 1 Pa and the phase of them is taken from a uniform random distribution between $\pm\pi$ with zero mean value. The diffuse field pressure is obtained by adding up these waves then dividing by the square root of the number of waves to ensure that the limit remains finite as the number of contributing waves becomes infinite [77]. A large number of numerically simulated samples of the diffuse field is also required in order to produce a good approximation to the theoretical spatial pressure correlation. In this chapter, the mean square error between the averaged spatial pressure correlation of the simulated diffuse field and that of the theoretical diffuse, i.e. $\frac{\sin kx}{kx}$, was calculated. The mean square error, as measured for the spatial correlation, was less than 4% when averaged over 100 different realizations of the diffuse field for a Helmholtz number, kx , less than 44. The error can be reduced further with an increased number of samples. However, a higher accuracy of the reproduced diffuse field was unnecessary in this study, so 100 samples were used in the numerical simulation without incurring a significant computational cost.

The comparison of the results for the unstiffened and stiffened plate are given to highlight the effect of the stiffeners. These results are given as the transfer function between the transverse displacement of the plates and the unit magnitude pressure input for the sound field. The frequency range is up to 1000 Hz, with a frequency resolution of 200 points per decade. The fundamental natural frequency is 6.87 Hz for the unstiffened plate and 66.57 Hz for the stiffened plate. The analytical model introduced in section 2.1 is used here to evaluate the effect of different excitation types, the effect of vibroacoustic coupling and that of the modal cross terms.

2.3.1.1 Plane wave and diffuse field excitation

Figure 2-4 shows the responses of the unstiffened plate and stiffened plate to three different acoustic excitations, namely a diffuse sound field, a normal incident plane wave sound field and an oblique incident plane wave sound field. The results are presented in the presence of vibroacoustic coupling and including the modal cross terms.

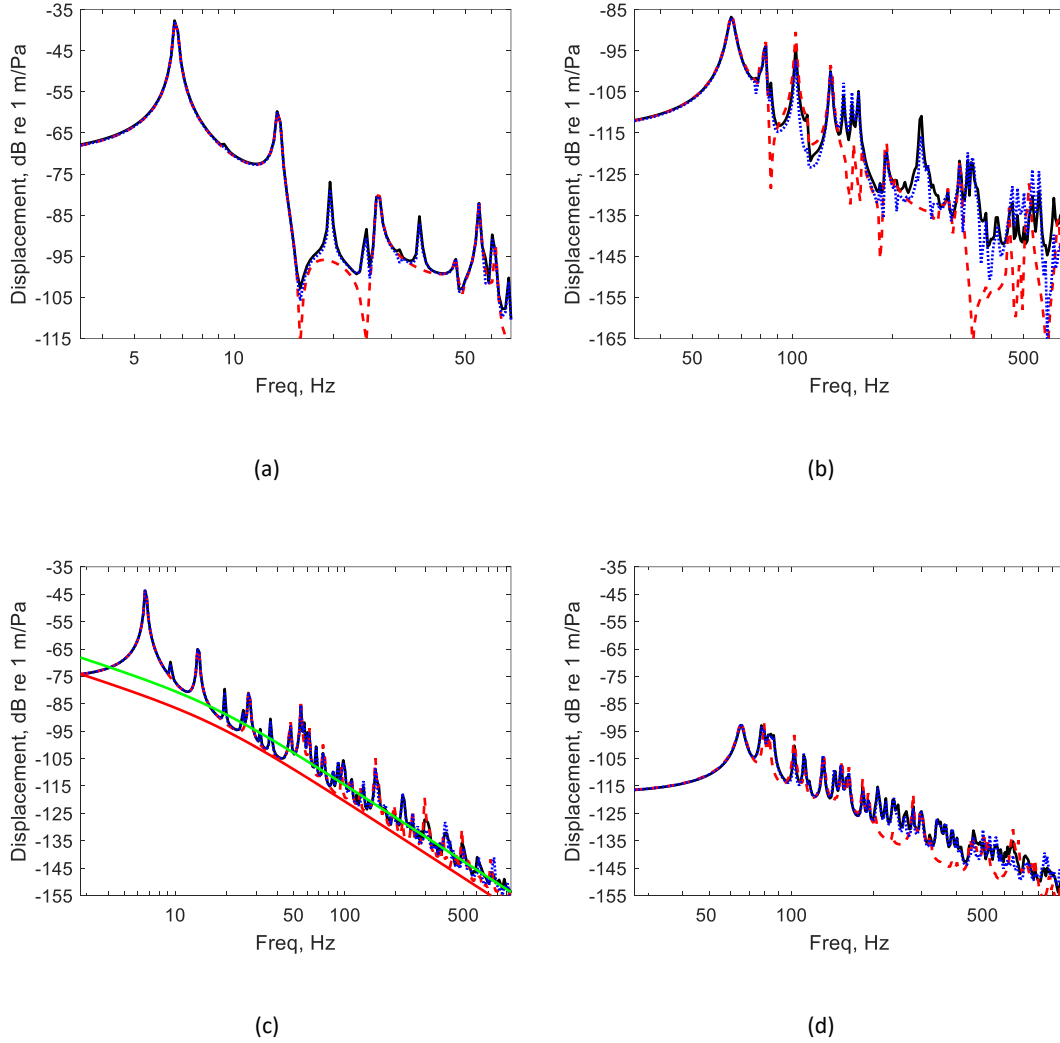


Figure 2-4 The transverse displacement for different acoustic excitation: diffuse sound field (black solid lines), normal incident plane wave (red dashed lines) and oblique incident plane wave $(\theta, \phi) = (\pi/4, \pi/4)$ (blue dotted lines). (a) Reference point response of the unstiffened plate. (b) Reference point response of the stiffened plate. (c) Spatial-averaged response of the unstiffened plate including a red solid line calculated from the Liamshev's plane-wave response theory for an oblique incident plane wave and a green solid line calculated from doubling of the Liamshev's predictions. (d) Spatial-averaged response of the stiffened plate.

The results for the reference point in Figure 2-4 (a) and (b) show that the responses are similar for the three different acoustic excitations at the lower frequencies (the fundamental and higher order plate natural frequencies are seen in Figure 2-3). This is because at these frequencies the structural wavelength is much smaller compared to the acoustic wavelength. Therefore, the JAFs for both the plane waves and the diffuse field are similar to the normal incidence case, i.e. only the symmetric modes can be excited and are dominated by the fundamental mode response. In the high frequency range, the number of resonances responding significantly decreases for normal plane wave excitation compared to the other two sound fields.

For the unstiffened plate case in Figure 2-4 (a) up to the frequency of 50 Hz, eight resonances can be clearly observed for both the diffuse field and the oblique plane wave excitation, while only four of them are excited by the normal incidence wave. A plot of the corresponding mode shapes at this frequency range (a total of 12 modes), as shown in Figure 2-5, shows that these non-responsive modes (mode 2, 4, 5, 7, 8, 9, 10 and 11 in Figure 2-5) are all antisymmetric modes about one or two axes, and this corresponds to JAFs equal to zero. While this is true for the unstiffened plate with fully simply supported edges, for a more general case, e.g. a mixture of clamped, elastically supported etc., which are not the same on opposite edges, the modes will not be purely symmetric or antisymmetric. Thus the number of excited modes will increase. The difference in the number of acoustically excited modes for the different acoustic fields is smaller for the stiffened plate case in Figure 2-4 (b). This is because the orthogonal stiffeners lead to a reduced number of antisymmetric modes. However, the response of the stiffened plate excited by a normal plane wave tends to be lower than that due to an oblique plane wave or the diffuse sound field excitation, both in terms of the number of excited modes and the peak amplitudes.

The results for the spatially-averaged displacement presented in Figure 2-4 (c) and (d) are calculated for a rectangular grid of 46×121 points and confirm the main behaviour found at the reference point in terms of the response due to different excitations.

For reference, the unstiffened plate is also compared with the result calculated from Liamshev's plane-wave response theory [76]. This theory gives, for the frequency well below the critical frequency,

$$\frac{v}{p_i} = \frac{\left(\frac{2}{\rho_0 c}\right) \cos \theta}{1 - i k h \left(\frac{\rho}{\rho_0}\right) \cos \theta}$$

where p_i is the incident plane wave amplitude in the original expression. It is only valid for an unstiffened, infinite plate excited by an oblique plane wave and it is a two dimensional expression.

Figure 2-4 (c) shows the Liamshev's prediction with $\theta = \frac{\pi}{4}$ as the red solid line. The comparison with Liamshev's formulation is satisfactory above 70 Hz, about 10 times of the fundamental natural frequency. However, Liamshev's prediction tends to underestimate the response and follows the minima. This may be because Liamshev's formula is a two dimensional calculation, assuming incidence at the angle of ϕ . This will underestimate the

response, as less modes will be excited, as shown in Figure 2-4 (a). If a factor of two is applied to Liamshev's prediction, which is shown in the green solid line in Figure 2-4 (c), a better agreement can be obtained.

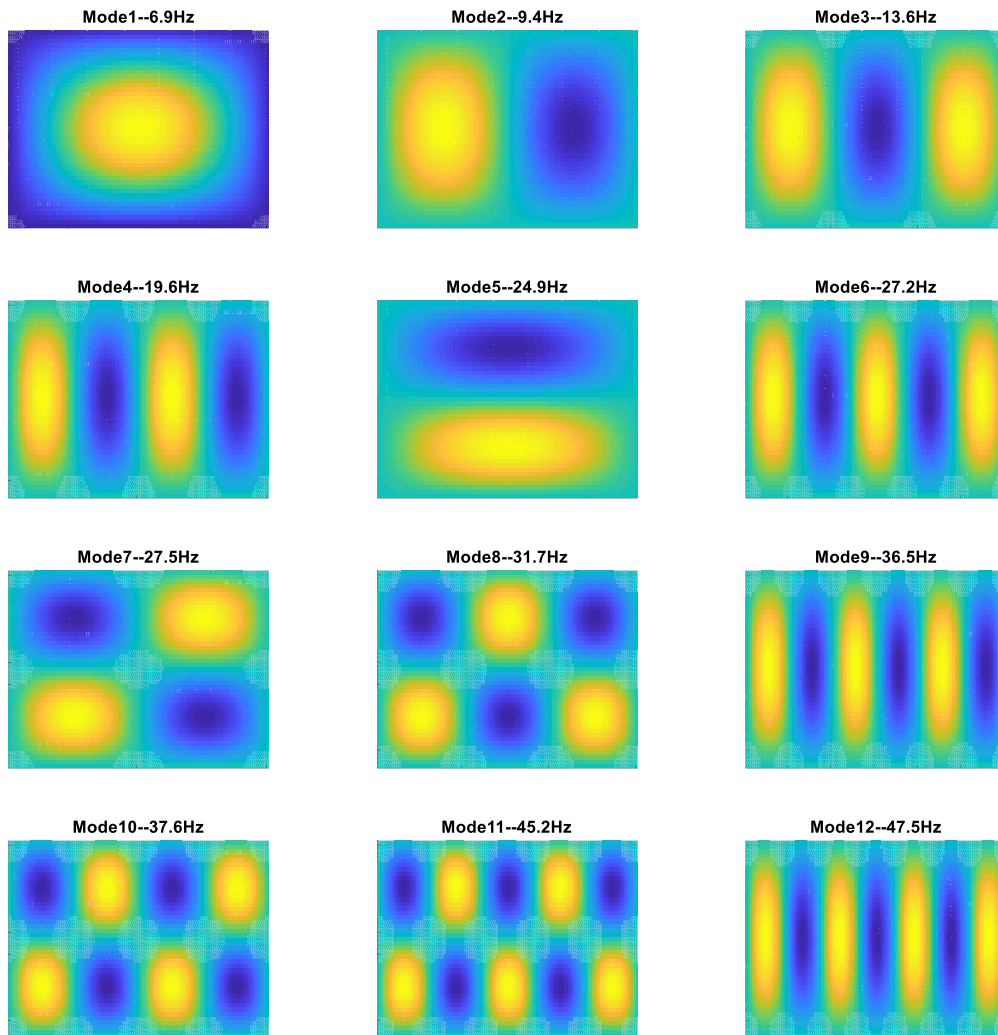


Figure 2-5 The mode shapes and natural frequencies of the lowest 12 modes for the unstiffened plate.

2.3.1.2 Effect of vibroacoustic coupling

To simulate the total pressure at the plate interface with the air domain, the sound field is divided into two parts. The first part comprises the incident and reflected pressure for a rigid surface, hence corresponding to a blocked pressure, while the second part consists of the pressure radiated from the vibrating plate [76], i.e.,

$$p_{total} = p_{incident} + p_{reflected} + p_{radiated} = p_{blocked} + p_{radiated} \quad \text{Eq.(2-28)}$$

An uncoupled response is obtained if the radiated pressure is neglected. Figure 2-6 shows both the uncoupled and the coupled responses to the diffuse field for both unstiffened and stiffened plates. The modal cross-terms are included in this analysis.

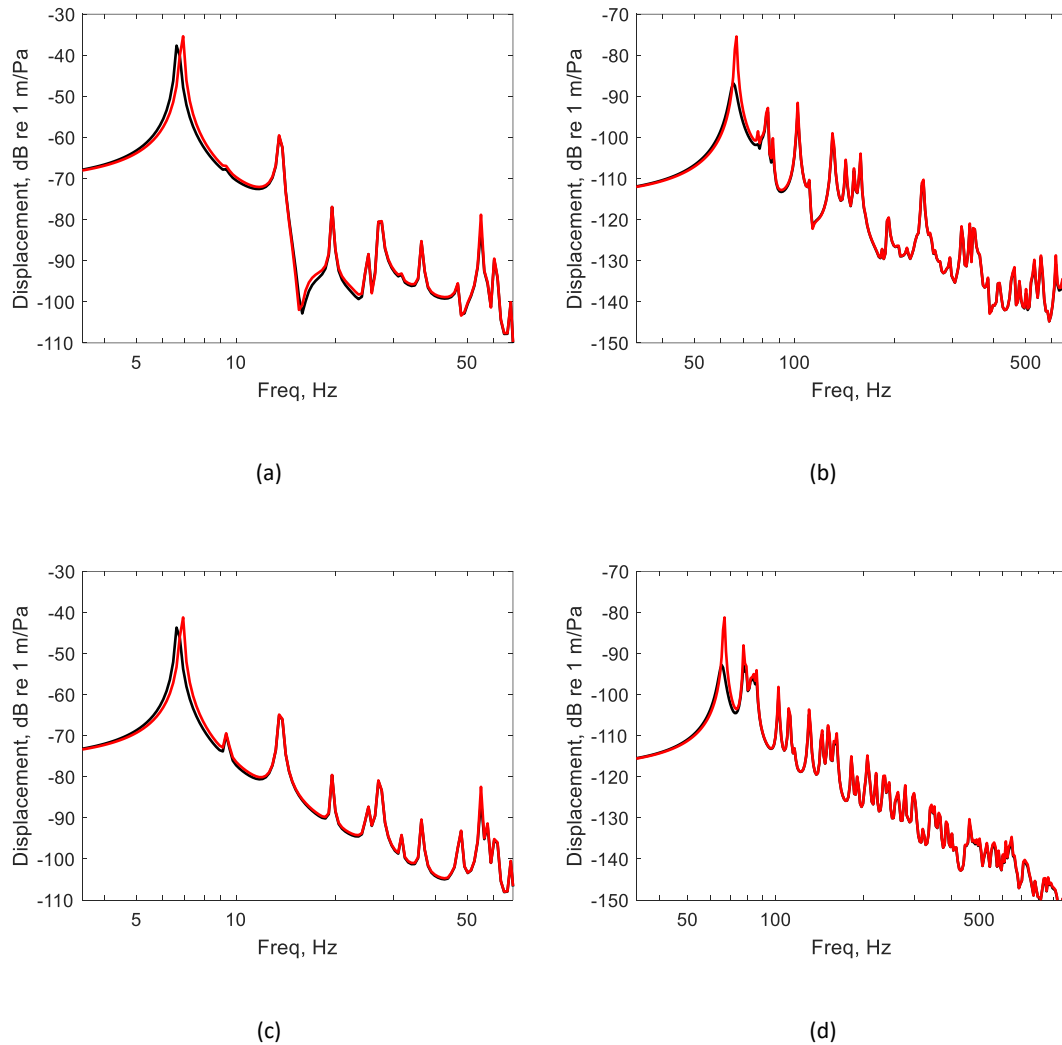


Figure 2-6 The effect of the vibroacoustic coupling on the transfer function of the transverse displacement. Black solid lines are the fully coupled response and the red solid lines are the uncoupled response. (a) Reference point response of the unstiffened plate. (b) Reference point response of the stiffened plate. (c) Spatially-averaged response of the unstiffened plate. (d) Spatially-averaged response of the stiffened plate.

In the comparison between the uncoupled and the fully coupled response at the reference point, there is a significant reduction in the level of the dominant resonance, about 11.4 dB, for the stiffened plate in Figure 2-6 (b), while a smaller difference, of about 2.3 dB, is observed for the unstiffened plate in Figure 2-6 (a). The radiation damping calculated for the stiffened plate in Eq.(2-19) was found to be larger than that of the unstiffened plate by a factor of five. This can be explained by noticing that the stiffeners increase the fundamental natural frequency of the plate (from 6.87 Hz for the unstiffened plate to 66.57 Hz for the stiffened

plate) and hence the corresponding modal radiation efficiency evaluated at this natural frequency increases as well, as shown in Figure 2-7, calculated from Eq.(2-16), thus leading to a larger value of the radiation damping at this frequency.

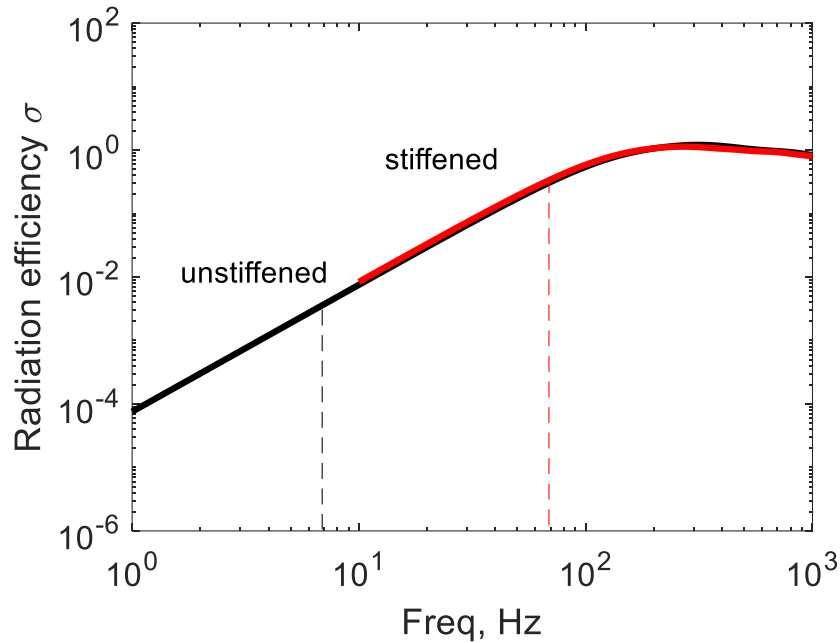


Figure 2-7 Radiation efficiency of the fundamental mode of unstiffened (black solid line) and stiffened (red solid line) plates. The radiation efficiency values are evaluated at the frequencies marked with dashed lines.

In addition, the stiffeners also cause the plate mode shapes to deviate from a sinusoidal form, which introduces lower wavenumber spatial vibration components that better match with the acoustic wavenumber and increase the modal radiation efficiency. For the structural configuration used in simulation, this effect is less significant than the effects due to the increase in the natural frequencies.

The spatially averaged response confirms again the main trend found for the single point response. The vibroacoustic coupling for the case in Figure 2-6 (d) reduces the amplitude of the first peak by 11.6 dB and makes the first 2 modes almost contribute equally to the overall response.

The vibroacoustic coupling effect for different stiffener configurations is also analysed here. In Figure 2-8 (a), four types of plates are used for comparison of different stiffener arrangements. The calculations for the three stiffened plates is made for two different heights of the stiffener cross-section. The first is the one specified in Table 2-1 and the second one corresponds to reducing the former by 1/3. Figure 2-8 (b) shows the dB difference of the spatially averaged RMS displacement evaluated by using the blocked pressure versus a full

vibroacoustic coupling including re-radiation. To calculate the RMS, a broadband random noise with flat spectrum up to 1000 Hz has been assumed.

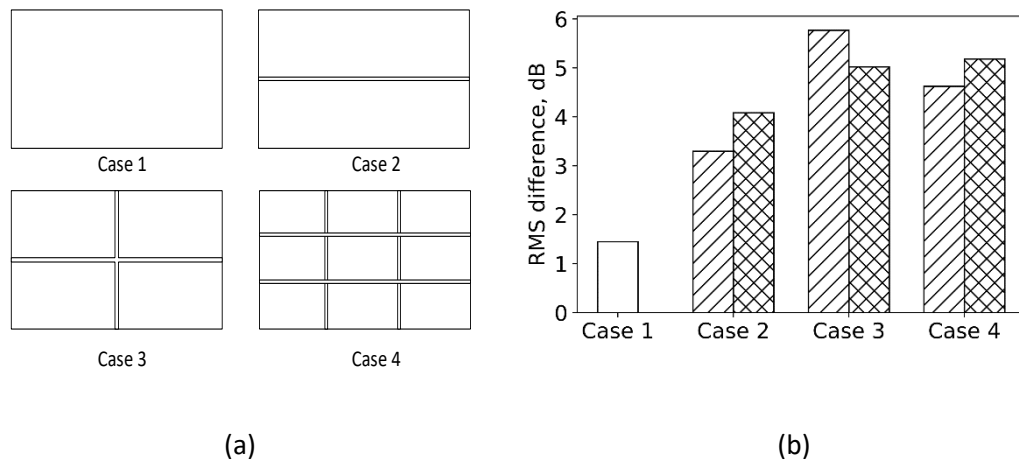


Figure 2-8 Comparison of vibroacoustic coupling effect for different cases. (a) Four types of plates. Case 1: unstiffened plate; Case 2: plate with 1 x -wise stiffener; Case 3: plate with 1 x -wise and 1 y -wise stiffeners; Case 4: plate with 2 x -wise and 2 y -wise stiffeners. (b) The dB difference of the spatially averaged RMS displacement for different cases using either a full vibroacoustic coupling or an uncoupled (blocked force) model. The bar without shading is for the unstiffened plate. The bars with parallel hatching shading are for the stiffeners with the original height. The bars with cross hatching shading are for the stiffeners with 2/3 of the original height

The results show that, in general, the effect of vibroacoustic coupling increases as the number of stiffeners increases and that on average there is also an increase in this effect when the height of the stiffeners decreases. The results in Figure 2-8 are however representative of an average 'single-number' response and specific results may vary for different points on the plate.

The modal contributions to the total RMS response are also affected by the vibroacoustic coupling. For example, for the stiffened plate (case 4) the contribution of the fundamental mode is 89% for the uncoupled (blocked force) response while it decreases to 63% for the fully coupled configuration. To obtain 99% of the total RMS for the stiffened plates, the required number of modes is 10 for the uncoupled response, and this is increased to 23 for the fully coupled response.

2.3.1.3 Effect of modal cross-terms

Figure 2-9 shows the effect of the modal cross-terms on the response to a diffuse field and in the presence of vibroacoustic coupling for unstiffened and stiffened plates. The black solid lines represent the response with the modal cross-terms coupling and the red dashed lines represent the response without the cross terms coupling.

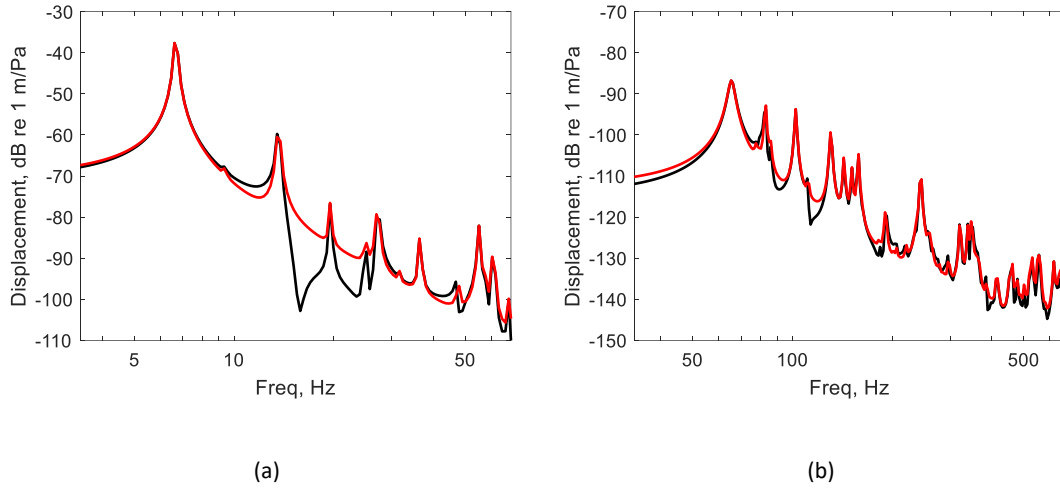


Figure 2-9 The effect of the modal cross-terms contribution on the transfer function of the displacement response of the reference point on the unstiffened (a) and the stiffened plate (b) excited by a diffuse field. Black solid lines: with modal cross-terms contribution. Red solid line: without the modal cross-terms contribution.

The results show that the contribution from the modal cross-terms is more significant at the lower frequencies and less significant at the higher frequencies for both the unstiffened and the stiffened plates. This is because the modal cross terms mainly influence the non-resonant frequency regions. The cross term contributions, due to modal orthogonality, have no effect on the spatially averaged response as seen in Eq.(2-23).

Although the results in Figure 2-6 and Figure 2-9 are for the diffuse sound field, the effects of the vibroacoustic coupling and the modal cross-terms are similar for the other acoustic excitation types analysed. The corresponding results are not presented here.

2.3.2 Sound transmission loss (TL)

2.3.2.1 Plane wave and diffuse field excitations

Figure 2-10 shows the TL for the three different acoustic excitations analysed above; the simulations are performed including the full vibroacoustic coupling. The modal cross-terms are also included in these results.

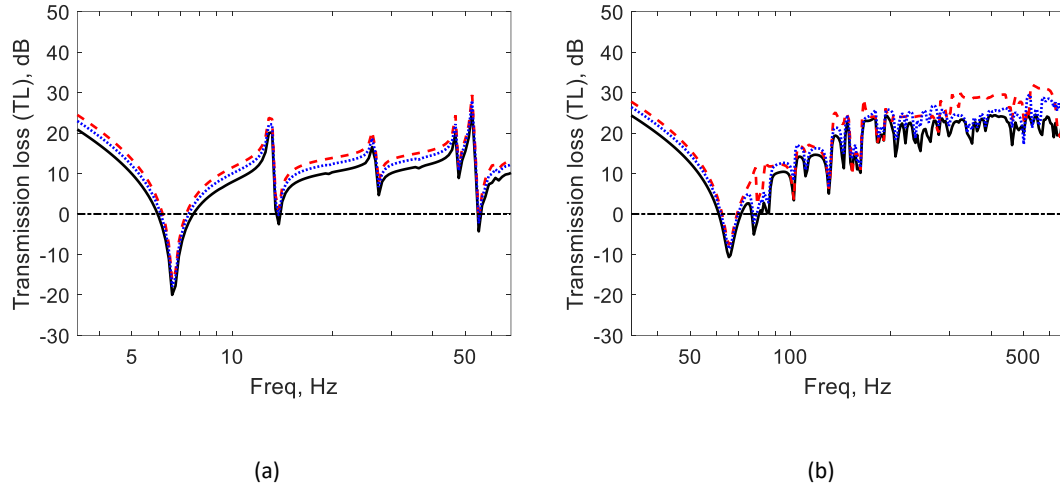


Figure 2-10 The effect of acoustic excitation on the TL of the unstiffened (a) and the stiffened (b) plates. Black solid lines: an incident diffuse field. Red dashed lines: a normal incident plane wave. Blue dotted lines: an oblique incident plane wave at an angle $(\theta, \phi) = (\pi/4, \pi/4)$. Horizontal dash-dotted line: 0 dB line.

The TL results show the behaviour characterised by a stiffness-controlled region and an intermediate frequency region which are separated by the first plate resonance. The effect of different acoustic excitation types is the same in the stiffness-controlled region for both the unstiffened plate and the stiffened plate, i.e. the TL decreases by 1 – 2 dB from the normal to oblique to diffuse field incidence. The same behaviour is also extended to the intermediate frequency region for the unstiffened plate. Although the number of the acoustically excited modes is different for the three types of acoustic excitation, only the symmetric modes effectively radiate sound. This can be observed from the dips in the TL, i.e. plate resonances, in Figure 2-10 (a). Figure 2-10 (b) shows that although the response of the stiffened plate differs from the unstiffened one, i.e. the number of dips present in the intermediate frequency region is significantly increased, the main differences in the TL for different acoustic fields are preserved. It is also worth noting that the TL is negative at some low-frequency plate resonances. This is a consequence of the normalisation used for the incident sound power as explained by Thompson et al. in [148].

Analytical formulae [76] [149] are available to produce comparisons with the unstiffened plate results. They include the ‘normal incident mass law’,

$$TL(0) = 20 \log_{10}(\rho h f) - 42 \text{ dB},$$

the ‘diffuse incidence mass law’,

$$TL_d = TL(0) - 10 \log_{10}(0.23 TL(0)) \text{ dB},$$

the ‘field incidence mass law’,

$$TL_f = TL(0) - 5 \text{ dB},$$

and Sewell's diffuse field model,

$$TL = TL(0) - 10 \log_{10}(\log k\sqrt{ab}) + 20 \log_{10} \left(1 - \left(\frac{f}{f_c} \right)^2 \right) \text{ dB}.$$

Note that Sewell's formula used in the calculation is simplified from the original one (formula (54) in [149]) by neglecting the small correction terms.

The results calculated from those analytical formulae are also presented in Figure 2-11 for comparison. They are valid for unstiffened plates and can approximate the behaviour of a finite plate in the high frequency range. Figure 2-11 shows the comparison of the results for the unstiffened plate subjected to both the normal incident plane wave and the diffuse field.

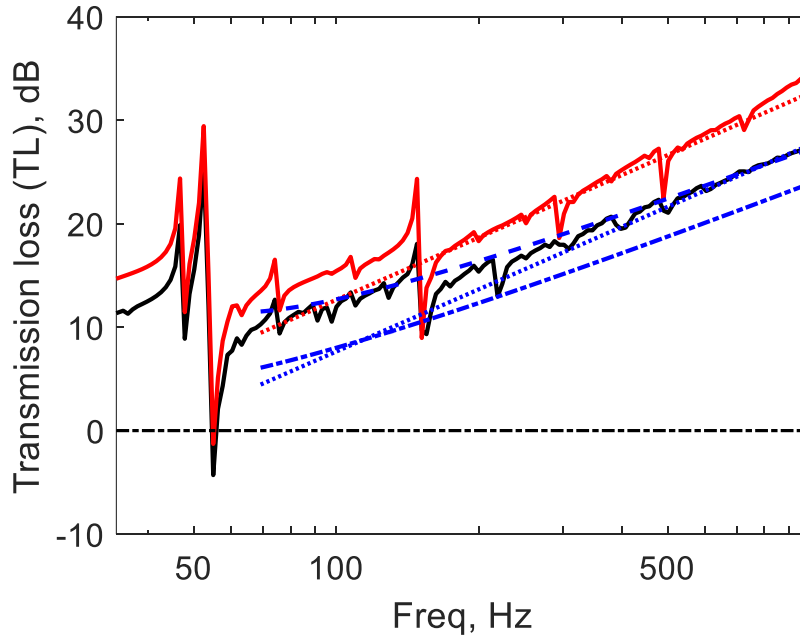


Figure 2-11 The comparison of TL results between the proposed model and the approximate formulae for the unstiffened plate subjected to a normal incident plane wave and a diffuse field excitation. Red, solid line: the proposed model subjected to normal incident plane wave. Black, solid line: the proposed model subjected to diffuse field. Red, dotted line: the normal incidence mass law. Blue, dash-dotted line: the diffuse field mass law. Blue, dotted line: the field incidence mass law. Blue, dashed line: Sewell's simplified formula. Horizontal black, dash-dotted line: 0 dB line.

The results show a good agreement for a normal incident wave in the high-frequency range (above 350 Hz). However, for the diffuse field results a significant difference in the TL is observed in comparison to the diffuse field mass law (in blue, dash-dotted line). The same phenomenon has been observed by Sewell, with the explanation that the finite plate cannot radiate well at high angles [76]. The agreement is improved with comparison to the field incidence mass law (in blue, dotted line), which excludes the contribution of the high angles

between 78° and 90° . A further improvement at the low frequencies is achieved in the comparison to Sewell's formula (in blue, dashed line), which explicitly includes the effect of the finite plate dimensions.

2.3.2.2 The effects of modal cross-terms

Figure 2-12 shows the effect of the modal cross-terms on the TL to a diffuse field and in the presence of vibroacoustic coupling. The black-solid lines represent the TL including the modal cross-terms and the red-solid lines represent the response with the modal cross-terms excluded.

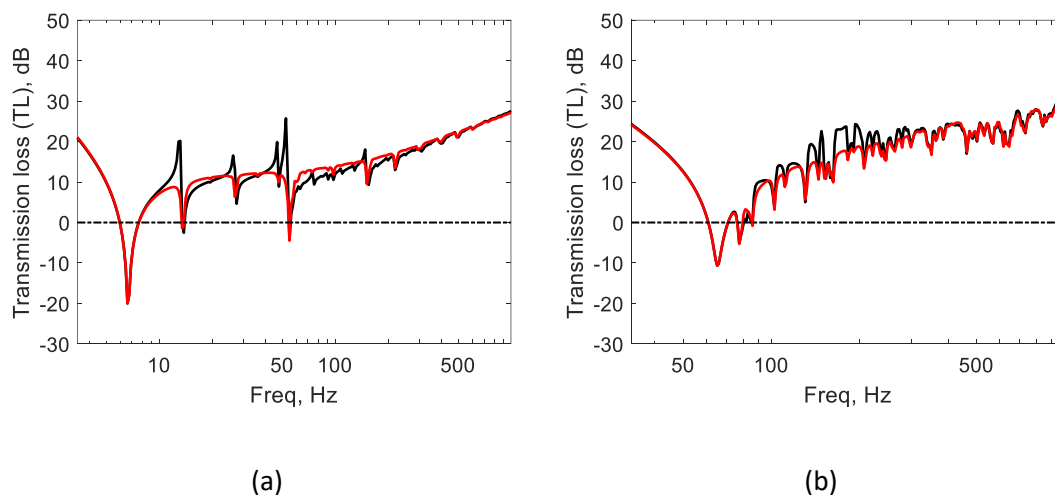


Figure 2-12 The effect of the modal cross-terms contribution on the TL on the unstiffened (a) and the stiffened (b) plate excited by the diffuse field. Black solid lines: include modal cross-terms contribution. Red solid lines: without the modal cross-terms contribution. Horizontal dash-dotted line: 0 dB line.

The results show that the modal cross-terms contribution is on average small, but it can be significant between resonances at some frequencies. The effect of excluding full vibroacoustic coupling on the TL for diffuse field has been examined and found to give results consistent with that of the plate response in Figure 2-6 (a) and (b), so it is not presented here.

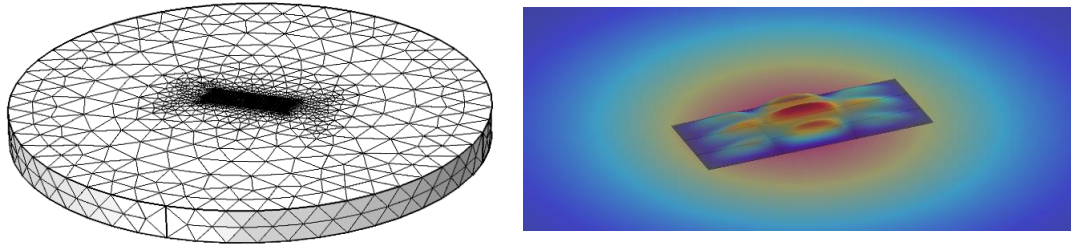
2.4 Comparison with a coupled FE-BE model

To validate the approach introduced in this work, the results obtained with the proposed model are compared with coupled FE-BE numerical simulations developed in COMSOL. For this comparison, the modal basis of the stiffened plate for the analytical modal model is obtained from the same structural model adopted in COMSOL for this validation. 431 modes are used in the modal summation which covers the frequency range up to 1500 Hz.

Figure 2-13 (a) shows the meshed FE-BE model. The details of the structural FE model have been given in section 2.2. The plate FE model is embedded in an upper surface of a rigid cylinder which approximates an infinite baffle. The acoustic BE model was then developed in the 'Pressure acoustic, boundary elements' module to model the external air domain. Quadratic boundary elements were used to mesh the boundary between the external air domain and the baffled, stiffened plate, including the rigid cylinder. The structural FE model and the acoustic BE model are coupled by the 'Acoustic-structure boundary' in the 'Multiphysics' module.

To allow the same diffuse field pressure field to be used in the analytical model and in the numerical approach, the term $p_{blocked}$ in Eq.(2-28) is imported from the modal model of Section 2.1 into the coupled FE-BE model in COMSOL. The term $p_{radiated}$, is automatically included in the numerical simulation via FE-BE coupling.

To minimise the effect of diffraction from the edges of the rigid cylinder, its radius was set to be at least half the largest acoustic wavelength. The mesh size of the boundary element was selected by verification of the solution's convergence over a frequency range up to 1000 Hz. The coupled FE-BE model was then solved in the frequency domain with an iterative solver. As with the analytical model, the radiated sound power above the plate surface is used to calculate the transmitted sound power to the other side of the plate. For harmonic excitation, the time-averaged acoustic intensity of the radiated sound field over the plate surface is evaluated using the equation $I = \frac{1}{2} Re\{p_{radiated} \times v^*\}$, where v is the complex acoustic velocity and is equal to the plate surface velocity. The acoustic intensity is then integrated over the plate surface to calculate the radiated sound power. The incident sound power for the incident diffuse field is calculated by summing that of each individual plane wave, using Eq.(2-8), then dividing by the number of waves based on the diffuse field model. As with the modal model, 100 realizations of the simulation were considered and the results were averaged to approximate a diffuse field. Figure 2-13 (b) shows the calculated displacement at the first resonant frequency of the stiffened plate for one realization of the diffuse field.

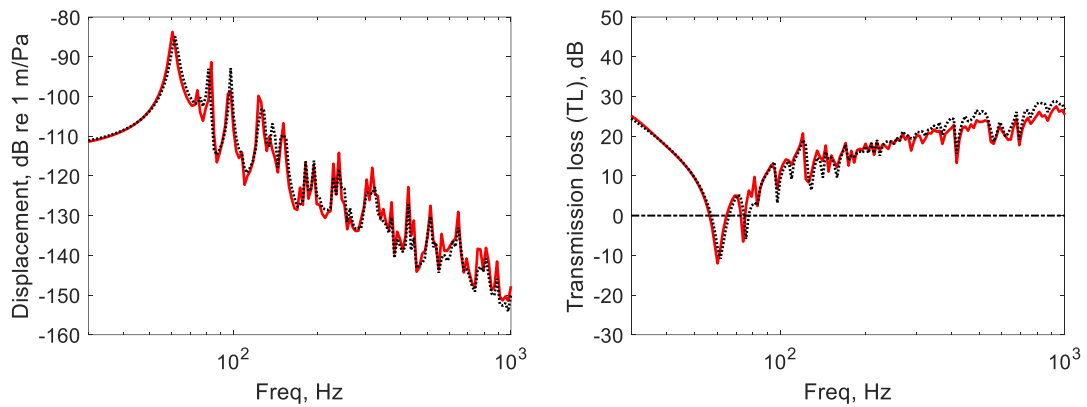


(a)

(b)

Figure 2-13 A coupled FE-BE COMSOL model for the baffled stiffened plate subjected to diffuse field. (a) The meshed model. (b) The displacement response for the incident diffuse field of amplitude 91 dB at the first resonance frequency of the stiffened plate (62.5 Hz)

Figure 2-14 (a) and (b) show the comparison of the results for the reference point displacement and the TL to the diffuse field between the proposed modal model and the coupled FE-BE model. Both the vibroacoustic coupling and the modal cross terms are included in the two models.



(a)

(b)

Figure 2-14 The comparison of the results for the stiffened plate displacement response (a) and the TL (b) for the diffuse field between the proposed modal model (in black, dotted lines) and the coupled FE-BE model (in red, solid lines). Horizontal dash-dotted line: 0 dB line.

Good agreement for both the displacement response and the TL between the two models is found over the entire frequency range presented in Figure 2-14. It can therefore be concluded that the model proposed here can accurately predict the vibroacoustic behaviour of flat plates excited by different forms of acoustic field.

The computation time of the proposed model and the FE-BE model were compared in the dual 2.0 GHz Intel Xeon E5-2670 processors with 40 cores and 394 GB memory. The CPU time of approximately 1190 hours was required for the coupled FE-BE simulation, while only 2 hours was used for the proposed model, which was 590 times faster than the fully coupled FE-BE model. The solution time can be further reduced if the modal cross-term contributions are neglected. In this study, the computational time for the coupled FE-BE model has been reduced to 164 hours by utilizing the parallelised simulation in the Iridis High Performance Computing (HPC) facility.

2.5 Summary

This chapter presents a linear modal model for the prediction of the fully coupled vibroacoustic response of stiffened plates subjected to incident plane and diffuse sound fields. A relationship between the JAF and the modal radiation efficiency was derived, which simplifies the analysis and reduces the computational cost. The numerical results give a systematic explanation of the factors influencing the displacement response and the TL for a baffled, orthogonally stiffened plate, including the form of the acoustic excitation, vibroacoustic coupling and the modal cross terms. A comparison was also made between the proposed models and a coupled FE-BE model.

The main findings can be summarised as:

- The stiffeners can enhance vibroacoustic coupling leading to a significant reduction of the dominant resonance level, which is about 11 dB in the presented model.
- Different acoustic excitation types and the modal cross terms affect the sound transmission loss more than the vibration response. Although the presence of stiffeners in general will reduce the overall vibration response levels, the effects of both different excitation types and modal cross-terms contribution are preserved for either the unstiffened or the stiffened plates.
- Overall, a good agreement between the proposed model and the coupled FE-BE model was achieved with a significant reduction in the computational cost.

Chapter 3 The acoustic response of stiffened cylinders

A cylinder is a basic structural component for aerospace vehicles. The prediction of the acoustic responses of cylinders differs from that of a plate due to the curvature. From the excitation point of view, the rigid acoustic scattering due to the non-uniform reflection of the sound waves on the cylindrical surface must be considered. From the structural point of view, its dynamics is influenced by the membrane effect arising from structural continuity around the circumference.

In this chapter, the sound rigid scattering is addressed by revisiting the calculations of the total surface pressures on a rigid cylinder subjected to two basic sound fields, that is an incident plane wave and a spherical wave field. The modal forces for both cases are also derived and the Joint Acceptance Function (JAF) for the plane wave is given. Then an existing energy approach is implemented to evaluate the normal modes of a stiffened cylinder. The numerical results are given for the acoustic response of stiffened cylinders subjected to plane wave excitation. The effects of curvature on the structural stiffness as well as the Joint Acceptance Function are discussed. The responses from the analytical model and a coupled FE-BE model are compared.

3.1 Surface pressure descriptions

The total pressure at the exterior (outer) surface of a cylinder is

$$p_{total,ex} = p_{incident} + p_{reflected} + p_{radiated,ex} = p_{blocked} + p_{radiated,ex}. \quad \text{Eq.(3-1)}$$

The pressure at the interior (inner) surface of a cylinder is

$$p_{total,in} = p_{radiated,in}. \quad \text{Eq.(3-2)}$$

Both the external and internal radiation are neglected in the analysis, i.e. the cylinder is in a vacuum (in vacuo). This is because these re-radiated pressures ($p_{radiated,ex}$ and $p_{radiated,in}$) are much smaller in the air domain compared with the total acoustic excitation. As shown in Chapter 2, the radiation damping can be used in the analytical result for comparison with a coupled FE-BE simulation where the external radiation is present. The internal radiation can be removed from the coupled FE-BE model by removing the acoustic domain inside the cylinder, which has been proven to produce a little effect on the structural response in a numerical study of the cylinder in Chapter 4 (see Figure 4-14). Therefore, the total surface pressure is approximated by the blocked pressure ($p_{blocked}$).

The reflected pressure ($p_{reflected}$) is from only the rigid scattering for an infinite cylinder. For a finite cylinder especially with short length, however, the cylinder's ends also play a role in the sound reflection.

3.1.1 Incident plane wave

Figure 3-1 shows a diagram of an incident plane wave impinging on a finite, elastic cylindrical shell. The cylinder length is $2L$. Its radius is R . The plane wave has an acoustic wavenumber vector \vec{k} with an incident angle of θ_i relative to cylinder axis (z axis) and an azimuthal angle of ϕ_i relative to the x axis. The pressure amplitude of the incident plane wave is p_0 . A rectangular coordinate system (x, y, z) and a cylindrical coordinate system (r, ϕ, z) are shown in the diagram. The origin of both of the coordinate systems is placed at the centre of the finite cylinder.

The boundary condition in the structural part is a shear diaphragm at both ends of the cylinder. This boundary condition restrains the radial and the circumferential components of the displacement at the cylinder ends and applies zero bending moment in the axial direction. The shear diaphragm boundary condition can be closely approximated by means of rigidly attaching a thin, flat, circular cover plate at each end and is equivalent to the simple-support boundary condition as realised for flat plates and beams. However, the shear diaphragm allows axial displacement components, because the thin cover plate would produce little restraint in this direction.

In the acoustic modelling, two rigid, semi-infinite cylindrical baffles are placed at the two ends of the elastic cylinder. This makes the structure acoustically infinite in the z direction, i.e. there is no finite boundary condition for the acoustic part in that direction.

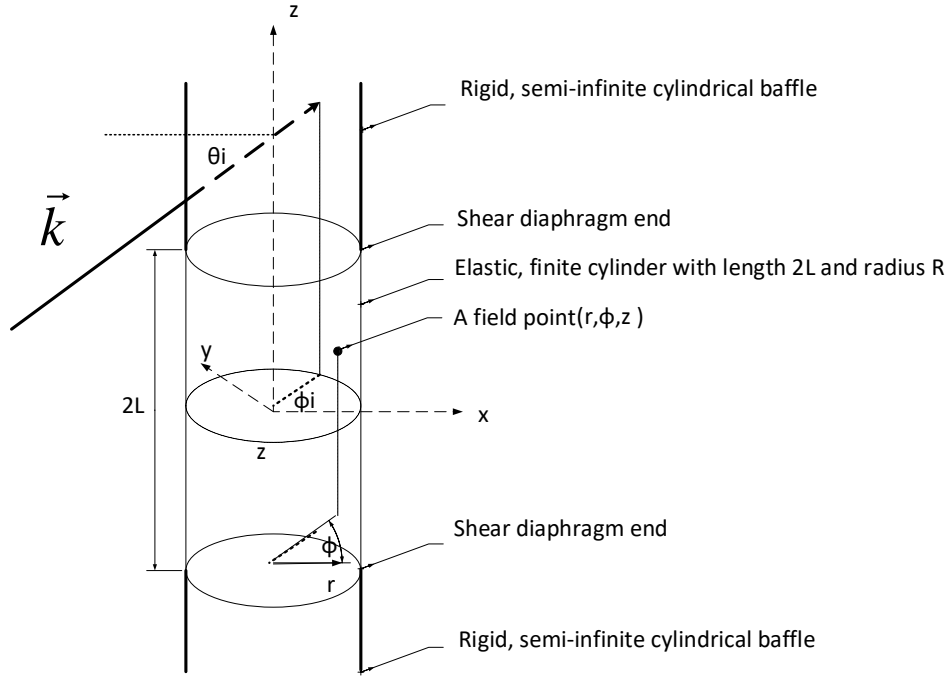


Figure 3-1 Diagram of an incident plane wave impinging on a finite cylinder with length of $2L$ and radius of R and with shear diaphragm ends. The plane wave has an acoustic wavenumber vector \vec{k} with an incident angle of θ_i relative to cylinder axis (z axis) and an azimuthal angle of ϕ_i relative to the positive direction of the x axis.

The incident plane wave propagating along the positive directions of the rectangular coordinate system can be written in the cylindrical coordinate system as

$$p_{incident}(r, \phi, z) = p_0 e^{-ikr \cos \theta_i \cos(\phi_i - \phi) - ikz \sin \theta_i} \quad \text{Eq.(3-3)}$$

By applying a complex Fourier series in the angle ϕ , Eq.(3-3) can be written as

$$p_{incident}(r, \phi, z) = p_0 e^{-ikz \sin \theta_i} \sum_{\nu=-\infty}^{\infty} (-i)^{\nu} J_{\nu}(kr \cos \theta_i) e^{i\nu(\phi_i - \phi)}, \quad \text{Eq.(3-4)}$$

where J_{ν} is the Bessel function of the first kind of order ν .

The reflected pressure from a rigid surface of the cylinder is necessarily in a form of an outgoing cylindrical wave [150], i.e.

$$p_{reflected}(r, \phi, z) = p_0 e^{-ikz \sin \theta_i} \sum_{\nu=-\infty}^{\infty} A_{\nu} H_{\nu}^{(2)}(kr \cos \theta_i) e^{i\nu(\phi_i - \phi)}, \quad \text{Eq.(3-5)}$$

where $H_{\nu}^{(2)}$ is the Hankel function of the second kind of order ν . In the following the symbol H_{ν} is used as an abbreviated form of $H_{\nu}^{(2)}$. A_{ν} can be evaluated by using the zero radial displacement on the rigid surface, i.e. $w_r(R, \phi, z) = 0$, yielding $A_{\nu} = -(-i)^{\nu} J'_{\nu}(kr \cos \theta_i) / H'_{\nu}(kr \cos \theta_i)$.

The blocked pressure on the cylinder surface can be obtained by summing Eq.(3-4) and Eq.(3-5), together with the recurrence formulae of $J_\nu H'_\nu - H_\nu J'_\nu = -\frac{2i}{\pi z}$, as

$$p_{blocked}(\phi, z) = -p_0 \frac{2i}{\pi k R \cos \theta_i} e^{-ikz \sin \theta_i} \sum_{\nu=-\infty}^{\infty} \frac{(-i)^\nu}{H'_\nu(kR \cos \theta_i)} e^{i\nu(\phi_i - \phi)}. \quad \text{Eq.(3-6)}$$

3.1.2 Incident spherical wave

In the next chapter validation tests for a cylindrical structure are described; in setting up the model in the anechoic chamber the sound source selected was close to a point source. This would generate spherical waves around the cylinder. In order to replicate the same type of excitation in the model, this section summarises the step adopted to evaluate the distribution of sound pressure around a cylinder for spherical wave excitation.

Figure 3-2 shows the geometry of a cylinder that is excited by an incident spherical wave from a point source outside the cylinder. The coordinate of the field point is (R, ϕ, z) and that of the point source is (r_s, ϕ_s, z_s) . The distance between the source and the field point is d_{fs} . The distance between the source and the projection of the field point on the cross-section plane of the source is d_{pfs} .

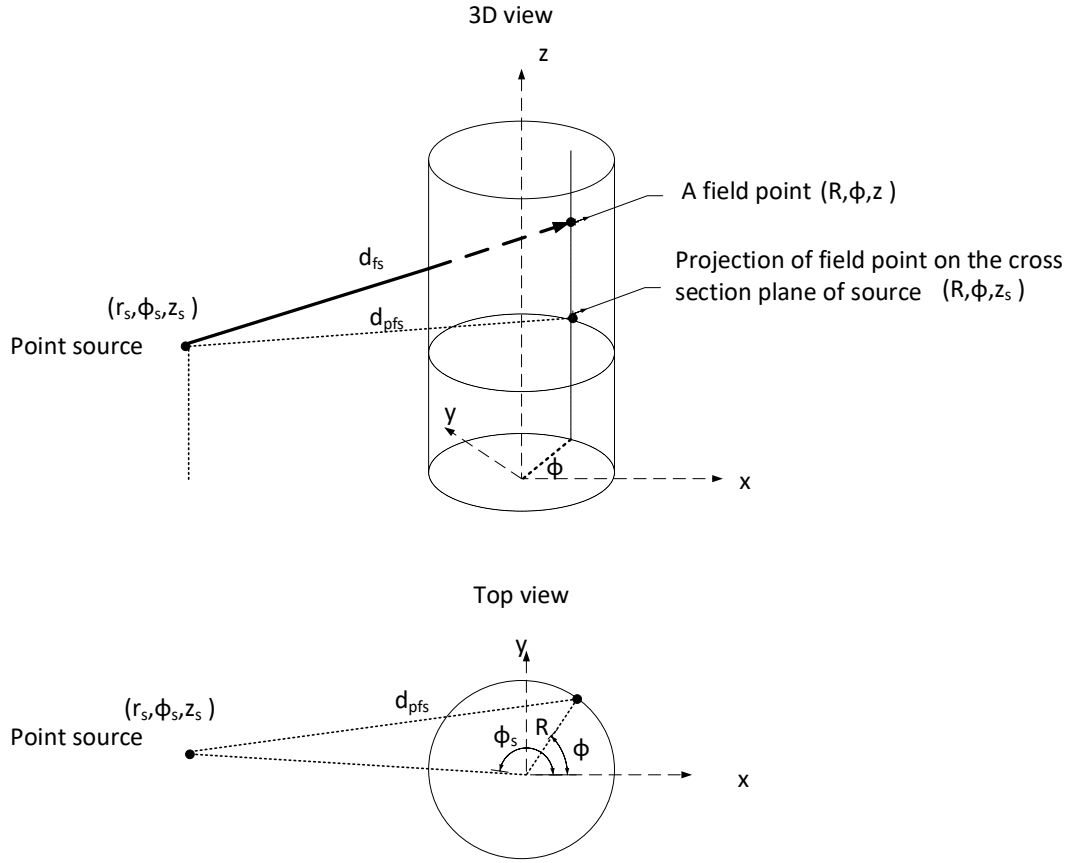


Figure 3-2 Diagrams of a spherical wave impinging on a cylinder from a point source (r_s, ϕ_0, z_0) outside the cylinder. The distance between the source and the field point on the cylinder surface is d_{fs} . The distance between the source and the projection of the field point on the cross section plane of the source is d_{pfs} .

If the origin of the cylindrical system is at the point source, the incident pressure on the field point from the source is

$$p_{incident} = i\omega\rho_0 Q \frac{e^{-ikd_{fs}}}{4\pi d_{fs}} = i\omega\rho_0 \Phi, \quad \text{Eq.(3-7)}$$

where Φ is the velocity potential. If the source strength Q is assumed to be $4\pi [m^3/s]$, the velocity potential is

$$\Phi = \frac{e^{-ikd_{fs}}}{d_{fs}}, \quad \text{Eq.(3-8)}$$

where $d_{fs} = \sqrt{d_{pfs}^2 + (z - z_s)^2}$.

By using Weyrich's formula [151], Eq.(3-8) can be expanded as

$$\Phi = -\frac{i}{2} \int_{-\infty}^{\infty} H_0 \left(d_{pfs} \sqrt{k^2 - \tau^2} \right) e^{-i\tau(z-z_s)} d\tau \quad \text{Eq.(3-9)}$$

where τ is the wavenumber and appears as a dummy variable in the integral.

From the geometric relation,

$$d_{pfs} = \sqrt{R^2 + r_s^2 - 2Rr_s \cos(\phi - \phi_s)} \quad \text{Eq.(3-10)}$$

For the calculation of the modal force and JAFs, Eq.(3-9) needs to be written in the same cylindrical coordinate system as the cylinder, so Graf's addition theorem is used. Figure 3-3 shows a point P with two polar coordinates (r_i, ϕ_i) and (r_j, ϕ_j) at two global coordinate systems centred at two origins O_i and O_j respectively.

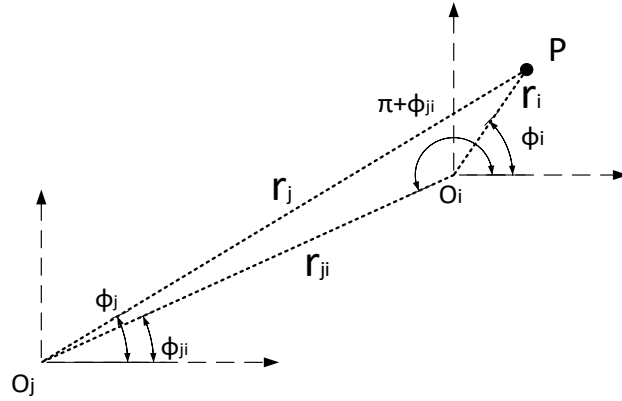


Figure 3-3 A point in two polar coordinate systems.

The following relation is given by Graf's addition theorem

$$H_m(\eta r_j) e^{-im(\phi_j - \phi_{ji})} = \sum_{v=-\infty}^{\infty} H_{m+v}(\eta r_{ji}) J_v(\eta r_i) e^{-iv(\pi + \phi_{ji} - \phi_i)} \quad \text{Eq.(3-11)}$$

provided $r_i < r_{ji}$. η is the wavenumber that can be related to the wavenumber k and τ in Eq.(3-9).

By letting the point source, the origin of the coordinate system and the projection of the field point in Figure 3-2 be the position of O_j , O_i and P in Figure 3-3 respectively, together with the following relations

$$r_j = d_{pfs}, r_{ji} = r_s, r_i = R, \phi_i = \phi, \phi_{ji} + \pi = \phi_s, m = 0, \eta = \sqrt{k^2 - \tau^2}, \quad \text{Eq.(3-12)}$$

Eq.(3-9) can be written as

$$\Phi = -\frac{i}{2} \sum_{v=-\infty}^{\infty} e^{-iv(\phi_s - \phi)} \int_{-\infty}^{\infty} H_v(r_s \sqrt{k^2 - \tau^2}) J_v(R \sqrt{k^2 - \tau^2}) e^{-i\tau(z - z_s)} d\tau. \quad \text{Eq.(3-13)}$$

Therefore, the incident pressure is

$$p_{incident} = \frac{\omega \rho_0}{2} \sum_{\nu=-\infty}^{\infty} e^{-i\nu(\phi_s - \phi)} \int_{-\infty}^{\infty} H_{\nu}(r_s \sqrt{k^2 - \tau^2}) J_{\nu}(R \sqrt{k^2 - \tau^2}) e^{-i\tau(z - z_s)} d\tau. \quad \text{Eq.(3-14)}$$

The reflected pressure from a rigid surface of the cylinder is necessarily in the form of an outgoing cylindrical wave [150], i.e.

$$p_{reflected} = \sum_{\nu=-\infty}^{\infty} e^{-i\nu(\phi_s - \phi)} \int_{-\infty}^{\infty} A_{\nu}(\tau) H_{\nu}(r_s \sqrt{k^2 - \tau^2}) e^{-i\tau(z - z_s)} d\tau, \quad \text{Eq.(3-15)}$$

where $A_{\nu}(\tau)$ are the unknown coefficients which can be evaluated by using the zero radial displacement on the rigid surface.

The blocked pressure on the rigid cylinder surface can be obtained by summing Eq.(3-14) and Eq.(3-15), which gives the expression

$$p_{blocked} = -\frac{i\omega \rho_0}{\pi R} \sum_{\nu=-\infty}^{\infty} e^{-i\nu(\phi_s - \phi)} \int_{-\infty}^{\infty} \frac{H_{\nu}(r_s \sqrt{k^2 - \tau^2})}{\sqrt{k^2 - \tau^2} H'_{\nu}(R \sqrt{k^2 - \tau^2})} e^{-i\tau(z - z_s)} d\tau \quad \text{Eq.(3-16)}$$

This expression for the blocked pressure is more accurate than the simple doubling of the incident pressure for a cylinder with curvature.

3.2 Modal force and JAF for plane wave excitation

It can be seen from Eq.(3-1) that if the re-radiated pressures from the structural vibration are neglected, the total surface pressure can be approximated by the blocked pressure. Hence the modal force can be approximated by using only the blocked pressures, i.e.,

$$l_{mn} \approx l_{mn}^{blocked} = - \int_0^{2\pi} \int_{-L}^L p_{blocked}(\phi, z) \psi_{mn}(\phi, z) dz (R d\phi). \quad \text{Eq.(3-17)}$$

where the negative sign indicates the opposite directions of positive external pressure (inwards) and the positive surface displacement (outwards). ψ_{mn} is the mode shape of the $(m, n)^{th}$ mode of a finite cylinder.

For the cylinder with shear diaphragm boundary conditions,

$$\psi_{mn}(\phi, z) = \sin \frac{m\pi(z + L)}{2L} e^{in\phi}, m = 1, 2, \dots, n = 0, \pm 1, \pm 2, \dots \quad \text{Eq.(3-18)}$$

Substituting the blocked pressures (Eq.(3-6) and Eq.(3-16)) and the mode shape in Eq.(3-18) into Eq.(3-17) and carrying out the integrals, the modal forces are then given as

$$l_{mn} \approx \frac{4p_0 I_m(k \sin \theta_i) (-i)^{n-1} e^{in\phi_i}}{k \cos \theta_i H'_n(Rk \cos \theta_i)} \quad \text{Eq.(3-19)}$$

for the plane wave excitation, and

$$l_{mn} \approx 2i\omega\rho_0 e^{-in\phi_s} \int_{-\infty}^{\infty} \frac{H_n(r_s \sqrt{k^2 - \tau^2})}{\sqrt{k^2 - \tau^2} H'_n(R\sqrt{k^2 - \tau^2})} e^{-i\tau z_s} I_m(\tau) d\tau \quad \text{Eq.(3-20)}$$

for the spherical wave excitation.

The function $I_m(\tau)$ is the integral of $\int_{-L}^L \sin \frac{m\pi(z+L)}{2L} e^{-i\tau z} dz$, which has a solution

$$I_m(\tau) = e^{-i\tau L} \left(\frac{2L}{m\pi} \right) \frac{(-1)^m e^{-2i\tau L} - 1}{\left(\frac{2\tau L}{m\pi} \right)^2 - 1}. \quad \text{Eq.(3-21)}$$

The JAF is calculated as the ratio between the modal force l_{mn} and the overall force l_o due to a uniform pressure field $2p_0$ over the cylinder surface, where $l_o = 8\pi RLp_0$.

This uniform pressure field is equal to the pressure amplitude for the plane wave, so the JAF can be written as

$$j_{mn}(\omega) = \frac{l_{mn}}{l_o} = \frac{1}{2\pi RL} I_m(k \sin \theta_i) (-i)^{n-1} \frac{e^{in\phi_i}}{k \cos \theta_i H'_n(Rk \cos \theta_i)}. \quad \text{Eq.(3-22)}$$

The circumferential and the axial components of the JAF can be separated as $j_{mn}(\omega) = j_{Am} j_{Cn}$.

For the blocked pressure assumption in Eq.(3-22), these are

$$j_{Cn} = \frac{1}{\pi R} (-i)^{n-1} \frac{e^{in\phi_i}}{k \cos \theta_i H'_n(Rk \cos \theta_i)} \quad \text{Eq.(3-23)}$$

$$j_{Am} = \frac{1}{2L} I_m(k \sin \theta_i)$$

If the blocked pressure is further approximated as the doubling of the incident pressure in Eq.(3-4) as discussed in [152], the corresponding JAF can be written as

$$j_{mn}(\omega) = \frac{1}{2L} I_m(k \sin \theta_i) (-i)^n J_n(kR \cos \theta_i) e^{in\phi_i} \quad \text{Eq.(3-24)}$$

with the circumferential and the axial components of the JAF

$$j_{Cn} = (-i)^n J_n(kR \cos \theta_i) e^{in\phi_i} \quad \text{Eq.(3-25)}$$

$$j_{Am} = \frac{1}{2L} I_m(k \sin \theta_i)$$

It can be seen from Eq.(3-23) and Eq.(3-25) that the sound scattering on the rigid surface affects the circumferential components of the JAF but not the axial one.

It is difficult to specify the uniform pressure field for the spherical wave directly, so a JAF may not be properly defined for this case. For the spherical wave case, the JAF, the modal force or

the responses from a modal approach are not required in this study. This is because the purpose of including spherical wave excitation is to derive the surface pressure distributions (Eq.(3-16)) for the test described in Chapter 4, where the modal approach is not appropriate to model the test structure, as detailed in Section 4.1.2.

3.3 Structural model

The surface blocked pressures hold for both unstiffened and stiffened cylinders provided the stiffeners are on the inner surface of the cylinder. The mode shapes required in the calculation of the modal forces, as discussed in section 2.2, can be obtained by both analytical models and structural FE models depending on the structural configuration.

Figure 3-4 shows the geometry of a cylinder which is internally stiffened by a set of rings (curved stiffeners around the cylinder circumference) and by a set of stringers (straight stiffeners along the cylinder axis).

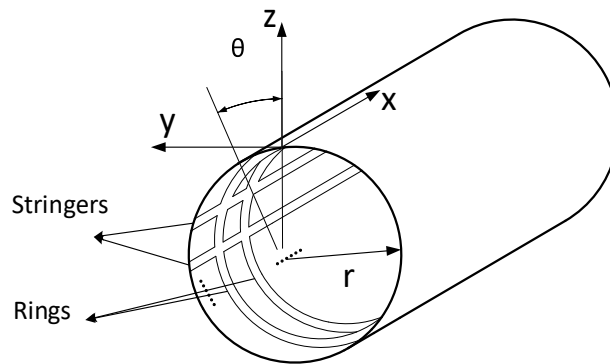


Figure 3-4 Geometry of a cylinder stiffened with stringers and rings.

In this chapter, an analytical model is used to facilitate the modelling for cylinders with different stiffener configurations. The analytical model for free vibration analysis is based on the energy approach and has been taken directly from reference [48]. For the cylindrical skin, both flexure and extension are considered. As a result of these deformations, the stiffeners are subjected to flexure about two perpendicular axes, extension along the axis and torsion.

Firstly, from the linear strain-displacement relation and the equation of state for plane stress, the strain energy for the cylinder and the stiffeners can be formulated as a function of the displacement. It is assumed the cross-section of the stiffeners does not warp and the depth of the ring cross-section is assumed negligible when compared with the cylinder radius. The displacement of the stiffeners is uncoupled using the elastic axis and referenced to that of the line of attachment.

Secondly, the compatibility conditions between the cylinder and the stiffeners are adopted to express the total energy in terms of the displacement of the cylinder middle surface. When the boundary conditions of the cylinder are assumed to be shear diaphragms, the displacements of the middle surface can be expressed as,

$$\begin{aligned} u &= \sum_m \sum_n (\bar{u}_{mn} \cos n\theta + \bar{u}'_{mn} \sin n\theta) \cos \frac{m\pi x}{a} \\ v &= \sum_m \sum_n (\bar{v}_{mn} \sin n\theta - \bar{v}'_{mn} \cos n\theta) \sin \frac{m\pi x}{a} \\ w &= \sum_m \sum_n (\bar{w}_{mn} \cos n\theta + \bar{w}'_{mn} \sin n\theta) \sin \frac{m\pi x}{a} \end{aligned} \quad \text{Eq.(3-26)}$$

where u, v, w are the displacements of the middle surface in the x, θ, z directions in Figure 3-4. $\bar{u}_{mn}, \bar{v}_{mn}$ and \bar{w}_{mn} are the modal coordinates of the symmetric circumferential modes and $\bar{u}'_{mn}, \bar{v}'_{mn}$ and \bar{w}'_{mn} are those of the antisymmetric modes.

Lastly, the equations of motion have been obtained by substituting the energy expression and Eq.(3-26) into Lagrange's equation [143]. The resulting frequency equation has been numerically solved in MATLAB to obtain the natural frequencies and mode shapes of the stiffened cylinder. The detailed derivation can be found in reference [48].

In this chapter, four types of structural configurations are considered for aluminium cylinders. They are an unstiffened cylinder, a cylinder stiffened by 9 equally spaced rings, a cylinder stiffened by 8 equally spaced stringers and a cylinder stiffened by both rings and stringers of the same number and positions.

Table 3-1 shows the structural and material parameters for the stiffened cylinders. The stiffeners, including both the stringers and the rings, have rectangular cross-section.

Table 3-1 The structural and material parameters for the stiffened cylinders

Cylinder (unit: mm)		Stiffener (unit: mm)		Material (aluminium)	
r_c , radius	900	w_s , width	2	E , Young's modulus (GPa)	71
l_c , length	300	d_s , depth	4	ρ , density (kg/m ³)	2700
t_c , thickness	2			ν , Poisson's ratio	0.3

This is a short and wide cylinder and the dimensions of the stiffened cylinders are selected based on three assumptions in the analytical model.

- The first one is the light beam assumption, which requires a low ratio between the stiffener's depth and the cylinder skin thickness. This ratio is 2 in the current configuration.
- The second one is the line contact assumption. This assumption was found valid when the stiffener width is not greater than the skin thickness [48], which is the case for the cross-section of the current stiffeners.
- In addition, the modal model also considers that the beam depth is negligible compared to the cylinder radius in the formulation of the strain energy of the beam. This is valid for the example structures where the stiffeners depth is less than 0.5% of the cylinder radius.

In the numerical calculation, hysteretic damping is assumed using a damping loss factor of 1%. The numerical simulation was performed in MATLAB.

Figure 3-5 shows the results of the natural frequencies of the lowest 20 modes for each structural configuration denoted by different marker symbols. The bare cylinder without stiffeners is in circle markers. The cylinder with only ring stiffeners is in square markers. The cylinder with only stringer stiffeners is indicated by plus sign markers. The cylinder with both ring and stringer stiffeners is indicated by asterisk markers.

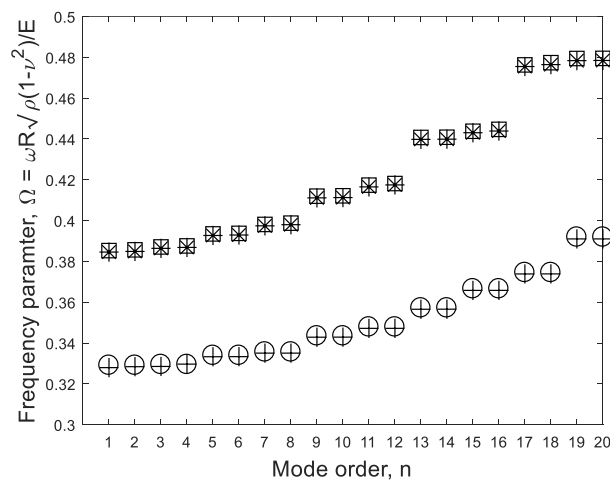


Figure 3-5 The natural frequencies of the lowest 20 modes for each case of the cylinders, plotted as non-dimensional frequency $\Omega = \omega/\omega_R$ where $\omega_R = \frac{1}{R} \sqrt{\frac{E}{\rho(1-\nu^2)}}$ is the ring frequency (951 Hz) for a cylindrical plain shell. Circle markers 'o': bare cylinder. Square markers '□': cylinder with only rings. Plus sign markers '+': cylinder with only stringers. Asterisk markers '*': cylinder with both rings and stringers.

The natural frequencies appear in pairs for each structural configuration. Each pair of frequencies corresponds to the symmetric/anti-symmetric modes. The frequencies are identical for the bare cylinder, which is axisymmetric, and slightly different for the ring-stiffened cylinders as the latter are periodic in the circumferential direction but no longer axisymmetric.

Compared to the plain cylinder, the rings increase the natural frequencies in each mode while the stringers decrease them slightly. This is because these modes are dominated by the circumferential deformation and the rings constrain the extensional or the flexural motions of these modes, which effectively stiffens the cylinder. In contrast, the stringers put no constraints but apply mass to these modes, which decreases the natural frequencies.

The grouped behaviour of the natural frequencies is not as significant as in the stiffened plate case considered [140]. This is because the stiffeners attached to the cylinder are light beams. In addition, the cylinder is also stiffened by the curvature, so the stiffness effect of the rings on the cylinder will not be as significant as that for the stiffeners applied to the plates.

3.4 Numerical results

In this subsection, the JAFs and the dynamic responses of the cylinders subjected to incident plane wave excitation are calculated.

3.4.1 Joint Acceptance Functions

The JAFs for the total surface pressures using two different assumptions are calculated and compared. They are using either the blocked pressure, including scattering, or pressure doubling (twice of the incident pressure). The latter is typically valid for plane structures and neglects any scattering effects due to the curvature. The structural modes from an unstiffened cylinder with shear diaphragm boundary condition are used so that the JAFs can be calculated analytically from the equations in Section 0.

Figure 3-6 shows the axial component of the JAF for the first 4 bending modes of the cylinder subjected to plane wave excitation. It is plotted against the ratio between the structural wavelength $\lambda_m = 2l_c/m$ and the acoustic trace wavelength $\lambda_{tA} = \frac{2\pi}{k \sin \theta_i}$ in the axial direction. This is proportional to frequency for each mode.

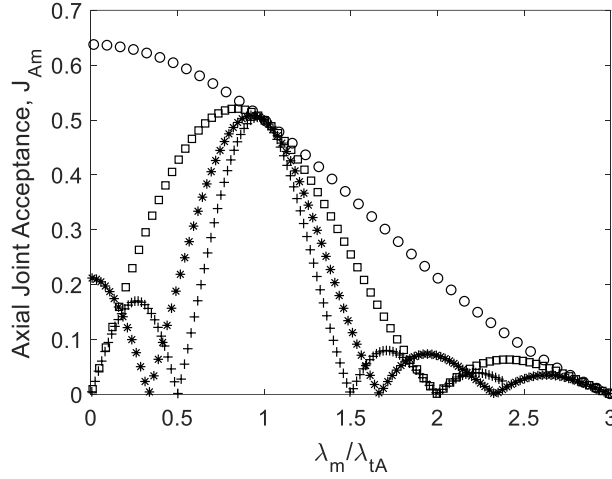


Figure 3-6 The axial component of the JAF for the first 4 bending modes of cylinder subjected to plane wave excitation. Circle markers 'o': the 1st mode. Square markers '□': the 2nd mode. Asterisk markers '*': the 3rd mode. Plus sign markers '+': the 4th mode.

The results show that the axial component of the JAF for the cylinder has the same shape as the JAF for a flat plate, shown in Figure 1-2. When the acoustic trace wavelength matches the structural bending wavelength at the coincidence frequency, a principal maximum will appear in the corresponding JAF, which is the coincidence effect. At higher frequency, the JAF consists of harmonic and subharmonic peaks and valleys, which shows a clear acoustic wavelength selectivity due to the cancellation of harmonics in the modal force distribution. The magnitude of the JAF is also higher than that in Figure 1-2. This is because the latter is for a two-dimensional plate, but the JAF shown here is only an axial component and is effectively equivalent to the case for a one-dimensional beam.

Figure 3-7 shows the circumferential component of the JAF for the 2nd to the 4th bending modes of the cylinder subjected to plane wave excitation. It is plotted against the ratio between the structural wavelength $\lambda_n = 2\pi r_c/n$ and the acoustic trace wavelength $\lambda_{tc} = \frac{2\pi}{k \cos \theta_i}$ in the circumferential direction. The 1st circumferential mode, the 'breathing mode', is excluded in this plot, as it has infinite structural wavelength, i.e. $\lambda_0 = \infty$, but it will be discussed separately in Figure 3-8.

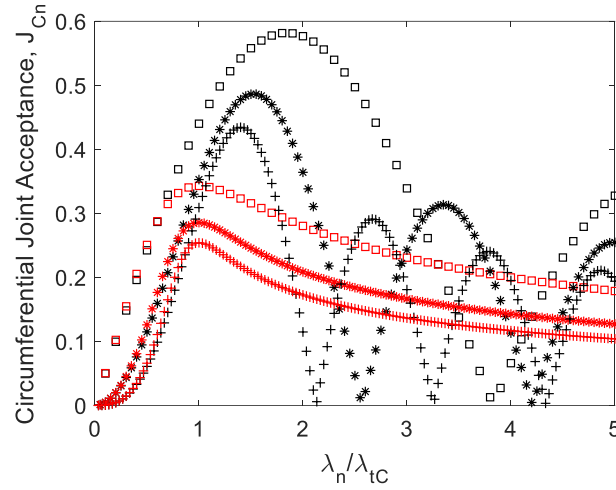


Figure 3-7 The circumferential component of the JAF for the 2nd to the 4th bending modes of cylinder subjected to plane wave excitation. Square markers '□': the 2nd mode. Asterisk markers '*': the 3rd mode. Plus sign markers '+': the 4th mode. The black markers are from the pressure doubling assumption. The red markers are from the blocked pressure assumption

The coincidence effect is weak in both the doubled pressure (the black colour results) and the blocked pressure (the red colour results). This is because the pressure distribution around the circumference from either of the two pressure models does not form a constant acoustic (trace) wavelength. For the results using the doubled pressure, there is a fundamental difference of the JAF between a cylinder and a plate. When one increases the cylinder radius, the curvature is reduced, but the JAF is still different from the plate JAF.

The acoustic wavelength selectivity is still preserved in the pressure doubling results (in black colour) for each mode, i.e. the JAF of one mode always has peaks and valleys at certain acoustic wavelengths. This is because the spatial correlation of the surface pressure is not changed for the pressure doubling results.

However, the acoustic wavelength selectivity is not present for the blocked pressure assumption as the wavelength ratio increases (in red markers). The JAF for each mode becomes smoother and more continuous and its magnitude tends to increase everywhere at low frequencies, except in the coincidence region, and the curves seem to coalesce for different modes at high frequencies. This is because the spatial variation of the distribution of the reflected pressure varies more rapidly around the circumference when the acoustic wavelength is small compared to the structural wavelength [150, 153]. This makes the total pressure field more like a diffuse field, i.e. the spatial correlation of the total pressure field is reduced. As a result, the mode shapes progressively lose their acoustic wavelength selectivity as the spatial correlation of the pressure field drops [36].

Figure 3-8 shows the circumferential component of the JAF for the first circumferential modes of a cylinder, i.e. the ‘breathing’ mode. The results for the doubled pressure are in black circles and those for the blocked pressure are in red circles. The acoustic trace wavelength may not be properly defined around the circumferential direction, so the results are plotted against the circumferential non-dimensional parameter $k_{tC}R$ where $k_{tC} = k \cos \theta_i$.

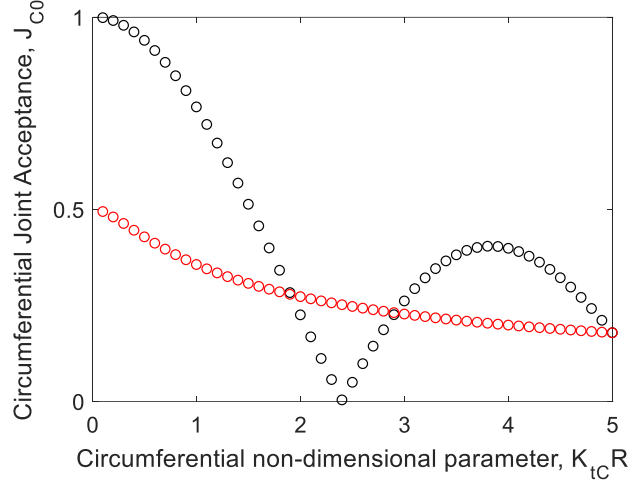


Figure 3-8 The circumferential component of the JAF for the first circumferential modes of cylinder subjected to plane wave excitation. The black circled markers ‘o’ are from the pressure doubling assumption. The red circled markers ‘o’ are from the blocked pressure assumption.

For the doubled pressure results, the maximum JAF is close to 1 at $k_{tC}R = 0$ for the first circumferential mode, i.e. $n = 0$. This is because the acoustic field is equivalent to the uniform static pressure for a specific cylinder radius. The acoustic wavelength can be regarded as infinite, which fully matches the circumferential structural bending wavelength of the ‘breathing’ mode.

For the blocked pressure results, the maxima occur at the same mode and position, but the value reduces to close to 0.5. This is because the reflected pressure is very small compared to the incident pressure for small values of $k_{tC}R$ [153]. So the JAF reduces to a half compared to the case of pressure doubling.

3.4.2 Dynamic response

The displacement responses are next calculated for the four cylinders subjected to an incident plane wave excitation. The sound pressure level (SPL) of the incident sound field is 91 dB for all the cases evaluated. The incident angle with the cylinder axis is $\frac{\pi}{4}$.

The response is calculated for the point on the surface that is on the middle plane of the cylinder axis and is on the rear side of the cylinder to the incident sound. This point is located

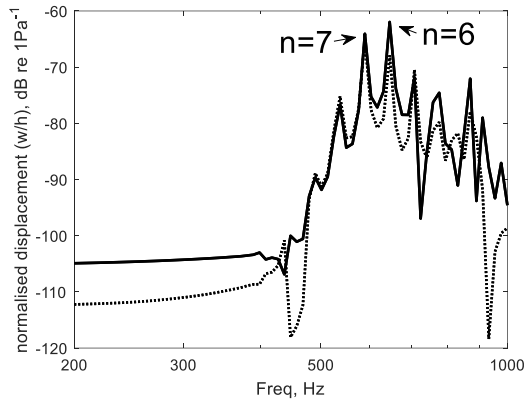
away from stringers and rings. The difference between the doubled pressure and the blocked pressure is also significant at this position.

The modal forces used in the calculations were evaluated by numerical integration. The infinite summation in the pressure expression in section 3.1.1 was approximated by a finite summation $|v| \leq 50$.

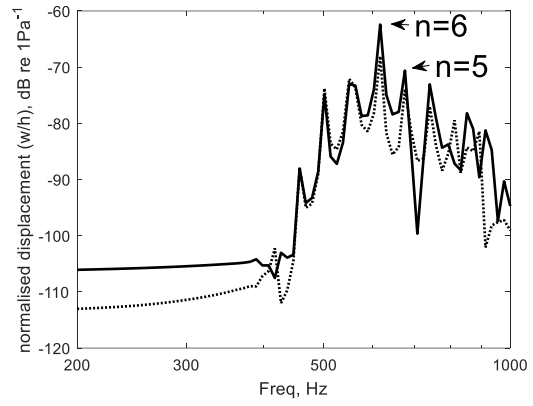
These results are given as the transfer function between the radial displacement of the cylinders and the unit magnitude pressure input for the sound field. The displacement is normalised by the cylinder thickness. The frequency range is up to 1000Hz, with a frequency resolution of 100 points per decade. All the modes up to 1200 Hz are included in the modal summation. The number of the modes for the four cylinders is 231, 189, 230 and 184 respectively.

Figure 3-9 (a) to (d) show the responses of the four cylinders (a) – (d) subjected to the plane wave excitations. The responses are for two different surface pressure assumptions. The solid lines are the doubled pressure (twice the incident pressure) and the dotted lines are the blocked pressure (the sum of the incident pressure and the reflected pressure from the rigid cylindrical surface).

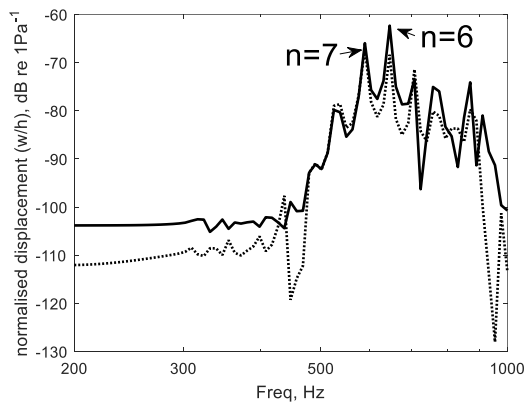
Figure 3-10 (a) to (d) show the orders of the modes in the frequency range below 1000 Hz. The modes associated with the predominant response peaks are marked with the solid circles and are within the bands highlighted in grey. The other modes are marked with the hollow circles.



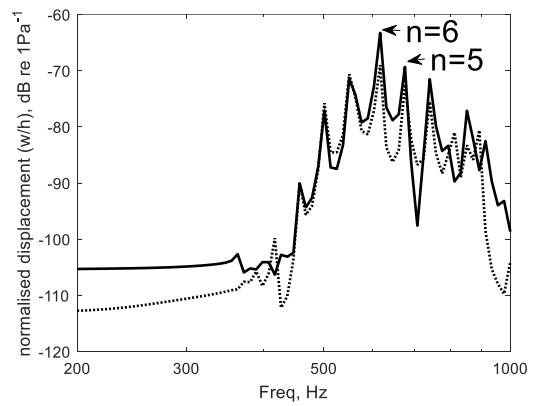
(a)



(b)



(c)



(d)

Figure 3-9 The normalized radial displacement transfer function for the bare cylinder (a), the stiffened cylinder with 9 rings (b), the stiffened cylinder with 8 stringers (c), and the stiffened cylinder with both 9 rings and 8 stringers (d). The responses are for two different surface total pressure assumptions. Solid line: the doubled pressure (twice of the incident pressure). Dotted line: the blocked pressure (the sum of incident pressure and the scattered pressure from rigid cylindrical surface).

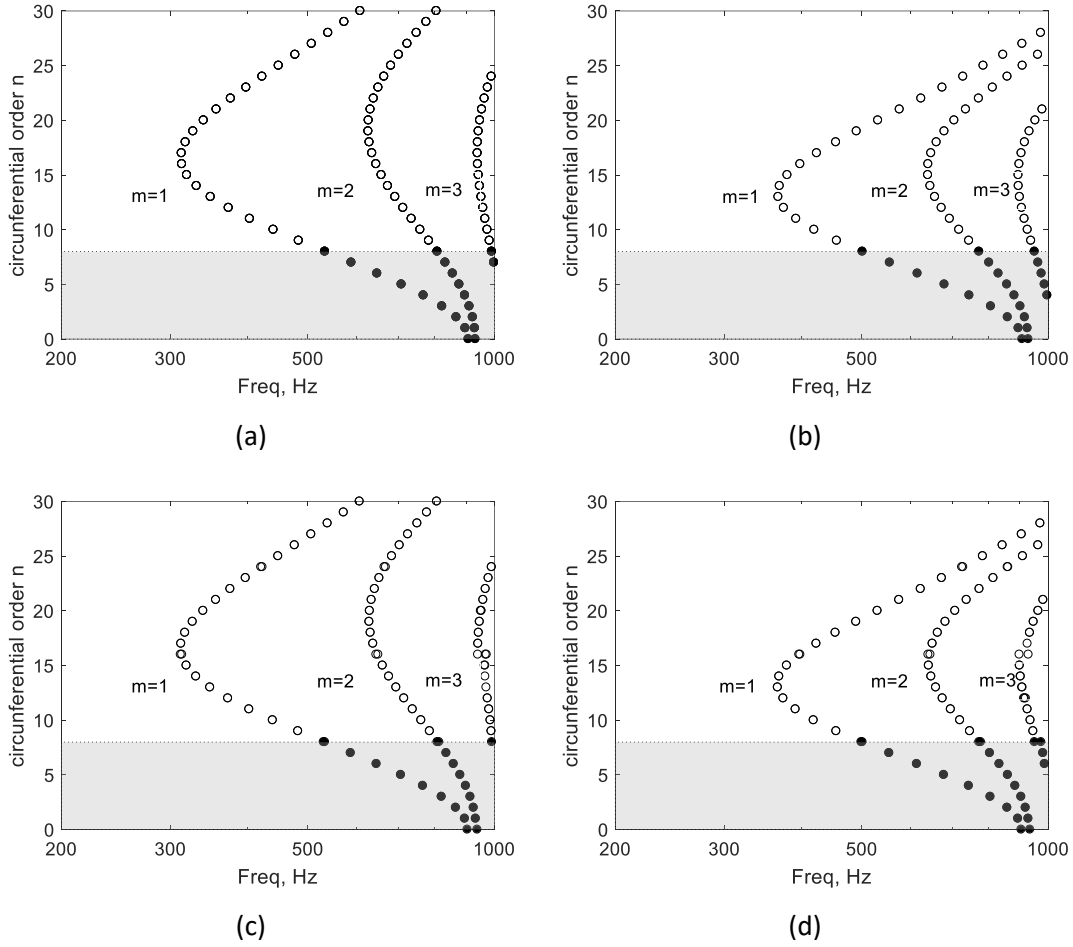


Figure 3-10 Orders of the cylinder modes below 1000 Hz for the unstiffened cylinder (a), stiffened cylinder with 9 rings (b), stiffened cylinder with 8 stringers (c) and with both rings and stringers (d). The modes associated with the predominant peaks in corresponding responses are marked by solid circles and are within the bands indicated in grey. Other modes are marked with hollow circles.

Figure 3-9 (a) to (d) all show three distinct frequency ranges in the responses results. Below 300 Hz the responses are mostly constant. This is due to the absence of modes, which can be confirmed in Figure 3-10 (a) to (d). Between 300 and 500 Hz the structures start to show small resonance peaks corresponding to the first few vibration modes. The response is not large in this range because these modes have relatively high circumferential orders ($n \geq 9$) and cannot be efficiently excited by the acoustic field. Between 500 and 1000 Hz the responses increase, showing a broad response peak superimposed by various resonance peaks. The modes presented in this frequency range have low circumferential orders ($n \leq 8$).

The results also show that for all four cylinders the highest peaks in the responses correspond to the mode $n = 6$ and $m = 1$. The presence of the rings affects the order of the second highest peak, from $n = 7$ to $n = 5$, as it changes the circumferential stiffness. The presence of the stringers has little effect on the responses.

Additionally, the results also show that the predictions using the doubled pressure excitation produce overestimates in the responses compared to using the blocked pressure. The assumption using the blocked pressure results in more accurate predictions compared to those using the doubled pressure, as discussed in [152].

3.4.3 Comparison with a coupled FE-BE model

To examine the assumption of the blocked pressure for the analytical model, the results for the unstiffened cylinder obtained in Figure 3-9 (a) are compared with a coupled FE-BE numerical simulation developed in COMSOL. As one purpose of the comparison is to verify the blocked pressure that includes the rigid scattering effect, an acoustic incident plane wave must be used as excitation instead of using the pressure loading described in Section 2.4. A direct consequence of this is that the incident plane wave will be diffracted from the edges of the cylinder. The vibroacoustic coupling in the coupled FE-BE model may also introduce additional differences in the comparisons. Some approximate measures are taken to minimise these effects. An uncoupled FE model with the blocked pressure is also used for reference.

Figure 3-11 (a) shows the meshed FE-BE model. The elastic cylinder FEM is embedded between two rigid cylinders to reduce the effects of the wave reflections from the ends of the elastic cylinder. The elastic cylinder FE is in the blue area and is meshed by Mapped Mesh with a size of $1/5$ of the structural bending wavelength for an infinite plate of identical thickness. The rigid cylinder BE is meshed by Free Triangular Mesh with size of $1/5$ of the acoustic wavelength. The length of each rigid cylinder BE mesh is equal to one acoustic wavelength. Both the mesh size and the length of the rigid cylinder are frequency dependent.

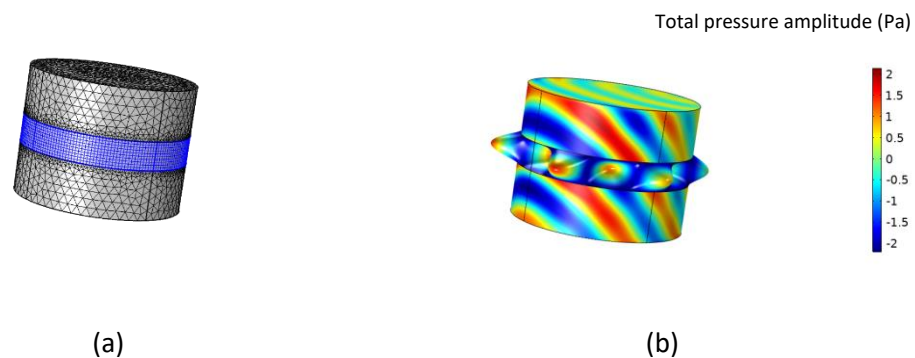


Figure 3-11 A coupled FE-BE numerical model for the baffled cylinder subjected to an incident plane wave with the incident angle of $\frac{\pi}{4}$ and the SPL of 91 dB at 650 Hz around the highest response peaks. (a) The meshed model. (b) The radial displacement (m) of the cylinder midplane with a scale factor of 1×10^6 and the total acoustic pressure (Pa) on the rigid cylindrical baffle surface.

Figure 3-12 shows the comparison between the analytical model, the FE model and the coupled FE-BE model. The result from the analytical model with blocked pressure is given by a black solid line. The result from the FE with blocked pressure is given by a blue dashed line. The result from the BE-FE model is shown by a red dashed line.

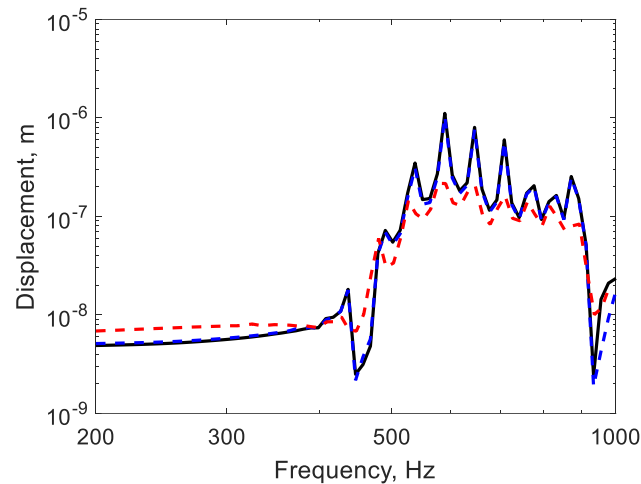


Figure 3-12 Radial displacement of the reference point for the unstiffened cylinder calculated by different models. Black solid line: analytical model with blocked pressure. Blue dashed line: FE model with blocked pressure. Red dashed line: coupled FE-BE model.

The results show that the agreement between the two uncoupled models, i.e., the analytical and the FE models, is very good. This indicates the structural modelling of the cylinder is accurate.

The responses from the two uncoupled models have a satisfactory agreement with that from the coupled FE-BE model in the non-resonance regions. At low frequencies the coupled and uncoupled results differ by about 40%. This difference might arise from the acoustic excitation. The blocked pressure approximation used in the uncoupled models includes the rigid scattering from an infinite cylinder. However, a finite cylinder was used. Although two rigid, finite cylindrical baffles are placed at the two ends of the elastic cylinder, the ends of the baffles still play a role in the sound reflection.

The agreement in the resonance regions is not good, especially in the frequency range between 500 – 1000 Hz. It can be observed that the resonance peaks in the coupled FE-BE model are more damped than those predicted by the uncoupled models. The reason for this may be the contribution of the radiation damping caused by the vibroacoustic coupling in the coupled FE-BE model, as discussed in Chapter 2 for the case of stiffened plates. As the goal of this chapter is to investigate the effect of curvature rather than vibroacoustic coupling, no attempt was made to develop a fully coupled analytical model for the cylinder. A qualitative estimation,

however, can still be made to verify the contribution of the radiation damping. Figure 3-13 shows an updated result (in red dashed line) where the radiation damping loss factor of 3% for all modes was included, increasing the total damping value of the uncoupled analytical model from 1% to 4%.

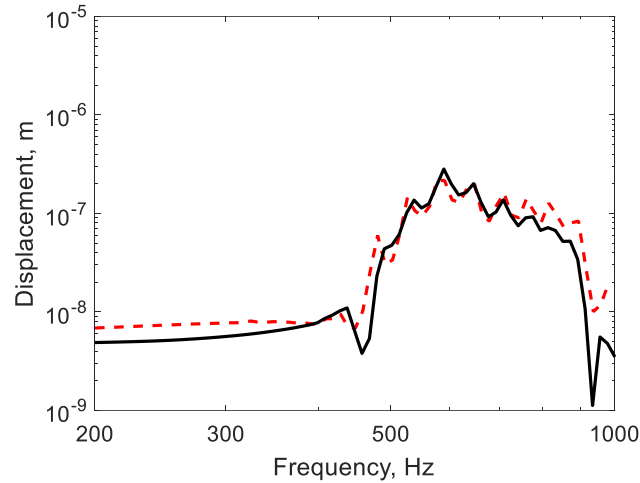


Figure 3-13 Radial displacement of the reference point for the unstiffened cylinder calculated by different models. Black solid line: analytical model with blocked pressure with radiation damping. Red dashed line: coupled FE-BE model.

It can be seen that the agreement in the comparison within the frequency range 500 – 700 Hz is largely improved by adding the radiation damping of 3% to all the modes used in the modal summation of the uncoupled model. Above 700 Hz, the response of the uncoupled model is overdamped compared to that of the coupled FE-BE model. This may be because the radiation damping of the modes in this frequency region is now overestimated.

However, in view of the severe approximate measures which have been made in the comparison this is considered to be satisfactory agreement. The reason for this satisfactory agreement is thought to be primarily due to the treatments of the finite rigid cylindrical baffles and the qualitative estimation of the radiation damping having opposite effects on the comparison.

In terms of the calculation time in using the same CPU, the runtime for coupled FE-BE model is about 40 hours, while that of the uncoupled model is about 5 minutes.

3.5 Summary

This chapter presented the prediction methodologies for the acoustic responses of stiffened cylinders subjected to both plane wave and spherical wave fields. Both the rigid acoustic scattering and the stiffener effects are included in the predictions. The total surface blocked

pressure for plane wave and spherical wave excitation are revisited. The Joint Acceptance Functions (JAFs) based on both the blocked pressure and the doubled pressure for the plane wave excitation were derived for an unstiffened cylinder with shear diaphragm boundary conditions. The numerical results of the dynamic responses are given for cylinders with different stiffener configurations and surface pressure assumptions. The response of the unstiffened cylinder subjected to the blocked pressure is also compared with that from a coupled FE-BE model.

The main findings can be summarised as:

- The effects of ring and stringer stiffeners on the modal stiffness of the cylinders depend on the direction of the dominating deformation of the modes. In the example cylinders, the natural frequencies are increased by the rings but is decreased by the stringers.
- The coincidence and the wavelength selectivity of Joint Acceptance Functions (JAFs), which are two significant features in plane structures, are reduced by structural curvature and rigid scattering of the sound respectively.
- The doubled pressure assumption resulted in overestimating the surface pressure and the subsequent response compared to the blocked pressure assumptions. The latter matches well with a fully coupled FE-BE model in the non-resonant regions, while the agreement in the resonant regions can be significantly improved by taking into account the vibroacoustic coupling by appointing of the radiation damping.

Chapter 4 Experimental investigation of the acoustic response of a scaled fuselage model

This chapter describes the measurements performed on a ring-stiffened, thin-walled aircraft fuselage model. The purpose is to investigate the predictions of the surface pressure and the subsequent vibration responses for the stiffened cylinder in the context of experiments on a practical structure. The finite element method instead of the normal mode method is used for such a complex test structure, as the complexity is too high for a simple representation. First, the mobility of the test structure was measured by an instrumented impact hammer test and this was compared with the results produced from several different FE models. Then an acoustic test was performed in the anechoic chamber, to examine both the excitation and the response models for the cylinder subjected to a spherical incident acoustic wave.

4.1 The test structure and modelling

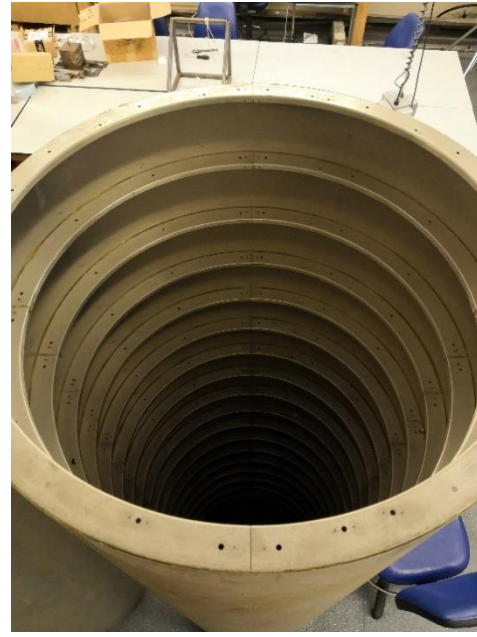
4.1.1 The scaled fuselage

A quarter scale aircraft fuselage model with ring stiffeners around the circumference was used as the test structure. It was mainly constructed by the technical staff in ISVR during the research work by Mason on the sound transmission through an aircraft fuselage [154].

Figure 4-1 (a) shows the fuselage test structure. Figure 4-1(b) shows the view of the ring stiffeners inside the test structure. Each ring stiffener is attached around the circumferential direction and they are all aligned in the axial direction on the inner surface of the cylinder. Adhesive materials and rivets are used in the joints. The material of the test structure is NS-4-H6 Aluminium.



(a)



(b)

Figure 4-1 The test structure: a quarter scale fuselage model (a) with ring stiffeners (b).

Figure 4-2 shows a drawing of the geometry of the test structure. The body of the test structure, a cylinder, is stiffened by 18 equispaced, thin-walled section frames. The section frame has a cross-section of 'C' shape. One of the section walls of each frame is attached around the circumference of the cylinder.

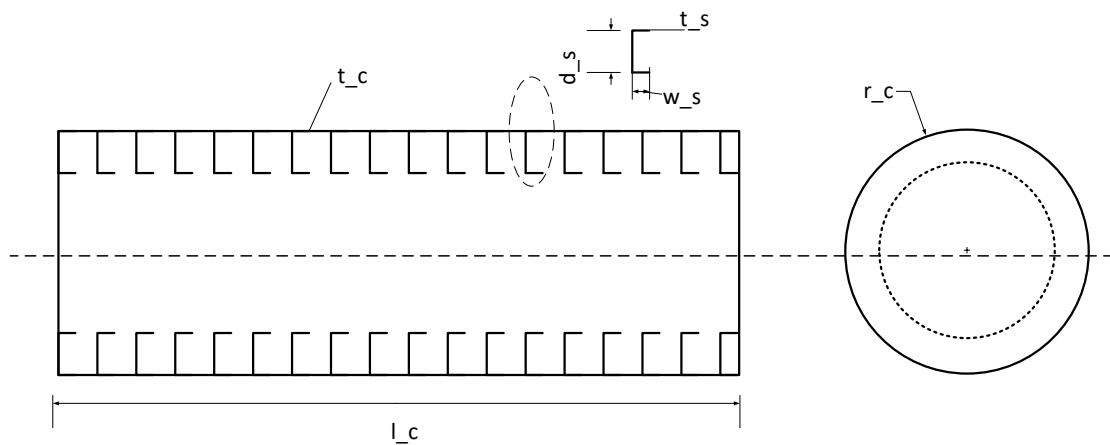


Figure 4-2 The drawing of the geometry of the ring-stiffened cylinder test structure.

The structural dimensions of the test structure are listed in Table 4-1.

Table 4-1 The structural dimensions of the test structure.

Name	Symbol	Value (m)
Cylinder radius	r_c	0.38
Cylinder length	l_c	2.43
Bay length	l_b	0.14
Cylinder skin thickness	t_c	5.60×10^{-4}
Ring stiffener width	w_s	1.27×10^{-2}
Ring stiffener depth	d_s	3.81×10^{-2}
Ring stiffener thickness	t_s	6.80×10^{-4}

A more detailed description of the model is given in [154].

4.1.2 The normal mode method

The normal mode method was considered initially for modelling the scaled fuselage. The modal model based on the normal mode method was developed for the test structure. However, the modal model failed to accurately represent the test structure.

The main issue is that the ill-conditioned eigenvalue problem resulted in non-physical negative eigenvalues. The reason for this is that the light beam stiffener representation is not valid for the test structure [46], because the bending stiffness of the stiffeners has a high contribution to the total bending stiffness of the structure. The stiffener cross-sectional area is 60 mm^2 , which is comparable to the cross-sectional area of the cylinder skin between stiffeners namely 80 mm^2 . This is mainly caused by the very high ratio, 68, between the stiffener depth and the cylinder skin thickness. A threshold value for this ratio to solve the issue was determined by a parameter study. In this study the cylinder skin thickness was increased gradually and the free vibration analysis was performed in both the modal model and a FEM. The natural frequencies of the two models were then compared with each other. It was found that the skin thickness should be increased to at least one fifth of the stiffener depth to obtain a convergent modal model whose free vibration results match that of the FEM model.

The other issues relate to the validity of the assumptions in the modal model, but they only affect the accuracy rather than the convergence of the model. Firstly, the warping stiffness of the beam stiffener is not included. The warping effect should be considered for a thin-walled open section beam [155]. The warping deformation will modify the shear strain throughout the cross-section and change the torsional behaviour of the beam [88]. This effect may be neglected for light stiffeners [48], but it is inadequate to do so in the current test structure.

Secondly, the stiffener-skin interface is treated as a line contact. The line contact assumption was found valid when the stiffener width is not greater than the skin thickness [48], which is not the case in the test structure, where the stiffener width is more than 200 times larger than the skin thickness. In addition, the modal model also considers the beam depth to be negligible compared to the cylinder radius in the formulation of the strain energy of the beam. This may not be appropriate for representing the test structure, where the stiffener depth is 10% of the cylinder radius, although this deficiency might not be significant.

Hence, the normal mode method is not used for modelling the test structure due to the complexity of the test structure.

4.1.3 The FE models

The finite element method was used to model the test structure for three reasons. Firstly, as discussed in last section, the light beam assumption that causes the ill-condition issue in the modal model of the test structure is not required. Secondly, a more general boundary condition can be considered. Thirdly, the vibroacoustic coupling effect can be more easily examined by combining the structural FE model with an acoustic FE or BE model.

To examine the effect of the line contact assumption, two different FE models were built in the 'Structural mechanics' module of COMSOL software. The details of the two FE models are listed in Table 4-2.

The stiffeners are modelled by beam elements in FE model A. In the contact line with the cylinder's skin, the 'Shell-Beam Connection' is used to couple the two parts together. The stiffeners were modelled by shell elements in FE model B. In the contact area with the cylinder's skin, the stiffener edges and the cylinder skin share the same nodes. In both of the FE models, the warping stiffness of the stiffeners is included. This is automatically included in FE model B where the stiffeners are modelled as shell elements. In FE model A, the Timoshenko beams with open cross-section were used to include the warping stiffness.

Table 4-2 Details of three FE models for test structure.

FE model No.	Stiffeners	Cylinder	Contact
A	Cubic beam element	Quadratic shell element	Shell-Beam Connection
B	Quadratic shell element	Quadratic shell element	Sharing nodes

An unstructured triangular mesh was used in both FE models by using a 'Free Triangular' meshing procedure in COMSOL. The mesh was automatically created and adapted for the models' physical settings, which means that the mesh close to the joints is finer than that far away from them.

A convergence study to determine the proper mesh size was performed in FE model B, as this modelling approach is more demanding in terms of the number of elements. The convergence criterion was set to be on the variation of the natural frequency of the first local mode, i.e. the first mode of the bay between two adjacent ring stiffeners, over the changing mesh size. The value of the mesh size is set to decrease from the bending wavelength for an infinite plate of identical thickness λ_p at the frequency of 1kHz, which is 0.074m. Table 4-3 lists the natural frequencies of the first local mode for different mesh size.

Table 4-3 The natural frequencies of the first local mode for different mesh size.

Mesh size (mm)	Natural frequency of first local mode (Hz)
74	640.17
37	602.80
24.7	591.90
18.5	590.69
14.8	590.67
12.3	590.98

The result shows that the natural frequency decreases rapidly as the mesh size decreases from 74 mm to 24.7 mm, but it converges to 590.69Hz for the mesh size of 18.5 mm. The frequency changes little when the mesh size is further reduced. So the maximum mesh size was set to be 18.5 mm. There are approximately 8 elements in the axial direction between two adjacent ring stiffeners. The FE model B with the selected mesh size is shown in Figure 4-3.



Figure 4-3 The meshed FE model B in COMSOL.

The total number of finite elements in the FE model A is 41872 and that in FE model B is 60088.

Table 4-4 shows a comparison of the lowest cylinder modes between FE models A and B with free boundary conditions. These modes include the eight lowest global modes and the first local mode. The global modes are those that involve deformation of the whole cylinder. The local mode is determined by the behaviour of a small cylindrical bay delimited by the ring stiffeners.

Table 4-4 The comparison of the predicted lowest global modes and lowest local mode in FE models A and B with free ends boundary conditions.

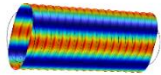
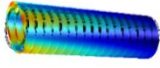
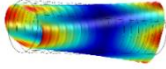
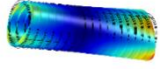
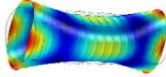
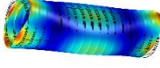
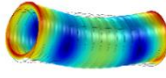

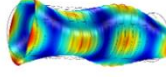



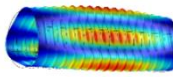
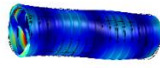
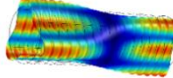
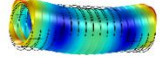
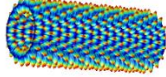
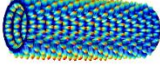
Mode	FE model A		FE model B	
	Mode shape	Natural frequency (Hz)	Mode shape	Natural frequency (Hz)
1 st global		162		148
2 nd global		165		151
3 rd global		243		234
4 th global		420		400
5 th global		432		406
6 th global		464		417
7 th global		490		457
8 th global		499		474
1 st local		570		591

Figure 4-4 shows the comparison of the modal properties in terms of the Modal Assurance Criterion [147], for the mode shapes, and the scatter plots for the lowest 8 global modes with modes 1 – 8 and the lowest local mode, i.e. ninth mode, of the test structures. Only one of the modes in each mode pair was used in the comparison.

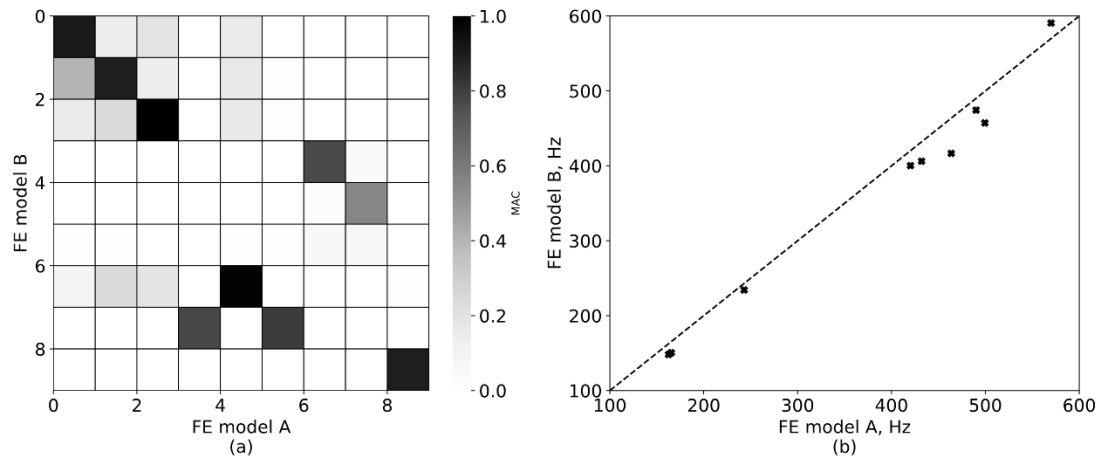


Figure 4-4 The comparison of modal properties between the FE model A and the FE model B for the lowest 8 global modes (mode order 1 - 8) and the lowest local mode (mode order 9) of test structure. (a) MAC plot; (b) Scatter plot.

The results in Table 4-4 and Figure 4-4 (a) show that both FE models have similar mode shape for global modes 1 – 3. This is because these low frequency modes possess long structural wavelengths. The stiffener details have little effect on changing these modes. Figure 4-4 (b) shows that the natural frequencies of the global modes 1 – 3 are lower in FE model B than FE model A. This is because the stiffeners modelled by shell elements allow for the cross-section deformation or warping, which makes them less stiff than the stiffeners modelled by beam elements.

Both the mode shapes and the natural frequencies of the two models are different for global modes 4 – 8. This is because of the different stiffener models used and their contacts with the cylinders affects these relatively high frequency global modes when the structural wavelength is shorter.

Table 4-4 shows that the two FE models again have similar circumferential mode shapes for the first local mode (mode number 9), with one axial half-wavelength between consecutive stiffeners and 18 circumferential wavelengths. This is also confirmed by the high MAC value seen in Figure 4-4 (a). The different stiffener models have little effect on the local mode shape. Figure 4-4 (b) shows that the natural frequency of the local mode is lower in FE model A than

FE model B. This is because the length of each bay is slightly longer in FE model A than in FE model B because of the contact area, which effectively stiffens this local mode.

4.2 The impact test and results

A set of impact tests were performed to explore the behaviour of the test structure and to decide which FE model can better represent the test structure and the potential differences between them. The measurements include both the driving-point mobility at some locations and a number of transfer mobilities.

4.2.1 The set-up

Figure 4-5 shows the layout of the measurement system used in the impact test.

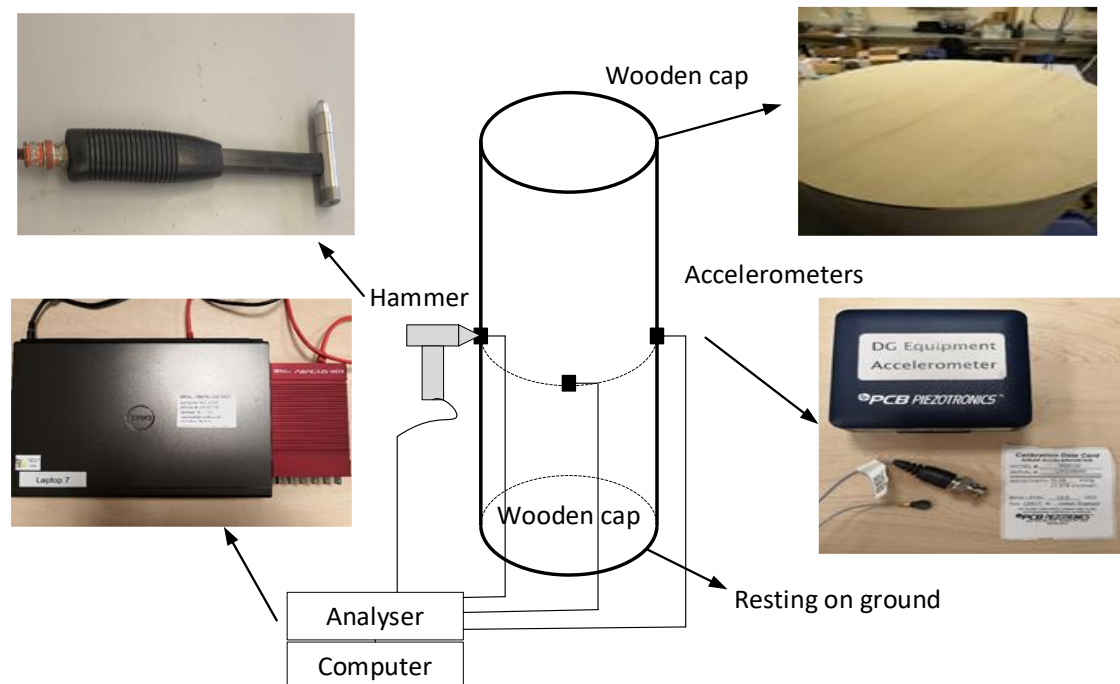


Figure 4-5 The layout of the measurement system used in the impact test.

Two wooden caps were fixed at the two ends of the cylinder. The purpose of using the caps is for the acoustic response test but they are used in the structural tests too for consistency; they can reduce the exterior sound field propagating into the interior of the cylinder. The top cap also adds a mass of about 10 kg which produces a small static compressive force in the axial direction. Resting the structure on the ground will introduce uncertainty in the boundary conditions of the test structures, which is expected to primarily affect the measured response at lower frequencies.

The impact excitation was provided by an instrumented hammer with a sensitivity of 2.25 mV/N. The tip and the head of the hammer were selected to provide an effective excitation to the cylinder over a frequency range up to 4 kHz. As the skin of the test structure is very thin, large loading should be avoided in case the structure is forced outside the linear range. In addition, the orientation of each impact should be well controlled so that it is normal to the cylindrical surface.

An accelerometer with a sensitivity of 1.078 mV/(m/s²) was attached to the cylinder surface to measure the radial acceleration. To measure the driving point mobility it would be appropriate to place the accelerometer on the interior skin surface at the point of impact, so that the orientation of the measured response point coincides that of the excitation in the mobility measurement. However, this was impractical due to the length of the structure. Therefore, the accelerometer was attached on the outer surface of the test structure and impacts were given next to it.

The acquisition system comprised an analyser ABACUS 901 and a laptop with processing software DP900. The transfer and coherence functions were produced by this acquisition system. The frequency range is up to 4 kHz with a frequency resolution of 0.625 Hz. The number of repeated impacts for each position was 6 to reduce the noise.

4.2.2 Test procedures

Five sets of impact tests were undertaken. The first set of impact tests was to measure the driving-point mobilities at the centre of different bays. The second and subsequent sets of impact tests were performed to measure the transfer mobilities on different parts of the cylinder. The driving-point mobility results, compared with the FE model results, were used to demonstrate the difference between the FE models and the measurements, as well as to examine the variability of the mobility for the different bays.

Figure 4-6 shows the measurement points of the first set of impact tests for the driving point mobilities. These positions were chosen to measure the acceleration of the surface in the radial direction as well as to be the hammer impact points. They were along an axial line of points on the cylinder surface and on the central points of the bays from Bay 7 to Bay 11. The other bays are not shown here. These 5 measurement points are indicated as red points with No.1 – 5.

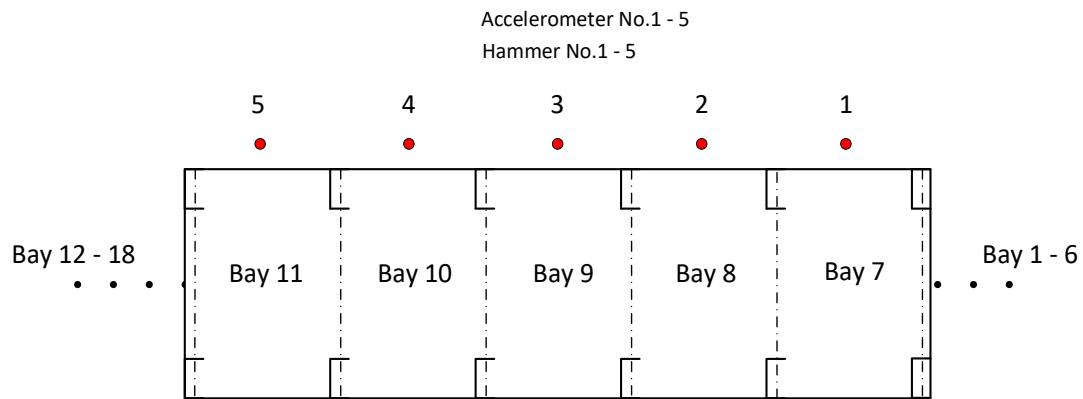


Figure 4-6 The measurement points of the first set of impact tests for the driving point mobility along the axial direction from Bay 7 to Bay 11. 5 measurement positions are on the centres of each bay and are indicated with the red points in the figure, No.1 – 5.

Figure 4-7 shows the measurement points of the second set of impact tests for the transfer mobility. The hammer impact points were along an axial line on the cylinder's surface, resulting in 71 equally spaced positions along the straight line across the six central bays of the cylinder, from Bay 7 to Bay 11. One accelerometer was placed at the midpoint of the cylinder to measure the acceleration in the surface radial direction. It is indicated as a red point in Figure 4-7, i.e. No. 36.

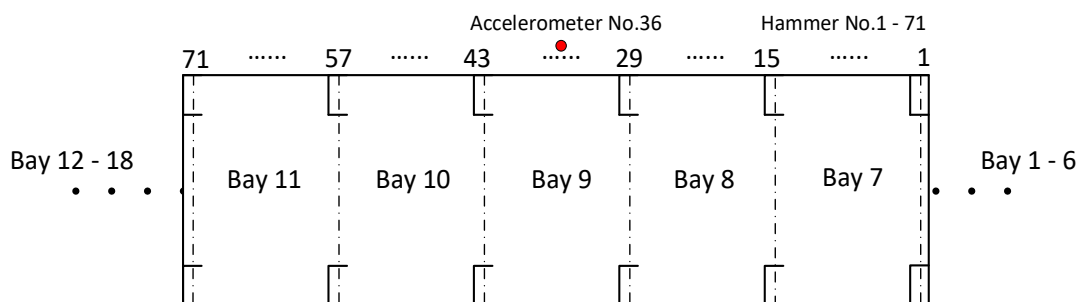


Figure 4-7 The measurement points of the second set of impact tests for the transfer mobility along an axial line on the cylinder's surface. The red point No.36 is for the accelerometer position and the 71 positions equally spaced along the six central bays (Bay 7 – 11) are for the impact points.

Figure 4-8 shows the measurement points of the third set of impact tests for the transfer mobilities. The hammer impact points were around the circumferential line in the central bay of the cylinder (Bay 9). 19 points were equally spaced around a half of the circumference with a separation angle of 10° between points. The 17 hammer impact points, No.1 – 17, are illustrated in Figure 4-8. The accelerometer position No.1 as indicated as a red point in Figure 4-8 is to measure the acceleration in the surface radial direction.

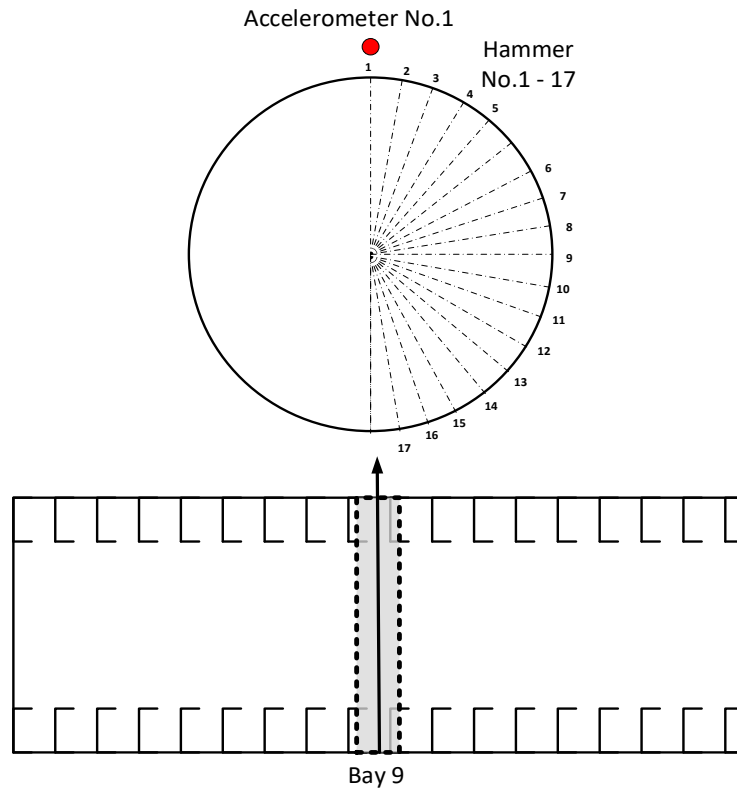


Figure 4-8 The measurement positions of the third set of impact tests for the transfer mobility around the circumference of the cylinder in the central bay (Bay 9). The red point No.1 is for the accelerometer position and the 17 impact points are marked around a half of the circumference.

Figure 4-9 shows the measurement points for the fourth set of impact tests for the transfer mobilities. The hammer impact points were around the circumferential line in the centre of Bay 9. These points were equally spaced with a separation angle of 1.5° . This separation angle is smaller than that of the third impact test, aiming to achieve a better spatial resolution particularly for the identification of the first local modes. The accelerometer position No.1 as indicated as a red point in Figure 4-9 measured the acceleration on the surface in the radial direction.

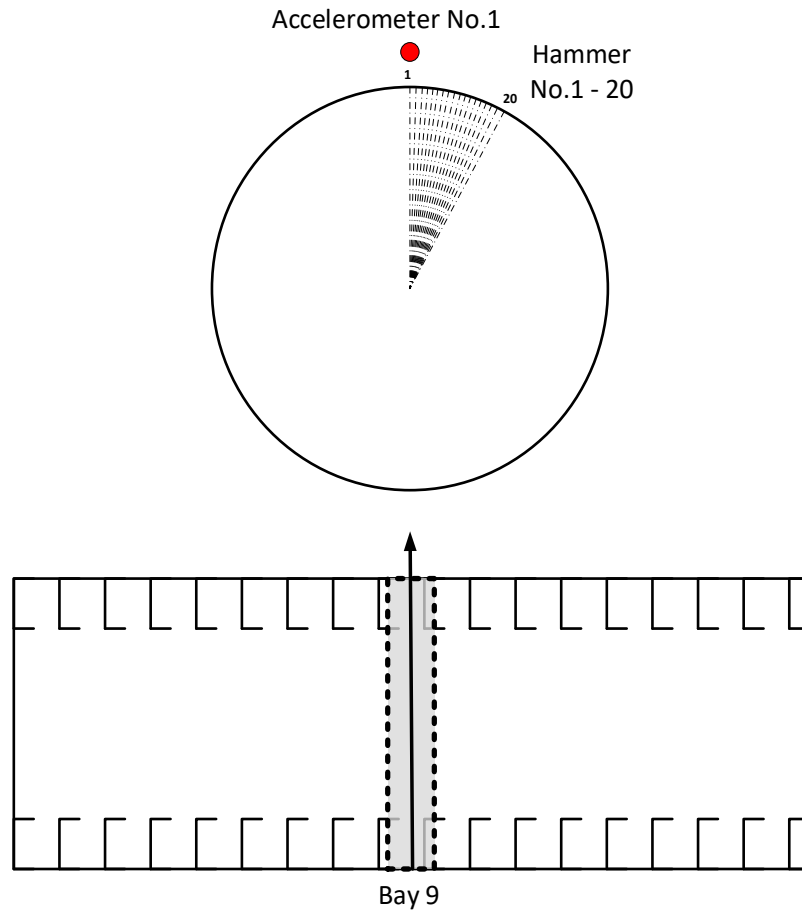


Figure 4-9 The measurement points of the fourth set of impact tests for the transfer mobility around the circumference of the cylinder in Bay 9. The red point is the accelerometer position. The 20 hammer impact points are equally spaced with a separation angle of 1.5° .

Figure 4-10 shows the measurement points for the fifth set of impact tests for the transfer mobility. The locations of the impacts and the accelerometer positions are the same as for the fourth set of impact tests as shown in Figure 4-10, but the measurements were performed on a different bay, Bay 7.

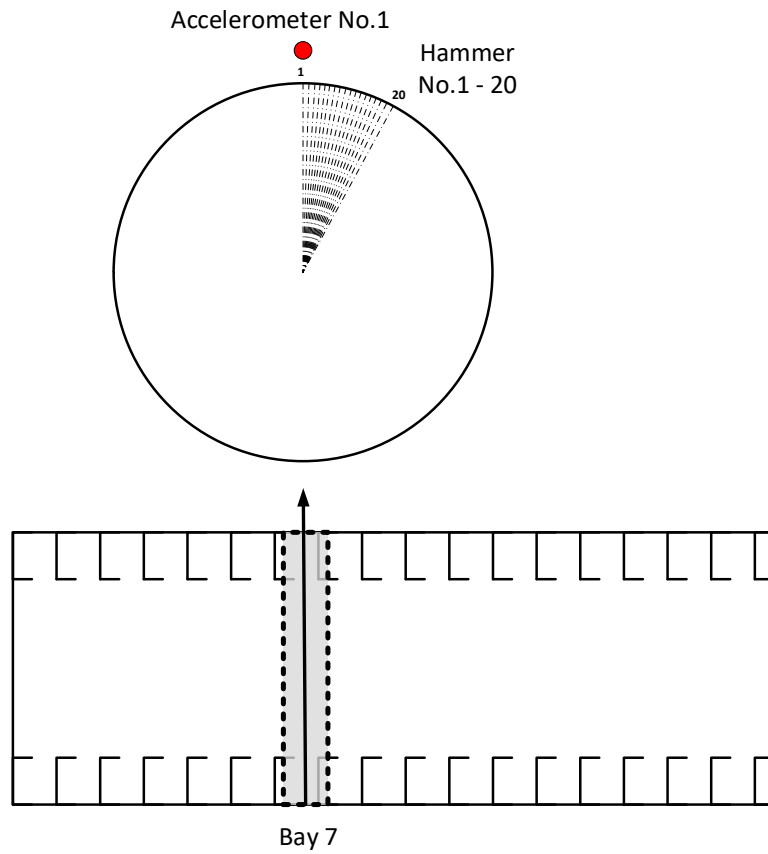


Figure 4-10 The measurement points of the fifth set of impact tests for the transfer mobility around the circumference of the cylinder in Bay 7. The red point is the accelerometer position. The 20 hammer impact points are equally spaced with a separation angle of 1.5° .

Table 4-5 summarises the five sets of impact measurements.

Table 4-5 A summary of the five sets of impact measurements

Test	Measurements points	Target
Set 1	<ul style="list-style-type: none"> No. 1-5 5 points at the middle of -bays from Bay 7 to Bay 11 	<ul style="list-style-type: none"> Driving mobilities
Set 2	<ul style="list-style-type: none"> No. 1 - 71 71 points along an axial line from Bay 7 to Bay 11 	<ul style="list-style-type: none"> 1 driving point mobility 70 transfer mobilities Both global and local modes
Set 3	<ul style="list-style-type: none"> No. 1 – 17 17 points around the circumference of Bay 9 	<ul style="list-style-type: none"> 1 driving point mobility 16 transfer mobilities Global modes
Set 4	<ul style="list-style-type: none"> No. 1 – 20 20 points around the circumference of Bay 9 	<ul style="list-style-type: none"> 1 driving point mobility 19 transfer mobilities Local modes
Set 5	<ul style="list-style-type: none"> No. 1 – 20 20 points around the circumference of Bay 7 	<ul style="list-style-type: none"> 1 driving point mobility 19 transfer mobilities Local modes

4.2.3 Comparison between measurements and FE results

4.2.3.1 Driving – point mobility

Figure 4-11 shows the results of the first set of impact tests. Figure 4-11(a) shows the driving-point mobility and Figure 4-11(b) shows the coherence of the corresponding measurements. The five measurement positions, labelled No.1 to No. 5 in Figure 4-6, are represented in solid lines with five different colors, with yellow for No.1, blue for No.2, black for No.3, green for No.4 and red for No.5.

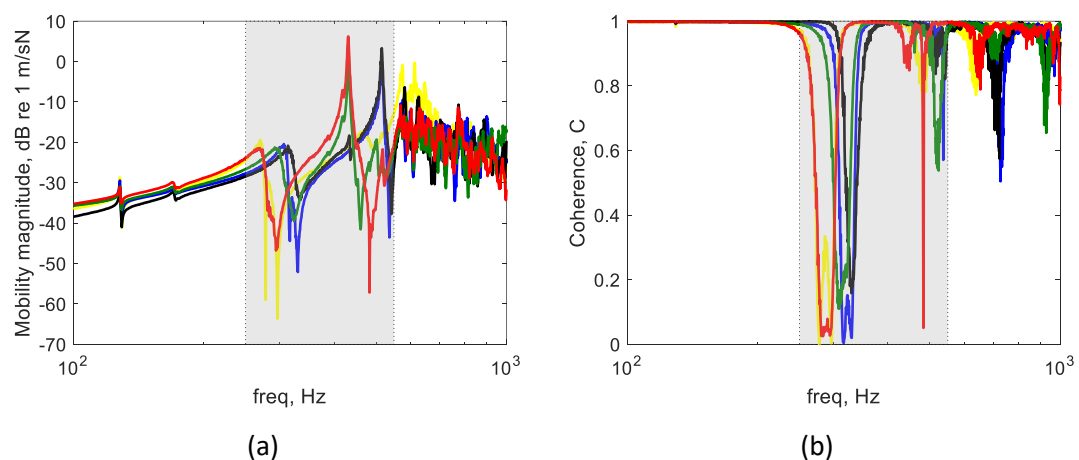


Figure 4-11 The results of the first set of impact tests showing driving-point mobilities (a) and the coherence (b) for the five measurement positions: yellow for position No.1, blue for No.2, black for No.3, green for No.4 and red for No.5.

If all the bays of the structure were constructed in the exact same way, one would expect that their driving point mobilities would be very similar. On the contrary, Figure 4-11 (a) shows that the driving-point mobilities of the five positions have substantial differences in the frequency range 250Hz – 550Hz, which is marked by a grey band.

In fact, a different outcome is found if the driving point mobilities at the same positions are calculated adopting an FE approach. This can be seen in Figure 4-12(a) for FE model A and in Figure 4-12 (b) for FE model B. This is because the bays are fully periodic in the FE models and the connection between stiffeners and skin is perfect. This does not seem to be the case in the test structure available.

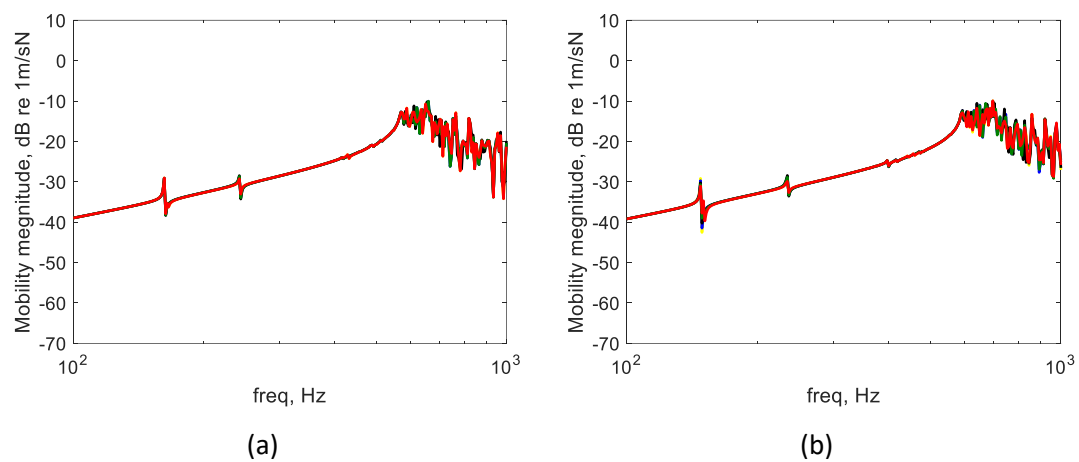


Figure 4-12 The driving-point mobility of the same five positions on the FE model A (a) and the FE model (b) with solid lines with yellow for No.1, blue for No.2, black for No.3, green for No.4 and red for No.5.

The measurements on the test structure show a significant variability, causing the disagreement of the measured driving-point mobilities of the five positions in Figure 4-11(a) in the grey highlighted frequency ranges. The joints between the ring-stiffeners and the cylindrical shell are likely to be the main factor of the variability. On the one hand, the joints comprising adhesive material and rivets are not well represented in the FE models. On the other hand, the joint details may vary in each ring-stiffener due to the manufacturing process. It was outside the scope of the study to model the joint details more accurately or investigate their variability on this test structure. However, what appears clearly from both measurements and modelling is that the response of the structure can be divided into two separate regions. Below about 550-600 Hz the response is stiffness-like, while at higher frequency many modes contribute to the response.

A simple evaluation of the effects of the joint connection and an explanation for the two frequency regions, can be obtained with a simple FE model. A cylinder having the dimension

of a single bay, excluding the stiffeners, was set up with shear diaphragm or a spring foundation at its boundaries. The mode shapes of such a cylinder can represent the mode shapes of the local modes of the whole test structure for each bay.

Figure 4-13 (a) shows the single bay FE model in COMSOL. The single bay was supported with either the shear diaphragm boundary condition (SD boundary condition) or a spring foundation. The latter was given the same distributed spring constant in the radial and circumferential direction, which was set to $7 \times 10^9 \text{ N/m}$. No axial constraint was given to this model. The damping in the FE models is modelled using a structural loss factor equal to 0.004. This value is estimated from the peak of the measured point mobility at 128 Hz.

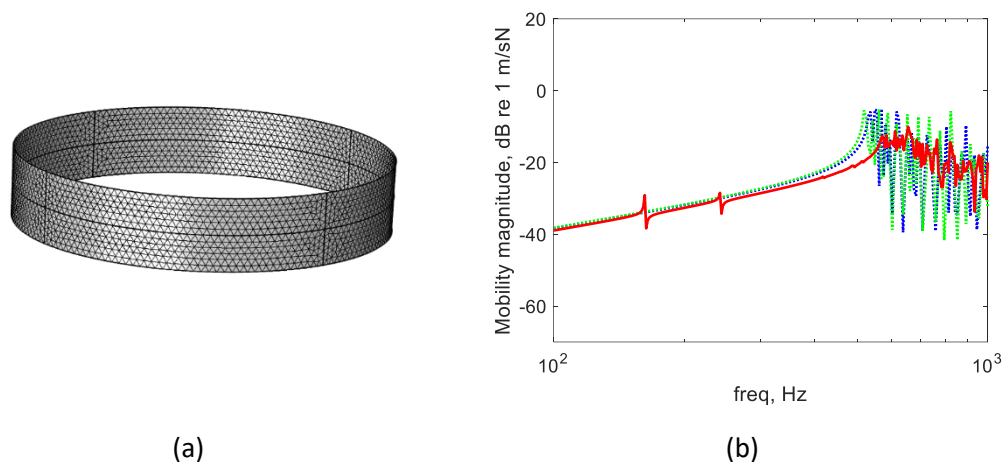


Figure 4-13 A single bay of the FE model A (a) and the comparison of the driving-point mobilities (b). The red solid line is the FE model A point mobility in No. 1. The blue dotted line is the point mobility of the single bay with SD boundary condition. The green dotted line is the point mobility of the single bay with spring foundation boundary condition.

The FE single bay model has the fundamental natural frequency 535 Hz and 522 Hz with the SD and spring foundation boundary conditions respectively. The natural frequency of the first local mode of FE model A is 570 Hz. The mode shape of the first mode of the single bay with the SD boundary condition is similar to the first local mode of the FE model A and B on one bay, i.e. 18 circumferential wavelengths, which means that the SD support is close to the modelling of the joint connection in FE model A. This might be a consequence of the much higher bending stiffness of the ring stiffener compared to the cylinder skin. Comparing FE model A and the single bay with SD boundary condition, the natural frequency is reduced from 570 Hz to 535 Hz. This might be due to the absence of the axial constraint which is present in the full model via the connection with adjacent bays. This constraint takes into account the membrane effect of the cylinder skin involved in the in-plane stretching in the coupled axial bending components. The first natural frequency of the single bay with the spring foundation is further reduced as the spring provides a finite value for the stiffness in the radial and

circumferential directions. Its fundamental mode has the same value for the circumferential wavelength compared to the other modelling approaches. What appears evident from the results in Figure 4-13(b) is that the point response of the structure has contributions by many modes above the fundamental mode, while it is dominated by stiffness below the fundamental mode. As the modes of this simpler model can represent the local modes of the full structure, one can conclude that the full structure is dominated by local modes above the frequency where the first local mode appears. This is fixed in the FE models for all the bays, but it is variable for the real structure. In the full structure the presence of global modes also contributes to the response below the first local mode.

The two wooden caps have two effects on the test structure. They add a mass of 10kg and enclose the air domain inside the cylinder. The mass effect can be modelled by a static, prestress in the FE model. The interior air domain can also be modelled as finite elements. These effects are examined using the FE model B. Figure 4-14 shows a comparison of the point mobility from FE model B with different conditions considering the effects of the prestress and the interior air domain. The result shows that the effects of the prestress and the interior air domain are negligible above 300Hz where the FE predictions are almost overlapping.

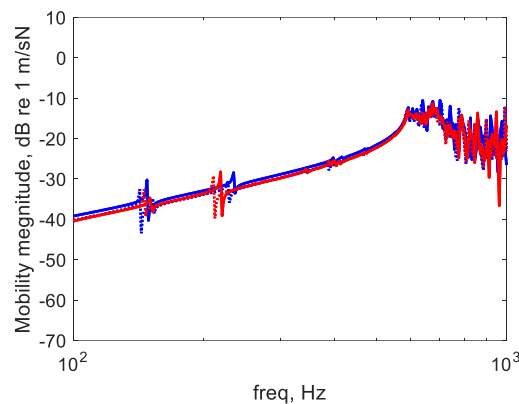


Figure 4-14 Comparison of the point mobility from FE model B with different conditions. Free boundary condition without interior air domain (blue solid line). Free boundary condition with interior air domain (blue dotted line). Prestress without interior air domain (red solid line). Prestress with interior air domain (red dotted line).

To better understand the behaviour of the test structure some modal analysis was performed to characterise the mode shapes present around a few dominant resonance peaks. Because it has been observed in the measured mobility that different bays can have different behaviour, the modal analysis is done for two of these bays (Bay 9 in the fourth set of impact tests and Bay 7 in the fifth set of impact tests). The measured and the FE driving point mobilities of the two bays selected are shown in Figure 4-15(a) for Bay 9 and Figure 4-15(b) for Bay 7. The resonance peaks analysed are marked in the figures.

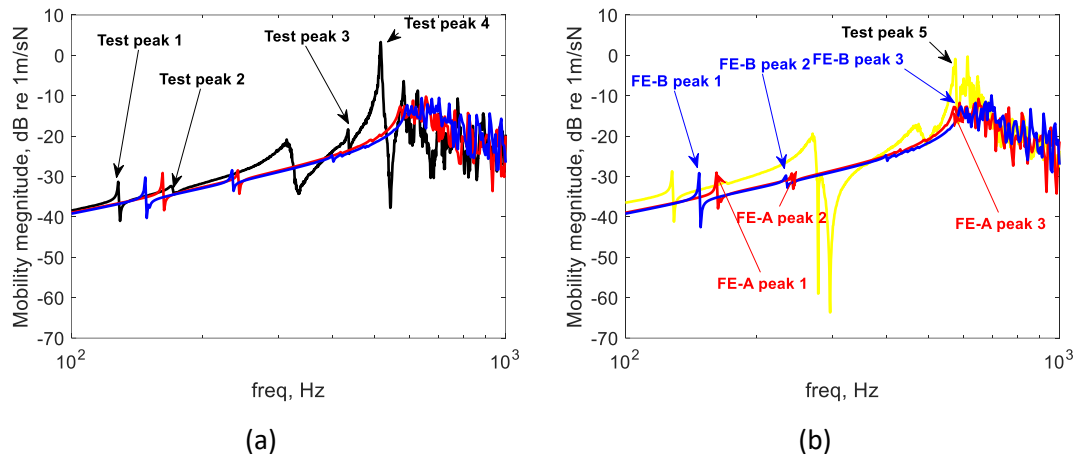


Figure 4-15 The measured and FE driving point mobilities of two bays. (a) Bay 9: black solid for measurement, red solid for FE model A, blue solid for FE model B. (b) Bay 7: yellow solid for measurement, red solid for FE model A, blue solid for FE model B.

For Bay 9 in Figure 4-15(a), below the Test peak 4 at 516 Hz, the result shows a stiffness-like behaviour with a few peaks possibly due to the global modes. Above this peak many modes contribute to the response. For Bay 7 in Figure 4-15(b), a similar behaviour is found, but the two regions are divided by an experimental peak 6 at 570 Hz. The mode shapes corresponding to these peaks will be shown next together with the mode shapes of a few other peaks indicated in the figures.

For the FE models, the first and the second peaks correspond to the first and the third global mode. The second global mode in the FE models is not present in the driving-point mobilities as the measured positions are on the nodal line of this mode. The third peak labelled in Figure 4-15 (b) corresponds to the first local mode. In the next section, the attempt is made to associate the peaks in the measurement to those in the FE models through modal analysis. These peaks and their corresponding frequencies and bay positions are listed in Table 4-6 for the measurement and Table 4-7 for the FE models.

Table 4-6 The peaks to be analysed and their corresponding frequencies and bay positions in the measurement.

Measurement		
Peak	Freq (Hz)	Bay No.
1	128	9
2	170	9
3	434	9
4	516	9
5	570	7

Table 4-7 The peaks to be analysed and their corresponding frequencies and bay positions in FE models.

FE model A			FE model B		
Peak	Freq (Hz)	Bay No.	Peak	Freq (Hz)	Bay No.
1	162	9 and 7	1	148	9 and 7
2	242	9 and 7	2	234	9 and 7
3	571	9 and 7	3	593	9 and 7

4.2.3.2 Measured mode shapes

The measured mode shapes from the measurement points, either along the axial or circumferential directions, were obtained by modal analysis. The modal analysis used in this study was based on a Least Square Complex Exponential method and curve fitting. A single mode is identified in each modal analysis.

A MAC comparison between the measured mode shapes and the FE mode shapes is not convenient due to the limited number of measurement points and also due to the bay-to-bay variability found in measurements. However, the measured mode shapes along the axial and the circumferential measurement points might be associated with some of the FE mode shapes in Table 4-4 by observation of some general features.

Figure 4-16 shows the measured mode shapes of the first test peak labelled in Figure 4-15 and listed in Table 4-6. Figure 4-16 (a) shows the mode shape from the measurements along the longitudinal axis extracted from the second set of impact tests. Figure 4-16 (b) shows the mode shape of the measurements extracted from the third set of impact tests in the circumferential direction. The maximum deflection in each plot was scaled to be 1. The scale factors of 2.47 and 3.84 are used for the axial and circumferential plots respectively.

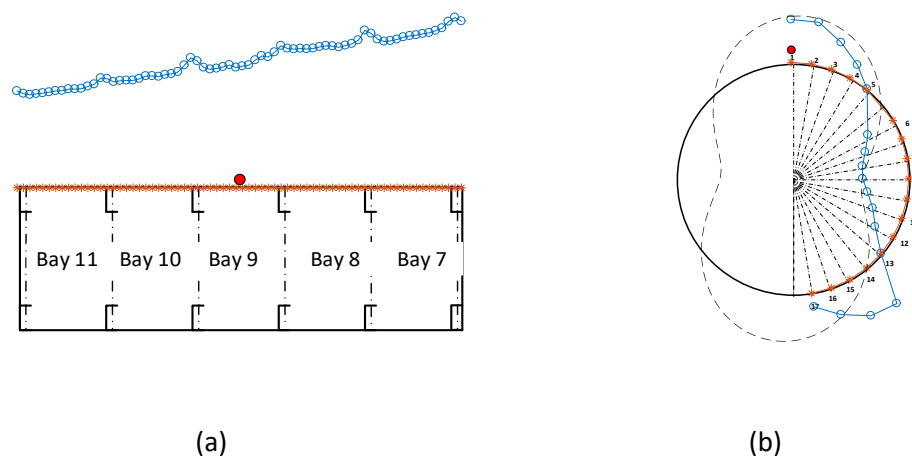


Figure 4-16 The measured mode shapes of the first test peak at frequency of 128 Hz. The red asterisk points are the undeformed shape and the blue circle points are the deformed shape. (a) Mode shape from the

measurements along the axial direction, extracted from the second set of impact tests. (b) Mode shape from the measurements around the circumferential direction, extracted from the third set of impact tests. The black dashed line is a plot of a sinusoidal function with 2 circumferential wavelengths. The position of the fixed accelerometer is highlighted as the red solid dot.

In the axial direction the mode shape is similar to that of the first global mode in both FE models A and B. It is close to a straight line along the axial direction with two nodal diameters present when observing the mode shape in the circumferential direction. Hence, the first test peak can be associated with the first FE resonance peak in Table 4-6 and can be recognised as the first global mode of the test structure.

Figure 4-17 shows the measured mode shapes for the second test peak labelled in Figure 4-15 and listed in Table 4-6. Figure 4-17 (a) is for the axial direction extracted from the second set of impact tests. Figure 4-17 (b) is for the circumferential direction extracted from the third set of impact tests. The maximum deflection in each plot was scaled to be 1. The scale factors of 2.52 and 4.51 are used for axial and circumferential plots respectively.

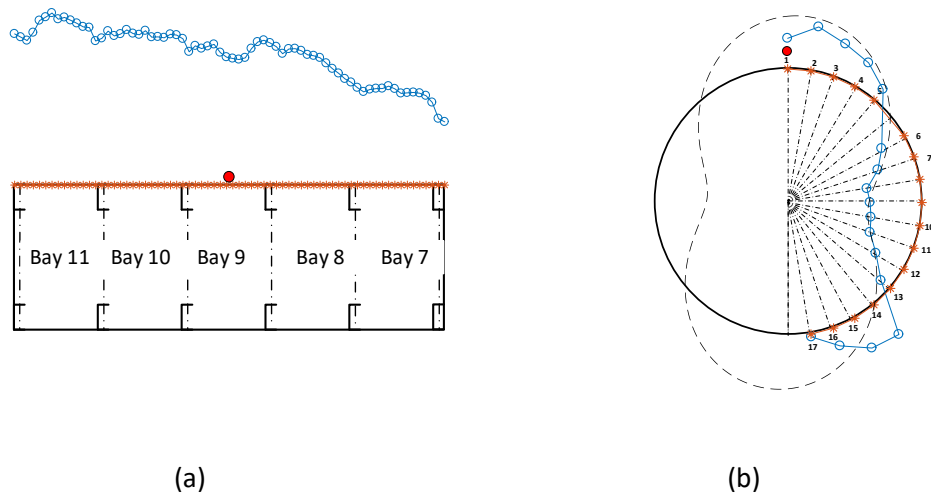


Figure 4-17 The measured mode shapes from the second test peak at frequency of 170 Hz. The red asterisk points are the undeformed shape and the blue circle points are the deformed shape. (a) Mode shape from the measurements along the axial direction, extracted from the second set of impact tests. (b) Mode shape from the measurements around the circumferential direction, extracted from the third set of impact tests. The black dashed line is a plot of a sinusoidal function with 2 circumferential wavelengths. The position of the fixed accelerometer is highlighted as the red solid dot.

Along the axial direction (Figure 4-17 (a)), the mode shape corresponding to the second test peak is close to a straight line but could also be associated with the shape of the third global mode in both FE models A and B. The mode observed from the circumferential measurement points (Figure 4-17 (b)) tends to have two complete circumferential wavelengths. It is also similar to the third global mode in both of the FE models. It is not easy to unequivocally associate this result to being one of the FE modes shown in Table 4-6. It could correspond to the third global mode but there is no certainty in this. The experimental mode shape might

see the effect of the variability in the stiffener connection and there is uncertainty in the actual boundary condition.

An attempt was made to identify the mode shape associated with the broad peak at around 300 Hz (see Figure 4-15 (a)). However, the coherence in this region is low and the results did not allow a correspondence between this peak and the FE results to be found.

Figure 4-18 shows the measured mode shapes of the third test peak labelled in Figure 4-15 and listed in Table 4-6. Figure 4-18 (a) is for the measurements in the axial direction extracted from the second set of impact tests. Figure 4-18 (b) is for the measurements points around the circumferential direction extracted from the third set of impact tests. The maximum deflection in each plot was scaled to be 1. The scale factors of 0.07 and 0.89 are used for axial and circumferential plots respectively.

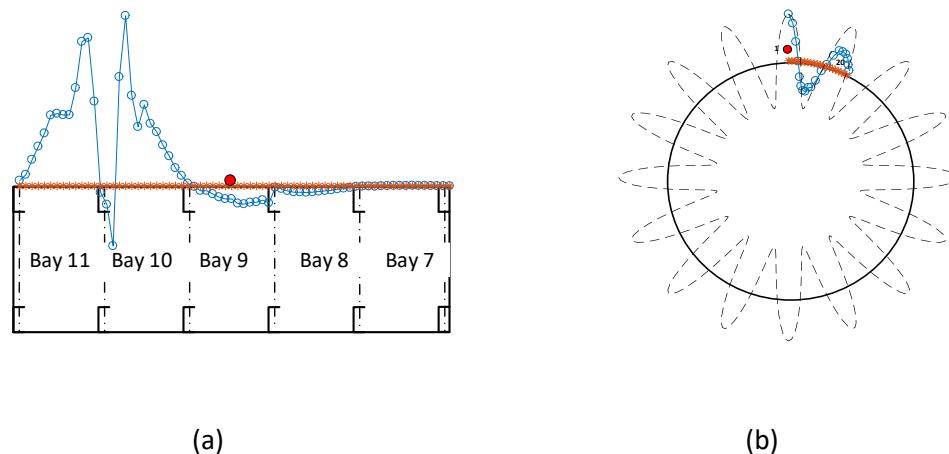


Figure 4-18 The measured mode shapes from the third test peak at frequency of 434 Hz. The red asterisk points are the undeformed shape and the blue circle points are the deformed shape. (a) Mode shape from the measurements along the axial direction, extracted from the second set of impact tests. (b) Mode shape from the measurements around the circumferential direction, extracted from the fourth set of impact tests. The black dashed line is a plot of a sinusoidal function with 16 circumferential wavelengths. The position of the fixed accelerometer is highlighted as the red solid dot.

The mode shape from the measurements along the axial direction shows a half wavelength across the Bays 9 - 11, while Bays 7 and 8 are close to being undeformed. This is consistent with the point mobility results in Figure 4-11, where the resonance peaks at 434 Hz are mostly present in Bay 9 – 11. In particular, Bays 10 and 11 have higher resonance peaks than Bay 9, which is also indicated in the measured mode shapes. The measurement along the circumferential direction of the third measured peak tends to have 16 complete circumferential wavelengths. Due to these features in the axial and circumferential directions, this mode can be recognised as the first measured local mode of the test structure.

Figure 4-19 shows the measured mode shapes of the fourth test peak labelled in Figure 4-15 and listed in Table 4-6. Figure 4-19 (a) is the axial direction extracted from the second set of impact tests. Figure 4-19 (b) is for the circumferential direction extracted from the fourth set of impact tests. The maximum deflection in each plot was scaled to be 1. The scale factors of 0.12 and 0.18 are used for axial and circumferential plots respectively.

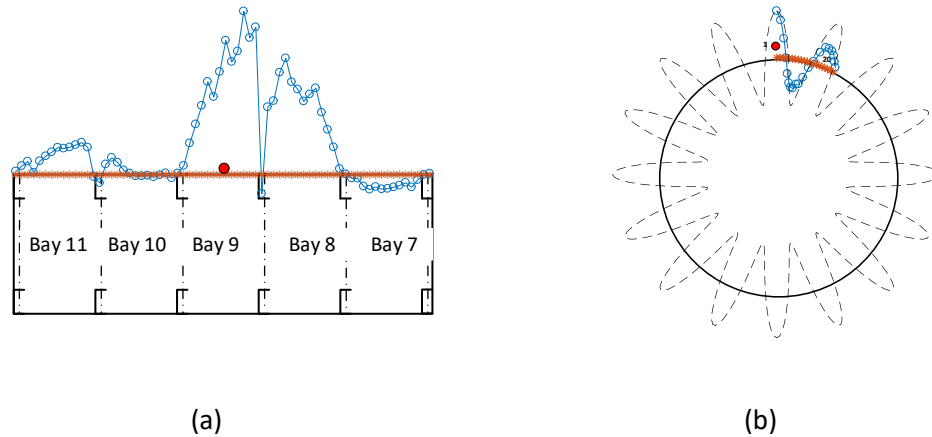


Figure 4-19 The measured mode shapes of the fourth test peak at frequency of 516 Hz. The red asterisk points are the undeformed shape and the blue circle points are the deformed shape. (a) Mode shape from the measurements along the axial direction, extracted from the second set of impact tests. (b) Mode shape from the measurements around the circumferential direction, extracted from the fourth set of impact tests. The black dashed line is a plot of a sinusoidal function with 17 circumferential wavelengths. The position of the fixed accelerometer is highlighted as the red solid dot.

The results along the axial direction tend to have a half wavelength across the Bay 8 and Bay 9. This is consistent with the point mobility results in Figure 4-11, where the resonance peaks at 516 Hz are mainly present in these two bays. The circumferential mode of the third measured peak tends to have 17 complete circumferential wavelengths. Due to these features of the axial and circumferential mode shapes, this mode can be recognised as the second measured local mode of the test structure.

Figure 4-20 shows the measured mode shapes of the fifth test peak labelled in Figure 4-15 and listed in Table 4-6. Figure 4-20 (a) is for the axial direction extracted from the second set of impact tests. Figure 4-20 (b) is for the circumferential direction extracted from the fifth set of impact tests. The maximum deflection in each plot was scaled to be 1. The scale factors of 0.24 and 0.18 are used for axial and circumferential plots respectively.

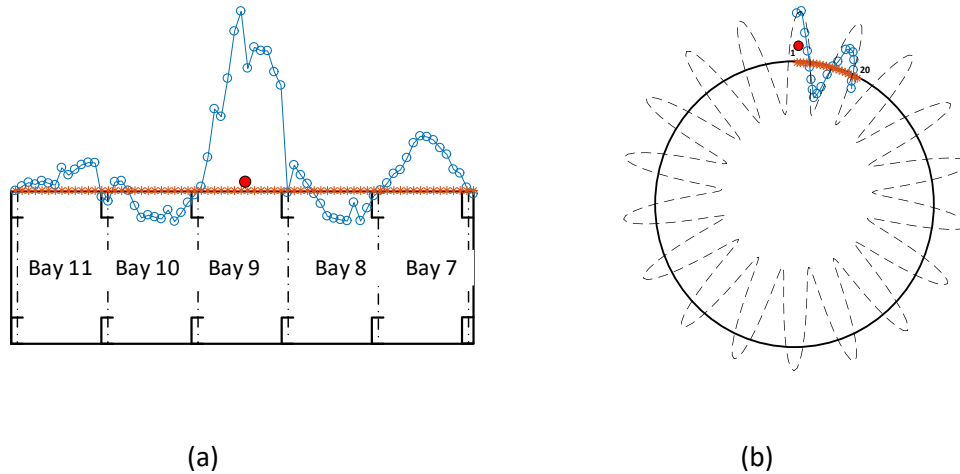


Figure 4-20 The measured mode shapes of the fifth test peak at frequency of 570 Hz. The red asterisk points are the undeformed shape and the blue circle points are the deformed shape. (a) Mode shape from the measurements along the axial direction, extracted from the second set of impact tests. (b) Mode shape from the measurements around the circumferential direction, extracted from the fifth set of impact tests. The black dashed line is a plot of a sinusoidal function with 18 circumferential wavelengths. The position of the fixed accelerometer is highlighted as the red solid dot.

In the axial direction the response is similar to the mode shape of the first local mode from the FE models. It tends to have a half wavelength across each bay with opposite phase between adjacent bays. The circumferential direction shows 18 circumferential wavelengths. This is also similar to the first local mode in both FE models. Hence, the fifth test peak can be associated with the third FE Peaks in Table 4-6 and can be recognised as the third measured local mode of the test structure.

The analysis also shows that both FE models A and B agree with the measurement for the first, second and fifth test peaks to a similar extent. However, FE model A has a smaller number of elements and less complexity compared to model B. Hence, FE model A is used in the comparison with the acoustic test results.

The modal analysis of this structure proved to be more complicated than what was originally envisaged, and the comparison between the modal tests and FE results is largely qualitative rather than quantitative. The main reasons for the problems found in the experimental investigations are:

- The large test structure with a thin skin and deep stiffeners is difficult to test.
- The periodicity of the structure results in many modes clustered in narrow frequency bands.
- The variability found in the measured results of the different bays was significant.
- Uncertainty exists in the actual boundary conditions present in the test structure when trying to ascertain the most appropriate FE representation.

The first two points listed are inherent characteristics of this structure and can be well represented by the FE models. There is no immediate approach to account for the other two limitations. These are therefore inevitably carried forward in the next modelling step.

4.3 The acoustic test and results

The acoustic response test was performed in an anechoic chamber, to obtain the surface pressure and the vibration response. The pressure results are compared to both the analytical and the numerical (boundary element) models. The vibration results are compared to a few different numerical models.

4.3.1 The set-up

Figure 4-21 shows the layout of the acoustic test.

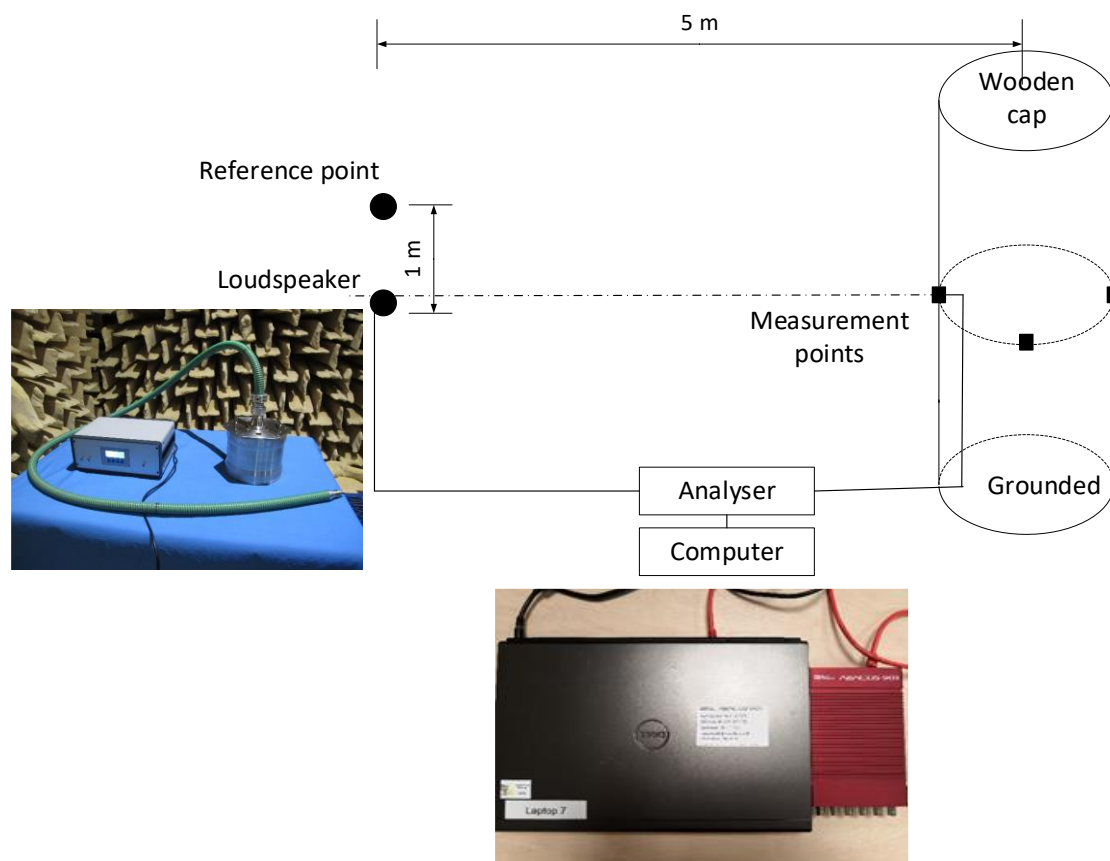


Figure 4-21 The acoustic test layout and the measurement system used.

The sound source consists of a horn driver unit connected to a flexible hose [156]. At the end of the hose a radiating orifice allows the white noise to be radiated in a nearly omni-directional manner. The 1/3 octave band sound pressure level at 1 m from the orifice is about 54 dB at 300 Hz and increases to above 81 dB for frequencies above 2 kHz. The flexible hose is 3 m long.

It is designed to allow the source to be placed in confined locations, but it also introduces peaks in the sound pressure due to the acoustic resonances of the column of air contained in it.

The sound source and the test structure cylinder were placed along the diagonal line of the anechoic chamber to achieve a maximum separation distance of 5 m. This is to ensure that the test structure is in the far field of the point sound source. The source was fixed on a stand at a height corresponding to the centre of the cylinder length.

Three measurement points were chosen in the median plane of the cylinder, shown as the black squares in Figure 4-21. They comprised the nearest point ($\theta = \pi$), the furthest point ($\theta = 0$) and a midpoint ($\theta = 3\pi/2$).

The pressure at these points was measured by a microphone with a sensitivity of 12.78 mV/Pa. The microphone was placed 50 mm away from the cylinder surface to minimize the influence of the microphone on the surface pressure. This distance (50 mm) should be taken into account in the prediction models when a comparison with the measurement data is made. The sound pressure at a reference point 1 m away from the sound source was also measured by a microphone with a sensitivity of 12.79 mV/Pa. This pressure was used to calculate the transfer functions for both the pressure and vibration.

The vibration response of three points on the fuselage were measured by both an accelerometer, with a sensitivity of 1.078 mV/(m/s²), and a laser vibrometer, with a sensitivity of 200 mV/(m/s).

The acquisition system was the same adopted in the impact test. Figure 4-22 shows the setup of the acoustic test in the anechoic chamber.

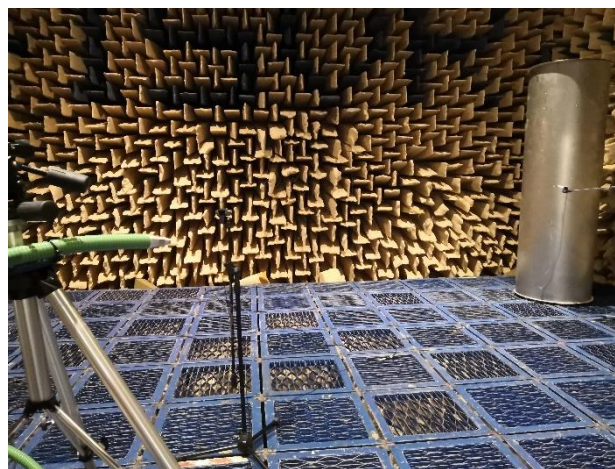


Figure 4-22 The acoustic test set up in the anechoic chamber.

4.3.2 Preliminary test on the source directivity

The first preliminary test was to examine the directivity of the sound source. The Sound Pressure Levels (SPLs) at 15 different specified positions were measured. Figure 4-23 shows the positions selected. These points were placed along five radial directions from the centre of the loudspeaker with separation angle of $\frac{\pi}{6}$ radians. In each radial direction, three reference points were placed with a spacing of 1 m.

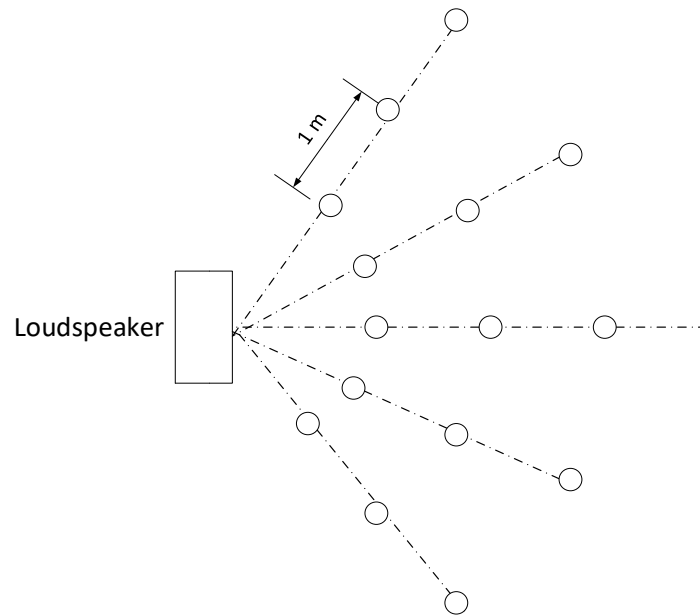


Figure 4-23 The positions of the reference points.

Figure 4-24 (a) shows the SPL at these points measured in narrow-band spectra with a frequency resolution of 0.625 Hz. Figure 4-24 (b) shows the calculated SPL in one-third octave bands. They are plotted against the centre frequencies of each band. In both figures, the results for the points 1 m, 2 m and 3 m away from the source are shown in the black, red and blue lines respectively. The results for different angles at the same distance to the source are plotted in the same colour but with different line types. The background noise is below 12 dB over the frequency range, as shown in green line in Figure 4-24 (b).

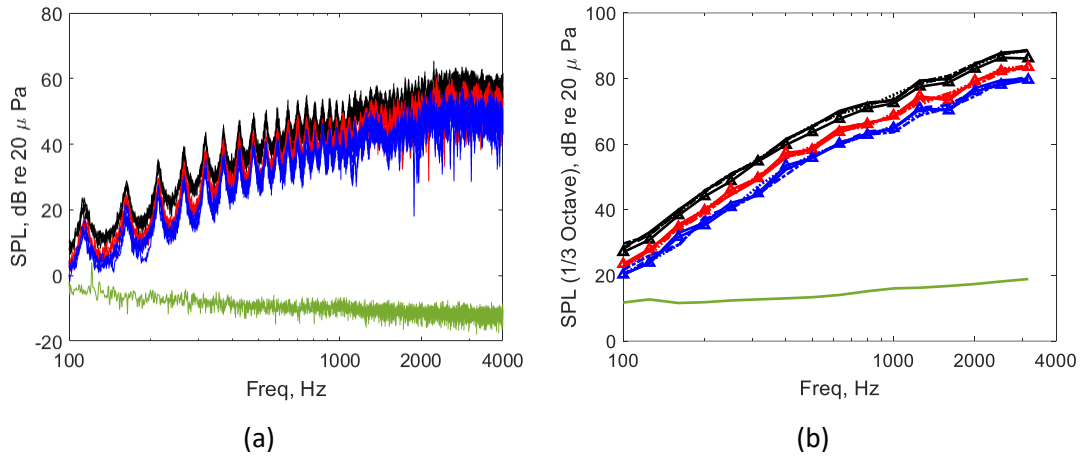


Figure 4-24 The SPLs at the different specified points. (a) Narrow-band measurement with the frequency resolution of 0.625 Hz. (b) One-third octave band spectra. Black lines: measurement points 1 m from the loudspeaker. Red lines: measurement points 2 m from the loudspeaker. Blue lines: measurement points 3 m from the loudspeaker. The results for positions at different angles are represented by different line types. Green dashed line: background noise level at measurement point 1 m from the loudspeaker.

The comparison of the results between the three different colours in both figures show that the SPL decreases as a function of the distance between the source and the measurement points. The SPL for different angles at the same distance are similar to each other with maximum difference within ± 2 dB, which means the source is not very sensitive to the horizontal angle range from $-\pi/3$ to $\pi/3$ radians and therefore is approximately omnidirectional.

Figure 4-24 (a) shows that there are fluctuations in the SPLs for different frequencies. These fluctuations are due to the resonance peaks caused by the acoustic modes in the source hose that is attached to the loudspeaker. These resonance peaks are averaged out in the one-third octave band results shown in Figure 4-24 (b) and relatively straight lines are obtained for each measurement. To remove the influence of source pressure fluctuations, it was decided to use the transfer function instead of the power spectral density in the measurement of the surface pressure and vibration.

Figure 4-25 is an estimation of the source strength calculated in terms of the volume velocity of an equivalent monopole. The result was averaged for points over different angles with the same distance to the source. The root mean square average was first adopted for the pressure measurement taken at different angles for the same distance from the sound source. Then the source strength for three different distances were calculated based on the formula for the far field of a monopole source [145].

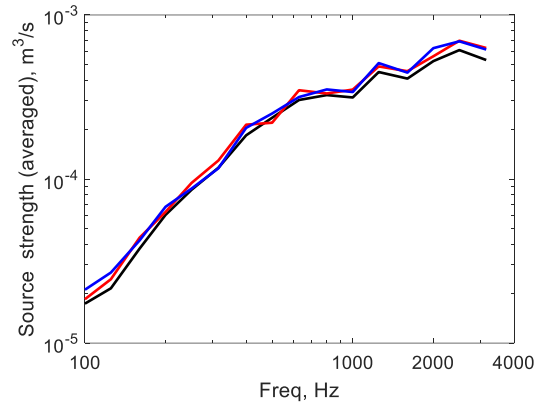


Figure 4-25 The estimated source strength in 1/3 octave bands averaged for points over different angles at the same distance from the source. Black lines: measurement points 1 m from the loudspeaker. Red line: measurement points 2 m from the loudspeaker. Blue line: measurement points 3 m from the loudspeaker.

The result shows that the three estimated source strength lines are very close to each other, which means the sound source can be approximated as a monopole for the angles in the range of $\pm \frac{\pi}{3}$ radians over the frequency range from 100 Hz to 1000 Hz.

4.3.3 Acoustic modelling

Three modelling approaches were used to predict the surface pressure of the test structure in the acoustic test.

The first model is the analytical model of spherical waves. This model has been described in the previous chapter and implemented in MATLAB. This model is used for comparison with the pressure measurement.

The second model is a numerical boundary element (BE) model of spherical waves built in COMSOL software. The pressure predicted by this model can be used as a term of comparison for the analytical approach of spherical waves. The reason for the comparison is that the first analytical model is for an infinite cylinder, i.e., the ends of the cylinder are not considered. The comparison with the numerical BE model for a finite cylinder can investigate the end effects. The BE model can also be coupled with the structural FE model for a full FE-BE simulation in the vibration comparison. The coupled FE-BE model was initially developed in this study, but effective results were not produced because of the prohibitive computational costs of the fully coupled simulation. As the vibroacoustic coupling has already been investigated in Chapter 2, only an uncoupled FE solution is sought in this chapter.

The third model is an analytical model using a plane wave to approximate the spherical wave model. The surface pressure predicted from this model is then applied to the structural FE

model for an uncoupled FE simulation in the vibration comparison. It should be noted that similar to the first model, the estimated pressure from the third model is also for an infinite cylinder. It was then applied to the structural FE model in the form of a blocked pressure, forming an approximate, uncoupled FE solution which is used to predict the vibration response.

The BE model comprises a rigid cylindrical shell with the same exterior dimension as the test structure and two rigid ends representing the wooden caps. The free triangular elements are used to mesh the model. The frequency range is 100 Hz to 1000 Hz with a frequency resolution of 2 Hz. To reduce the computational cost, the frequency range was divided into 9 sub frequency ranges of 100 Hz. The mesh size is 1/5 of the acoustic wavelength for the highest frequency for each sub frequency range.

Figure 4-26 (a) shows the meshed BE model and Figure 4-26 (b) shows the estimated surface pressure distribution at the frequency at 1000 Hz.



Figure 4-26 The meshed BE model (a) and the surface pressure distribution (b) at the frequency of 1000 Hz.

Figure 4-27 shows a comparison of the predicted pressure between the analytical model of spherical waves and the BE model. The results are plotted in terms of the pressure ratios between the three observation points on the cylinder surface and that at the reference point close to the source.

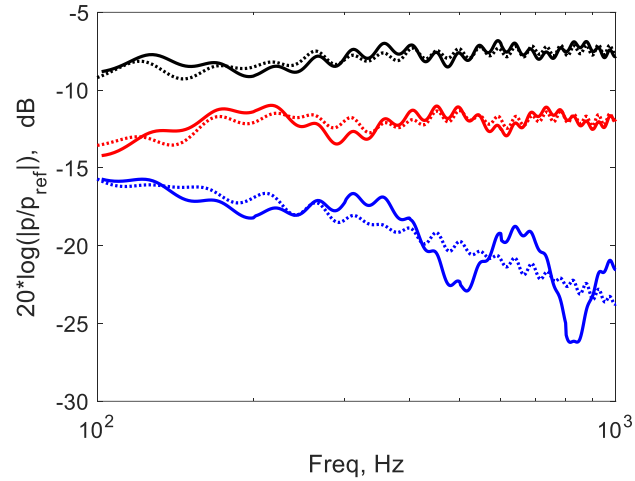


Figure 4-27 The comparison of the predicted pressure between the first (the analytical model of spherical wave, in dotted lines) and the second model (BE, in solid lines). The pressure ratios between the three observation points on the cylinder surface and that at the reference point are plotted: the front point (black), the midpoint (red) and the rear point (blue).

The results from the two models show good agreement at measurement points close to the front point and at the midpoint of the cylinder. The agreement between predictions and the measurements at the rear point deteriorates, especially in the high frequency range. The disagreement is due to the end effects that are not taken into account in the first analytical model. This can be verified indirectly by the following parameter study in terms of the cylinder length in the BE model.

In the parameter study, the cylinder length values are 0.1, 0.5, 1, 2 and 5 times the original cylinder length. As the cylinder length increases, the cylinder ends should have a smaller effect on the pressure at the median plane of the cylinder. A normally incident plane wave rather than a monopole was set as the background pressure field. This is to avoid the possible influence of the approximations in the analytical model of the spherical wave. The end effect should be independent of the type of acoustic source. An analytical model of plane wave for an infinite cylinder was used for comparison.

Figure 4-28 shows a comparison between the third (analytical) model (for infinite cylinder) and the second models (BE) for a finite cylinder with different length. The results are plotted as the ratio between the predicted pressures at the three surface points and that at the reference point near the source. To make comparison with the reference results [157], the results are plotted against kR , where k is the wavenumber of the incident wave and R is the radius of the cylinder.

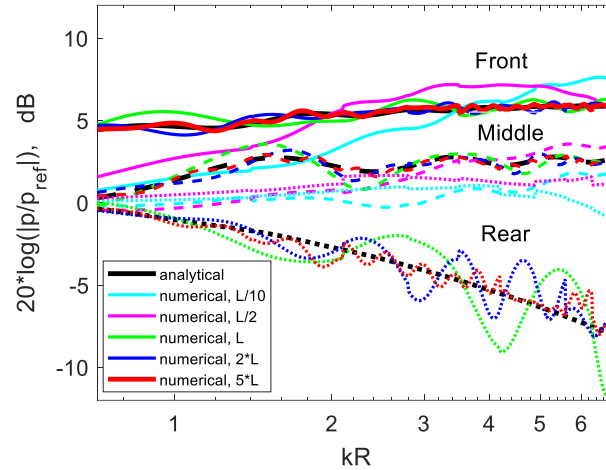


Figure 4-28 The effect of the cylinder length on the predicted pressure of the points at the median plane wave the cylinder. Solid lines: the front point. Dashed lines: the midpoint. Dotted lines: the rear point. The analytical results for each point are in black. The BE results for different cylinder lengths are in different colours as indicated in the figure legend.

The result shows that the simulation result becomes closer to the analytical result as the cylinder length increases. For the original cylinder length L , the predicted pressures at the rear point fluctuates more than those for the front and the midpoint.

The analytical results in black lines all match the reference results in [157].

Finally, a comparison between the first model (analytical model of spherical wave) and the third model (analytical model of equivalent plane wave) is made. In the third model, the decay of the spherical pressure, spreading from the point source to the surface point, has already been taken into account in the pressure ratio of the plane wave. The result is shown in Figure 4-29.

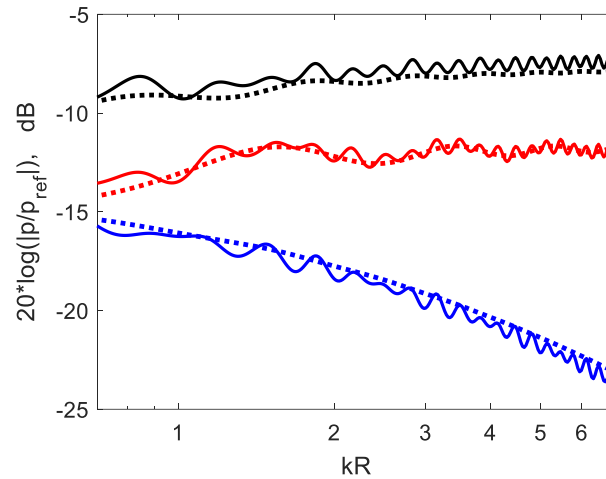


Figure 4-29 The comparison of the predicted pressure between the first (the analytical model of spherical wave, in solid lines) and the third (the analytical model of plane wave, in dotted lines) model. Black lines: the point at the front of the cylinder. Red lines: the midpoint. Blue lines: the rear point.

The result shows that the pressure ratios predicted by the two models agree well. The plane wave approximation is effective in representing the spherical wave. It should be noted that at other points which are not in the median plane of the cylinder, the error will be larger.

4.3.4 The comparison of the measured pressures

The coherence of the transfer functions for the measurement should be checked before the comparison is made. Figure 4-30 shows the coherence of the transfer functions between the surface pressure and the reference pressure. The results for the nearest point (the front point), the midpoint and the furthest point (the rear point) are represented in black, red and blue lines respectively.

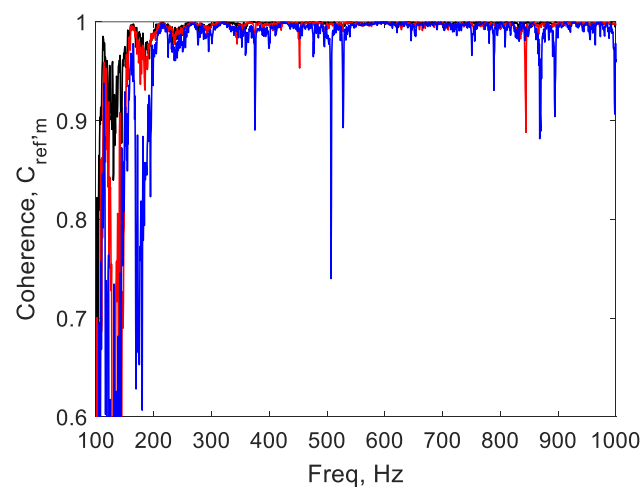


Figure 4-30 Coherence of the transfer functions between the surface pressure and the reference pressure. Black solid line: the front point. Red solid line: the midpoint. Blue solid line: the rear point.

The result shows that the coherence mostly larger than 0.95 can be achieved in the frequency range 200 Hz – 1000 Hz. The poor coherence at low frequency is due to the sound source, which is incapable of radiating well in this range. The 1/3 octave band sound pressure at 1 m from the source is in fact below 45 dB for frequencies lower than 200 Hz as shown in Figure 4-24.

Figure 4-31 shows a comparison of the measured pressure and the predicted pressure in the form of the ratios of the pressure at the measurement points to the pressure at the reference point. Both the first (analytical) model prediction and the second (BE) model prediction are given for the rear point where the end effect is significant. The frequencies below 200 Hz are not included because of the low coherence found. The frequency resolution is 0.625 Hz, 5 Hz and 20 Hz respectively for the measurement, the analytical model and the BE model.

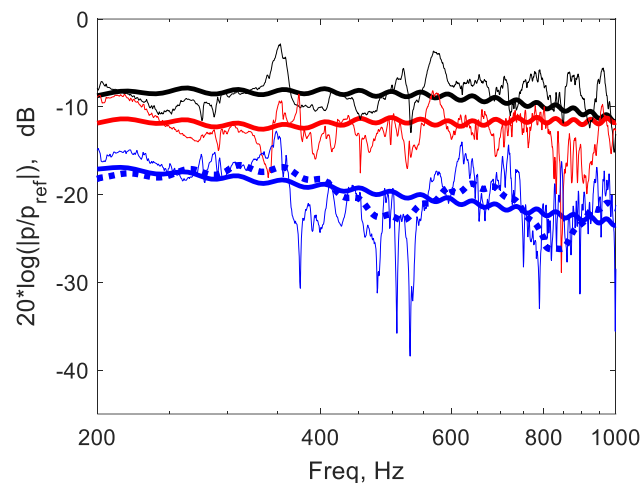


Figure 4-31 Comparison of the measured pressure ratios (thin, solid lines) with the predicted pressure ratios from the first (analytical) model (thick, solid lines) and from the second (BE) model (dotted lines). Black: the front point. Red: the midpoint. Blue: the rear point.

The results show that a satisfactory agreement is achieved over the frequency range for comparison between the measurement and the models. At the rear point, where the end effect is significant, the measurements agree better with the BE model predictions. The sharp peaks and dips in the measurements are possibly caused by the structural resonances, which are not included in the two prediction models.

4.3.5 The comparison of the vibration response

The vibration response was measured by both an accelerometer and a laser vibrometer. The latter provides a better sensitivity and does not require any part of the surface to be contacted. Figure 4-32 (a) shows the coherence between the acceleration response on the surface and

the reference pressure measurement. Figure 4-32 (b) shows the coherence between the velocity response on the surface and the reference pressure using the laser vibrometer measurement.

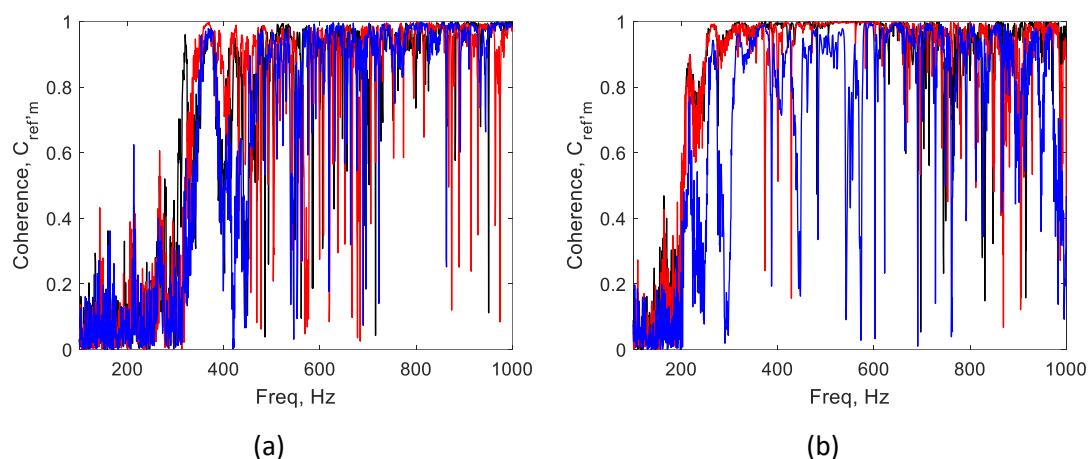


Figure 4-32 Coherence of the transfer functions between the response at the surface points and the reference pressure. Black solid line: the front point. Red solid line: the midpoint. Blue solid line: the rear point. (a) Accelerometer measurement – acceleration response. (b) Laser vibrometer measurement – velocity response.

The results show that the laser measured transfer function has a better coherence than the accelerometer, particularly in the frequency range between 300 Hz and 700 Hz. This relates to the signal to noise ratios for the laser and accelerometer measurements.

Below 700 Hz, the SPLs of the sound source are all below 70 dB in one-third octave bands, as shown in Figure 4-24. It is difficult for the low sound levels to excite the stiffened cylinder to vibrate with an acceleration that can be measured effectively by the accelerometer. The laser vibrometer has a much lower background noise level compared to the accelerometer at this frequency range, so it is able to pick up the velocity signal with relatively high coherence. The result also shows that the coherence for all points below 300 Hz is very poor, as the background noise in the instrumentation surpasses the effective signals which are very low for both the laser and the accelerometer.

Above 700 Hz, the coherence of the accelerometer measurement is slightly higher than that of the laser measurement. The acceleration response level of the structure increases due to the increasing excitation level. In the high frequency range, the laser has a higher background noise than the accelerometer.

Overall, the laser vibrometer measurement has a higher coherence and is therefore used in the following comparisons.

Figure 4-33(a), Figure 4-33(b) and Figure 4-33 (c) show a comparison of the response in terms of the transfer function between the acceleration and the reference pressure (1 m away from the sound source). The measured results are in black solid lines. They were calculated from the laser vibrometer measured velocity. The predicted results are given by the red solid lines. They were from FE model A with the pressure calculated from the approximate plane wave model, i.e. the third analytical model mentioned in Section 4.3.3. The frequency resolution in the measurement is 0.625 Hz and that in the FE model is 300 frequency points per decade. The results below 300 Hz are indicated by a grey band. The coherence of the measured transfer function is very low in this range and the measured results are not reliable.

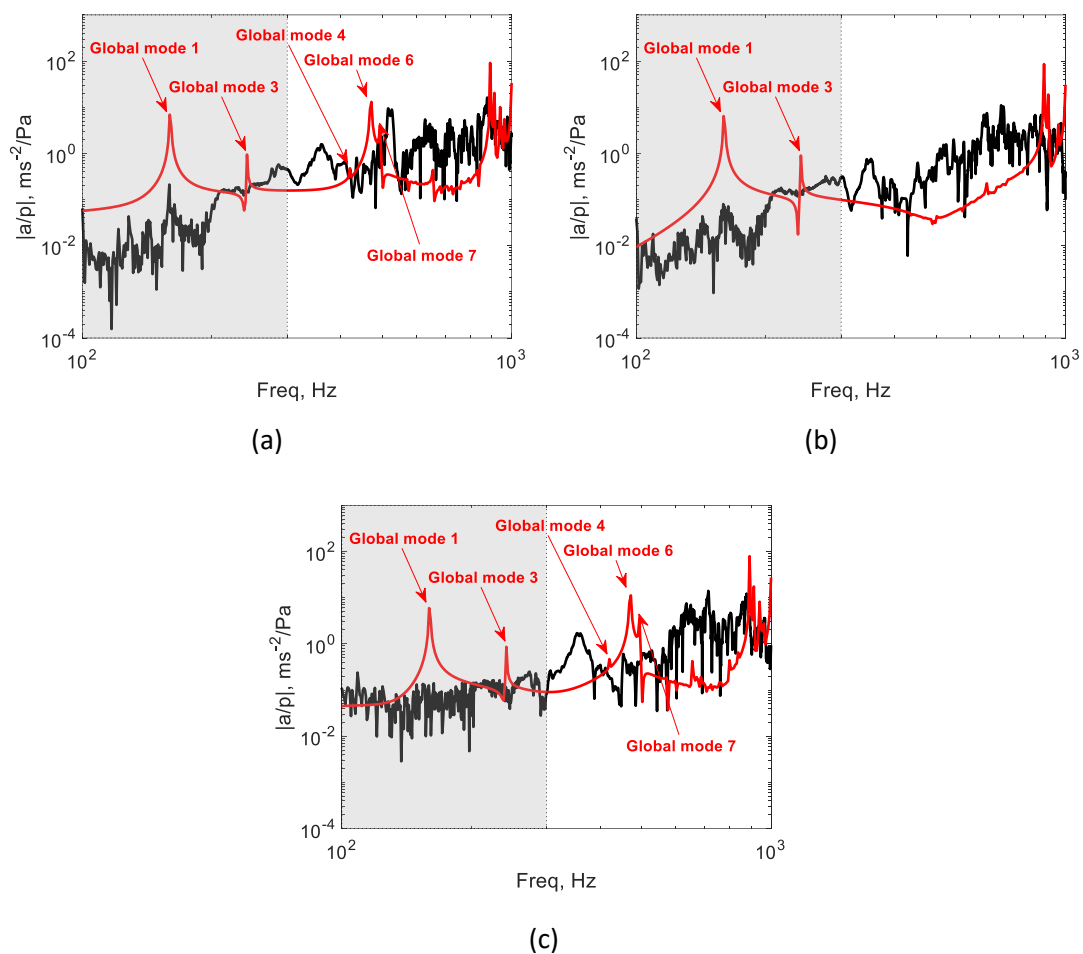


Figure 4-33 The comparison of the measured acceleration (calculated from the measured velocity) and the predicted acceleration in terms of the transfer function to the pressure at the reference point. Black solid lines: measurement. Red solid lines: FE model A with the blocked pressure from the 3rd analytical model (an approximate plane wave). (a) The front point. (b) The midpoint. (c) The rear point.

The results show that the agreement of response between the measurement and the model is not satisfactory, despite the overall trends of them matching in some regions.

Table 4-4 shows that the 1st, 3rd, 4th, 6th and 7th global modes of FE model A can be excited by a plane wave. In the predicted response, all the five resonances associated with these five global modes can be found in both the front and rear points, while only those associated with the 1st and 3rd modes are present for the midpoint as the measurements lie in the nodal line of these modes. In the measured response, however, the corresponding peaks are difficult to identify due to the poor coherence in the grey area below 300 Hz and the inadequate structural modelling between 300 Hz – 700 Hz as discussed in Section 4.2.3. The results also show that the overall level of the measured response between 600 Hz and 900 Hz is higher than that predicted.

When the structure is excited by acoustic waves, the global modes and therefore the boundary conditions play an important role in defining the responses. This is because for the acoustically excited modes, the JAF is generally smaller for the local modes compared to the global modes, while, as seen in the mobility tests, the local modes are predominant when the structure is excited by a point force inside the bays. To assess the effect of the boundary conditions in the case of acoustic excitation, a model was developed with a different boundary condition of fully clamped cylinder ends and was compared with the measurement for the front point, as shown in Figure 4-34.

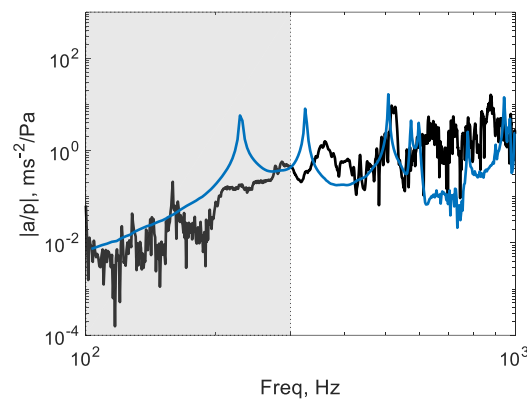


Figure 4-34 The comparison of the measured acceleration and the predicted acceleration for the front point in terms of the transfer function to the pressure at the reference point. Black solid lines: measurement. Blue solid lines: FE model with fully clamped boundary conditions and the blocked pressure from the 3rd analytical model (an approximate plane wave).

The result shows that the agreement between measurements and predictions is generally improved. The level of the predicted response is closer to the measurements. The numerical results show clear peaks which can be associated with the global modes, while this is not equally clear in the measurements.

To examine the effect of the acoustic excitation, both the first model (spherical wave) and the third model (plane wave approximation) were applied to a structural FE model of the test structure. Figure 4-35 shows the acceleration response in terms of the transfer function to the pressure for the front facing point on the cylinder. The result calculated with a pressure distribution obtained from the first model, the analytical spherical wave model, is presented in the black solid line. The result calculated from the third model, the analytical plane wave model, is presented in the black dotted line. The result shows a good agreement of the predicted response between the two excitation models, showing that the different types of acoustic excitations do not have a significant difference in the structural response.

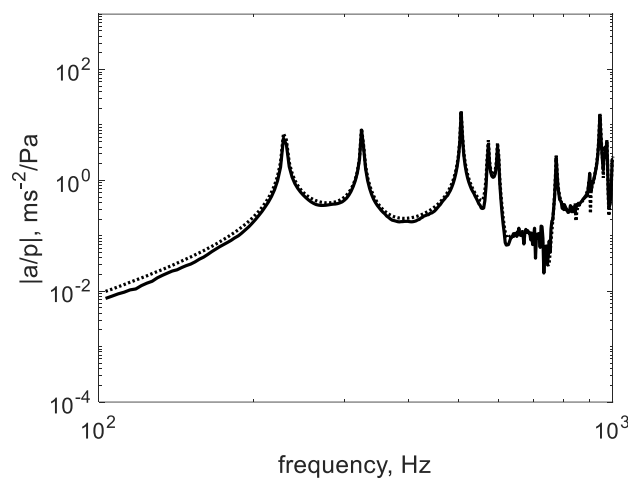


Figure 4-35 The comparison of the acceleration response in terms of the transfer function to the pressure for the front point estimated from the first model (analytical spherical wave excitation in the black solid line) and the third model (analytical plane wave excitation in the black dotted line).

On reflection, the acoustic test comparison might be improved by using a different sound source with a more flat spectrum and higher excitation level. In the current acoustic test the acoustic modes of the pipe cause significant pressure fluctuations, as shown in Figure 4-24 (a). This means that the responses can only be compared in terms of the transfer functions. In the meantime, as the sound level of the source is low the test structure cannot be excited effectively and the coherence in the measurements is poor at lower frequencies. In addition, the uncertainty present in the manufacturing of the test structure, as highlighted in Section 4.2.3.1 illustrating the driving point mobilities, is also in part responsible for the differences found.

4.4 Summary

This chapter investigated the acoustic response of a scaled fuselage model. Two structural FE models and three acoustic models (two analytical models and one numerical BE model) were

implemented and compared. An impact test and an acoustic test were performed. The comparisons between the measurement and the predictions were made for the point mobility, surface pressure and the vibration response.

The main findings can be summarised as follows:

- The two structural FE models agree well with the test structure for the lowest global modes below 300 Hz. However, these models cannot represent the structure well in the frequency range 300 Hz – 700 Hz due to the inaccurate modelling of the joint details.
- The surface pressures predicted by the analytical model of a spherical acoustic wave incident upon an infinite cylinder agree well with measurements. The end effects were proved to be only significant for the response at the rear of the test structure and were verified by a numerical BE model. This analytical model can be approximated well by an equivalent plane wave model.
- Good agreement between the measurement and prediction for the vibration response was not obtained, although the agreement can be improved by changing the model for the boundary conditions to being more representative of the physical realisation. The comparison might also be improved by using an acoustic source with a relatively flat spectrum and higher excitation level at lower frequencies, but at the same time the uncertainty and variability present in the test structure made this part of the validation exercise very difficult. Additional measurements with other sound sources were initially planned but could not take place due to the 2020 Covid pandemic.

Chapter 5 Numerical investigation of the nonlinear response to high level acoustic excitation

A common assumption of the previous chapters is that the structural response is linear. For high level acoustic excitation, the dynamic response can become nonlinear when this corresponds to large amplitudes. Typically the structures, which are in flexure, deform with a combination of flexure and axial extension of their mid-plane axis. This coupling of the out-of-plane and the in-plane motions of the structure is caused by geometric nonlinearity for flat plates and is present for the structural dynamics of structures possessing curved geometries. Geometric nonlinearity may affect the response, both its frequency content and its statistics, which cannot be predicted by the linear model. One option is to use a full order numerical FE simulation, but its computational costs, especially for complex structures subjected to random loading, are prohibitive for these methods to be used at early design stages.

This chapter investigates the nonlinear response of stiffened plates and cylinders subjected to high level acoustic excitations based on the nonlinear reduced order model (NLROM). The NLROM uses a reduced number of linear modes to represent the response under geometric nonlinear behaviour. The nonlinear dynamic modal equations of motion are solved under a finite series expansion. In practice, the nonlinear modal stiffness in the nonlinear dynamic modal equations of motion are determined from a nonlinear static analysis performed with a finite element model. The NLROM is generally used to achieve an efficient calculation of the geometrically nonlinear dynamic response for large and complex structures. The numerical results are given to address the effects of NLROM implementation procedures. An original contribution from this research is to apply the NLROM to a stiffened cylinder.

5.1 Nonlinear reduced order model

5.1.1 General formulation

The nonlinear response is derived in terms of a series expansion of the linear structural modes. Applying a reduced number of the linear modes to the nonlinear equation of motion Eq.(1-3), the modal representation of the equation of motion for a structure with geometric nonlinear response becomes

$$[m]\{\ddot{q}(t)\} + [k]\{q(t)\} + [k_{n1}(q(t))] + [k_{n2}(q(t))] = \{l(t)\} \quad \text{Eq.(5-1)}$$

where $[m]$ and $[k]$ are the linear modal mass and stiffness matrices and $\{l\}$ are the linear modal force vector. $[k_{n1}]$ and $[k_{n2}]$ are the nonlinear modal stiffness matrices as functions of the modal displacement q .

For the n^{th} linear mode, it can be represented as

$$m_n \ddot{q}_n(t) + k_n q_n(t) + \theta_n(q_1, q_2, \dots, q_r) = l_n(t) \quad \text{Eq.(5-2)}$$

where m_n , k_n and l_n are the linear modal mass, stiffness and force for this mode. Here the geometric nonlinearity appears as a vector function θ . The subscript $n = 1, 2, \dots, N_l$ represents the order of the linear modes; the subscript $r = 1, 2, \dots, N_{nl}$ represents the order of the linear modes whose modal coordinates are used in the functional expression for the nonlinear vector function θ . The damping matrix is neglected at this stage.

The nonlinear vector function comprises some polynomial terms typically involving the quadratic and cubic combinations of the modal displacements $q_r(t)$, which can be written as [90]

$$\theta_n = \sum_{i=1}^3 A_n^{(s^i, t^0)} q_s^i + \sum_{i=1}^2 \sum_{j=1}^{3-i} A_n^{(s^i, t^j)} q_s^i q_t^j, \quad \text{Eq.(5-3)}$$

where A_n are the unknown stiffness coefficients associated with each mode and q_s, q_t are the modal displacement identified by the indices s, t . The indices i and j represent powers of the modal displacements. It has been found that it is sufficient to couple the linear modes in groups of no more than two [90]. When selecting the linear modes, it may not be necessary to make use of three adjacent modes. This will be discussed below in Section 5.1.2. The nonlinear stiffness coefficients $A_n^{i,j,k}$ need to be first identified by means of a static analysis. Eq.(5-2) can then be solved using an appropriate direct time integration scheme to evaluate the nonlinear displacement response for the situation considered.

Several procedures can be used to identify the nonlinear stiffness coefficients in Eq.(5-3). They include direct methods [158-160] and indirect methods [90, 161].

In a direct method, the nonlinear stiffness coefficients can be evaluated directly by applying the modal transformation and truncation [160] on the physical nonlinear stiffness matrix. The latter is usually extracted from the FE model implemented using commercial codes. The modal nonlinear stiffness matrix obtained is then cast into the form of Eq.(5-3). The detailed formulation for the direct method has been presented in [158]. Although the implementation of the direct method seems straightforward, it requires access to the nonlinear stiffness

matrices. This access is not always straightforward and available in commercial FE codes, which makes the direct method less attractive.

In an indirect method, the nonlinear stiffness coefficients are approximated by a set of static, nonlinear FE solutions, which is usually referred to as nonlinear static identification. Access to the internal matrices of the FE codes is not required.

In a static, nonlinear FE analysis, the acceleration terms in Eq.(5-2) are set to zero and the time dependencies are eliminated. The static modal equation of motion may be written as

$$k_n q_n + \theta_n(q_1, q_2, \dots, q_r) = l_n. \quad \text{Eq.(5-4)}$$

The left hand side of Eq.(5-4) may be regarded as a stiffness restoring modal force, with the linear components $k_n q_n$ and the nonlinear stiffness components $\theta(q_1, q_2, \dots, q_r)$. l_n may be regarded as the static modal forces and needs to be defined differently for the characterisation of the different coefficients.

The linear modal stiffness k_n can be derived from natural frequencies which can be obtained from a linear free vibration analysis of the FE model. The outputs of such a linear free vibration analysis are the modal mass m_n , natural frequencies ω_n and mode shapes ψ_n . For the n^{th} mode, the linear modal stiffness can be evaluated as

$$k_n = m_n \omega_n^2. \quad \text{Eq.(5-5)}$$

The nonlinear components of the restoring force can then be expressed as

$$\theta(q_1, q_2, \dots, q_r) = l_n - m_n \omega_n^2 q_n. \quad \text{Eq.(5-6)}$$

In Abaqus, only the static displacement w and static force F are used, so a modal transformation with the linear modes is required to obtain the modal displacement q_n and /or the modal forces l_n , i.e. $w = \psi q$ and $l = \psi F$. The mass normalised mode shapes are used, so $m_n = 1$ and ω_n is the natural frequency.

In order to obtain the displacement w and /or force F from a static analysis, two different approaches can be followed. These are the so-called the static loads method and the enforced displacement method. Both of the methods are briefly explained below, while an in-depth comparison of the two can be found in reference [162].

In the static loads method, static loads F can be applied in a static nonlinear FE to estimate the nonlinear coefficients. The approach followed in this thesis goes under the name of the Implicit Condensation (IC) method [90]. A set of static loads is formed by the linear combination of the linear bending modes and is applied to the FE structure. The formation of

the static forces is provided in details in 5.1.3. Then the nonlinear static FE problem is solved to obtain the static displacement w . The static forces F and the displacements w are then projected into the modal space and a regression analysis is used to estimate the nonlinear coefficients. The primary advantage of this method, compared to the enforced displacement method, is that the membrane modes are not directly required. This is because the membrane effect is already implicitly included in the computed nonlinear static displacement. However, the estimated nonlinear coefficients are sensitive to the modal basis selection and the scaling factors.

In the enforced displacement method, the displacement vectors w are formed from a linear combination of a selected set of a scaled modal basis. Then the nonlinear static FE problem is solved to obtain the corresponding constraint forces F . The constraint forces obtained and the enforced displacements are then projected into the modal space and the nonlinear coefficients are determined via an estimation process for Eq.(5-3). The details of the method have been presented in references [163, 164]. This method is not used in this chapter.

For stiffened plates and cylinders, pure bending or membrane modes do not exist due to the linear coupling between the bending and stretching motion. Consequently, compared to the unstiffened flat plate, a larger number of membrane modes may need to be included in the modal basis selection if the enforced displacement method is used. For this reason, the IC method is used in this study.

The general formulations and the implementation procedures for the IC method have been presented by McEwan et al. [90]. In the following sections, some details on implementation procedures of the nonlinear static identification and the direct time integration are presented giving particular attention to the cases of plates with deep stiffeners and stiffened cylinders.

5.1.2 Modal basis selection

Initially a set of modes needs to be selected for inclusion in the nonlinear functions θ . The aim of the modal basis selection is to achieve an accurate estimation of the nonlinear stiffness coefficients with the minimum number of modes included.

A general rule has been suggested in [87] and consists of using all the bending modes with natural frequencies less than twice the maximum frequency of excitation. This is because the bending modes that are out of the excitation bandwidth may still be indirectly excited through the nonlinear coupling. However, for thin-walled plates and cylinders with high modal density, a large number of modes may be included by using this rule, which requires a significant

number of static FE nonlinear tests in the nonlinear static identification. For example, from Equation (3.11) in reference [90], the number of static nonlinear tests equals 2313 if 34 modes are used in the modal basis selection. High computational cost and considerable large post-processing efforts would then be required.

The calculation time can be reduced taking advantage of symmetries in the structural modes as suggested in [90]. For example, for an unstiffened plate subjected to normal plane wave excitation, the anti-symmetric modes may be excluded to reduce the computational cost. In addition, symmetric/antisymmetric boundary conditions can be used to reduce the size of the FE model when possible. It is argued that the nonlinear effects can cause the anti-symmetric modes to be excited by the symmetric loading [87], but the participation of these modes that will not be linearly excited may be very low and hence the accuracy of nonlinear static identification may not be significantly reduced by their exclusion. However, this method may not particularly be applicable for structures with complicated mode shapes. These structures include plates and cylinders with complex stiffener configurations such as eccentric, deep cross sections. It may not be straightforward to deal with symmetric and antisymmetric modes. In addition, this method is not applicable for structures subjected to non-symmetric loading and mechanical point force excitation.

A system-identification guided method has been suggested in [91]. A short time history of the full order FE simulation is required in this method. The proper orthogonal decomposition (POD) is performed on the time record to determine the proper orthogonal modes (POMs) and the corresponding proper orthogonal values (POVs). The POMs are then ordered by the POVs and the ones contributing most are used to determine the modal basis through the modal assurance criterion (MAC). Thus this method is also named POD/MAC-based technique [165]. Although this technique can identify any modes present in the nonlinear response, it requires the time history of all DOFs for the structure. In addition, the time history should be long enough to remove the initial transient effects by excluding the first few seconds' data. These can lead to quite a high computational cost for a large structure. Thus, it is recommended that the POD method should only be considered if the nonlinear coupling is large enough to excite any modes that are not linearly excited and if the FE model is not too large.

Alternatively, a linear frequency response analysis can be used to eliminate modes possessing small contributions. The linearly excited modes that are determined from the resonances present in the linear FRFs will be used in the modal basis selection. As the analysis can be effectively solved in the frequency domain, it is much more computationally efficient than the

full order FE simulation in the POD/MAC-based method. However, as with the method using the symmetry of the modes and the loading, the main drawback of this method will be that modes that are not linearly active may still be excited through nonlinear coupling. The effect of selecting different numbers of modes for the nonlinear characterisation of the structures has been addressed and is discussed separately in Section 5.2.2.1.

5.1.3 Static loading specification

Following the modal basis selection, the static loadings are formed from a linear combination of pairs of these bending modes, which can be represented as

$$F = a_n \psi_n + a_m \psi_m, \quad \text{Eq.(5-7)}$$

where a_n and a_m are scaling factors for the n^{th} mode and the m^{th} mode as defined below. In order to define the static loading it has been found that considering two modes is sufficient and it is not necessary to account for the couplings between three or more modes [90].

The scaling factors in Eq.(5-7) determine the distribution of the static forces on the structure. The values of the scaling factors determine the overall magnitude of the static loadings that will result in the geometric nonlinearity being exercised to a greater or lesser extent. There are two possible ways to specify the values of the scaling factors. One is the ‘characteristic load method’ (see [90]) and the other one has been suggested in [87] and is called ‘desired displacement’.

According to the ‘characteristic load method’ there are two different approaches for the fundamental mode and for all the other modes. The scaling factor associated with the fundamental mode is defined as

$$a_1 = \psi_1^T F_c, \quad \text{Eq.(5-8)}$$

where F_c is a vector of uniform loads over the structure.

If acoustic excitation is considered, a pressure-to-force transfer matrix is required and Eq.(5-8) is modified as

$$a_1 = \psi_1^T T_p P_c, \quad \text{Eq.(5-9)}$$

where T_p is the pressure-to-force transfer matrix and P_c is the ‘characteristic pressure’, that is the sound pressure distribution considered in the analysis. For example, in the case of flat plates this is a uniform pressure while for the cylindrical structures this corresponds to the distribution of the scattered pressure around the surface.

For the other modes in the nonlinear static identification, the values of the scaling factors are calculated from the ratio of the squared natural frequencies, i.e.,

$$a_m = \frac{\omega_m^2}{\omega_1^2} a_1, \quad \text{Eq.(5-10)}$$

to guarantee that these modes are excited in proportion to the fundamental mode.

Trial and error may be needed for the selection of an appropriate value for the overall magnitude of the characteristic load F_c or the characteristic pressure P_c . McEwan [90] used the characteristic loadings/pressure of 1.2 – 2 times the highest dynamic loadings for an unstiffened plate and a moderately stiffened plate. However, there may be a quite large range of variation of this estimation across different structures. In addition, this method may not be applied to cylinders. This is because a uniform characteristic loading or pressure results in non-zero modal forces only for the breathing modes. All the circumferential modes are anti-symmetric and cannot be excited by the characteristic loading. In this case, a nonuniform characteristic loading is suggested. These nonuniform characteristic loadings can be effectively approximated by the quasi-static loadings including the sound scattering over the rigid surface of the cylinder. In previous studies, the NLROM has not been applied to a stiffened cylinder and the method of defining the nonuniform characteristic loading is also an original contribution from this research. The transfer matrix T_p in Eq.(5-9) can be regarded as a constant matrix if the area of each element does not significantly vary during the deformation.

This transfer matrix can be calculated given the coordinates of the nodes and the formulation of the finite elements [90]. It can also be extracted from an independent static FE analysis where a uniform loading is applied on the surface of the FE model with all its DOFs being constrained. Then the transfer matrix can be derived from the following relation,

$$f = T_p P, \quad \text{Eq.(5-11)}$$

where P is the specified uniform pressure vector and f is the nodal force vector. The nodal force can be obtained by extracting the reaction force F_r from each node and letting $f = -F_r$.

If the area of an element significantly varies during the deformation, the transfer matrix varies significantly during the deformation of elements. The variation depends on the level of the applied loads and the resultant deformation. In a static FE analysis, it means that the applied loads need to vary across different time steps, which makes this method less practical to

implement. However, this effect may be significantly alleviated by decreasing the mesh size of the elements.

Alternatively, the ‘required displacement method’ can be followed [87]. The values of the scaling factors are chosen based on the linear estimates of the desired displacement at one or more positions of maxima or minima of the structure as

$$a_n = \frac{\omega_n^2 w_P}{N \psi_n^T \psi_n \psi_{nP}}, \quad \text{Eq.(5-12)}$$

where w_P is the desired displacement at position P and ϕ_{nP} is the mode shape n evaluated at point P and the force is expressed as in Eq. (5.6). The factor N equals 2, which is the number of modes that have been included in Eq.(5-7), as they all give same contribution to the desired displacement at point P , i.e. w_P .

Similar to the ‘characteristic loads’ method, the desired displacement w_p should be large enough to allow the primary modes to be nonlinear. For unstiffened plates, a displacement of one thickness of the plate is sufficient to cause a detectable nonlinear effects [87]. However, for a plate with deep stiffeners or a stiffened cylinder, a much larger required displacement is expected. This might cause difficulty for the direct time integration to converge. In addition, buckling may occur for a stiffened cylinder with a large required displacement, which causes a convergence issue for the static nonlinear FE solutions.

In FE software these static, distributed loadings can usually be applied either as nodal forces at each node or as pressures over each element. Two options are available in specifying the directions of these loadings: dead loads and follower loads [88]. Dead loads have a constant direction whilst follower loads rotate with the nodes/element to which they are applied during the structural deformation.

The dead loads have been generally used in the nonlinear static identifications for the IC method [90]. In this sense, the direction of the static loadings is set to be normal to the initial undeformed surface of the structures, including straight beams, unstiffened flat plates, moderately stiffened plates and shallow, curved beams/plates. The assumption is that the deformation of these structures is small enough to have a negligible effect on the amount of the applied loadings whether or not the static loadings rotate with the deforming surface. For these structures, a maximum displacement of one panel thickness is sufficient for their primary modes to become nonlinear.

However, for plates with deep stiffeners, a much higher maximum displacement may be required to exhibit nonlinear effects. The response of these structures may be dominated by the behaviour and contribution of the deep stiffeners. Consequently, a much larger plate displacement than one plate thickness, which would normally fail any linear assumption for an unstiffened plate, is required for the deep stiffeners' behaviour to become nonlinear. In addition, for stiffened cylinders with high curvatures, the deformation of the surface may be more sensitive to the direction of the applied loads. The accuracy of the nonlinear stiffness coefficients that are evaluated may deteriorate. Hence, the necessity of using follower loads in the nonlinear identification may need to be examined and this issue is revisited in Section 5.2.2.2.

5.1.4 NLROM combined with thermal effects

In addition to high levels of dynamic excitation, many aerospace structures are often exposed to thermal loading. In terms of the NLROM, two methods have been previously investigated and reported in the literature: the cold-mode method and the hot-mode one [87, 166].

The cold-mode NLROM is formulated and solved using the modes of the non-thermally loaded structure. Eq.(5-2) is subsequently modified by any thermal effect with the introduction of two additional terms. They are the change in the linear modal stiffness $k_{\Delta T}$ and the thermal modal force vector $l_{\Delta T}$. Hence, the cold-mode NLROM formula becomes

$$m_n \ddot{q}_n(t) + (k_n - k_{n\Delta T}(\Delta T))q_n(t) + \theta(q_1, q_2, \dots, q_r) = l_n(t) + l_{n\Delta T}. \quad \text{Eq.(5-13)}$$

The nonlinear stiffness coefficients in θ are assumed to have no temperature dependency, as the mode shapes and the natural frequencies of the cold modes are used in Eq.(5-7) and Eq.(5-10) in the nonlinear static identification.

The thermal loading only primarily affects the natural frequencies of flat, unstiffened structures. This is because no out-of-plane deformation is caused by thermal loading which only acts in the plane of the structure, unless excessive temperature rises ultimately cause buckling. The mode shapes differ little from those at constant temperature.

The linear modal stiffness change, $k_{n\Delta T}$, is linearly related to the temperature change ΔT , if a uniform temperature field is applied. In this case, $k_{n\Delta T}$ can be calculated by performing a normal modal analysis of the structure with and without a specific temperature change of ΔT_0 , i.e.

$$k_{n\Delta T} = \frac{k_n - k_{n\Delta T_0}}{\Delta T_0}, \quad \text{Eq.(5-14)}$$

where the linear modal stiffness $k_{n\Delta T_0}$ is assembled making use of the natural frequency of the n^{th} mode of the structure under a temperature rise of ΔT_0 .

The thermal modal force vector $l_{n\Delta T}$ can be found by constraining all DOFs of the structure then by applying the thermal loading in a static FE analysis. Eq.(5-3) now becomes

$$0 = l_n + l_{n\Delta T}, \quad \text{Eq.(5-15)}$$

so $l_{n\Delta T}$ is opposite to the applied modal force l_n . The latter can be extracted as the reaction force from the FE model in terms of nodal positions and is multiplied by the n^{th} (cold) mode shape.

Eq.(5-13) is still valid for curved/stiffened structures. However, the calculations of the linear modal stiffness matrix and the thermal modal force vectors are different.

The first difference arises from the change in the structural geometry due to the thermal loading. The change of the linear structural stiffness matrix $K_{\Delta T}$ is no longer a linear function of the temperature change ΔT . It is also dependent on the geometric change of the structure, which may result in a considerably different set of mode shapes in comparison to the cold modes. The linear modal stiffness ($k_n - k_{n\Delta T}(\Delta T)$) that is calculated with the cold modes becomes non-diagonal. Hence, the linear modal stiffness matrix should be directly assembled from the natural frequencies of the structure with thermal loading rather than obtained by applying the Eq.(5-14).

The thermal modal force vectors are also changed by the static deformation. Eq.(5-15) may still be used as an approximation when the static deformation is small, but considerable error may be expected as the temperature increases.

These issues may be solved by application of a hot-mode NLROM approach. This approach uses the mode shapes and the natural frequencies of the structure under the thermal loading and temperature conditions (hot modes). The hot-mode NLROM formula is in an equivalent stress-free form that is similar to Eq.(5-2), i.e.

$$m'_n \ddot{q}'_n(t) + k'_n q'_n(t) + \theta'(q'_1, q'_2, \dots, q'_r) = l'_n(t). \quad \text{Eq.(5-16)}$$

m'_n , k'_n and l'_n are the modal mass, stiffness and force that are calculated from the hot modes. The linear modal stiffness k'_n is now diagonal and dependent on the thermal loading. In the same way, the temperature dependency is also introduced in the nonlinear stiffness coefficients in θ' , as now the hot modes used in the nonlinear static identification are

dependent on the temperature changes. q'_n is the dynamic modal displacement referenced to the static modal displacement due to the thermal loading, i.e.

$$q'_n = q_n - q_{nT}, \quad \text{Eq.(5-17)}$$

where q_n is the dynamic modal displacement and q_{nT} is the static modal displacement due to the thermal loading for the n^{th} mode.

The hot-mode NLROM with its equivalent stress-free form applies to both flat, unstiffened structures as well as curved/stiffened ones. However, as the thermal loading is applied in the normal modal analysis and in conjunction with the static nonlinear tests, a convergence issue usually occurs due to buckling when the temperature rise is high. The steps in the cold-mode and the hot-mode NLROM approaches may be summarised as in Table 5-1 and Table 5-2.

Table 5-1 Steps of a cold-mode NLROM

1	Obtain the cold flexural modes from a normal mode analysis for the non-thermally loaded structure, i.e. at the ambient temperature.
2	Select the proper modal basis based on one of the criteria in Section 5.1.2.
3	Build the applied loading for the nonlinear static identification based on Eq.(5-7) - Eq.(5-10).
4	Calculate the nonlinear stiffness coefficients required in the vector function θ .
5	Determine the linear modal stiffness matrix. For the flat, unstiffened structure, apply Eq.(5-14); for curved or stiffened structure, assemble it from the natural frequencies of the structure with thermal loading.
6	Determine the thermal modal loading vector by applying Eq.(5-15). It leads to an exact solution for the flat, unstiffened structure and an approximate solution for the curved or stiffened structure.
7	Calculate the modal displacement by solving Eq.(5-13) using numerical time integration and obtain the subsequent physical displacement by modal transformation.

Table 5-2 Steps of a hot-mode NLROM

1	Obtain the flexural hot modes at the elevated temperature from a normal modal analysis for a thermally loaded structure.
2	Select the proper modal basis based on one of the criteria in Section 5.1.2.
3	Build the applied loading for the nonlinear static identification based on Eq.(5-7) - Eq.(5-10). The thermal loading is also applied in the static tests.
4	Calculate the nonlinear stiffness coefficients required in the vector function θ' .
5	Determine the linear modal stiffness matrix by assembling it from the natural frequencies of the structure with thermal loading present.
6	Calculate the modal displacement by solving Eq.(5-16) using numerical time integration and reference the result to the initial condition (non-thermal) by applying Eq.(5-17)
7	Calculate the physical displacement by modal transformation using the hot modes.

Figure 5-1 shows a flow chart that summarises the steps listed in Table 5-1 and Table 5-2, together with a preliminary step of determining the in-plane boundary conditions for the thermal condition. The details of the latter will be explained in Section 5.2.1.4. At this stage one may note that this consists of tuning/relaxing the in-plane boundary conditions to avoid buckling due to the temperature rise. In the flow chart, two rounded rectangles, dashed line for cold-mode and dotted line for hot-mode, are used to highlight the different and the common steps of the two approaches.

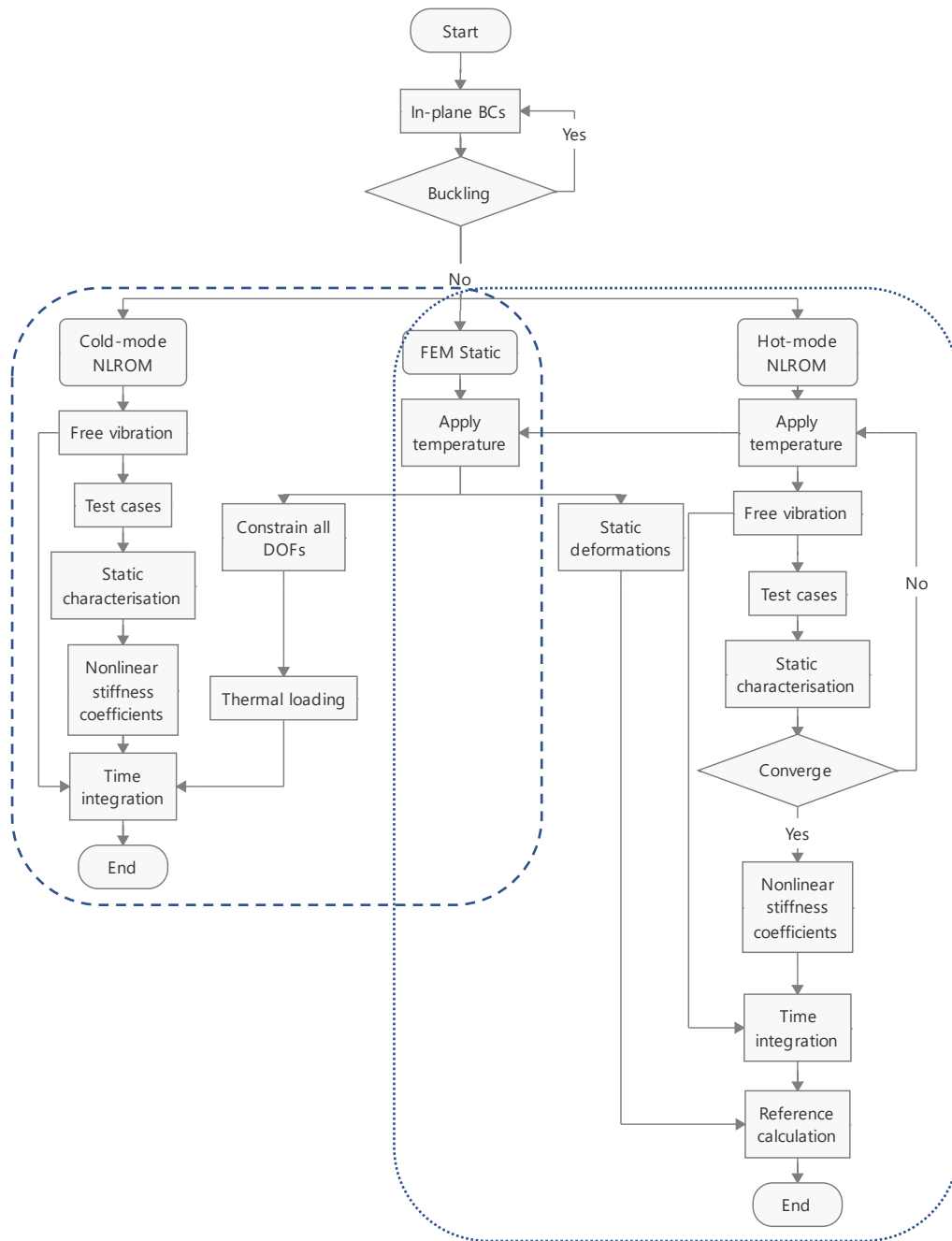


Figure 5-1 A flow chart illustrating the steps of a cold-mode NLROM and a hot-mode NLROM. Two rounded rectangles (dashed line for cold-mode and dotted line for hot-mode) are used for highlighting the different and common steps.

5.1.5 Numerical integration schemes

A direct numerical integration must be used in solving the nonlinear dynamic response in either NLROM or a full order FEM analysis. The relative accuracy and the computational efficiency are primarily important on the selection of the numerical integration methods.

For NLROM, direct time integration is used to solve the modal equations of motion with the identified nonlinear coefficients. Three available numerical integration methods, i.e., the Newmark- β method, the 4th order Runge-Kutta method and the Adaptive time step Runge-Kutta method have been presented and compared in [90]. A general trend of the comparison may be summarised as shown in Table 5-3.

Table 5-3 The relative accuracy and efficiency of three potential numerical integration methods that can be implemented.

	Relative accuracy	Relative efficiency
Adaptive time step Runge-Kutta	High	Low
4 th order Runge-Kutta	Medium	Medium
Newmark- β	Low	High

The equations describing these methods have also been given in [90] and can be implemented in code such as MATLAB. Alternatively, a number of built-in functions such as ode45 and ode15s are also available in MATLAB for the numerical integration. The 4th order Runge-Kutta method was used in the NLROM results produced in this chapter.

For the full order FE simulation, the numerical integrations are categorised as being either implicit or explicit schemes. A brief comparison of the two schemes for the Abaqus software is summarised in Table 5-4.

Table 5-4 A comparison of the implicit and the explicit schemes in ABAQUS.

	Numerical integration	Relative accuracy	Relative efficiency	Memory cost
Implicit	Newton-Raphson (Hilbert-Hughes-Taylor)	High	Low	Large
Explicit	Euler (central-difference)	Low	High	Small

The implicit scheme is unconditionally stable, while the explicit scheme is conditionally stable. This is because that the implicit scheme is iterative by using the tangent stiffness matrix at each time step to satisfy the equilibrium conditions, whilst the explicit scheme does not. Therefore, the implicit scheme usually has high accuracy but demands large memory cost. In this chapter, the implicit scheme was used to produce the full order FE results. A description of this nonlinear solver in Abaqus together with an example input file are provided in Appendix 1.

5.1.6 Damping models and the effects of the solution sample rate

Once an appropriate time integration method has been selected, for either a NLROM or a FEM analysis, the efficiency and the accuracy of the implementation of the numerical integration are also significantly affected by the choice of damping model and the required sample rate.

Damping dissipates vibrational energy and most of the mechanisms involved are generally approximated by a linear model for small levels of dissipation in practice. A damping model must be determined and either inserted in to Eq.(5-2) for NLROM or specified in the solver for full order FE model before the numerical integration can be performed. A number of possible different damping models are summarised in Table 5-5 [167, 168].

Table 5-5 Different forms of damping models.

	Evaluation	Applications
Viscous damping	$f_d \propto \dot{x}$ (f_d is damping force and \dot{x} is the velocity)	Viscous dampers, dashpots and shock absorbers
Hysteretic damping	$f_d \propto x$	Viscoelastic, thermal and micromechanical effects; internal friction. Typically applicable for a frequency domain solution but acausal and not to be used for time domain predications
Velocity-squared damping (nonlinear)	$f_d \propto \dot{x}^2$	Turbulent fluid flow Wind resistance
Coulomb damping (nonlinear)	Constant and determined by the friction coefficients between the surfaces	Sliding and static friction
Acoustic radiation damping	Loss factor $\eta = \frac{W}{\omega \bar{E}}$ (W is the radiated sound power and \bar{E} is the time averaged vibrational energy)	Vibroacoustic

The viscous and the hysteretic damping models are typically used in structural vibration. For time domain calculations the viscous damping representation is preferable. The hysteretic

damping model cannot be applied directly in a time domain calculation as it fails to obey causality.

Rayleigh damping is a specific representation of the viscous damping and is generally used in FE analysis. This representation assumes that the viscous damping matrix can be constructed by a linear combination of the mass matrix and the stiffness matrix.

In this study, Rayleigh damping was used by specifying the modal damping calculated from the linear modal mass m_n and modal stiffness k_n . The Rayleigh damping for the n^{th} mode can be written as

$$c_n = \alpha_n m_n + \beta_n k_n, \quad \text{Eq.(5-18)}$$

where α_n and β_n are the damping factors for this mode.

The viscous damping ratio of the n^{th} mode is

$$\xi_n = \frac{c_n}{c_{n0}} = \frac{\alpha_n m_n + \beta_n k_n}{2\sqrt{m_n k_n}} = \alpha_n \sqrt{\frac{m_n}{k_n}} + \beta_n \sqrt{\frac{k_n}{m_n}} = \frac{1}{2} \left(\frac{\alpha_n}{\omega_n} + \beta_n \omega_n \right), \quad \text{Eq.(5-19)}$$

where ω_n is the natural frequency of the n^{th} mode. c_{n0} is the critical damping coefficient for the n^{th} order mode. The general procedure adopted here for defining damping was to impose the damping ratio of the first mode either using the mass-proportional parameter α or the stiffness-proportional one β . The values of α or β selected for the first mode were also adopted for all of the others.

It can be seen from Eq.(5-19) that the damping ratios increase with frequency for stiffness-proportional damping, i.e. the term with β_n , and decreases with frequency for mass-proportional damping, i.e. the term with α_n . A desired damping ratio at a certain frequency or mode of structure can be obtained by tuning or selecting either of the two damping terms.

The stiffness-proportional damping may be used to facilitate a nonlinear solution if the high frequency responses are strong. To avoid aliasing from the high frequency component in the PSD estimation, a sample rate above twice of the highest excitation frequency is sufficient. For the nonlinear response, however, a much higher sample rate is required as the higher order modes or higher nonlinearly produced harmonics of lower order modes, with frequencies well above twice the excitation bandwidth, may also be excited due to the nonlinear coupling. This effect becomes more significant for a stiffened plate subjected to point excitation. A very high sample rate will significantly increase the computational cost of a full order FE model. In this sense, the stiffness-proportional damping may be preferred as it

can be used to suppress the high frequency resonances, although the mass-proportional damping has been generally used in the full order FE models in ABAQUS [166] This will be explored in Section 5.2.3.

However, some caution is needed if a high level of stiffness-proportional damping is considered. In a full order FE simulation, the linear and the nonlinear parts of the stiffness matrix are not necessarily separated so the damping is proportional to the overall stiffness matrix and hence nonlinear, whilst in the NLROM the damping can only be made proportional to the linear stiffness as the nonlinear stiffness is not explicitly available. This may introduce additional difference in the comparison between NLROM and FEM, especially when the damping term β is large. In addition, a high damping ratio may also make the presence of the nonlinear behaviour of the resonance less detectable.

Hence, there is a trade-off that must be made in the selection of the level of stiffness-proportional damping and the sample rate in terms of the accuracy and efficiency when producing the comparison of NLROM and FEM results.

5.2 Numerical results

Some of the methods described in Section 5.1, which might affect the implementation of the NLROM for stiffened and curved structures, were applied to two example structures. They are a thin plate and a thin-walled cylinder, both with deep stiffeners. In addition, and as a term of comparison, some results for an unstiffened plate are also included in Sections 5.2.3 and 5.2.4.

5.2.1 Example structures and general FE parameters

This section presents the details of the structural models and the forms of excitation adopted in this numerical study.

5.2.1.1 Stiffened plate

The first example structure is the same thin plate with deep stiffeners used in Chapter 2. Figure 2-2(a) shows the geometry of the stiffened, rectangular plate and Figure 2-2 (b) shows the geometry of the cross-sections of the stiffeners (see Chapter 2). Table 2-1 lists the parameters for the geometry and material properties of the stiffened plate. The four edges of the stiffened plate are fully clamped in the current analysis.

The nonlinear equations of motion for the stiffened plate are given in Eq.(5-1) and Eq.(5-2). The source of the nonlinearity comes from the geometric nonlinear deformation, which can be characterised as θ in Eq.(5-2).

A three dimensional Cartesian coordinate system was used to model the stiffened plate and the plate is in the $x - y$ plane. The linear mode shape of the plate is represented as $\psi_n(x, y)$. The plate bays were modelled with the 4-node shell element S4R in Abaqus and in this instance shell elements were also used to represent the stiffeners as shown in Figure 5-2. The elements at the joint area between the plate bay and the stiffeners have a thickness of 0.007 m.

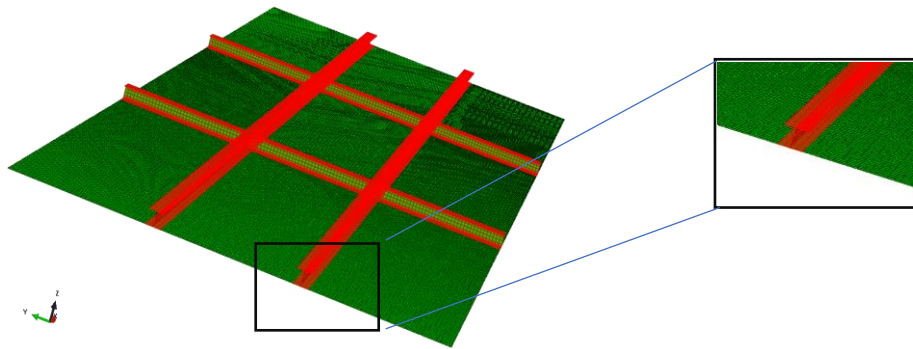


Figure 5-2 The meshed FE model of the stiffened plate with shell elements in Abaqus. The expanded view shows part of one x -wise stiffener joined with the plate.

The size of the shell element was set to be $15 \times 15 \text{ mm}^2$. The mesh size was selected by verification of the solution's convergence over a frequency range up to 250 Hz. The maximum error of the natural frequency is less than 1% compared to a finer mesh size of $7.5 \times 7.5 \text{ mm}^2$. There are 34 bending modes present in this frequency range. The total number of finite elements in the model is 10904, including 9600 for the plate bays and 1304 for the stiffeners.

There are 11117 nodes used for the FE model, each having 6 DOFs. The constraint of the fully-clamped edges eliminates 2640 DOFs. Therefore, the total number of DOFs present in the final FE model is 64062.

5.2.1.2 Stiffened cylinder

The second example structure is a thin-walled, stiffened cylinder as already used in Chapter 4. Figure 4-2 (a) shows the geometry of the stiffened cylinder. The geometry of the cross-section of the stiffeners is shown in Figure 4-2 (b). Table 4-1 lists the parameters of the geometry and

material properties of the stiffened cylinder. The two ends of the stiffened cylinder are fully clamped in the current analysis.

Compared to the first example structure, the stiffened plate, a different modelling approach was used for the stiffened cylinder. The cylinder bays were modelled with the 8-node curved shell element S8R, whilst the stiffeners were modelled with the 3-node beam element B32. This is because the stiffened cylinder has a larger size and a higher structural complexity compared to the stiffened plate.

Firstly, a higher order shell element was used to account for the high curvature of the structure while avoiding a high number of elements.

Secondly, the beam elements were used to model the deep stiffeners. Although this may not be as accurate as using shell elements it reduces the computation cost of the numerical simulations, especially the full order FE, which would otherwise be prohibitive. However, should experimental test results other than the full order FE simulation be used as the comparison, the stiffeners should be ideally modelled as shell elements as applied for the stiffened plates in Section 5.2.1.1.

The nonlinear equations of motion for the stiffened cylinder are given in Eq.(5-1) and Eq.(5-2). The source of the nonlinearity comes from the geometric nonlinear deformation, which can be characterised as θ in Eq.(5-2).

A three dimensional cylindrical coordinate system was used to model the stiffened cylinder. The linear mode shape of the cylinder is represented as $\psi_n(r = R, \phi, z)$. The size of the S8R elements are 47.4 mm in the cylinder axial direction and $\frac{\pi}{16}$ radians in the cylinder circumferential direction. The mesh size was selected by verification of the solution's convergence over a frequency range up to 650 Hz. There are 22 bending modes, within the total number of 38 modes present in this frequency range. The total number of elements required in the model is 2208, including 1632 shell elements for the cylinder bays and 576 beam elements for the stiffeners. There are 4960 nodes used for the model, each of which has 6 DOFs. The constraint of the fully clamped cylinder ends eliminates 768 DOFs. Therefore, the number of the total DOFs presented in this FE model is 28992. This value has been reduced to be less than a half of the number for the stiffened plate, despite a larger structural dimension and a higher complexity.

5.2.1.3 Excitation types and their numerical evaluation

The spatial and frequency characteristics of the excitations are briefly described in this section. Two different types of random excitation were applied to the structures. They include mechanical point force excitation and acoustic plane wave excitation.

The mechanical point force was applied on the plate/cylinder surface at positions where the stiffeners are attached. The positions of the nodes of the forcing points are shown in Figure 5-3 (a) and (b) for the two example structures as black solid circles. The red solid circles indicate the points where the responses are measured and these always correspond to the centre of the structures. These pairs of input/output positions are chosen as an example to show the applicability of the proposed method.

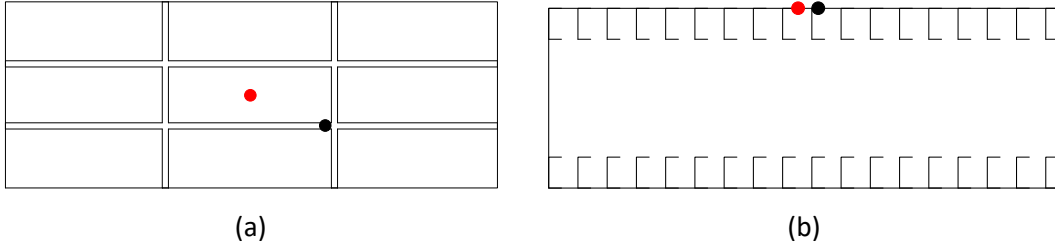


Figure 5-3 The positions of the forcing points, marked in the black solid circles, and the positions of the example response points, marked in the red solid circles, for the stiffened plate (a) and the stiffened cylinder (b).

An acoustic plane wave was applied to the plates/cylinder surfaces with a normal incident angle. For the plate, this is equivalent to a spatially uniform pressure. For the cylinder, an additional rigid scattering problem has to be solved as described in Chapter 3.

The random time history of the excitation was generated by using the method detailed in reference [169]. This method is based on the Inverse Fourier Transform (IFT).

In the numerical simulations, a band-limited white noise with a flat spectrum within the excitation bandwidth BW was specified with a given root mean square (RMS) value. The power spectral density (PSD), S_x , is therefore a constant value over the bandwidth BW and can be represented as

$$S_x = \frac{RMS^2}{2BW},$$

where BW is the excitation bandwidth.

The magnitude of the Fourier transform of the excitation, $|X|$, for a finite length of period, T , can be calculated from its relation to the PSD, i.e.

$$|X| = \sqrt{TS_x}, \quad \text{Eq.(5-20)}$$

The phase of the Fourier transform is frequency dependent and is specified as a uniformly distributed random angle $\epsilon(f)$ between 0 and 2π . So the Fourier transform of the excitation can be fully defined as

$$X(f) = |X|e^{i\epsilon(f)}$$

at the positive frequencies and

$$X(f) = |X|e^{-i\epsilon(f)}$$

at the negative frequencies.

By using the IFT, the random time history of the excitation can be calculated as

$$x(t) = \int_{-\frac{f_s}{2}}^{\frac{f_s}{2}} X(f)e^{-i2\pi ft} df,$$

where f_s is the sample rate.

For the stiffened plate, the excitation bandwidth is set to be 0 – 125 Hz and the total time length is 30 seconds. For the stiffened cylinder, the excitation bandwidth is set to be 0 – 400 Hz and the total time length is 10 seconds.

More detailed parameters such as the sample rates f_s and the RMS values of each excitation will be given for each specific example in the following sections, as they are subjected to change for comparisons.

5.2.1.4 Thermal loading and boundary condition treatment

The thermal effect on the NLROM was studied by using the stiffened plate example only. The constraint of fully clamped edges allows no motion of the plate edges despite the thermal expansion. Physically, it may no longer be a realistic representation of the boundary conditions under thermal conditions, where the boundaries of the structure could not be ideally isolated from the thermal transfer from the body of the structure. Numerically, the fully clamped edges will lead to a singularity of the stiffness matrix even for a small temperature rise and cause the structure to prematurely buckle in a non-physical simulation. However, a temperature rise of at least 100°C is sought in this study.

To resolve this issue, the simulated boundary condition is modified such that the plate edges have partially constrained in-plane DOFs and are fully constrained in all the other DOFs used. Spring elements are used to introduce the partial constraints. The values of the spring

constants are 100kN/m in the x direction and 200kN/m in the y direction (see Figure 2-2). These stiffness values were determined through a trial and error process in an empirical manner. In this process, normal modal analysis calculations for the thermally loaded plate each with a different value for the spring stiffness were performed. The final values of the stiffness were tuned and adopted so that buckling does not occur when the temperature change is 100°C.

Three different thermal conditions are then applied. They are at 0°C, 50°C and 100°C for a uniform temperature field throughout the stiffened plates by using the static analysis in Abaqus.

5.2.1.5 Response analysis

After the structural FE and the excitation were generated, the nonlinear responses were predicted by the NLROM in MATLAB and by the full FE model solver in Abaqus. The NLROM implemented in MATLAB used the IC method (see Section 5.1.1). The full order FE simulations implemented in Abaqus used the Implicit Scheme in Table 5-4.

The selected points for presenting predictions for the out-of-plane response are at the centres of all of the structures. They are shown as red solid circles in Figure 5-3. For the cylinder case, the response point is at the front of cylinder facing the normal plane wave excitation.

The PSD of the response time history was generated by using the 'Pwelch' function in MATLAB. The PSD was evaluated by averaging 8 segments, with 50% overlap. Each segment was windowed with a Hamming window. The sample rates are 10 kHz for the NLROM results and 100 kHz for the FEM results for the example structures. The PSD is displayed with the frequency resolution of 1 Hz.

5.2.2 NLROM static identification schemes

5.2.2.1 The effect of the modal basis selection

For stiffened plate, four sets of the modal basis, represented as sets A – D, were used to examine the effect of the modal basis selection on the NLROM prediction against that of the full order FE simulation for the stiffened plate. These modal sets were grouped by either using all bending modes or linearly excited bending modes within two frequency ranges – one within the excitation bandwidth (0 – 125 Hz) and the other one within twice the excitation bandwidth (0 – 250 Hz). Table 5-6 lists the total number and the order of the modes included in each set. The natural frequencies associated with these modes are listed in Table 5-7. Note

that the modes are obtained by the free vibration analysis, but the set of linearly excited modes can only be selected following a linear simulation up to 250 Hz and an analysis of the response for the different excitation types.

Table 5-6 Four different modes sets A – D for stiffened plate. A: Linearly excited flexural modes within the excitation bandwidth. B: All flexural modes within the excitation bandwidth. C: Linearly excited modes within twice the excitation bandwidth. D: All modes within twice the excitation bandwidth.

Mode set	Point force excitation		Plane wave excitation	
	Number of modes	Mode order	Number of modes	Mode order
A	4	1 – 3, 5	3	1, 3, 5
B	9	1 – 9	9	1 – 9
C	11	1 – 3, 5, 10, 17, 20, 23, 30, 33, 34	7	1, 3, 5, 17, 20, 30, 33
D	34	1 – 34	34	1 – 34

Table 5-7 The natural frequencies associated with the 34 modes in Table 5-6.

Mode order	1	2	3	4	5	6	7	8	9
Frequency (Hz)	65.9	84.6	104.3	110.3	111.3	113.3	113.5	117.5	118.9
Mode order	10	11	12	13	14	15	16	17	18
Frequency (Hz)	145.9	152.9	153.1	153.6	155.2	155.8	156.1	158.1	163.8
Mode order	19	20	21	22	23	24	25	26	27
Frequency (Hz)	166.1	172.8	174.9	177.9	181.4	195.2	196.7	196.8	197.1
Mode order	28	29	30	31	32	33	34		
Frequency (Hz)	197.5	198.9	199.7	209.3	210.2	211.9	241.9		

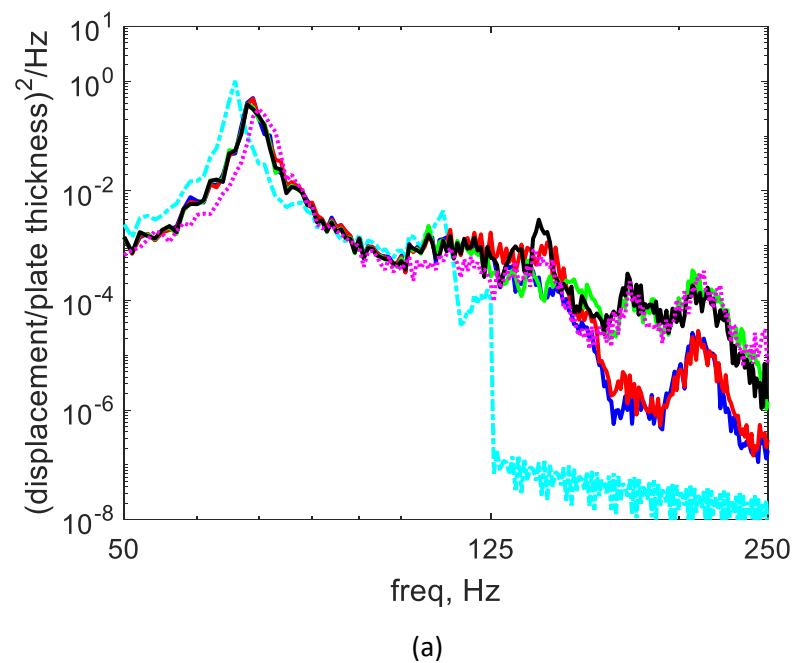
The RMS value of the point force excitation was set to be 593N and that of the plane wave excitation was set to be 146dB. The magnitude of the excitation was selected to ensure a non-linear response of the structure. To achieve this a linear frequency domain analysis was performed in the FE software and the input was tuned to obtain a maximum response at the reference response point of about 10 times the plate thickness. It is expected that a nonlinear simulation would result in a different level of the response due to the nonlinearities.

The sample rate used to generate the excitation was set to be 10kHz in the NLROM, whilst that was set to be 100kHz in the full order FE simulation. Stiffness-proportional damping

provided 1% damping ratio at 65.9Hz, which is the frequency of the first mode of the stiffened plate.

Figure 5-4 (a) and Figure 5-4 (b) show the PSD estimations of the displacement response for the stiffened plate subjected to the mechanical point force and to the acoustic plane wave excitation respectively. The excitation bandwidth was 0 – 125Hz. The frequency range of twice the excitation bandwidth was used for the frequency range presented, i.e., 0 – 250Hz. The displacement was normalised by the thickness of the plate.

Different types and colour of lines are used to represent results from different models. The NLROM predictions with four mode sets are given in solid lines with four different colours: mode set A in blue, mode set B in red, mode set C in green and mode set D in black. The linear predictions, obtained by removing all nonlinear stiffness terms in NLROM, are given in cyan dash-dotted line for the reference comparison between the linear and the nonlinear predictions. The full order FE predictions are given in magenta dotted lines as the benchmark for the comparisons of the predictions of nonlinear responses.



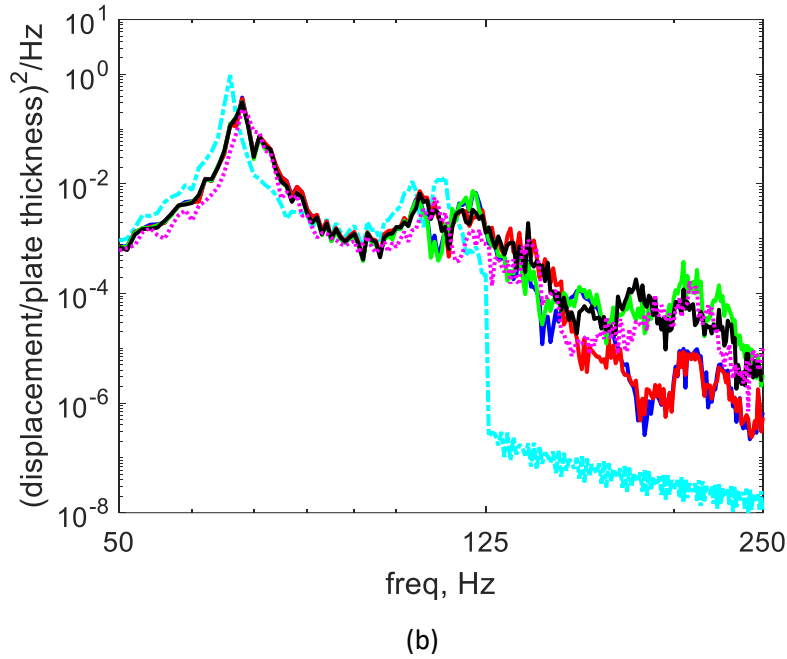


Figure 5-4 PSD estimations of the normalised displacement for the stiffened plate subjected to the mechanical point force (a) and to the acoustic normal plane wave excitation (b). Cyan dash-dotted lines: linear response predictions. Magenta dotted lines: nonlinear response predictions from the full order FE simulations. Solid lines: nonlinear response predictions from NLROM with mode set A (in blue), mode set B (in red), mode set C (in green) and mode set D (in black).

The results show two significant differences between the linear responses and the nonlinear responses, from either NLROM or FEM. The first one is that the response peaks in the nonlinear predictions are shifted and broadened. This is due to the nonlinear stiffening effect. The second one is that there is a response at frequencies outside the excitation bandwidth in the nonlinear predictions. This out-of-band response is caused by the nonlinear coupling between the low frequency and the high-frequency flexural modes as well as high frequency contributions from the geometrical nonlinear in-plane stretching of the lower order flexural modes. For the linear predictions, ideally there should be no response outside the excitation frequency range, but a very low PSD level is still present due to the finite length of the loading history and response and some numerical noise.

The behaviour and the relative differences among the NLROM predictions with different mode sets vary significantly over the frequency bands. Within the excitation bandwidth (up to 125Hz), all the NLROM predictions agree well with that from the full order FE simulations. The effects of using different mode sets here are minimal. Outside the excitation bandwidth, the agreement between the FEM and the NLROM predictions varies over different mode sets. The agreement is improved significantly from sets A and B to sets C and D, i.e. when the frequency of the modes chosen is extended from the excitation bandwidth to twice the excitation bandwidth. Meanwhile, the improvement is minor between mode sets C and D (or between

mode set A and B), i.e. between all modes being used and only linearly excited modes being used. It means that using only linearly excited modes may only sacrifice a little accuracy. However, using only linearly excited modes can significantly reduce computation cost for the NLROM. For example, the number of the nonlinear static FE tests required in the nonlinear identification can be reduced by almost one order of magnitude, in this case from 2313 to 243, if set C is used instead of mode set D.

Figure 5-5(a) and Figure 5-5(b) show the band limited RMS values of the normalised displacement for the stiffened plate subjected to the mechanical point force and to the acoustic plane wave excitations, respectively. The band limited RMS values were calculated from integrating PSD over three frequency ranges, i.e., range 1 (0 – 125Hz) the excitation bandwidth, range 2 (125 – 250Hz) and range 3 (0 – 250Hz) twice the excitation bandwidth.

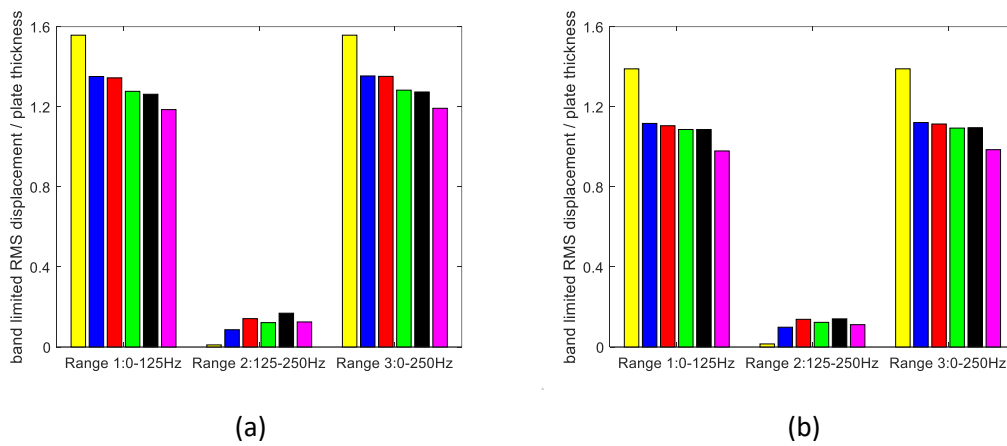


Figure 5-5 Band limited RMS of the normalised displacement of stiffened plate subjected to the mechanical point excitation (a) and to the acoustic plane wave excitation (b). ■: linear response predictions. ■: NLROM response prediction with mode set A. ■: NLROM response prediction with mode set B. ■: NLROM response prediction with mode set C. ■: NLROM response prediction with mode set D. ■: nonlinear response predictions from the full order FE. Three frequency ranges are considered for the responses, i.e. range 1 (0 – 125Hz), range 2 (125 – 250Hz) and range 3 (0 – 250Hz).

The results in ranges 1 and 3 for both types of excitation show higher values of RMS response in the linear response predictions (in yellow bars) than those in the nonlinear responses (other bars). This is because the geometric nonlinearity tends to limit the response amplitude. A small RMS value is present in range 2 for the linear response predictions due to the finite length of the loading time history and response and some numerical noise.

The RMS values for the NLROM predictions with the mode sets C/D are closer in agreement to those for the FE predictions compared to the results with the mode sets A/B. It means that the NLROM predictions are improved when the frequency range within which the modes are covered is doubled, although they are still too high compared to the FE predictions. This indicates that using an insufficient number of modes in the nonlinear static identification of

NLROM underestimates the nonlinear stiffening effect present in the model, compared to the FE predictions. The differences in the RMS values between mode set A and B or between mode set C and D are very small for point force excitation in Figure 5-5 (a) and can be hardly discriminated for the plane wave excitation in Figure 5-5 (b). This is consistent with the behaviour in the PSD results in Figure 5-4, i.e., using the linearly excited modes can achieve a nonlinear identification with relatively high accuracy. The drawback of this modal basis selection is that it is loading specific, whilst using all the flexural modes is not restricted to the loading types.

An equivalent procedure has been adopted for the stiffened cylinder, but it has been found that it was not possible to excite the stiffened cylinder in a nonlinear regime before buckling occurs. However, the results for the case of the cylinder will be discussed again later in Section 5.2.4 to illustrate the features of deep stiffeners and high curvature.

5.2.2.2 The effect of static loading types

Figure 5-6 (a) and Figure 5-6 (b) show the PSD estimations of the normalised nonlinear displacement for the stiffened plate subjected to the mechanical point force and to the acoustic plane wave excitation. These results are all NLROM predictions using mode set C in Table 5-6, i.e. linearly excited modes within twice of the excitation bandwidth. The results from the NLROM with nonlinear static identification using the dead loads are in black solid lines and that using the follower loads are in red dashed lines.

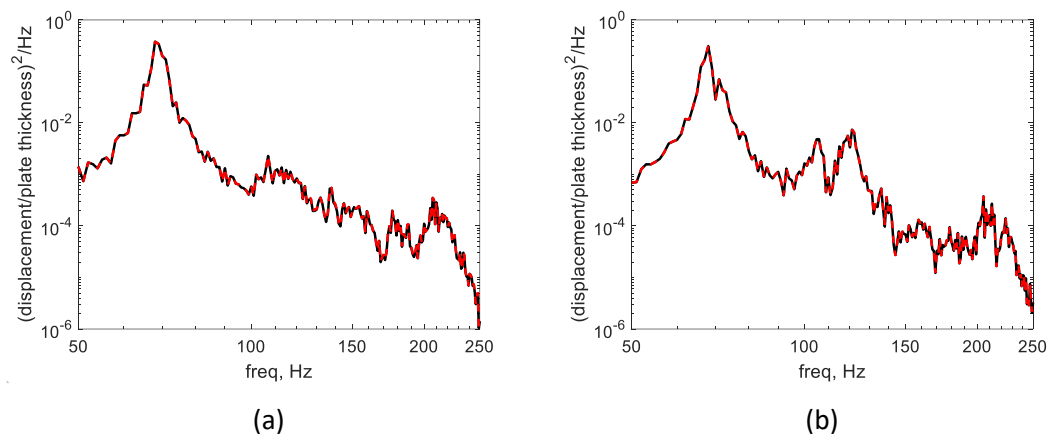


Figure 5-6 PSD estimations of the nonlinear response for stiffened plate subjected to the point force excitation (a) and to the acoustic plane wave excitation (b). The NLROM results with the nonlinear static identification using the dead loads is in black solid lines and that using the follower loads are in red dashed lines.

The results show that the two predictions are almost identical over the entire frequency range. The effect of the type of static loading on the nonlinear static identification is negligible for the stiffened plate. Although the deformation of the plate is large enough for the onset of the

geometric nonlinearity, it is still yet to form a significant curvature in the structure and therefore there is no noticeable difference between using the dead loads and using the follower loads.

5.2.2.3 The effect of the scaling factors

This section studies the effect of using different values of the scaling factors as introduced in Section 5.1.3, i.e. a_m and a_n in Eq.(5-7) for the static loadings used for the nonlinear static identification. The static loadings were applied in the form of uniform pressure over each element, which is a simple approximation that can be relatively convenient to be implemented in Abaqus provided the mesh is fine enough.

The scaling factors were calculated by the ‘desired displacement’ method using Eq.(5-12). A desired displacement of 10 times of the plate thickness (h) was used as a reference at the point chosen as the example response position in Figure 5-3 (a). Three other values of the scaling factors were set which resulted in a desired displacement of 5, 20 and 40 times the plate thickness and were used in the nonlinear static identification, spanning the range of a ‘small’ desired displacement ($5h$) to a large desired displacement ($40h$).

Figure 5-7 (a) and Figure 5-7 (b) show the PSD estimations of the normalised nonlinear displacement for the stiffened plate subjected to the mechanical point force and to the acoustic plane wave excitation. The frequency range of the excitation was again 0-125 Hz. These results are all NLROM predictions using mode set C in Table 5-6, i.e. linearly excited modes within twice of the excitation bandwidth. The dead loads were used in the nonlinear static identification. The NLROM results using the scaling factors corresponding to the desired reference displacement of $5h$, $20h$ and $40h$ are in blue, green and black solid lines. The full order FE results are in red dotted lines. An attempt was made for a required displacement of $100h$ but the model failed to converge statically.

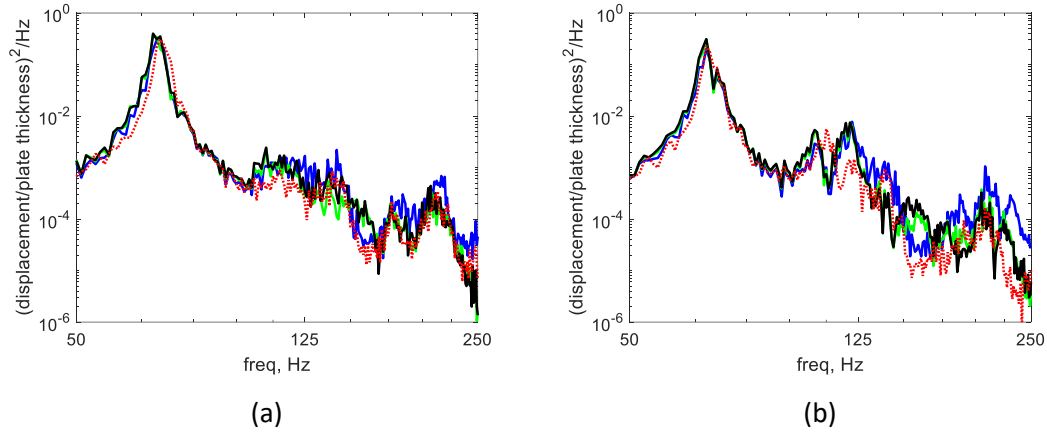


Figure 5-7 PSD estimations of the normalised nonlinear displacement for the stiffened plate subjected to the point force (a) and to the acoustic plane wave (b) excitations. The NLROM results using the scaling factors corresponding the desired reference displacement of $5h$ are in the blue solid lines, $20h$ are in the green solid lines and $40h$ are in the black solid lines. The full order FE results are in red dotted lines.

The results in the figure show that all of the solid lines agree well with the red dotted lines within the excitation bandwidth. This indicates that the effect of using different scaling factors, as long as they lead to a converged static solution, is small within the excitation bandwidth.

Outside the excitation bandwidth, the results corresponding to the small required reference displacement of $5h$ overestimate the nonlinear response as the frequency increases. This is because a small required reference displacement will overestimate the nonlinearity. No significant difference is visible between the results based upon $20h$ and $40h$. They both have improved agreement with the FE results.

In summary, it means that the accuracy of the nonlinear static identification may not be affected by increasing the value of the required displacement from the reference value ($10h$ in this example), provided that it is not too large so that the nonlinear static and dynamic analysis do not converge. It is to be noted that the nonlinear coefficients from the static characterisation need to be recalculated when the reference value is increased due to the increased level of the excitation.

5.2.2.4 The effect of thermal loading

Figure 5-8 shows the natural frequencies and mode shapes of the cold modes of the stiffened plate (i.e. without any temperature loading). As part of the NLROM procedure, in this case these have been calculated in the FE software Abaqus with the model setup explained in Sections 5.2.1.1 and 5.2.1.4. The natural frequencies and mode shapes of two sets of hot modes, corresponding to a temperature rise of 50°C and 100°C , are shown in Figure 5-9 and Figure 5-10. As an example, only the lowest nine modes are shown for all cases.

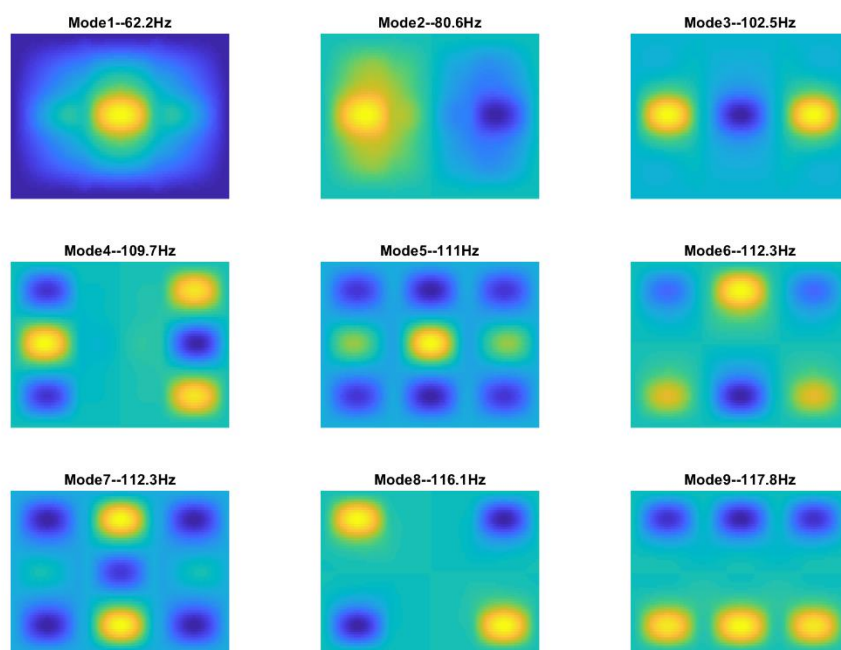


Figure 5-8 The natural frequencies and mode shapes of the lowest 9 cold modes.

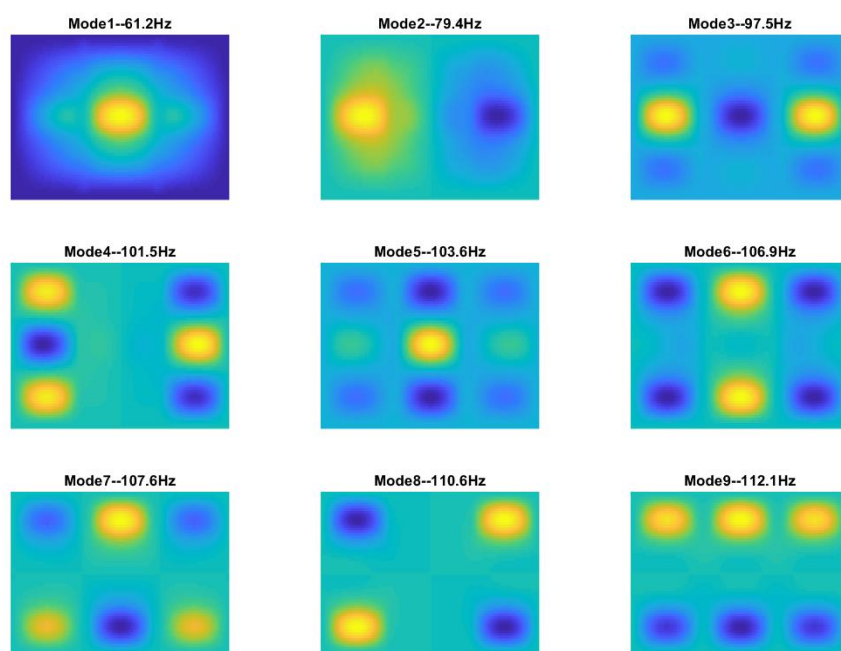


Figure 5-9 The natural frequencies and mode shapes of the lowest 9 hot modes with a temperature rise of 50°C.

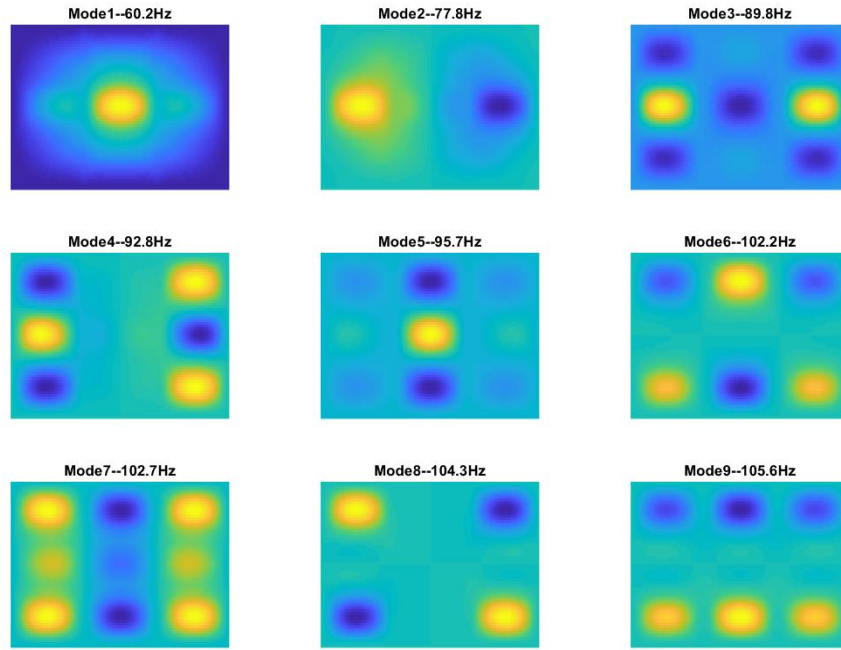


Figure 5-10 The natural frequencies and the mode shape of the lowest 9 hot modes with a temperature rise of 100°C.

The results from Figure 5-8 to Figure 5-10 show that the main effect of thermal loading is to reduce the natural frequencies of the modes. In addition, some neighbouring modes can appear in a different order. For example, the 6th mode and the 7th mode in Figure 5-8 swap when a temperature rise of 50°C is applied (Figure 5-9). Then they swap again in Figure 5-10 when a temperature rise of 100°C is present. In the case of normal plane wave excitation, the 1st, 3rd, 5th, 7th and 9th modes are expected to be excited at both 0°C and 100°C. The 1st, 3rd, 5th, 6th and 9th modes are expected to be excited at 50°C.

Figure 5-11 (a) and Figure 5-11 (b) show the PSD estimations of the normalised nonlinear displacement for the stiffened plate subjected to the normal plane wave excitation with a temperature rise of 50°C and of 100°C. Mode set D in Table 5-6, i.e. the first 34 lowest modes, was used in both of cold-mode NLROM predictions, which are in the black solid lines, and hot-mode NLROM predictions, which are shown by the red solid lines. The full order FE predictions are used for comparison and are shown by the blue dotted lines.

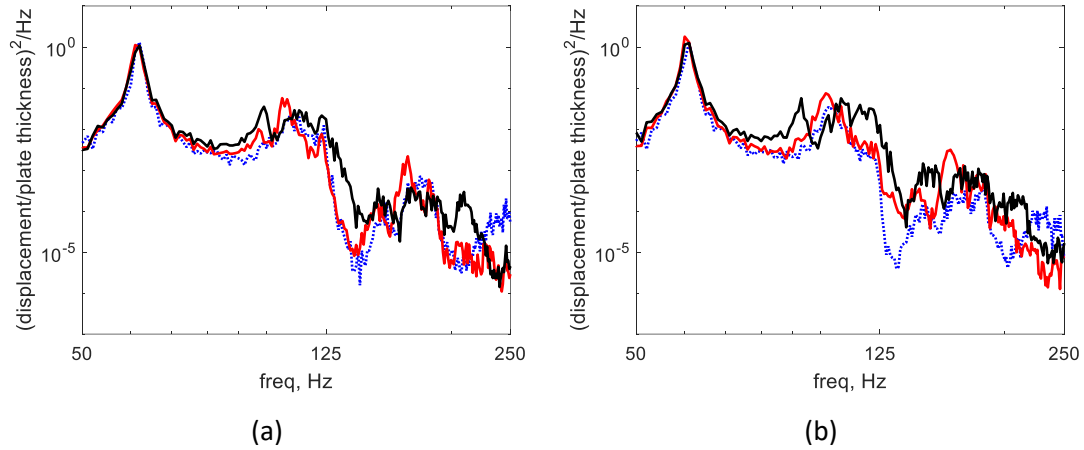


Figure 5-11 PSD estimations of the normalised nonlinear displacement for the stiffened plate subjected to the normal plane wave excitation with a temperature rise of 50°C (a) and 100°C (b). The cold-mode NLROM predictions are in the black solid lines and the hot-mode NLROM predictions are in the red solid lines. The full order FE predictions are in the blue dotted lines.

The results for both temperature conditions show that the hot-mode NLROM predictions agree better with the FEM predictions than the cold-mode NLROM predictions. For example, the resonance peaks between 95 – 125 Hz tend to merge together from 50°C to 100°C in the FEM predictions. This behaviour is well replicated by the hot-mode NLROM predictions. The good accuracy of the hot-mode NLROM is preserved outside the excitation bandwidth up to 210Hz, about 1.7 times the excitation bandwidth for the temperature rise of 50°C. The accuracy at this frequency is reduced when the temperature rise is increased to 100°C. The source of the increased error could not be determined.

The prediction capacities of the cold-mode and hot-mode NLROM also need to be examined. This capacity is compared in terms of the solution convergence. To provide the data for comparison, an additional three higher levels of excitation, 149dB, 152dB and 158dB, were used.

Table 5-8 shows the comparison of the convergence between the hot-mode and the cold-mode NLROM predictions for two different temperatures and for four different excitation levels.

Table 5-8 The convergence for the hot-mode and the cold-mode NLROM with different temperatures and different excitation levels. The tick symbol '✓' means that a converged NLROM solution was guaranteed. The cross symbol '✗' means that the NLROM solution cannot converge for the time integration dynamic solution. The symbol 'N/A' means that the nonlinear static tests cannot converge.

			SPL (dB)			
			146	149	152	158
T (°C)	0		✓	✓	✓	✗
	50	hot-	✓	✓	✓	N/A
		cold-	✓	✓	✗	✗
	100	hot-	✓	✗	✗	N/A
		cold-	✓	✓	✗	✗

None of the NLROM predictions could converge at the highest level of excitation 158dB. For the thermally loaded plates, the convergence issues are in the nonlinear static solutions for the hot-mode NLROM (represented with the symbol of 'N/A') and in the numerical integration for the cold-mode NLROM (represented with the symbol of cross '✗'). The latter cannot be resolved by using a higher sample rate. A separate test showed that the NLROM can converge for an excitation level up to 164dB if the plates' edges are fully clamped, so the treatment or choice of the boundary conditions may also affect the convergence of the NLROM.

The convergence is also dependent on the temperature rises and is different between the cold-mode and hot-mode NLROM. At a rise of 50°C, the hot-mode NLROM can converge at the excitation level up to 152dB and the cold-mode NLROM can only converge up to 149dB. When the temperature rises by 100°C, the hot-mode NLROM can only converge at 146dB, but the cold-mode NLROM can still converge up to 149dB. This observation might indicate that the cold-mode NLROM can converge more easily at a higher temperature, although it generally results in poorer accuracy as shown in Figure 5-11.

5.2.3 The selection of damping and sample rate

This section intends to assess the selections of the damping ratio and sample rate that can balance the accuracy against efficiency of the FE solution. The key issue is the aliasing that is caused by the high frequency response. A most straightforward way to avoid the aliasing would be to apply an anti-aliasing filter prior to sampling, but this is not available in the Abaqus/Implicit solver. Thus, a very high sample rate might be required to avoid the distortion due to the sampling, which in the meantime causes high computational cost. The frequency

dependency of the Rayleigh damping presented in Section 5.1.6 offers the possibility of dealing with the high frequency response.

The nature of this problem is shown in Section 5.2.3.1 by the example of an unstiffened plate and in Section 5.2.3.2 by the example of the stiffened plate, respectively. A trade-off must be made in the selection of the level of stiffness-proportional damping and the value of sample rate when producing the comparison of NLROM and FEM results. This is shown in Section 5.2.3.3.

5.2.3.1 Case of an unstiffened plate

The effects of using two types of viscous damping models, i.e. the mass-proportional and the stiffness-proportional Rayleigh damping, are examined in this section. An unstiffened plate was initially used in the numerical example for simplicity. The structural parameters and the positions of the measurement and excitation for the unstiffened plate are the same as those of the stiffened plate, except all the stiffeners were removed.

For this study the RMS value of the point force excitation was set to be 1.38N and that of the plane wave excitation was set to be 106dB. It was verified that this was enough to cause a nonlinear behaviour of the structure, which in the absence of stiffeners has become very flexible. The excitation bandwidth was set to be 0 – 50Hz and the time span was set to be 50 seconds. The frequency resolution of the PSD was 0.2Hz. A 50% overlap and Hamming window were used for the segment averaging. The first 10 seconds of the total response time history for the unstiffened plate were removed to achieve the steady state of the response data. All 22 modes up to the frequency of 100Hz were used in the nonlinear static identification. The sample rate used in generating the excitation was set to be 5kHz in the NLROM, whilst that used in the full order FE simulations was set to be 10kHz. The viscous damping, set either by the mass-proportional or stiffness-proportional terms, corresponded to 0.5% damping ratio at 14.4Hz. This is in line with the value set in Chapter 2 and typical of aircraft panels. The damping term α for the mass-proportional damping and β for the stiffness-proportional damping were calculated from Eq.(5-19) separately by setting the other damping term to zero.

Figure 5-12 shows the values of the viscous damping ratio for the 22 lowest modes within the frequency range 0 – 100Hz. The results for the stiffness-proportional damping model are shown by the blue bars. The results for the mass-proportional damping model are shown by the red bars.

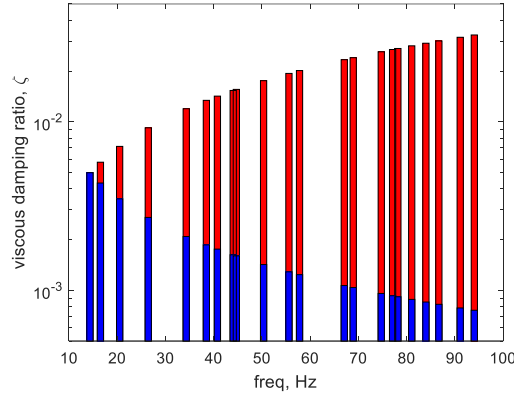


Figure 5-12 The frequency dependency of the viscous damping ratio for the first 22 modes within the frequency range 0 – 100Hz. ■: stiffness-proportional damping; ■: mass-proportional damping.

The result shows that as the frequency increases, the value of the mass-proportional damping decreases whilst it increases for the stiffness-proportional damping (see Eq.(5-19)).

Figure 5-13 (a) and Figure 5-13 (b) show the PSD estimations of the normalised displacement for the unstiffened plate with the two damping models and subjected to the point force excitation. Figure 5-13 (a) is for the mass-proportional damping and (b) is for the stiffness-proportional damping.

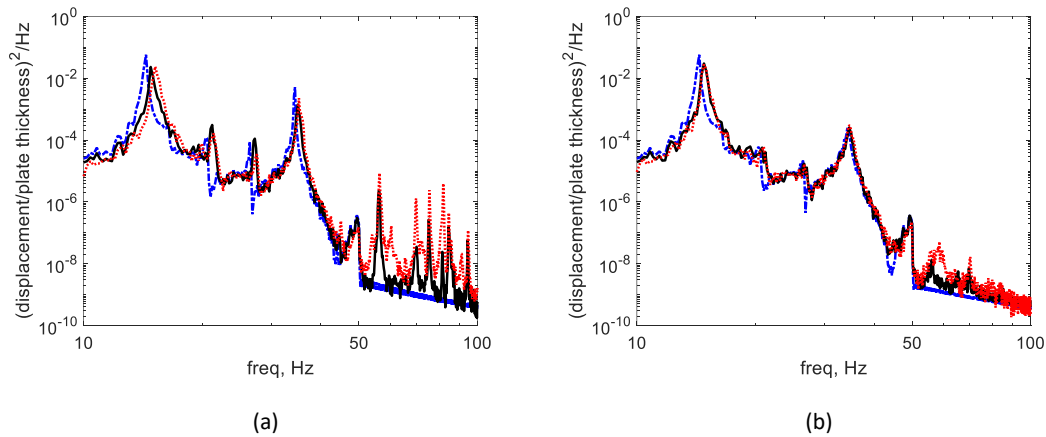


Figure 5-13 PSD estimations of the normalised displacement for the unstiffened plates with different damping models and subjected to different excitations. (a) Mass-proportional damping. (b) Stiffness-proportional damping. The linear response predictions are in the blue dash-dotted lines. The NLROM response predictions are in the black solid lines. The full order FE predictions are in the red dotted lines.

The main difference between using either the mass- or stiffness-proportional damping is in the level of response of modes outside the frequency range of excitation. As the damping decreases with frequency, a mass only term results in higher peaks for the high frequency modes. As a result, the FE predictions in Figure 5-13 (a) show some discrepancies with the NLROM model at the first resonance and differences are also present for frequencies above 50 Hz. It is possible that this is due aliasing effects caused by all the high frequency modes that

are excited because of the nonlinearities and have low damping. When the stiffness-proportional damping model is used, as shown in Figure 5-13 (b), the high frequency modes experience more damping as indicated in Figure 5-12, and the agreement at the first resonance improves. Alternatively, the aliasing effects can be alleviated by increasing the sample rate. Figure 5-14 shows the results when the sample rate for the full order FE prediction is increased from 10kHz to 25kHz.

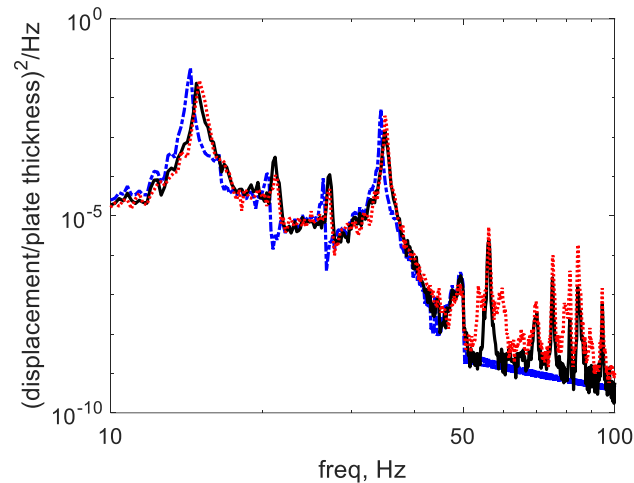


Figure 5-14 PSD estimations of the normalised displacement for the unstiffened plates with the mass-proportional damping model. The sample rate for the full order FE prediction has been increased from 10kHz to 25kHz. The linear response predictions are in the blue dash-dotted lines. The NLROM response predictions are in the black solid lines. The full order FE predictions are in the red dotted lines.

The result shows that the full order FE prediction agrees with the NLROM prediction better at the first resonance compared to Figure 5-13 (a). There are still differences for the frequency range outside the excitation range, but the agreement has improved here too. This means that if a higher sample rate is used, the accuracy of the FE predictions can be further improved. This will be also explored in the stiffened plate example in the next section.

Figure 5-15 (a) and (b) show the PSD estimations of the normalised displacement for the unstiffened plate with the two damping models and subjected to the plane wave excitation. Figure 5-13 (a) is for the mass-proportional damping and (b) is for the stiffness-proportional damping.

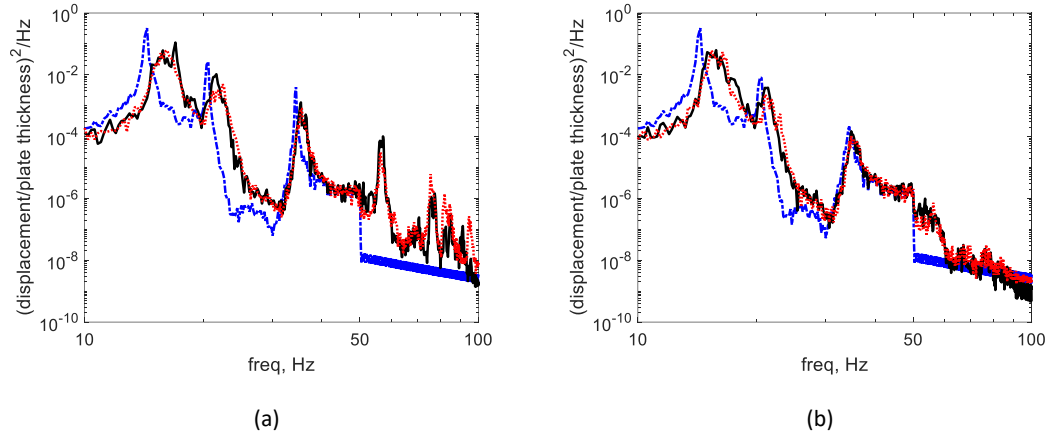


Figure 5-15 PSD estimations of the normalised displacement for the unstiffened plates with different damping models and subjected to the plane wave excitation. (a) Mass-proportional damping. (b) Stiffness-proportional damping. The linear response predictions are in the blue dash-dotted lines. The NLROM response predictions are in the black solid lines. The full order FE predictions are in the red dotted lines.

A better agreement between the NLROM and FEM is also shown in the plane wave excitation results in Figure 5-15 (a) and (b) compared to the point excitation results in Figure 5-13 (a) and (b), despite the fact that more nonlinearity is exhibited in the plane wave excitation case (shifting and broadening of the resonance peaks). The improved agreement is more apparent in the frequency above the excitation bandwidth than within the excitation bandwidth. This may be because fewer modes can be excited by the plane wave excitation.

5.2.3.2 The stiffened plate case

Three different sample rates, 100kHz, 50kHz and 10kHz, were used for comparison in the stiffened plate example. The NLROM predictions with the lowest sample rate of 10kHz were used as the reference for comparison, as they will not be affected when the sample rate increases. Mode set D, i.e., all flexural modes within twice the excitation bandwidth, were used in the nonlinear static identification.

The damping ratio of the stiffness-proportional damping was set to be 1% at the first natural frequency of 65.9Hz. This higher level of damping was considered for the stiffened plate compared to that of the unstiffened plate, as the structural damping might be increased by the stiffeners and their joints with the plate.

Figure 5-16 (a) and Figure 5-16 (b) show the PSD estimations of the normalised displacement for the stiffened plates subjected to the point force and the plane wave excitations. The FEM predictions with the sample rates of 10kHz, 50kHz and 100kHz are shown by the green, blue and red dotted lines respectively. The NLROM predictions with the sample rate of 10kHz are in the black solid lines.

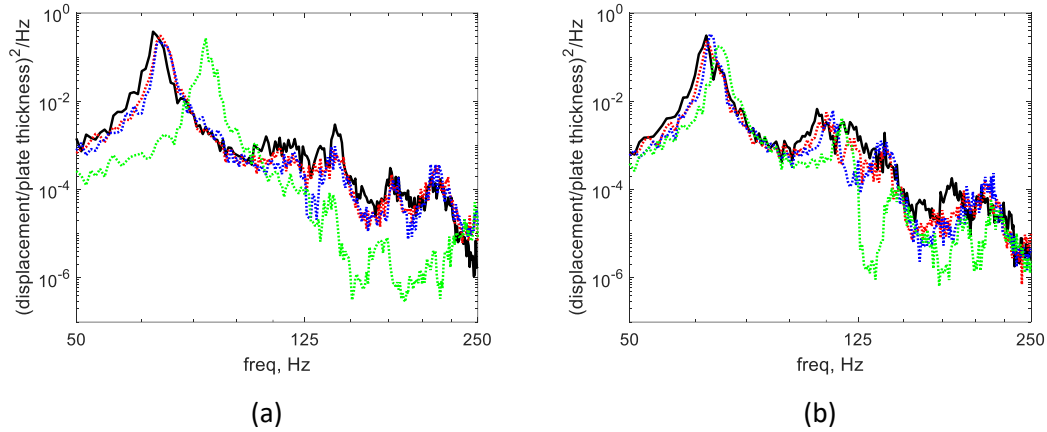


Figure 5-16 PSD estimations of the stiffened plate subjected to the point force excitation (a) and to the plane wave excitation (b). The NLROM predictions are in black lines (sample rate 10 kHz). The FEM predictions with the sample rates of 100kHz, 50kHz and 10kHz are in the red dotted lines, the blue dotted lines and the green dotted lines.

The FEM predictions with the highest sample rate of 100kHz best match with the NLROM predictions for both plane wave and point force excitations. As the sample rate is halved to 50kHz, the response peaks in the FEM results are slightly shifted to higher frequencies due to the aliasing. This effect becomes more significant when the lowest sample rate of 10kHz is used. It indicates that the FEM results demand a much higher sample rate to obtain an accurate prediction compared to the NLROM. This is because the FEM solutions contain high frequency contributions from the nonlinear coupling that are aliased in the time domain predictions.

5.2.3.3 Comparisons on the effects of higher sample rate and level of damping

The results in the last two sections show that the aliasing issue of the FEM predictions can be alleviated by either using a higher sample rate or a higher level of damping, i.e. using the stiffness-proportional damping. The extent of the improvement by using the two methods are further compared in the example of the stiffened plate subjected to the plane wave excitation. The FEM predictions with the sample rate of 50kHz and the stiffness-proportional damping ratio of 1% was used as a reference. The comparisons were made by doubling only the sample rate and by doubling only the damping level.

Figure 5-17 (a) – (c) show the PSD estimations of the normalised displacement for the stiffened plate subjected to the plane wave excitation. The FEM predictions in the red dotted lines were calculated with three sets of configurations, i.e., low sample rate (50kHz) and low damping (1%) in Figure 5-17 (a), high sample rate (100kHz) and low damping (1%) in Figure 5-17 (b), and low sample rate (50kHz) and high damping (2%) in Figure 5-17 (c). The NLROM predictions with sample rate of 10kHz and with mode set D were also given in the black solid lines.

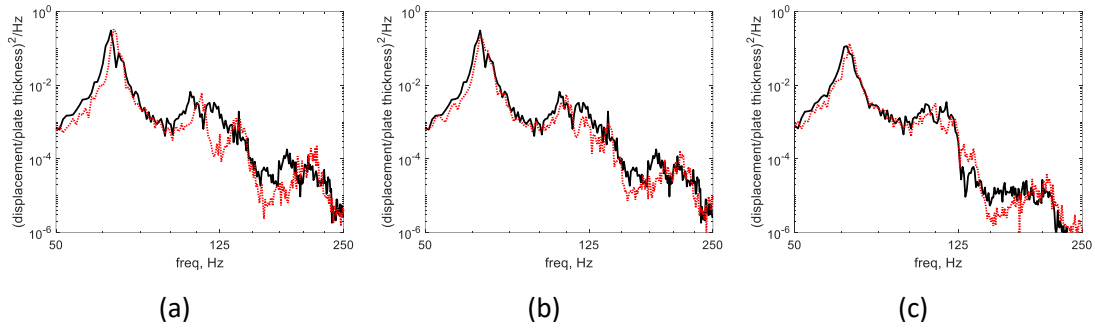


Figure 5-17 PSD estimations of the normalised displacement for the stiffened plate subjected to the plane wave excitation. Three combinations of sample rate and stiffness-proportional damping level are used: (a) Low sample rate (50kHz) and low damping (1%). (b) High sample rate (100kHz) and low damping (1%). (c) Low sample rate (50kHz) and high damping (2%). The NLROM predictions are in black solid lines. The FEM predictions are in red dotted lines.

In comparison with Figure 5-17 (a), the agreement between the NLROM and the FEM predictions were improved by doubling the sample rate in Figure 5-17 (b). This is because the increasing sample rate extends the frequency range to reduce the aliasing effect. However, the solution time of 300 hours for the FE results in Figure 5-17 (a), which is already much larger than that of the NLROM (less than one hour), is doubled to 600 hours in Figure 5-17 (b). The required memory for the data storage is also increased from 24GB to 48GB. So the consequence of using a very high sample rate is a significantly increased computational cost.

In comparison with Figure 5-17 (a), the agreement between the NLROM and the FEM predictions were also improved by doubling the level of the stiffness-proportional damping in Figure 5-17 (c). The higher level of damping alleviates the aliasing effect by further suppressing the high frequency response, which can be seen in the frequency range between 125 – 250Hz. However, the response peaks in Figure 5-17 (c) are broadened because of the increased level of damping; this may make the presence of the nonlinear behaviour on the resonance less detectable.

5.2.4 A comparison between the unstiffened plate, stiffened plate and a stiffened cylinder

In the previous Sections 5.2.2 and 5.2.3, the NLROM results have been compared with the full FE results and the different parameters and their effects relating to the comparison have been explored. Provided that an appropriate static identification process and a suitable selection of damping and sample rate has been achieved, the NLROM prediction can achieve a good agreement with the full FE prediction.

In this section, a comparison is made between the unstiffened plate, the stiffened plate and the stiffened cylinder by using the NLROM prediction. This is to explore the differences as well

as the common features of the nonlinear responses of structures in the presence of deep stiffeners and high curvatures. In addition, the capability of the NLROM is also verified in the case of practical structures such as the stiffened cylinder.

Two different levels of broadband random excitation are considered for each structure. They are all subjected to a mechanical point force and a normal plane wave excitation at two different levels.

Table 5-9 lists the parameters associated with the excitations and analyses of the NLROM predictions. For both excitation types two levels have been selected, 'low' and 'high'. The selection of these excitations was initially intended to give an equivalent nonlinear response of the different structures. However, it was soon discovered that the criterion for this selection (such as defined by the amount of shifting in the first natural frequency due to the nonlinearity) may not easily be obtained for the three different structures. In fact, the presence of the deep stiffeners and high curvature significantly change the structural dynamic behaviour. For example, for the stiffened cylinder it might not be possible to excite the structure to have any observable shifting of the first natural frequency before buckling happens. This shall be seen more fully later from the comparison of the nonlinear response results.

Therefore, an absolute target of defining the 'low' and 'high' excitations is not sought in this case due to the varying features of the nonlinear response for each structure. Instead, these selected excitations aim at exciting the nonlinearity of each structure to some extent. Figure 5-18 (a) and Figure 5-18 (b) show the maximum amplitude of the response to a random input for the three structures and for the two excitation levels selected. This was obtained by performing a linear FE analysis. Typically a displacement-to-thickness ratio around or above unity is expected to give a nonlinear response. It will be seen below that for stiffened and curved structures this is not the case.

Table 5-9 The parameters of the excitations and the PSD estimations in the NLROM predictions.

		Unstiffened plate		Stiffened plate		Stiffened cylinder	
		low	high	low	high	low	high
RMS	Point force (N)	0.62	1.38	342	593	1000	2000
	Plane wave (dB)	99	106	141	146	148	154
Excitation band (Hz)		0 – 50		0 – 125		0 – 400	
Outside of excitation band (Hz)		50 – 100		125 – 250		400 – 1000	
Time record length (sec)		50		30		10	
Removed time period (sec)		0 – 10		0 – 10		0 – 3	
Sample rate (kHz)		5		100		10	
PSD resolution (Hz)		0.2		1		1	
Modal basis		First 22 flexural modes		First 34 flexural modes		First 10 linearly excited modes	

Figure 5-18 (a) and Figure 5-18 (b) show the maximum linear normalised displacement for the example structures subjected to the two different levels of excitations listed in Table 5-9. The results show a significant difference in the maximum displacement for the three structures subjected to the low level and the high level of excitations.

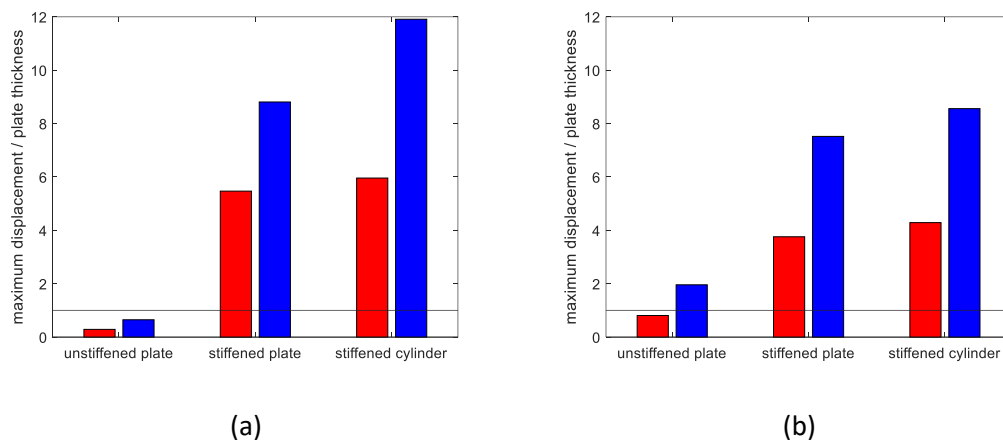


Figure 5-18 The linear predictions of the maximum normalised displacement of the three structures to the point excitation (a) and the plane wave excitation (b). The red bars represent the predictions for the low excitation levels in Table 5-9. The blue bars represent the predictions for the high excitation levels in Table 5-9. The horizontal lines correspond to the value of 1.

Figure 5-19 (a) – Figure 5-19 (f) show the PSD estimations from the NLROM for the unstiffened plate, the stiffened plate and the stiffened cylinder. The results for the point force excitations are given in Figure 5-19 (a) - Figure 5-19 (c) and those for the plane wave excitation are given in Figure 5-19 (d) - Figure 5-19 (f). All the nonlinear predictions are represented by solid lines, in comparison to the linear predictions shown by the dash-dotted lines. The results for the

low level of the excitations are given by blue lines. The results for the high level of the excitations are given by the black lines.

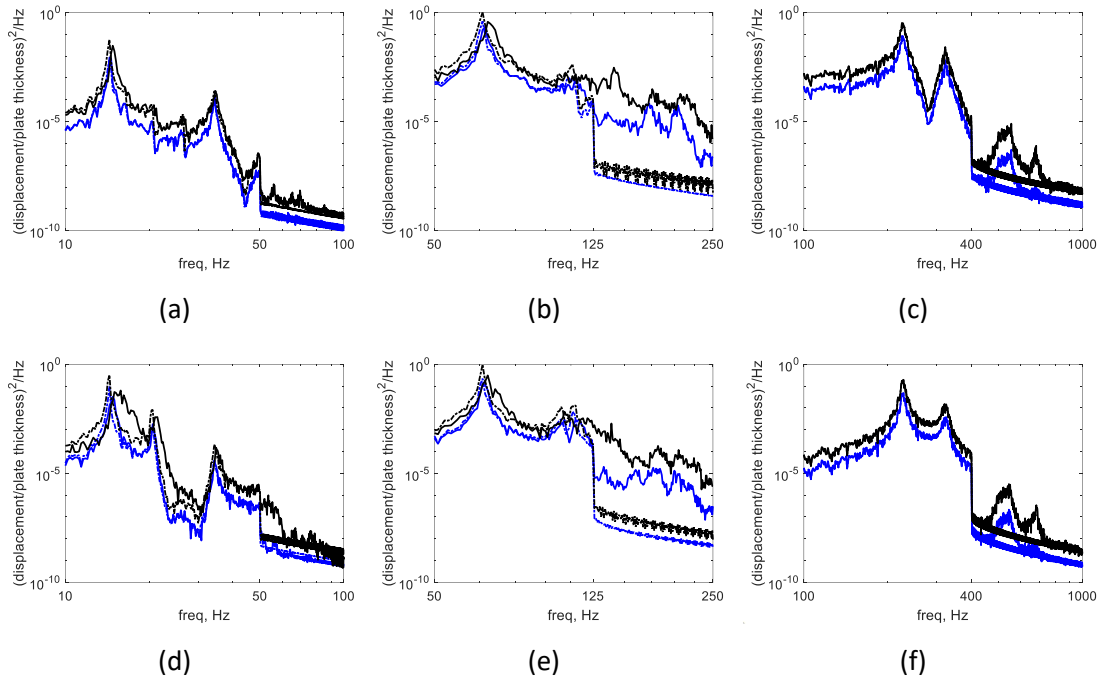


Figure 5-19 PSD estimations from the NLROM for the three different structures subjected to the point force and plane wave excitations: (a) the unstiffened plate subjected to the point force excitation; (b) the stiffened plate subjected to the point force excitation; (c) the stiffened cylinder subjected to the point force excitation; (d) the unstiffened plate subjected to the plane wave excitation; (e) the stiffened plate subjected to the plane wave excitation; (f) the stiffened cylinder subjected to the plane wave excitation. — · — : the linear response prediction to low level of excitation. — : the nonlinear response prediction to low level of excitation. — · — : the linear response prediction to high level of excitation. — : the nonlinear response prediction to high level of excitation.

For the unstiffened plate, the results in Figure 5-18, Figure 5-19 (a) and Figure 5-19 (d) show that when the maximum linear displacement response is much smaller than one plate thickness (the first red bar in Figure 5-18 (a)), no nonlinear behaviour is observed (the blue lines in Figure 5-19 (a)). The unstiffened plate exhibits some nonlinear behaviour only when the maximum linear displacement response is close to or greater than one plate thickness (the first blue bar in Figure 5-18 (a) and the first two bars in Figure 5-18 (b)). This confirms that a displacement of one plate thickness is large enough to exceed the limits for the linear plate response assumption for the unstiffened plate.

Figure 5-19 (b), Figure 5-19 (e) and Figure 5-18 show that for the stiffened plate the threshold of one plate thickness increases to be around six plate thicknesses to exhibit significant nonlinear behaviour. This is because the deep stiffeners with the stiffener height to plate thicknesses ratio of 15, which dominate the response of the stiffened plate at lower frequencies, still essentially behave in a linear fashion.

For the stiffened cylinder, Figure 5-19 (d) and Figure 5-19 (f) show that no significant nonlinear behaviour occurs for the range of excitation considered, even when the maximum linear response exceeds 12 times the cylindrical shell thickness. This is because of a higher stiffener height ratio of 68 compared with the stiffened plate, together with the high curvature which also stiffens the structure and allows the linear coupling between the in-plane and out-of-plane motion. For this stiffened cylinder, a significant deviation between the nonlinear and the linear predictions would only appear when the maximum linear displacement exceeds 84 times that of the cylindrical shell thickness. This has been tested by performing a full FE simulation with increasing levels of excitation. A noticeable shift in the first natural frequency occurred when the maximum linear displacement was above 84 times the thickness and corresponded to plane wave excitation of 174dB, as shown in Figure 5-20. However, the NLROM prediction could not be completed for such excitation levels, because the static solutions in the nonlinear static identification failed to converge due to buckling.

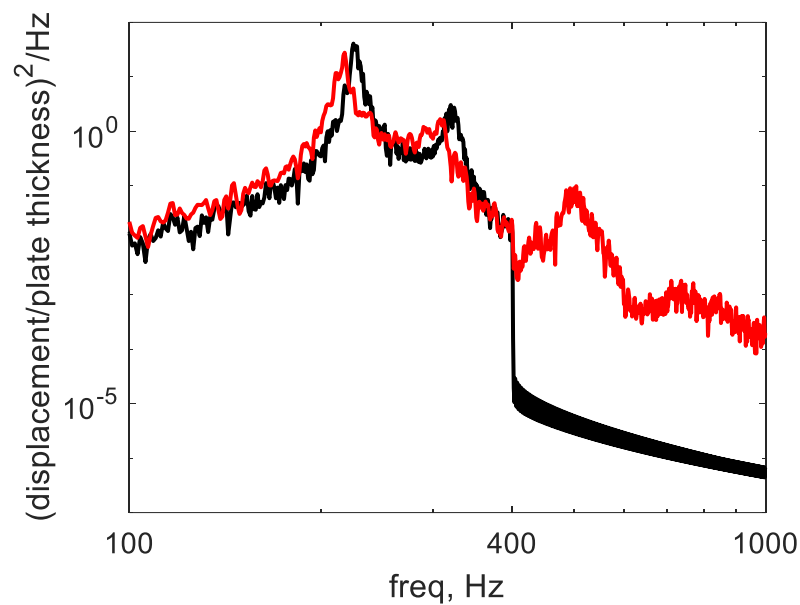


Figure 5-20 PSD estimations from the full order FE for the stiffened cylinder subjected to the normal plane wave of 174 dB. The black solid line is the linear prediction and the red solid line is the nonlinear prediction.

The results also show that response peaks can be observed outside the excitation bandwidth for all conditions except at the lowest excitation level for the unstiffened plate (the blue lines in Figure 5-19 (a) and Figure 5-19 (d)). The response of the unstiffened plate is still within range of the linear assumption.

Figure 5-21 (a) and Figure 5-21 (b) show the mean square value of the nonlinear component of the total response for the three structures which occurs at frequencies outside the

excitation bands listed in Table 5-9. The same quantities for the linear component of the response were also calculated and have been subtracted from the total nonlinear mean square values, so that the mean square values shown in the results are solely due to the nonlinearity. The mean square displacement was nondimensionalised with respect to the square of the thickness of the structure and is displayed in dB with a reference value of 10^{-10} m^2 . This reference value was chosen to obtain the positive decibel values for all cases. The quantity shown is a measure of the level of the response outside the excitation bandwidth.

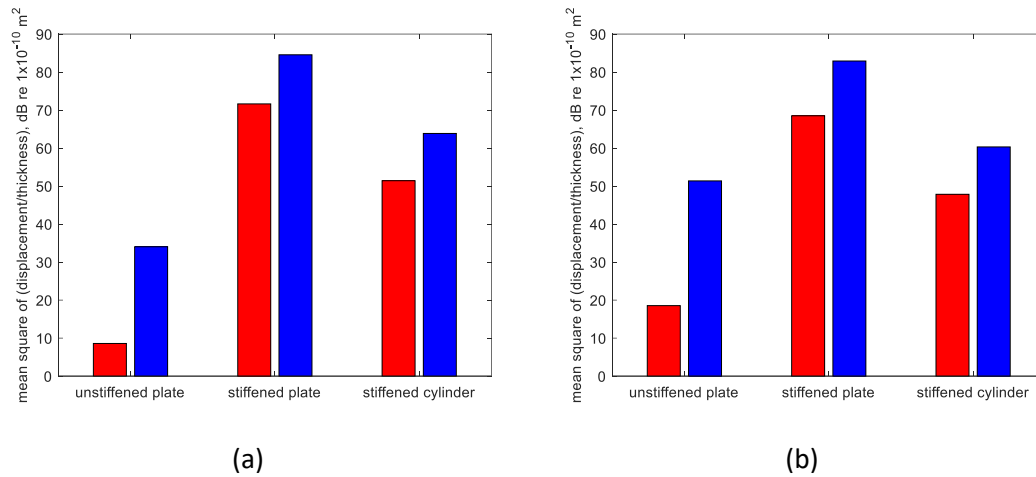


Figure 5-21 The band limited mean square value of the nonlinear displacement for the three structures subjected to the point excitation (a) and to the plane wave excitation (b) outside the excitation. ■: the results for the low excitation levels in Table 5-9. ■: the results for the high excitation levels,.

Figure 5-21 (a) and Figure 5-21 (b) confirm that the responses contain energy outside the excitation bandwidth for all conditions except for the lowest excitation level of the unstiffened plate, corresponding to the blue lines in Figure 5-19 (a) and Figure 5-19 (d) where the plate response is well below one plate thickness. As the processing of the results guarantee that there should be no response outside the excitation bandwidth for a linear behaviour or the spectral leakage, these high frequency response components then correspond solely to the structural nonlinearity.

5.2.5 The effects of elevated temperatures on the nonlinear stiffness contribution

The thermal effects on the nonlinear stiffness matrix are complex and difficult to quantify explicitly. However, as indicated in Eq.(5-16), the temperature dependence is restricted to being in the nonlinear stiffness function θ' in the hot-mode NLROM. These functions form a set of multi-dimensional nonlinear restoring forces in the modal space. In the case of using two modes in the static analysis, (see Eq.(5-7)), the coefficient of the modes form mathematical surfaces that can be addressed to as 'restoring force surfaces'. The nonlinear

stiffness in each mode is characterised by these restoring force surfaces. So it is possible to compare the relative changes in the nonlinear stiffness for the different temperatures in an indirect way, where the similarity between these surfaces is compared.

To measure the similarity of any two nonlinear restoring force surfaces, the correlation coefficients between the two sets of nonlinear stiffness coefficients are used. The calculation process is similar to that of Modal Assurance Criterion (MAC) [147] which is normally a comparison of the similarity of the mode shapes for two different modal sets. Here it is that of the similarity of the nonlinear restoring force surface shapes for the two different modal sets. Hence, the comparison method may be called Restoring Force Assurance Criterion (RFAC). The RFAC for two modes (m^{th} and n^{th} order) is given as

$$RFAC(m, n) = \frac{|A_m^T A_n|^2}{(A_m^T A_m)(A_n^T A_n)} \quad \text{Eq.(5-21)}$$

where A_m and A_n are the nonlinear stiffness coefficients associated with the m^{th} and the n^{th} order modes.

Figure 5-22 (a) - Figure 5-22 (d) show the RFAC of the first 9 modes for the three different temperatures, 0°C, 50°C and 100°C. They are compared in pairs with 0°C - 0°C in Figure 5-22 (a), 0°C - 50°C in Figure 5-22 (b), 0°C - 100°C in Figure 5-22 (c), and 50°C - 100°C.

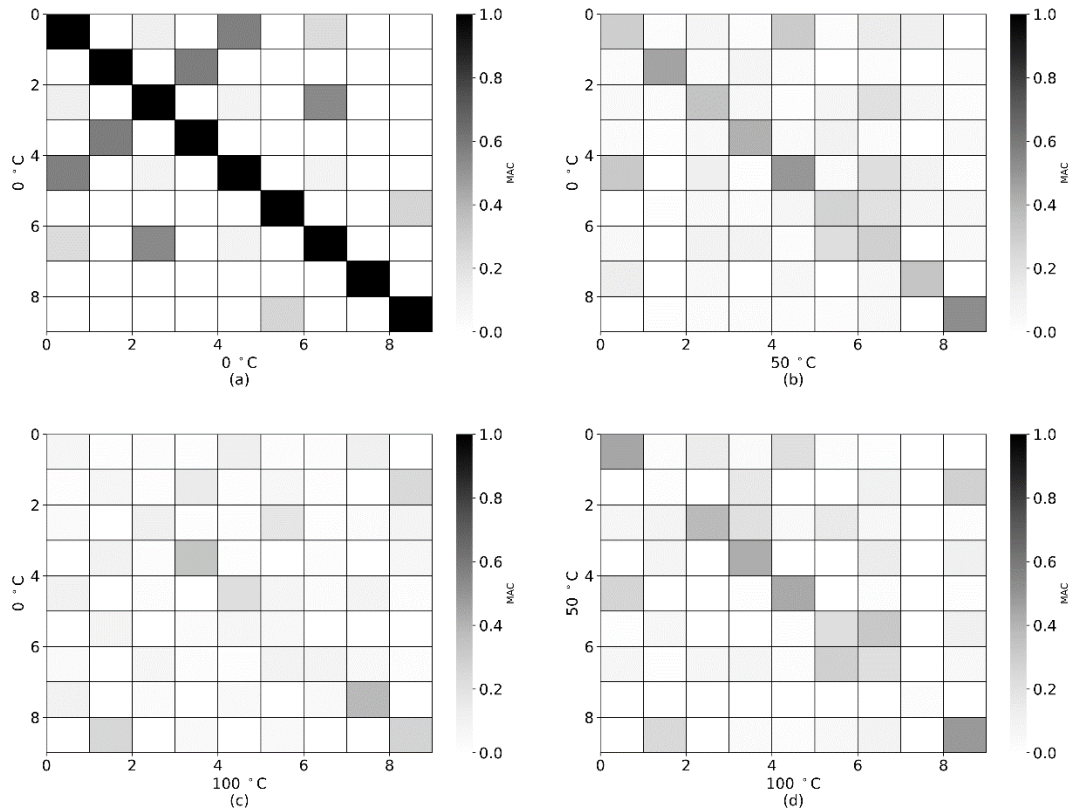


Figure 5-22 The RFAC of the first 9 modes for the three different temperatures, 0°C, 50°C and 100°C in pairs of the four comparisons: (a) 0°C - 0°C. (b) 0°C - 50°C. (c) 0°C - 100°C. (d) 50°C - 100°C.

Figure 5-22 (a) shows the self-correlation of the nonlinear restoring forces at 0°C. It is a symmetric matrix with a diagonal line with values of unity. Figure 5-22 (b) and Figure 5-22 (d) show that the values of the diagonal line are smaller than unity. It means the nonlinear restoring forces for each individual mode after a temperature rise of 50°C are less correlated than those before the temperature rise (Figure 5-22 (a)). Figure 5-22 (c) shows that with a higher temperature rise of 100°C, the correlations represented along the diagonal are further reduced to very small values. These results indicate that the nonlinear stiffness matrices, characterised by the nonlinear restoring force surfaces, in general differ from each other and the differences increase as the temperature rises increase. However, the thermal dependency of these changes may not solely be dependent on the range of the temperature rise. This can be seen from the unequal changes of the relative correlation values along the diagonal elements for each temperature condition. This may reveal the complex nature of the thermal effect on the nonlinear stiffness, which is outside the scope of this study.

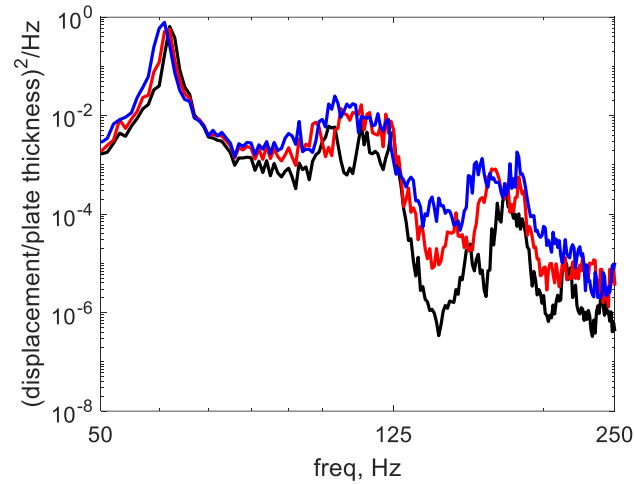


Figure 5-23 The NLROM estimated PSD of the normalised displacement for the stiffened plates with temperature and subjected to the plane wave excitation. The mode set D (34 modes) is used in NLROM prediction. The three different temperatures, 0°C, 50°C and 100°C are represented by the black, red and blue solid lines.

Figure 5-23 shows that some response peaks, both within and out of the excitation bandwidth, are shifted to lower frequencies. This is consistent with the results shown in Figure 5-8 to Figure 5-10. In addition, some resonance peaks are merged when the temperature increases.

5.3 Summary

This chapter investigated the effects of the modal basis selections, the static loading schemes, the time integration and the elevated temperature for the nonlinear characterisation and the subsequent response predictions by using the nonlinear reduced order model (NLROM). Two example structures from the previous chapters were revisited to illustrate the effects of the different NLROM configurations.

The main findings in this chapter are:

- Using linearly excited modes up to twice the frequency of the excitation bandwidth in the static nonlinear identification is sufficient to achieve an efficient and accurate approximation for use in the NLROM when compared to the full order FE simulations.
- The accuracy of the nonlinear identification is less affected by the type of the static loading and the range of the scaling factors.
- For thermally loaded structures, using the hot-mode NLROM produces a more accurate set of simulations compared to the cold-mode NLROM predictions. The remaining issue for the former is that the capacity for it to converge during the static characterisation step is reduced, compared to the static characterisation using the cold-mode NLROM at a higher temperature level.

- Compared with the mass-proportional damping, the stiffness-proportional damping can produce a more stable integration at high dynamic input levels and reduces the required sample rate for the converged time domain predictions for both the NLROM and the FEM. However, a trade-off may be required in the selection of the damping and the sample rate when producing the comparison of NLROM and FEM simulations.
- The deep stiffeners and the high curvature, creating a much stiffer structure statically, also make the appearance of the nonlinearity less detectable in the response range that is normally outside of the typical range for the linear behaviour for a uniform thin plate..

Chapter 6 **Fatigue life evaluation with the effects of vibroacoustic coupling, nonlinearity and temperature**

One application requiring vibroacoustic response predictions is acoustic fatigue, particularly for structures subjected to high levels of acoustic excitation where a nonlinear response can occur. The response can be generated by the NLROM model developed in the previous chapter to account for the vibroacoustic coupling, geometric nonlinearity and the elevated temperature.

Firstly, the spectral and time domain methods for the acoustic fatigue life estimation are briefly introduced. These methods are then compared in the context of the multi-modal response and the nonlinear response. The time domain rainflow counting approach is then adopted to predict the fatigue life of a stiffened plate. The NLROM model is used for the response prediction.

6.1 Methods for the acoustic fatigue life estimation

Acoustic fatigue is the high-cycle fatigue caused by the stress reversals of the structural response due to the acoustic excitation. The estimation methods for the acoustic fatigue life have been well developed and summarised in available design standards, e.g. ESDU 06009 – 06011 [50]. Some of the definitions and formulae from ESDU reference [50] are reported in this section as they form the basis of the discussion and calculations of this chapter.

6.1.1 The stress-life approach and the S - N curve

The stress-life approach is used to provide the fatigue information of a material or component. It is a basis upon which to estimate the fatigue life. It is in the form of S - N curves, that is the stress (S) to the number of cycles (N) to failure. These are experimentally obtained.

Two types of quantities are usually used for the stress (S). The first one is the stress amplitude S_a . It corresponds to the structure's failure from a fully reversed bending test. The second one is the RMS value of the stress, S_{rms} . Instead of the complete failure, a '2% criterion of failure' is more often used, i.e. a 2% decrease in the value of the fundamental resonance. However, the '2% criterion of failure' is not necessarily reliable in the presence of nonlinearity, because the latter causes the shift in the resonance as shown in the previous chapter.

Figure 6-1 shows a general $S-N$ curve. Two fatigue regimes may be identified in this curve – the low cycle fatigue and the high cycle fatigue. The boundary between these two regimes depends on whether or not the structure's deformation is within its elastic range. For the low cycle fatigue, the fatigue failure occurs after a few cycles of the loading, so only finite fatigue life is possible. For the high cycle fatigue life, failure occurs typically after more than 10^4 to 10^5 cycles. Acoustic fatigue is normally associated with the high cycle fatigue.

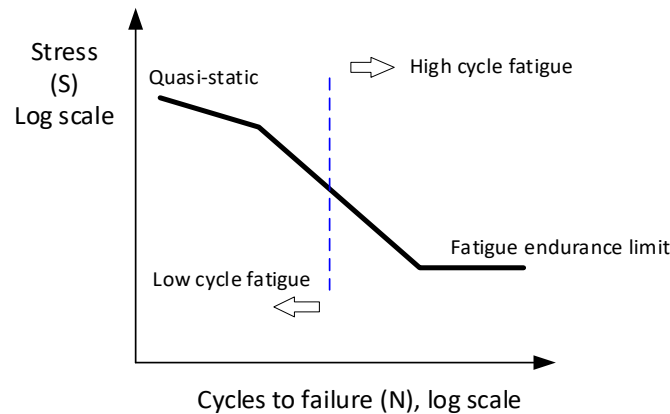


Figure 6-1 A general $S-N$ curve showing different fatigue ranges.

Figure 6-1 also shows an exponential relationship, i.e. power law, between the stress (S) and the number of the cycles to failure (N) in the fatigue range between the quasi-static failure and the fatigue endurance limit. It is expressed as

$$NS^b = K \quad \text{Eq.(6-1)}$$

where K and b are constants. This corresponds to a straight line in the log scale plot, that is

$$\log S = \frac{1}{b} \log K - \frac{1}{b} \log N$$

Below the fatigue endurance limit, the material and the structure will in principle have an infinite life. Some materials such as aluminium alloys do not exhibit a clear endurance limit [50]. The aerospace components that are investigated in this research are assumed to be aluminium, therefore failure is inevitable. For these materials the term endurance limit is often taken to be in engineering practice the stress amplitude for a chosen number of cycles to failure, usually 10^7 cycles.

6.1.2 Palmgren-Miner damage rule and the time domain method

The $S-N$ curves relate the fatigue life of the material/component to a constant amplitude or RMS value of their stress/strain responses. For the stress response with a number of varying

amplitudes, the fatigue life can be estimated by using the Palmgren-Miner rule [3]. This rule assumes that the fatigue damage can be accumulated linearly after each stress cycle.

The accumulated damage is represented as

$$D = \sum_{i=1}^k \frac{n_i}{N_i} \quad \text{Eq.(6-2)}$$

D is the total accumulated damage. The failure is estimated to occur when D equals to 1. The subscript i represents a certain level of stress. Under stress S_i , n_i is the number of cycles, N_i is the cycles to failure in the S - N curve, and therefore n_i/N_i is the accumulated damage by stress S_i . k is the number of the levels of the stresses presented in the loading. The sequence of the stress cycles is ignored within this accumulation.

The Palmgren – Miner rule allows the fatigue life to be estimated directly from the time domain methods, such as the rainflow cycle counting approach [103-105]. A brief illustration of the rainflow cycle counting approach is shown in Figure 6-2. It is reproduced from [170] where a full description of the method is provided.

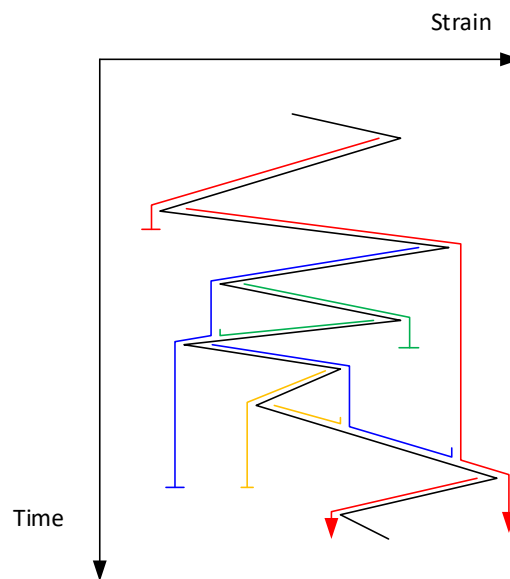


Figure 6-2 An illustration of the rainflow counting method.

Figure 6-2 shows a strain history where the time axis is vertically downward, and the lines connecting the local maxima and minima of the strain are imaged to be a series of pagoda roofs. Each rainflow starts from the inside of each peak. It is allowed to drip down and continues unless a certain condition is met. That is, if the rainflow starts from a maximum, it must stop when it meets a maximum that is larger than the one where it starts. Similarly, if

the rainflow starts from a minimum, it must stop when it meets a minimum that is smaller than the one where it starts. In addition, a rainflow must end if it meets another rainflow from a roof above. Following this procedure the number of half or full cycles is counted for different amplitudes. In the example shown three different half cycles can be found in the three red rainflow lines. The blue, green and yellow lines represent three different full cycles.

This method is especially useful for the wideband response signals, where the stress cycles might not be easily counted. It can identify cycles associated with closed stress-strain hysteresis loops. Different numerical algorithms have been developed for performing the rainflow cycle counting process, such as the four-point and the three-point counting methods [50]. The implementation of the algorithm ASTM E1049-85 for the rainflow counting has been made available in built-in functions in MATLAB and Python for example. A detailed procedure of this algorithm can be found in [171].

6.1.3 Generalised Palmgren-Miner rule and the spectral methods

The Palmgren-Miner rule can be generalised by using the concepts of the probability density function (PDF) for the rainflow counting ranges and the expected values. The accumulated damage for a stationary, random Gaussian process can be expressed as

$$D = F_p T \int_0^{\infty} \frac{1}{N(S_r)} p_{rfr}(S_r) dS_r \quad \text{Eq.(6-3)}$$

D represents the damage that is accumulated in the time length T by the signal. F_p is the expected value of the peak occurrence rate, which can be expressed in terms of the moments of the PSD function [172]. $N(S_r)$ is the number of cycles at the stress level S_r which causes failure. $p_{rfr}(S_r)$ is the PDF for the rainflow stress cycle ranges.

The generalisation of the Palmgren-Miner rule allows the fatigue life to be estimated by the spectral methods. The spectral methods are based on the spectrum of the stress response, such as the frequency response function (FRF) or the power spectral density (PSD). Eq.(6-3) applies to both the narrow band and the wide band Gaussian processes.

For a narrow band process of the stress response with a single dominating resonance, $p_{rfr}(S_r)$, the PDF for the rainflow stress cycle ranges in Eq.(6-3), can be approximated by a Rayleigh distribution [97]. F_p , the expected value of the peak occurrence rate is equal to F_{zc} , the expected rate of the zero crossing with the positive slope. The expected damage can be expressed as

$$D_{ray} = \frac{F_{zc}}{K_r} (2\sqrt{2}S_{rms})^b \Gamma(1 + b/2) \quad \text{Eq.(6-4)}$$

where F_{zc} is the zero crossing rate which can be either expressed by the spectral parameters [172] or be approximated by the fundamental natural frequency of the structure. K_r is the constant in Eq.(6-1) for stress range.

For a wide band process, the PDF for the response peaks can be expressed in an analytical form [173]. Although the PDF for the response can be approximated as a Gaussian distribution for an ideal white noise process, this is not the case for a practical stress response which usually has multiple, comparable resonances.

In this case, the Rayleigh approximation can be used together with a damage correction factor [109]

$$\lambda = D/D_{ray} \quad \text{Eq.(6-5)}$$

where D_{ray} is the expected damage calculated from the Rayleigh approximation.

Published work has addressed the evaluation of the damage correction factor. They include using a single spectral parameter like irregularity factor and using multiple spectral parameters. However, there is no simple way to know which bandwidth parameter will work best. The calculation used in this chapter is based on the work of Lutes and Sarkani [174] where the damage accumulation is estimated in terms of a single moment. The expected damage can be expressed as

$$D = \frac{2^{3b/2} m_{2/b}^{b/2}}{K_r} \Gamma(1 + b/2) \quad \text{Eq.(6-6)}$$

where m is the moment of the one-sided PSD $G(f)$ and can be calculated as $m_k = \int_0^\infty f^k G(f) df$.

Alternatively, the PDF for the rainflow stress cycle ranges can be approximated using an empirical formulation as a function of the spectral moments derived from the response PSD. In this sense, Dirlik's method has been proven to give the most accurate results when compared directly within the rainflow counting. This method builds a link between the PSD and the fatigue life based on the rainflow counting approach. The derivation and the empirical formulation of Dirlik's method are based on numerical time domain simulations of a wide range of the numerical models/systems. Firstly, the time history of the stress from the PSD is generated by using the Inverse Fast Fourier Transform (IFFT) technique through a Monte Carlo process. Then an empirical formulation of the PDF for the 'rainflow counting ranges' is derived,

which is in the form of a sum of an exponential function, a Rayleigh function with a few Rayleigh parameters and a standard Rayleigh function. The formulas of Dirlik's methods have been listed in [110] and are given in Appendix 2.

6.2 Modal models for the response prediction

In Chapter 2 and Chapter 5, both the efficiency and the accuracy of the modal models have been shown in accounting for the vibroacoustic coupling and the nonlinearity in comparison with the full numerical models, either the FEM-BEM or the nonlinear time domain FEM. For this reason, a modal model is used in this chapter to predict the dynamic responses with different modelling assumptions to investigate their consequences on the fatigue life estimation.

6.2.1 Vibroacoustic coupling and nonlinearity

The vibroacoustic coupling is included in the modal model presented in Chapter 2. This model predicts the linear vibroacoustic response in the form of the frequency response function (FRF).

When using the rainflow counting method to estimate the fatigue life, the time domain results are needed. These time domain results can be obtained from the calculated FRF from a loading spectrum by using an IFT. The FRF can be linked to an equivalent PSD given over a specific time length. This method has been detailed in reference [169].

However, this approach is no longer appropriate when the nonlinear response is considered. The reason for this is that the PDF of the nonlinear response may be non-Gaussian when the excitation is Gaussian [87, 111, 175]. It means that the IFT method, assuming a Gaussian distribution of the independent random phases [172], i.e. phase is uniformly distributed, cannot strictly be used to generate the time response. In the general nonlinear case, there is no generalisation for what the PDF of the phases of the response might be.

An alternative way, instead of the full frequency domain results (FRF or PSD), consists of using the modal radiation damping and the added mass which can be extracted from the linear vibroacoustic coupling model. They can then be imported into the nonlinear reduced order model (NLROM) to characterise the vibroacoustic coupling effect. It is noted that the damping model used in NLROM, i.e. the Rayleigh damping, is different from that in the frequency domain model, i.e. the structural loss factor. However, primarily only the resonance peaks will be affected by using the different damping representations. For plate structures, the

vibroacoustic coupling effect is only significant and obvious in the fundamental mode. Hence, this difference in the transformation may not be significant, provided that the modal damping and the modal mass are guaranteed and accurate for the fundamental mode if the frequency dependent Rayleigh damping model is applied.

In this chapter, the linear frequency domain model from Chapter 2 is used to study the scenario where the vibroacoustic coupling is addressed in the absence of nonlinearity. This gives a more accurate prediction of the fully coupled response, as it accounts for the radiation damping for all modes included in the calculation. The corresponding result is presented below in Section 6.3.3.1.

For the other scenarios and especially when the nonlinearity is addressed, the NLROM from Chapter 5 is used. This enables the response model to address various assumptions and to maintain the capacity to include the nonlinearity. However, it should be noted that compared to the linear frequency domain model, this may underestimate the fatigue life when the vibroacoustic coupling is included, because only the radiation damping and added mass of the fundamental mode is considered. The corresponding results are reported in Section 6.3.2, Section 6.3.3.2 and Section 6.3.3.3.

6.2.2 Nonlinear stress and elevated temperature

The NLROM presented in Chapter 5 is used for including the effect of the geometric nonlinearity and the elevated temperature. However, the stress responses, instead of the displacement responses in Chapter 5, need to be calculated from the NLROM for the fatigue life estimation.

Firstly, the linear stress modes are used to transform the modal displacement to a point stress. The linear stress mode is defined by McEwan [89] as linear stress state when the maximum amplitude of the physical displacement is equal to unity for the mode shape in free vibration analysis. The superposition property holds for the linear components of the stress, i.e. the linear stress state of the structure may be regarded as a sum of the stress modes multiplied by the respective modal displacements. The linear stress can be represented as

$$\sigma_p = \sum_{n=1}^N \psi_{\sigma_p n} q_n \quad \text{Eq.(6-7)}$$

where σ_p is the p component of the normal stress and $\psi_{\sigma_p n}$ is a stress mode for the n^{th} mode. The basis of this definition is that the linear normal strain responses can be derived with

respect to the second derivative of the mode shapes [176]. The corresponding normal stress can be expressed as

$$\sigma_x = -\frac{Ez}{1-\nu^2} \left(\frac{\partial^2 w}{\partial x^2} + \nu \frac{\partial^2 w}{\partial y^2} \right), \sigma_y = -\frac{Ez}{1-\nu^2} \left(\frac{\partial^2 w}{\partial y^2} + \nu \frac{\partial^2 w}{\partial x^2} \right), \quad \text{Eq.(6-8)}$$

using Hooke's law. The stress modes of a structure can be readily obtained from ABAQUS following a free vibration analysis where the stress data corresponding to a unit mode shape is extracted. Then, a static characterisation is required for calculating the nonlinear components of the stress. The details of the static characterisation has been presented in [89], where the nonlinear components of the stress at each point can be characterised by the multi-dimensional nonlinear restoring surfaces as a function of the modal displacement.

Lastly, a hot-mode NLROM was used to include the effect of any elevated temperature. For this method one uses the mode shape and the natural frequencies of the structure under the thermal loading and the temperature conditions. The details of this method together with the comparison with the cold-mode NLROM were presented in Chapter 5.

6.3 Numerical results

The aluminium stiffened plate model used in Chapter 2 and Chapter 5 was used in the numerical study. The details of the structural parameters were listed in Table 2-1 and the details of the FE model were given in Section 5.2.1.1. The parameter values for the fatigue law used in the fatigue calculations are $b = 4.78$ and $K = 3.31 \times 10^{43}$ [95] (see Eq.(6-1)). The yield stress range is about 600 MPa. An endurance limit of 154.8 MPa is assumed to correspond to 10^7 cycles to failure [50]. The $S-N$ curve is shown in Figure 6-3.

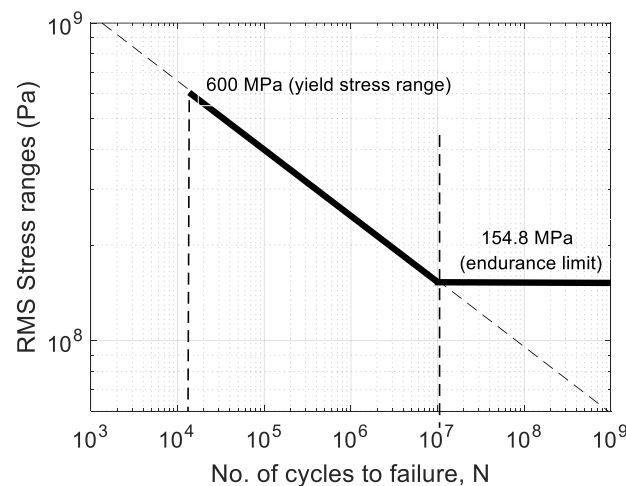


Figure 6-3 The $S - N$ curve used in the fatigue calculations in the numerical study.

The time length of the response used in the fatigue calculations is 30 seconds. The accumulated damage within this 30s is then calculated and the total fatigue life can be estimated.

In the following sections some example results are reported with the aim of investigating the effect of different factors on the estimate of fatigue life.

Firstly, Section 6.3.1 illustrates the intermediate steps required in the fatigue life analysis taking one of the cases analysed as an example. Some preliminary results such as the time histories and the PDF are presented for reference.

Then Section 6.3.2 compares different methods of predicting fatigue life. In order to cover multiple scenarios two different forcing conditions are used:

- Point force excitation in a linear case. This is selected to show the effect of having a single dominant mode in the response in comparison to a situation where there are two comparable contributing modes.
- Plane wave excitation. This is chosen to look at the effect of nonlinearities on the fatigue life prediction using different estimation methods.

Finally, Section 6.3.3 evaluates the effects of vibroacoustic coupling and nonlinearity when using the rainflow counting approach. Different excitation types, boundary conditions and temperature conditions are also considered in the comparisons.

6.3.1 Preliminary results

For one of the cases analysed, and with the aim of clarifying the intermediate steps required in the fatigue analysis, this section shows the time histories of the stress predicted by means of NLROM. The corresponding PDFs are also given as an example and some initial comments on expected fatigue life are presented. Detailed results for fatigue prediction will follow in later sections.

The stiffened plate subject to the broadband point force excitation with the RMS value of 593N the maximum frequency 125 Hz was used. The position and the values of the parameters of the point force excitation can be found in Section 5.2.2.1. The response point is at the end of the joint in one of the y -wise stiffeners, which has the maximum stress at the first resonance around 66 Hz. More details of the position are included in the next section. The nonlinearity is neglected in this section.

Figure 6-4 (a) shows the time history of the stress in the y direction. Figure 6-4 (b) shows the corresponding probability density function (PDF). Figure 6-5 shows the corresponding PSD where the contribution of different resonant modes can be observed.

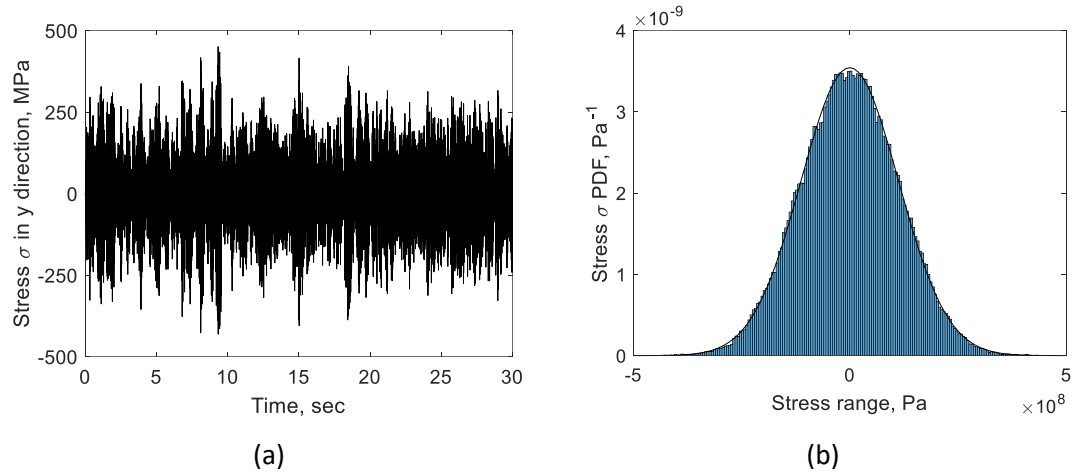


Figure 6-4 The time history (a) and the PDF (b) of the maximum stress in the y direction.

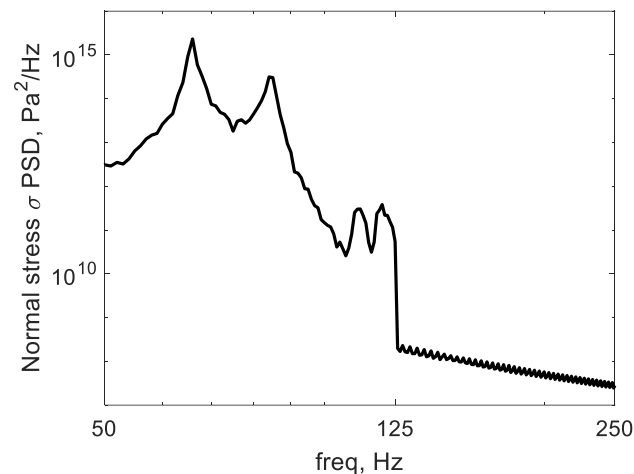


Figure 6-5 The PSD of the maximum stress in the y direction.

For the case analysed here the RMS value of the stress is 113 MPa and the peak value of it is 450 MPa. Referring to the $S-N$ curve in Figure 6-3, the RMS value is below the fatigue endurance limit of 154.8 MPa, corresponding to an infinite fatigue life. However, the peak value of stress corresponds to around 60000 cycles, which would correspond to a fatigue life of 15 minutes at the frequency of 66 Hz in the peak resonance. The actual fatigue life of the structure is therefore expected to be between the two limits and will depend on the actual statistical distribution of the stress levels. So, it is not unexpected that low RMS can have low fatigue life if there are substantial cycles at high stress levels. This is measured by the rainflow counting ranges. This is the distribution of rainflow cycles at different levels. The case shown

here would give the distribution shown in Figure 6-6. Rayleigh distribution is shown in red line in this figure.

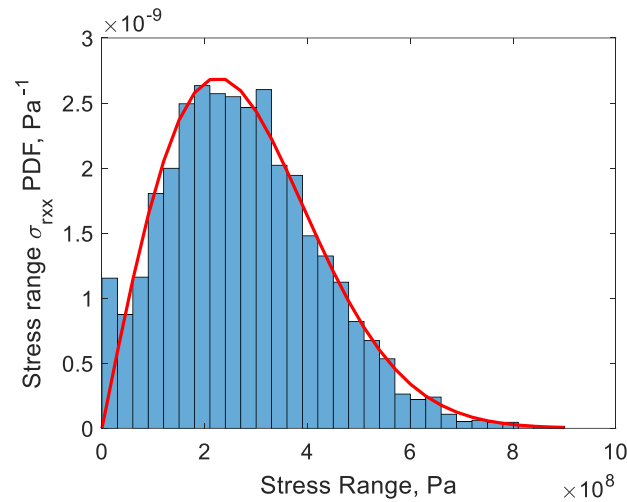


Figure 6-6 The PDF of the rainflow counting ranges as a histogram in comparison to a theoretical Rayleigh distribution.

This PDF follows a Rayleigh distribution, with the number of cycles at high ranges, i.e. the upper tail, playing a dominant role in defining the fatigue life. The spectral methods approximate this distribution from various spectral parameters.

The different methods for fatigue life predictions rely on the quantities shown here. The rainflow counting method will make use of results such as those in Figure 6-4 (time histories and pdfs). The spectral methods will rely on the PSD spectra as in Figure 6-5.

6.3.2 Comparison of different fatigue estimation methods

This section presents a study to compare the fatigue life results estimated from three spectral methods. They are the Rayleigh approximation [97], Rainflow damage factor [109] and Dirlik's method [110]. The accuracy of these results is discussed with reference to the Rainflow counting method [103-105]. Two sets of the stress responses covering the multi-modal property and the nonlinearity were used in the comparisons. These responses were calculated from the NLROM.

6.3.2.1 Multi-modal property

The first comparison is between a stress response with one dominating resonance and a stress response with two comparable magnitude resonances, both linear. The nonlinear terms are not included here, so that this case is solely given to compare a situation where the response

is dominated by a single mode or there are two comparable contributions from different modes i.e. multi-modal.

For the first comparison, the point force excitation with the RMS value of 593N was used. The position and the values of the parameters of the point force excitation can be found in Section 5.2.2.1. Two reference points on the upper surface of the stiffened plate were chosen for the fatigue life calculation. They are the points with the maximum element normal stress in the y direction and in the x direction respectively (see Figure 2-2) at the first resonance around 66Hz. The location possessing maximum stress are chosen for a fatigue assessment. The positions of these two reference points together with the stress distributions are shown in Figure 6-7 (a) and Figure 6-7 (b).

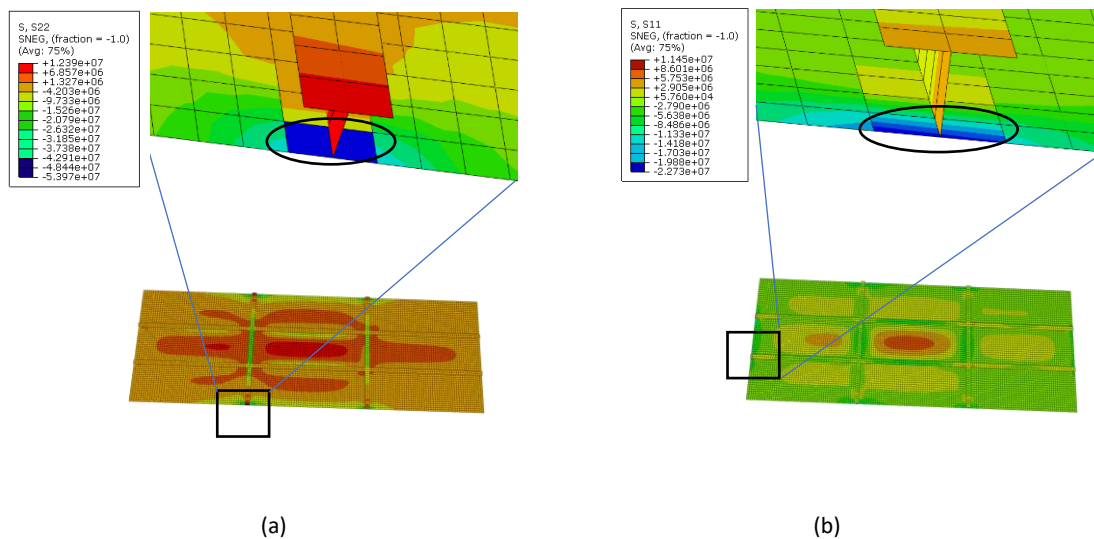


Figure 6-7 Stress distributions in the y direction (a) and in the x direction (b) when the plate is subjected to the point force excitation. The positions corresponding to the stress maxima are marked by the black circles.

Figure 6-7 shows that the maximum stress positions are all at locations close to the ends of the stiffeners and coincident to the directions of the element normal stress. For a general stiffened structure, the maximum stress/strain usually happens close to the stiffeners where failure is likely to start. Referring back to the cracked panel at start of the thesis in Figure 1-1, the failure starts at the edges of the stiffeners and propagates towards the middle of the panel bay. The exact position of the maximum stress also depends on the boundary conditions and stiffener configuration of a specific structure. Since the structures are different, these positions are not in the middle of the plate as shown in Figure 1-1. The PSD estimations of the element normal stress responses for the two reference points are shown in Figure 6-8.

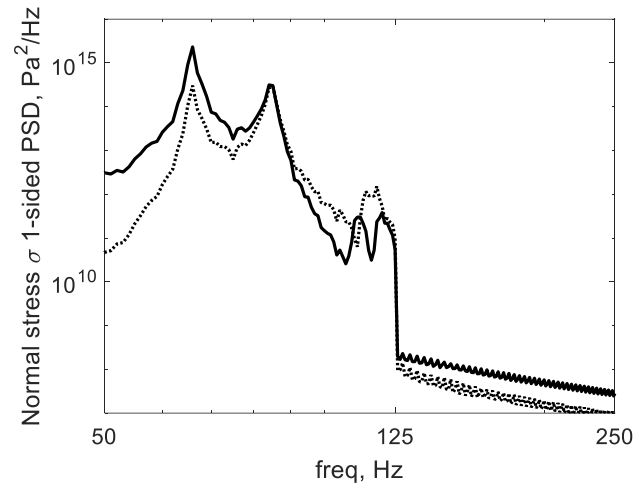


Figure 6-8 The PSD estimations of the maximum element normal stress at two directions when the plate is subjected to the point force excitation. The maximum normal stress response in the y direction is in the solid line. The maximum normal stress response in the x direction is in the dotted line.

The results show that PSD prediction of the maximum stress in the y direction is dominated by the resonant peak of the first mode which is about one order of magnitude higher than the second resonant peak. The PSD prediction shows that the maximum stress in the x direction is characterised by two peaks of comparable level.

Figure 6-9 (a) and Figure 6-9 (b) show the comparisons of the estimated fatigue life ratios for the points on the plate possessing the two maximum surface stresses, with Figure 6-9(a) for the maximum stress in the y direction and Figure 6-9 (b) for the maximum stress in the x direction. The fatigue life ratio is obtained when the fatigue life estimated from the three spectral methods is normalised by that obtained from the rainflow counting method (indicated as horizontal red lines in the figures). A fatigue life ratio of 1 means that the fatigue life estimated by one of the methods is the same as that predicted with the rainflow counting method.

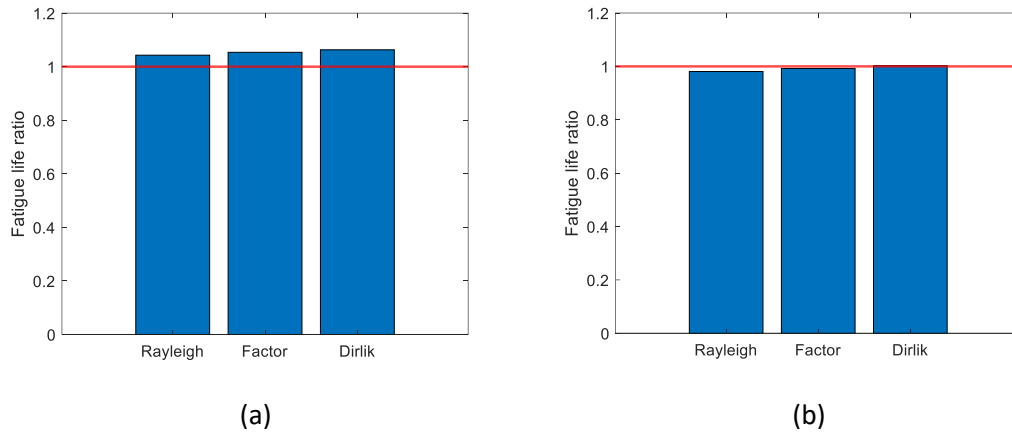


Figure 6-9 Comparison of the fatigue life ratios calculated from three different spectral methods: Rayleigh approach, Factor approach and Dirlik's approach. (a) The fatigue life ratios for the response of the maximum stress in the y direction with one dominating peak. (b) The fatigue life ratios for the response of the maximum stress in the x direction with two comparable dominating peaks.

Figure 6-9 (a) shows that the three spectral methods overestimate the fatigue life by 2-4% for the response with one dominating resonance peak compared to the rainflow counting results. Figure 6-9 (b) shows that the three spectral methods slightly underestimate the fatigue life for the response with two comparable resonance peaks, which may be desirable in engineering practice as it provides a conservative prediction. In this case, it is also observed that Dirlik's method gives the best agreement to the predictions from the rainflow counting.

6.3.2.2 Nonlinearity

The second comparison is between a linear and a nonlinear stress response. The normal plane wave excitation with a RMS value of 146 dB is used. The values of the parameters for the plane wave excitation can be found in Section 5.2.2.1. The reference point with the maximum element normal stress in the y direction at the first resonance around 66Hz is used. The NLROM with the modal basis selection of the first seven lowest linearly excited modes (mode set C in Table 5-6) is used for the calculation of the nonlinear stress.

Figure 6-10 shows the PSD estimations of the maximum element normal stress in the y direction. The linear prediction is in a solid line and the nonlinear prediction is in a dotted line. The resonance peaks in the nonlinear result are shifted to higher frequencies and broadened due to the nonlinear stiffening effect. In addition, there is a response at frequencies outside the excitation bandwidth in the nonlinear predictions. This out-of-band response is caused by the nonlinear coupling between the low frequency and the high-frequency flexural modes, as well as high frequency contributions from the geometrical nonlinear in-plane stretching of the lower order flexural modes.

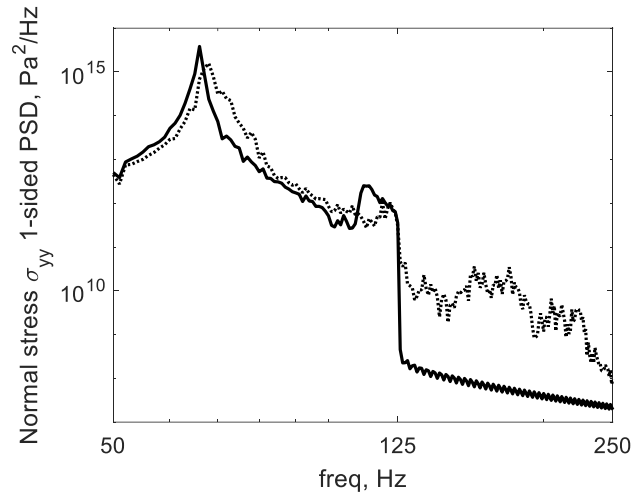


Figure 6-10 The PSD estimations of the maximum element normal stress at y direction when the plate is subjected to the plane wave excitation. The linear prediction is in the solid line and the nonlinear prediction is in the dotted line.

Figure 6-11 (a) and Figure 6-11 (b) show the comparisons of the fatigue life ratios for a point on the plate possessing the maximum surface stress in the y direction, with Figure 6-11 (a) for the results calculated from the linear response and Figure 6-11 (b) for the results calculated from the nonlinear response.

Figure 6-12 (a) and Figure 6-12 (b) show the comparisons of the stress range PDFs for the responses. Three stress range PDFs calculated from the rainflow counting, the Rayleigh approximation method and Dirlik's approach are in the solid lines, dotted lines and the dashed lines respectively. Figure 6-12 (a) shows that results calculated from the linear responses. Figure 6-12 (b) shows the results calculated from the nonlinear responses.

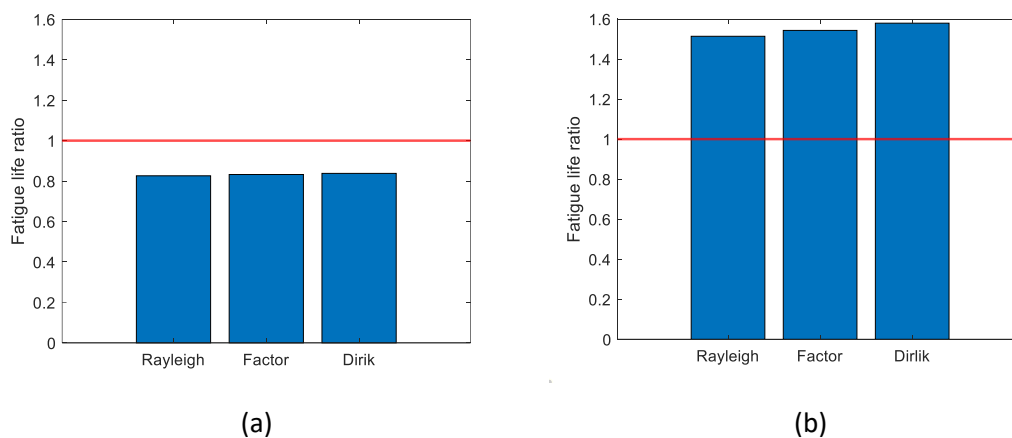


Figure 6-11 Comparison of the fatigue life ratios calculated from three different spectral methods: Rayleigh approach, Factor approach and Dirlik's approach. The fatigue life ratio is calculated by normalising the fatigue life calculated from the three spectral methods with that from Rainflow counting method (the horizontal red lines). (a) Fatigue life ratios for the linear response of the maximum stress in the y direction. (b) Fatigue life ratios for the nonlinear response of the maximum stress in the y direction.

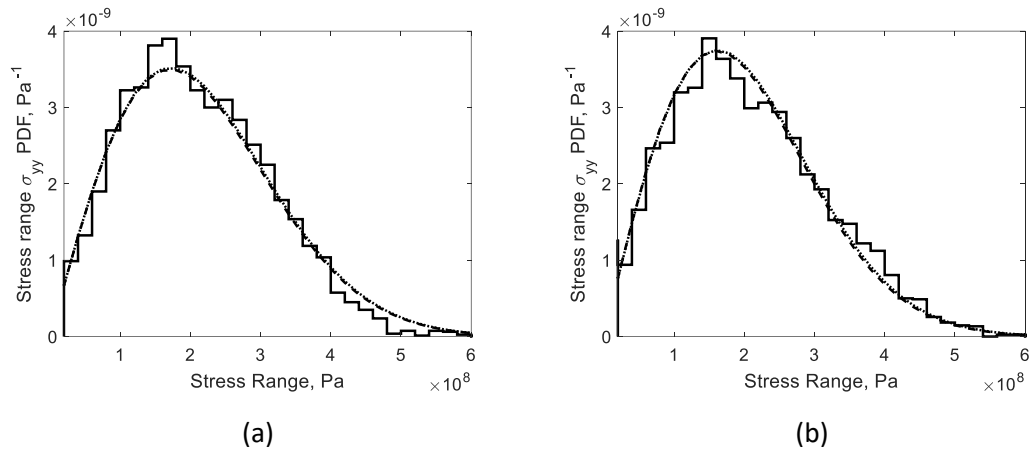


Figure 6-12 Stress range PDFs of the linear responses (a) and the nonlinear responses (b). The results calculated from the Rainflow counting method are in the solid lines. The results calculated from the Rayleigh approximation method are in the dotted lines. The results calculated from Dirlik's approach are in the dashed lines.

Figure 6-11 (a) shows that the three spectral methods in this case underestimate the fatigue life for the linear responses compared to the rainflow counting estimations. This can be explained by the comparisons of the stress range PDFs for the linear responses in Figure 6-12 (a). In this case, the stress range PDFs calculated by the spectral methods tend to overestimate the rainflow PDF in the high stress range portion of the distribution, e.g. stress range above 350MPa. This has the consequence of producing a conservative fatigue life estimate.

Figure 6-11 (b) shows that the spectral methods overestimate by 50-60% the fatigue life for the nonlinear responses compared to the rainflow counting estimations. This can be explained in Figure 6-12 (b). For the nonlinear responses, the stress range PDFs obtained by the spectral methods tend to underestimate the rainflow PDF in the high stress portion of the distribution. This results in a non-conservative estimate for the fatigue life, which is not desirable for engineering practice.

One can conclude from the two studies in this section that the three spectral methods may be reliable in the presence of multi-modal response with a point excitation but seem less reliable in the presence of a nonlinear response. This is due to the assumptions in the form of the PDF distributions. Therefore, only the rainflow counting method is used in the next section for fatigue life estimation.

6.3.3 Comparison of the effects of the different physical conditions and behaviours

6.3.3.1 Vibroacoustic coupling effect

The effect of vibroacoustic coupling on the estimated fatigue life is now investigated. Both the vibroacoustically uncoupled and coupled responses were calculated in the frequency domain. Then they were transformed into the time domain by applying the IFT with the time history of 30 seconds and the sample rate of 250Hz. The responses that were used in the fatigue life calculation are assumed linear. This means that the nonlinear terms in the NLROM are not included. Three different configurations, including excitation types, boundary conditions and the elevated temperature are considered.

Figure 6-13 (a) shows the comparison between the rainflow estimated fatigue life calculated from the responses to the plane wave excitation of 146dB and the point force excitation of 593N. These two excitations are equivalent to give a maximum linear displacement response of about 10 times the plate thickness at the reference point (Figure 2-2). The two different bars (blue and orange) are for the results without vibroacoustic coupling and for the results with vibroacoustic coupling.

Figure 6-13 (b) shows the comparison of the rainflow estimated fatigue life calculated from two different configurations including a spring foundation and fully clamped edges. For the spring foundation boundary condition, the plate edges are partially constrained for in-plane DOFs and are fully constrained in all of the other DOFs. The spring elements are used to introduce the partial constraints. The value of the spring total stiffness are 100kN/m in the x direction and 200kN/m in the y direction. These stiffness values were determined through a trial and error process in an empirical manner, which was described and explained in Section 5.2.1.4. The plane wave excitation of 146dB was used. The two different bars (blue and orange) are for the results without vibroacoustic coupling and for the results with vibroacoustic coupling.

Figure 6-13 (c) shows the comparison of the rainflow estimated fatigue life calculated from the responses at three different elevated temperatures 0°C, 50°C and 100°C with a uniform spatial distribution applied to the structure. The spring foundation was used to represent a practical and realistic representation of the boundary condition under the thermal conditions. The plane wave excitation of 146dB was used.

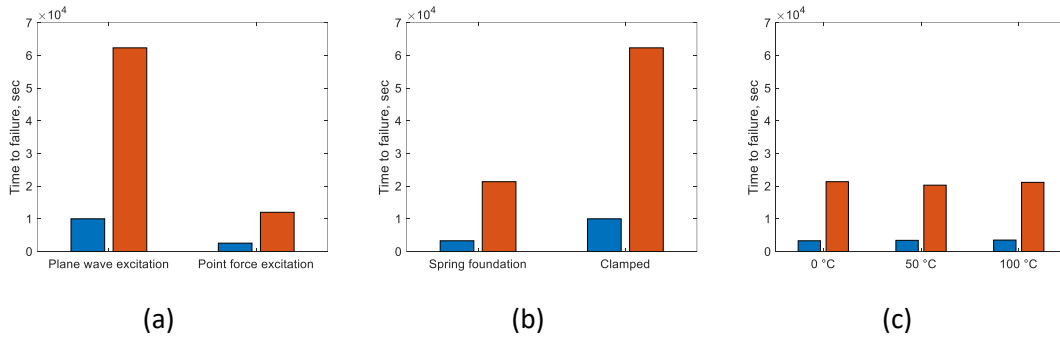


Figure 6-13 Comparison of the rainflow estimated fatigue life calculated for three different configurations. (a) Excitation type: plane wave against point force. (b) Boundary condition: Spring foundation against clamped edges. (c) Elevated temperature: 0°C, 50°C and 100°C. The results of the uncoupled responses are in the blue bars. The results of the coupled responses are in the red bars.

The results show that for each set of comparisons the orange bars are higher than the blue bars, which mean that the estimated fatigue life is increased in all cases when the full vibroacoustic coupling is taken into account. This is because in the coupled responses the level of the resonant peak is reduced by the radiation damping and the resonant frequency is reduced by the added mass, which all increase the fatigue life. As discussed in Section 2.3.1.2, this full vibroacoustic coupling can be enhanced by stiffeners. The results also show that the estimated fatigue life of both the uncoupled and the coupled model is less affected by the elevated temperature.

6.3.3.2 Nonlinear effect

The nonlinear effect on the estimated fatigue life is presented here. The fatigue life estimations for comparison were calculated from three sets of responses, (i) linear response without vibroacoustic coupling, (ii) nonlinear response without vibroacoustic coupling, and (iii) nonlinear and in the presence of vibroacoustic coupling. The elevated temperatures and the increased excitation levels were also considered. The reason to examine different excitation levels is that the extent of the nonlinearity being exhibited is associated with the excitation levels.

Figure 6-14 (a) and Figure 6-14 (b) show the comparison of the rainflow estimated fatigue life calculated from the linear stress without vibroacoustic coupling (in the blue bars), the nonlinear stress without the vibroacoustic coupling (in the red bars) and the nonlinear stress with vibroacoustic coupling (in the yellow bars). Three different elevated temperatures, 0°C, 50°C and 100°C, were considered. Figure 6-14 (a) is for the plane wave excitation level of 146dB. Figure 6-14 (b) is for the plane wave excitation level of 149dB. The spring foundation boundary conditions was used in all cases.

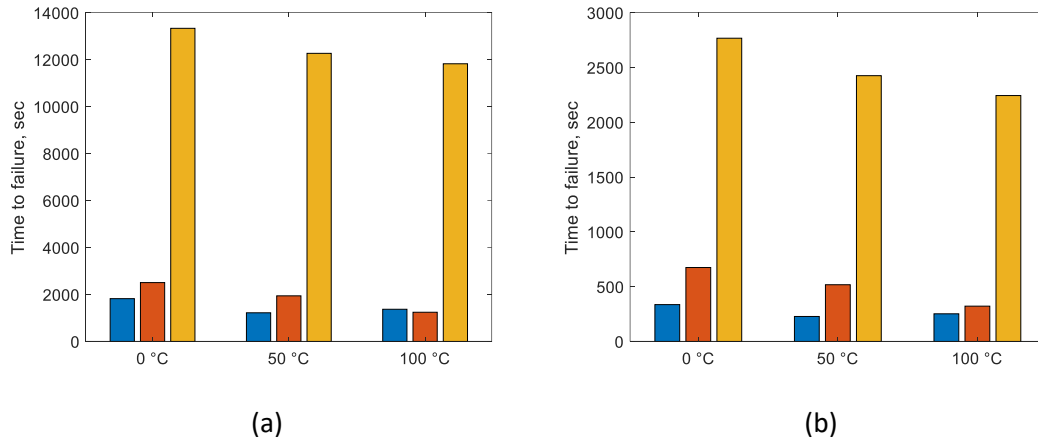


Figure 6-14 Comparison of the fatigue life estimated from the responses with and without the nonlinearity and the vibroacoustic coupling and over three different temperature conditions of 0°C, 50°C and 100°C. The results for the linear, uncoupled predictions are in the blue bars. The results for the nonlinear, uncoupled predictions are in the red bars. The results for the nonlinear, coupled predictions are in the yellow bars. Two different levels of the plane wave excitations, 146dB in (a) and 149dB in (b), are used.

The results show that the yellow bars are about six times larger than the blue and the red bars, which means that the effect of the vibroacoustic coupling on the estimated fatigue life is larger than that of the nonlinearity in all the simulated cases. Compared to the vibroacoustic coupling, the effect of the nonlinearity on the estimated fatigue life increases as the excitation level increases, but it decreases as the temperature increases.

Another observation from the result is that the linear results (blue bars) in Figure 6-14 (a) are smaller compared to those in Figure 6-13 (c). The difference is that the linear response in Figure 6-13 (c) was from the FRF of the linear frequency domain model, but the linear response in Figure 6-14 (a) was from the time domain NLROM without the nonlinear stiffness. A possible reason is that in the linear frequency domain model the radiation damping, which reduces the peak value of the resonance, is only considered for the fundamental mode. In the time domain NLROM, the radiation damping is present in all the included modes..

6.4 Summary

This chapter investigated the effects of the vibroacoustic coupling, nonlinearity and elevated temperature on the fatigue life prediction. The vibroacoustic model and the NLROM of the stiffened plate were used in the predictions. Several spectral methods were compared with each other, including the multi-modal response and the nonlinear behaviour. The time domain rainflow method was used for the fatigue life estimations, which were compared to examine the effects of the different physical conditions and environmental conditions.

The main findings in this chapter are:

- Dirlik's method gives the closest prediction to that of Rainflow counting method when the response has two comparable resonances. The spectral methods overestimate the fatigue life compared to the Rainflow counting method for the nonlinear response.
- The effect of the nonlinearity on the estimated fatigue life is less than that due to vibroacoustic coupling for this level of excitation in the simulations. Compared to the vibroacoustic coupling, the effect of the nonlinearity increases as the excitation level increases, but it decreases as the temperature increases.

Chapter 7 Conclusions and future work

The overall aims of this research were to improve the existing simplified methodology for vibroacoustic response prediction and to achieve a general, efficient and accurate vibroacoustic prediction for thin reinforced structures. Stiffened plate and cylinders were used as particular structural configurations, but in principle the procedures are not limited to just these scenarios. This was achieved by providing a new framework of reduced order structural dynamics models for vibroacoustic predictions that could also be applied in the case of the nonlinear behaviour under high dynamic excitation. The framework can be used as an effective tool to explore and explain the key parameters in the early stage of the design and the optimisation of aerospace structures in harsh conditions, both in terms of elevated sound pressure levels and high temperature.

7.1 Conclusions

The overall outcomes of this research include the findings that stiffeners, curvature, nonlinearity and elevated temperature can have significant impacts on the vibroacoustic response and subsequent fatigue life. This is supported by a number of key conclusions that have been obtained from the numerical/experimental results of the research in addressing and answering the main four research questions.

The first research question is how to improve the existing simplified methodology for estimating the vibroacoustic response of stiffened plates. Based on a relationship between the Joint Acceptance Function (JAF) and the modal radiation efficiency, a linear modal model was improved for the prediction of the vibroacoustic responses of stiffened plates subjected to incident plane wave and diffuse sound fields in Chapter 2. A systematic explanation of the factors influencing the vibration/sound transmission responses for stiffened plates was provided by a numerical study and comparison.

- The results show that the vibroacoustic coupling can be enhanced by the stiffeners, which leads to a significant reduction of the dominant resonance response level for plate structures. Different acoustic excitation types and the modal cross terms affect the sound transmission loss more than the vibration response. The effects of both different excitation types and modal cross-terms contribution are preserved for either the unstiffened or the stiffened plates.

- The strengths of the work are accounting for full vibroacoustic coupling, simplifying the diffuse field analysis and reducing the computational costs. A good agreement between the proposed model and the coupled FE-BE model was achieved with a significant reduction in the computational cost.
- The limitation of the proposed model is that it is not generally applicable for more complex radiation surface geometries, where the coupled FE-BE model might be preferable to be used.

The second research question is whether the prediction method can be extended to analyse and predict the behaviour of a cylinder which is either isotropic or orthogonally stiffened. By including curvature in the structural model, and the rigid scattering in the pressure model, the approach was extended for the vibroacoustic response prediction of the stiffened cylinders subjected to incident plane and spherical wave excitation in Chapter 3. The required formulation for the surface pressure and the JAFs were produced. Numerical examples for cylinders with different stiffener configurations and pressure assumptions were used to explore how the curvature influenced the JAFs and the subsequent response. The surface pressure models were also validated by both numerical simulations and the experimental work on a scaled fuselage model presented in Chapter 4.

- The results show that the presence of curvature can weaken the coincidence effect and the wavelength selectivity as seen in the Joint Acceptance Functions (JAFs), which possess significant features and dominating characteristics for flat plate-like structures.
- The use of the blocked pressure for the subsequent structural response predictions is more accurate than the simple approximation and use of the doubled incident pressure. The pressures predicted by the analytical model of a spherical acoustic wave incident upon an infinite cylinder agree well with measurements.
- For the vibration response results, the agreement with a fully coupled FE-BE model can be improved by taking account of the vibroacoustic coupling by incorporating appropriate values for the radiation damping. The future development of the model is to derive and validate the formulations for evaluating the vibroacoustic coupling for stiffened cylinders.
- The limitation of the work is that limited agreement between the measurement and prediction for the vibration response were obtained, due to the low level and frequency characteristics of the spectrum of the acoustic source and the uncertainty

of the test structure properties and construction details. Additional measurements with other sound sources were initially planned, but could not take place due to the 2020 Covid pandemic.

The third research question is how to incorporate the effects of the nonlinear response and elevated temperature into a general, efficient and accurate structural response prediction. This was achieved by using the nonlinear reduced order model (NLROM), where the nonlinear stiffness and the thermal expansion were characterised using nonlinear static identification.

- The strength of the work was to develop the NLROM to be applicable to more general aerospace structures possessing deep stiffeners and high curvature under elevated thermal conditions.
- The results show that the onset of nonlinearity is initiated at higher excitation levels when there is presence of stiffeners and curvature. Using linearly excited modes up to twice the frequency of the excitation bandwidth in the static nonlinear identification is sufficient to achieve an efficient and accurate approximation for use in the NLROM when compared to the full order FE simulations. For thermally loaded structures, using the hot-mode NLROM produces a more accurate set of simulations compared to the cold-mode NLROM predictions. A trade-off may be required in the selection of the damping and the sample rate when producing the comparison of NLROM and FEM simulations.
- The buckling issue limits the applicability of NLROM to high excitation level and high temperature. For example, the NLROM of the stiffened cylinder is incapable to capture the nonlinear behaviour in high excitation level due to the buckling of the example structure.

The fourth research question concerns the consequences of the vibroacoustic coupling, nonlinearity and elevated temperature on the subsequent acoustic fatigue life. These consequences were investigated in Chapter 6. Use was made of the vibroacoustic model (in Chapter 2) and the NLROM (in Chapter 4) for the stiffened plate to produce the response data with different physical and environmental conditions. The results show that the effect of the nonlinearity on the estimated fatigue life is less than that due to vibroacoustic coupling for this level of excitation for the simulations. Compared to vibroacoustic coupling, the effect of the nonlinear behaviour increases as the excitation level increases, but it decreases as the temperature increases.

There were difficulties and limitations encountered in this research. Firstly, the prime difficulty was in producing the complementary numerical predictions for comparison and validation by the experiment data in Chapter 4. The issue is the construction of an accurate FE model that can replicate a handmade complex structure. The primary sources of error are the modelling of the joints and their variability present in the test structure due to the manufacturing processes. Another issue is in the experimental setup; a source of error is that the physical acoustic source possessed high variations with frequency of the pressure amplitude and low SPL at low frequency. Secondly, some numerical difficulties include convergence issues in applying the NLROM at high excitation levels, temperature rises and for high amounts of curvature. In most cases, these issues are caused by the buckling during the nonlinear static characterisation solution stage. The cold-mode NLROM could help the convergence at higher temperatures with some corresponding detrimental cost in the accuracy, but the stability problems with the hot-mode NLROM were not resolved.

7.2 Future work

More experimental work on the validation of the proposed model is recommended. In this research the surface pressure predictions for cylinders and related approximations were essentially validated experimentally. However, the predictions for the vibration response and the fatigue life were only compared with numerical simulation results. The accuracy of these predictions should be eventually examined by further experiments on plates and cylinders.

More technical work on the development of the proposed model is also recommended. In this study, the formulations accounting for the vibroacoustic coupling effect for stiffened plates were given. However, this effect also plays an important role for thin-walled stiffened cylinders, as shown in Chapter 3. Hence the formulations should be extended for stiffened cylinders as well. The future development of the model is to account for structural geometry that conforms to constant coordinate surfaces in coordinate systems where the acoustic wave equation is separable, such as cylindrical and spherical. In this case, an additional rigid scattering problem has to be solved as discussed in Chapter 3. Rigid scattering from general shaped objects would though have to be performed numerically.

In the future development of the NLROM model, more structural configurations, ideally those with existing experimental results, can be considered. Likewise more investigation into the issues with non-convergence of the nonlinear static characterisation, especially for the hot-mode NLROM for stiffened cylinders, is recommended. The structures considered did not

undergo thermal buckling and this was achieved by suitable refinement and adaptation of the boundary conditions to reproduce a more physically realistic behaviour. There is more research needed in how to solve the thermal static modal solution in a robust manner and then subsequently consider a wider number of forced vibration cases, including exploring the sensitivity and variability when either the conditions or parameters have change from a specified set of conditions.

Appendix 1: Implicit solver description in Abaqus

This appendix briefly describes the implicit nonlinear solver used in Chapter 5. A more comprehensive description of the nonlinear solvers in Abaqus can be found in the Abaqus User's Manual [88]. This appendix references the relative information in [88] for the purpose of providing necessary details and parameters for the full order FE simulations used in Chapter 5. To this end, an example input file for the stiffened plate is also provided. Implicit time integration is used in Abaqus/Standard to calculate the nonlinear transient dynamic or quasi-static response of a system. The 'implicit' is for the type of the time integration operators, which means that the operator matrix must be inverted and a set of simultaneous nonlinear dynamic equilibrium equations must be solved at each time increment. This solution is done iteratively using Newton's method.

Typical dynamic applications in Abaqus are 'transient fidelity', 'moderate dissipation' and 'quasi-static' [88]. The application type selected for the nonlinear implicit time integration is 'transient fidelity'. This type allows for small time increments which are taken to accurately resolve the vibrational response of the structures, and numerical energy dissipation is kept at minimum.

The Hilber-Hughes-Yaylor time integration is used [177]. The parameters for the Hilber-Hughes-Taylor operator are: $\alpha = -0.05$, $\beta = 0.275625$, and $\gamma = 0.55$. In the solver configuration, only α needs to be changed (if necessary), and the other parameters will be adjusted automatically to control the numerical damping while preserving desirable characteristics of the integrator. Negative values of α provide damping; whereas $\alpha = 0$ results in no damping (energy preserving). The setting $\alpha = -1/3$ provides the maximum numerical damping. It gives a damping ratio of about 6% when the time increment is 40% of the period of oscillation of the mode being studied. The Rayleigh damping is used for the material damping in addition to the numerical damping associated with the time integrator

Both the direct time incrementation (fixed time step) and the automatic time incrementation are available in the implicit solver. Initially, the direct time incrementation was used to ensure a fixed time step. However, it was found that this resulted a poor convergence performance for the nonlinear analysis of the structures in Chapter 5. Hence, the automatic time incrementation was used. The time history with the fixed time step can be obtained by interpolating the output data.

The predefined field in the solver can be used to apply the thermal loading. The temperature values are set for both the initial and predefined fields. The temperature difference between these two fields will create the thermal strains. The thermal expansion coefficient is given in the material properties and the temperature field type is isotropic.

To illustrate the parameters and options used in the full order FE analysis, one input file example for the stiffened plate is given in the following.

```
*HEADING

*PART, name=stiffened_plate // define the part name

*NODE

*Include, Input=node_coor_s4r.txt // read the node coordinates from.txt file

*Element, type=S4R // define the element type

*Include, Input=ele_node_s4r.txt // read the node connectivity from .txt file

*Elset, elset=section_roofs, generate // allocate the nodes to the element set
'section_roofs'

9601, 10464, 1

*Shell Section, elset=section_roofs, material=a1, offset=0.5 // define the
shell section

5e-3,

** (allocate nodes to the other 3 element sets and define the shell section,
including 'section_walls', 'section_rib_basis', 'section_bays')

*End Part

*Assembly, name=assembly1

*Instance, name=stiffened_plate_inst, part=stiffened_plate // define the
instance

*End Instance

*Nset, nset=plate_nodes, instance=stiffened_plate_inst, generate // allocate
the node number to node set 'plate_nodes'

1, 9821, 1

** (allocate the node number to the other node sets, including 'all_nodes',
'edges')

*Elset, elset=plate_center_el, instance=stiffened_plate_inst // allocate the
element number to element set 'plate_center_el'
```

```

4840

** (allocate the element number to the other element set 'plate_surface')

*Spring,elset=edges_spring_x // define Spring1 elements in the x direction

1 // degree of freedom

1e5. // real spring stiffness

*Element, type=Spring1, elset=edges_spring_x // allocate the Spring1 elements
from the instance

*Include, Input=ele_node_spr1.txt

** (define and allocate the Spring1 elements in the y direction)

*End Assembly

*Amplitude, name=random_pressure146dB // define the time history for the random
pressure amplitude

*Include, Input=random_pressure146dB30s50kHz.txt

*Material, name=al // define material properties

*Density

2700.,

*Elastic

70e+9,0.33

*Damping, beta=4.8302e-5

*Expansion, type=iso

10.5e-6

*Initial Conditions, type=temperature // define initial temperature field

all_nodes,0.

*Step, name=hot,nlgeom=yes // define the step of applying the temperature field

*Static

0.1,10,1e-4,10.

*Boundary // define the boundary conditions for static step

edges,3,3

edges,4,4

edges,5,5

edges,6,6

```

```

*Temperature // define the temperature rise of 50 °C

all_nodes,50.

*End Step

*Step, name=forced, nlgeom=yes, inc=1510001 // define the dynamic analysis
step with nonlinear option open, a maximum number of incrementation 1510001

*Dynamic

2e-5, 30, 1e-10,2e-5 // suggested initial time increment of 2e-5; time period
of 30; minimum time increment of 1e-10; maximum time increment of 2e-5

*Boundary // boundary conditions for dynamic step

edges, 3,3

edges, 4,4

edges, 5,5

edges, 6,6

*Dload, amplitude=random_pressure146dB // define the distributed load

PLATE_SURFACE, P, 1

*Restart, write, overlay, frequency=1000 // configure the writing of the
restart data, the restart information is written every 1000 increments

*Output, field, frequency=1 // configure the writing of the output data, the
output information is written every increment

*Node Output, nset=PLATE_CENTER // configure the output node set

UT,

*Element Output, direction=yes, elset=PLATE_CENTER_EL // configure the output
element set

S,

*End Step

```

Appendix 2: Dirlik's method for fatigue estimation

The expected fatigue damage D is

$$D = \frac{T}{K_r} F_p S_{eq}^b$$

where T is the time length of the signal. F_p is the expected value of the peak occurrence rate, which can be expressed in terms of the moments of the PSD function as

$$F_p = \left(\frac{m_4}{m_2} \right)^{0.5}$$

S_{eq}^b is the equivalent stress to the power b and is given as

$$S_{eq}^b = D_1 (2\sigma_s Q)^b \Gamma(b+1) + \left(2^{\frac{3}{2}} \sigma_s \right)^b \Gamma\left(1 + \frac{b}{2}\right) [D_2 R^b + D_3]$$

where

$$D_1 = \frac{2(\chi_m - \gamma^2)}{1 + \gamma^2},$$

$$D_2 = \frac{(1 - \gamma - D_1 + D_1^2)}{1 - R}$$

$$D_3 = 1 - D_1 - D_2$$

$$Q = \frac{1.25(\gamma - D_3 - D_2 R)}{D_1}$$

$$R = \frac{(\gamma - \chi_m - D_1^2)}{1 - \gamma - D_1 + D_1^2}$$

$$\gamma = \frac{m_2}{(m_0 m_4)^{0.5}}$$

$$\chi_m = \left(\frac{m_1}{m_0} \right) \left(\frac{m_2}{m_4} \right)^{0.5}$$

List of References

- [1] J. J. Hollkamp, "Experiences with nonlinear modeling and acoustic fatigue," *Journal of Sound and Vibration*, Article vol. 437, pp. 437-446, 2018, doi: 10.1016/j.jsv.2018.04.029.
- [2] J. W. Miles, "On Structural Fatigue Under Random Loading," *Journal of the Aeronautical Sciences*, vol. 21, no. 11, pp. 753-762, 1954, doi: 10.2514/8.3199.
- [3] M. A. Miner, "Cumulative damage in fatigue," *J. Appl. Mech.*, vol. 12, no. 3, pp. A159-A164, 1945.
- [4] A. Powell, "On the fatigue failure of structures due to vibrations excited by random pressure fields," *The Journal of the Acoustical Society of America*, vol. 30, no. 12, pp. 1130-1135, 1958, doi: 10.1121/1.1909481.
- [5] B. L. Clarkson, "Stresses in skin panels subjected to random acoustic loading," *The Aeronautical Journal of the Royal Aeronautical Society*, vol. 72, pp. 1000-1010, 1967.
- [6] AGARD, "Symposium on Acoustic Fatigue, in: 35th meeting of the Structures and Materials Panel," Toulouse, France, 1972: North Atlantic Treaty Organization, Advisory Group for Aerospace Research and Development.
- [7] W. J. Trapp and D. M. Forney, *Acoustical fatigue in aerospace structures*. Ohio: Syracuse University Press, 1965.
- [8] P. R. McGowan, "Structural design for acoustic fatigue," Douglas Aircraft Company, Inc., California, ASD-TDR-63-820, 1963.
- [9] J. A. Cockburn and A. C. Jolly, "Structural-acoustic response, noise transmission losses and interior noise levels of an aircraft fuselage excited by random pressure fields," Air Force Flight Dynamics Laboratory, Alabama, AFFDL-TR-68-2, 1968.
- [10] F. F. Rudder and H. E. Plumblee, "Sonic fatigue design guide for military aircraft," AF Flight Dynamics Laboratory, Ohio, AFFDL-TR-74-112, 1975.
- [11] C. Mei and D. B. Paul, "Nonlinear multimode response of clamped rectangular plates to acoustic loading," *AIAA Journal*, vol. 24, no. 4, pp. 643-648, 1986, doi: 10.2514/3.9320.
- [12] T. K. Caughey, "Derivation and Application of the Fokker-Planck Equation," *Journal of the Acoustical Society of America*, vol. 35, no. 11, pp. 1683-1691, 1963, doi: 10.1121/1.1937117.
- [13] T. K. Caughey, "Nonlinear Theory of Random Vibrations," in *Advances in Applied Mechanics*, vol. 11, C.-S. Yih Ed.: Elsevier, 1971, pp. 209-253.
- [14] S. H. Crandall, "Perturbation Techniques for Random Vibration of Nonlinear Systems," *The Journal of the Acoustical Society of America*, vol. 35, no. 11, pp. 1700-1705, 1963, doi: 10.1121/1.1918792.
- [15] S. T. Ariaratnam, "Response of a Loaded Nonlinear String to Random Excitation," *Journal of Applied Mechanics*, vol. 29, no. 3, pp. 483-485, 1962, doi: 10.1115/1.3640592.
- [16] T. S. Atalik and S. Utku, "Stochastic linearization of multi-degree-of-freedom non-linear systems," *Earthquake Engineering & Structural Dynamics*, vol. 4, no. 4, pp. 411-420, 1976, doi: 10.1002/eqe.4290040408.
- [17] W. D. Iwan and I. M. Yang, "Application of Statistical Linearization Techniques to Nonlinear Multidegree-of-Freedom Systems," *Journal of Applied Mechanics*, vol. 39, no. 2, pp. 545-550, 1972, doi: 10.1115/1.3422714.
- [18] E. T. Moyer, "Response of composite plates subjected to acoustic loading," National Aeronautics and Space Administration, Washington, DC, NASA-CR-184618, 1989.
- [19] C. Mei, "Nonlinear analysis of composite aerospace structures in sonic fatigue," Old Dominion University, Virginia, NASA-CR-190565, 1991.

- [20] R. R. Chen, C. Mei, and H. F. Wolfe, "Comparison of finite element non-linear beam random response with experimental results," *Journal of Sound and Vibration*, vol. 195, no. 5, pp. 719-737, 1996, doi: <https://doi.org/10.1006/jsvi.1996.0458>.
- [21] C. Mei and R. R. Chen, "Finite Element Nonlinear Random Response of Composite Panels of Arbitrary Shape to Acoustic and Thermal Loads," Old Dominion University, WL-TR-1997-3085, 1997.
- [22] K. Abdel-Motagaly, B. Duan, and C. Mei, "Nonlinear Response of Composite Panels Under Combined Acoustic Excitation and Aerodynamic Pressure," *AIAA Journal*, vol. 38, no. 9, pp. 1534-1542, 2000, doi: 10.2514/2.1175.
- [23] J.-M. Dhainaut, X. Guo, C. Mei, S. M. Spottswood, and H. F. Wolfe, "Nonlinear Random Response of Panels in an Elevated Thermal-Acoustic Environment," *Journal of Aircraft*, vol. 40, no. 4, pp. 683-691, 2003, doi: 10.2514/2.3146.
- [24] R. Vaicaitis, E. H. Dowell, and C. S. Ventres, "Nonlinear Panel Response by a Monte Carlo Approach," *AIAA Journal*, vol. 12, no. 5, pp. 685-691, 1974, doi: 10.2514/3.49320.
- [25] R. D. Blevins, "Non-Gaussian Narrow-Band Random Fatigue," *Journal of Applied Mechanics*, vol. 69, no. 3, pp. 317-324, 2002, doi: 10.1115/1.1428332.
- [26] A. Radu, K. Kim, B. Yang, and M. Mignolet, "Prediction of the Dynamic Response and Fatigue Life of Panels Subjected to Thermo-Acoustic Loading," presented at the 45th AIAA/ASME/ASCE/AHS/ASC Structures, Structural Dynamics & Materials Conference, 2004. [Online]. Available: <https://arc.aiaa.org/doi/abs/10.2514/6.2004-1557>.
- [27] Y. Xiao, R. G. White, and G. S. Aglietti, "An experimental characterization of the acoustic fatigue endurance of GLARE and comparison with that of CFRP," *Composite Structures*, vol. 68, no. 4, pp. 455-470, 2005, doi: 10.1016/j.compstruct.2004.04.011.
- [28] H. F. Wolfe, C. A. Shroyer, D. L. Brown, and L. W. Simmons, "An experimental investigation of nonlinear behaviour of beams and plates excited to high levels of dynamic response," Wright Laboratory, WL-TR-96-3057, 1995.
- [29] S. M. Spottswood and H. F. Wolfe, "Comparing Fatigue Life Estimates Using Experimental and Spectral Density Based Probability Distributions," *Journal of Aircraft*, vol. 39, no. 3, pp. 493-498, 2002, doi: 10.2514/2.2955.
- [30] J. Q. Sun and R. N. Miles, "Acoustic fatigue life prediction for non-linear structures," *Journal of Sound & Vibration*, vol. 150, no. 3, pp. 531-535, 1991.
- [31] C. Mei and C. B. Prasad, "Effects of Large Deflection and Transverse Shear on Response of Rectangular Symmetric Composite Laminates Subjected to Acoustic Excitation," *Journal of Composite Materials*, vol. 23, no. 6, pp. 606-639, 1989, doi: 10.1177/002199838902300605.
- [32] M. P. Singh, A. A. Khdeir, G. O. Maldonado, and J. N. Reddy, "Random response of antisymmetric angle-ply laminated plates," *Structural Safety*, vol. 6, no. 2, pp. 115-127, 1989, doi: [https://doi.org/10.1016/0167-4730\(89\)90014-3](https://doi.org/10.1016/0167-4730(89)90014-3).
- [33] D. Tougaard, "Brite-Euram programme: ACOUFAT acoustic fatigue and related damage tolerance of advanced composite and metallic structures," in *Advances in Acoustics Technology*. Chichester: Wiley, 1995, pp. 83-195.
- [34] M. P. Mignolet, A. Przekop, S. A. Rizzi, and S. M. Spottswood, "A review of indirect/non-intrusive reduced order modeling of nonlinear geometric structures," *Journal of Sound and Vibration*, vol. 332, no. 10, pp. 2437-2460, 2013, doi: <https://doi.org/10.1016/j.jsv.2012.10.017>.
- [35] E. J. Richards and D. J. Mead, "Elements of periodic vibration theory," in *Noise and acoustic fatigue in aeronautics*. London: Wiley, 1968, ch. 13, pp. 296-297.
- [36] D. J. Bozich, "Spatial Correlation in Acoustic-Structural Coupling," *The Journal of the Acoustical Society of America*, vol. 34, no. 12, pp. 1989-1989, 1962, doi: 10.1121/1.1937052.

- [37] C. E. Wallace, "Structural response and acoustic fatigue for random progressive waves and diffuse fields," *Journal of Spacecraft and Rockets*, vol. 22, no. 3, pp. 340-344, 1985, doi: 10.2514/3.25753.
- [38] R. D. Blevins, "An approximate method for sonic fatigue analysis of plates and shells," *Journal of Sound and Vibration*, vol. 129, no. 1, pp. 51-71, 1989.
- [39] J. M. Larko; and V. Cotoni, "Vibroacoustic response of the NASA ACTS Spacecraft Antenna to Launch Acoustic Excitation," NASA, Ohio, NASA/TM-2008-215168, 2008.
- [40] E. P. Division, *Structural acoustics design manual*. The Netherlands: ESA Publications Division, 1996.
- [41] J. P. Coyette, G. Lielens, M. Robbe, and P. Neple, "An efficient method for evaluating diffuse field joint acceptance functions for cylindrical and truncated conical geometries," *Journal of the Acoustical Society of America*, vol. 117, no. 3, pp. 1009-1019, 2005, doi: 10.1121/1.1850368.
- [42] A. R. Wenzel, "Pressure Correlation for a Cylinder in a Diffuse Sound Field," *The Journal of the Acoustical Society of America*, vol. 41, no. 6, pp. 1459-1466, 1967, doi: 10.1121/1.1910507.
- [43] A. Wenzel, "Joint acceptance for cylinders," Wyle Laboratories, Huntsville, WR 67-9, 1967.
- [44] Aerospaceengineering.net. "Verifying of a fuselage frame symmetrically loaded." (accessed 21-12, 2018).
- [45] A. L. Abrahamson, "The response of periodic structures to aero-acoustic pressures, with particular reference to aircraft skin-rib spar structures," PhD, Institute of sound and vibration research, University of Southampton, Southampton, 1973.
- [46] L. Dozio and M. Ricciardi, "Free vibration analysis of ribbed plates by a combined analytical-numerical method," *Journal of Sound and Vibration*, vol. 319, no. 1-2, pp. 681-697, 2009, doi: 10.1016/j.jsv.2008.06.024.
- [47] A. Mejdí and N. Atalla, "Dynamic and acoustic response of bidirectionally stiffened plates with eccentric stiffeners subject to airborne and structure-borne excitations," *Journal of Sound and Vibration*, vol. 329, no. 21, pp. 4422-4439, 2010, doi: <https://doi.org/10.1016/j.jsv.2010.04.007>.
- [48] D. M. Egle and J. L. Sewall, "An analysis of free vibration of orthogonally stiffened cylindrical shells with stiffeners treated as discrete elements," *AIAA Journal*, vol. 6, no. 3, pp. 518-526, 1968, doi: 10.2514/3.4528.
- [49] A. Rosen and J. Singer, "Vibrations of axially loaded stiffened cylindrical shells," *Journal of Sound and Vibration*, vol. 34, no. 3, p. 357, 1974, doi: [https://doi.org/10.1016/S0022-460X\(74\)80317-2](https://doi.org/10.1016/S0022-460X(74)80317-2).
- [50] ESDU, "Vibration and Acoustic Fatigue," in "Engineering Sciences Data Unit Design Guide Series," ESDU International, London, 1997, vol. Vol 1-7.
- [51] A. Rosen and J. Singer, "Vibrations of axially loaded stiffened cylindrical shells," *Journal of Sound and Vibration*, vol. 34, no. 3, pp. 357-IN3, 1974, doi: [https://doi.org/10.1016/S0022-460X\(74\)80317-2](https://doi.org/10.1016/S0022-460X(74)80317-2).
- [52] L. H. Donnell, "Stability of thin-walled tubes under torsion," National advisory committee for aeronautics, No. 479, 1933.
- [53] W. Flügge, *Statik und Dynamik der Schalen*. Berlin: Springer, 1957.
- [54] C. M. Wang, S. Swaddiwudhipong, and J. Tian, "Ritz Method for Vibration Analysis of Cylindrical Shells with Ring Stiffeners," *Journal of Engineering Mechanics*, vol. 123, no. 2, pp. 134-142, 1997, doi: doi:10.1061/(ASCE)0733-9399(1997)123:2(134).
- [55] S. Parthan and D. J. Johns, "Vibration and flutter of unstiffened and orthogonally stiffened circular cylindrical shells," Loughborough University of Technology, UK, TT 7106, 1971.

- [56] M. Bagheri and A. A. Jafari, "Analytical and experimental modal analysis of nonuniformly ring-stiffened cylindrical shells," *Archive of Applied Mechanics*, vol. 75, pp. 177-191, 2006.
- [57] A. Sestieri and A. Carcaterra, "Vibroacoustic: The challenges of a mission impossible?," *Mechanical Systems and Signal Processing*, vol. 34, no. 1, pp. 1-18, 2013, doi: <https://doi.org/10.1016/j.ymssp.2012.08.010>.
- [58] T. Beberniss and R. Gordon, "Finite Element Prediction of Acoustic Radiation Damping," presented at the 49th AIAA/ASME/ASCE/AHS/ASC Structures, Structural Dynamics, and Materials Conference, Schaumburg, USA, 2008.
- [59] R. S. Langley, "A Dynamic Stiffness/Boundary Element Method for the Prediction of Interior Noise Levels," *Journal of Sound and Vibration*, vol. 163, no. 2, pp. 207-230, 1993, doi: <https://doi.org/10.1006/jsvi.1993.1161>.
- [60] G. Rodrigues and J. Santiago-Prowald, "Qualification of Spacecraft Equipment: Random-Vibration Response Based on Impedance/Mobility Techniques," *Journal of Spacecraft and Rockets*, vol. 45, no. 1, pp. 104-115, 2008, doi: 10.2514/1.29734.
- [61] H. Djojodihardjo, "BEM-FEM acoustic-structural coupling for spacecraft structure incorporating treatment of irregular frequencies," *International Astronautical Federation - 58th International Astronautical Congress 2007*, vol. 8, 2007.
- [62] B. Rafaely, "Spatial-temporal correlation of a diffuse sound field," *The Journal of the Acoustical Society of America*, vol. 107, no. 6, pp. 3254-3258, 2000, doi: 10.1121/1.429397.
- [63] D. M. Mead, "wave propagation in continuous periodic structures: research contributions from southampton 1964 - 1995," *Journal of Sound and Vibration*, vol. 190, no. 3, pp. 495-524, 1996, doi: <https://doi.org/10.1006/jsvi.1996.0076>.
- [64] F. Errico, M. Ichchou, S. De Rosa, O. Bareille, and F. Franco, "A WFE and Hybrid FE/WFE technique for the Forced Response of Stiffened Cylinders," *Advances in Aircraft and Spacecraft Science*, vol. 5, pp. 1-19, 2018, doi: 10.12989/aas.2018.5.1.001.
- [65] J. M. Renno and B. R. Mace, "On the forced response of waveguides using the wave and finite element method," *Journal of Sound and Vibration*, vol. 329, no. 26, pp. 5474-5488, 2010, doi: <https://doi.org/10.1016/j.jsv.2010.07.009>.
- [66] B. R. Mace and E. Manconi, "Modelling wave propagation in two-dimensional structures using finite element analysis," *Journal of Sound and Vibration*, vol. 318, no. 4, pp. 884-902, 2008, doi: <https://doi.org/10.1016/j.jsv.2008.04.039>.
- [67] C. M. Nilsson, A. N. Thite, C. J. C. Jones, and D. J. Thompson, "Estimation of Sound Transmission through Extruded Panels Using a Coupled Waveguide Finite Element-Boundary Element Method," Berlin, Heidelberg, 2008: Springer Berlin Heidelberg, in *Noise and Vibration Mitigation for Rail Transportation Systems*, pp. 306-312.
- [68] H. Li *et al.*, "Using a 2.5D boundary element model to predict the sound distribution on train external surfaces due to rolling noise," *Journal of Sound and Vibration*, vol. 486, p. 115599, 2020, doi: <https://doi.org/10.1016/j.jsv.2020.115599>.
- [69] Y. K. Lin and T. J. McDaniel, "Dynamics of Beam-Type Periodic Structures," *Journal of Manufacturing Science and Engineering*, vol. 91, no. 4, pp. 1133-1141, 1969, doi: 10.1115/1.3591761.
- [70] J. P. Henderson and T. J. McDaniel, "The analysis of curved multi-span structures," *Journal of Sound and Vibration*, vol. 18, no. 2, pp. 203-219, 1971, doi: [https://doi.org/10.1016/0022-460X\(71\)90345-2](https://doi.org/10.1016/0022-460X(71)90345-2).
- [71] D. J. Mead, "Vibration Response and Wave Propagation in Periodic Structures," *Journal of Manufacturing Science and Engineering*, vol. 93, no. 3, pp. 783-792, 1971, doi: 10.1115/1.3428014.

- [72] B. R. Mace, "Periodically stiffened fluid-loaded plates, I: Response to convected harmonic pressure and free wave propagation," *Journal of Sound and Vibration*, vol. 73, no. 4, pp. 473-486, 1980, doi: [https://doi.org/10.1016/0022-460X\(80\)90662-8](https://doi.org/10.1016/0022-460X(80)90662-8).
- [73] B. R. Mace, "Periodically stiffened fluid-loaded plates, II: Response to line and point forces," *Journal of Sound and Vibration*, vol. 73, no. 4, pp. 487-504, 1980, doi: [https://doi.org/10.1016/0022-460X\(80\)90663-X](https://doi.org/10.1016/0022-460X(80)90663-X).
- [74] D. J. Mead, "A new method of analyzing wave propagation in periodic structures; Applications to periodic timoshenko beams and stiffened plates," *Journal of Sound and Vibration*, vol. 104, no. 1, pp. 9-27, 1986, doi: [https://doi.org/10.1016/S0022-460X\(86\)80128-6](https://doi.org/10.1016/S0022-460X(86)80128-6).
- [75] D. J. Mead, "A general theory of harmonic wave propagation in linear periodic systems with multiple coupling," *Journal of Sound and Vibration*, vol. 27, no. 2, pp. 235-260, 1973, doi: [https://doi.org/10.1016/0022-460X\(73\)90064-3](https://doi.org/10.1016/0022-460X(73)90064-3).
- [76] F. J. Fahy and P. Gardonio, *Sound and structural vibration : radiation, transmission and response*. Oxford, UK: Academic Press, 2007.
- [77] D. J. Thompson, "Noise control," in *Fundamentals of sound and vibration*. London: CRC Press, 2015, ch. 5, p. 292.
- [78] C. E. Wallace, "Radiation Resistance of a Rectangular Panel," *The Journal of the Acoustical Society of America*, vol. 51, no. 3B, pp. 946-952, 1972, doi: 10.1121/1.1912943.
- [79] R. H. Lyon, *Statistical energy analysis of dynamical systems : theory and applications*. United States: MIT Press, 1975.
- [80] F. J. Fahy, "Statistical energy analysis: a critical overview," *Philosophical Transactions of the Royal Society of London. Series A: Physical and Engineering Sciences*, vol. 346, no. 1681, pp. 431-447, 1994, doi: 10.1098/rsta.1994.0027.
- [81] R. H. Lyon, R. G. DeJong, and R. H. Lyon, *Theory and application of statistical energy analysis*. Boston: Butterworth-Heinemann, 1995.
- [82] T. Irvine, "Vibration response of a thin cylindrical shell to external acoustic pressure via statistical energy analysis," *Vibrationdata.com*, 2008.
- [83] T. Irvine, "Vibration response of a cylindrical skin to acoustic pressure via the franken method," *Vibrationdata.com*, 2008.
- [84] P. J. Shorter and R. S. Langley, "Vibro-acoustic analysis of complex systems," *Journal of Sound and Vibration*, vol. 288, no. 3, pp. 669-699, 2005, doi: <https://doi.org/10.1016/j.jsv.2005.07.010>.
- [85] V. Cotoni, P. Shorter, and R. Langley, "Numerical and experimental validation of a hybrid finite element-statistical energy analysis method," *The Journal of the Acoustical Society of America*, vol. 122, no. 1, pp. 259-270, 2007, doi: 10.1121/1.2739420.
- [86] B. L. Clarkson, "Review of sonic fatigue technology," National Aeronautics and Space Administration, Hampton, Virginia, CP-4587, 1994.
- [87] R. W. Gordon and J. J. Hollkamp, "Reduced order models for acoustic response prediction," Air Force Research Laboratory, United States, AFRL-RB-WP-TR-2011-3040, 2011.
- [88] M. Smith, *ABAQUS/Standard User's Manual, Version 6.9*. Simulia, 2009.
- [89] M. I. McEwan, "A combined modal/finite element technique for the non-linear dynamic simulation of aerospace structures," PhD, University of Manchester, UK, 2001.
- [90] M. I. McEwan, J. R. Wright, J. E. Cooper, and A. Y. T. Leung, "A combined modal finite element analysis technique for the dynamic response of a nonlinear beam to harmonic excitation," *Journal of Sound and Vibration*, vol. 243, no. 4, pp. 601-624, 2001, doi: <https://doi.org/10.1006/jsvi.2000.3434>.

- [91] S. A. Rizzi and A. Przekop, "System identification-guided basis selection for reduced-order nonlinear response analysis," *Journal of Sound and Vibration*, vol. 315, no. 3, pp. 467-485, 2008, doi: <https://doi.org/10.1016/j.jsv.2007.12.031>.
- [92] S. A. Rizzi and A. Przekop, "The Effect of Basis Selection on Static and Random Acoustic Response Prediction Using a Nonlinear Modal Simulation," NASA Langley Research Center, Washington, DC, NASA/TP-2005-213943, 2005. [Online]. Available: <https://books.google.co.uk/books?id=7nPBzQEACAAJ>
- [93] S. Spottswood, T. Eason, X. Q. Wang, and M. Mignolet, "Nonlinear Reduced Order Modeling of Curved Beams: A Comparison of Methods," in *50th AIAA/ASME/ASCE/AHS/ASC Structures, Structural Dynamics, and Materials Conference*. California, 2009.
- [94] ESDU, "Introduction and guide to ESDU data on acoustic fatigue," in "Vibration and Acoustic Fatigue," ESDU International, London, 2020.
- [95] ESDU, "Fatigue damage and life under random loading," in "Vibration and Acoustic Fatigue," ESDU International, London, 2006.
- [96] ESDU, "Cycle counting methods for the estimation of fatigue life," in "Vibration and Acoustic Fatigue," ESDU International, London, 2006.
- [97] ESDU, "Spectral methods for the estimation of fatigue life," in "Vibration and Acoustic Fatigue," ESDU International, London, 2006.
- [98] R. N. Miles, "Effect of spectral shape on acoustic fatigue life estimates," *Journal of Sound and Vibration*, vol. 153, no. 2, pp. 376-386, 1992, doi: [https://doi.org/10.1016/S0022-460X\(05\)80015-X](https://doi.org/10.1016/S0022-460X(05)80015-X).
- [99] D. Benasciutti, F. Sherratt, and A. Cristofori, "Recent developments in frequency domain multi-axial fatigue analysis," *International Journal of Fatigue*, vol. 91, pp. 397-413, 2016, doi: 10.1016/j.ijfatigue.2016.04.012.
- [100] N. Bishop and F. Sherratt, *Fatigue life prediction from power spectral density data*. University of Warwick, 1989, pp. 11-19.
- [101] D. E. Newland, "Application notes," in *An Introduction to Random Vibrations, Spectral & Wavelet Analysis*, 3 ed. United Kingdom: Longman Group UK Ltd., 1994, sec. 2, pp. 191-196.
- [102] N. Dowling, "Fatigue Failure Predictions for Complicated Stress-Strain Histories," University of Illinois, Illinois, NO.337, 1971, vol. 7.
- [103] P. H. Wirsching and A. M. Shehata, "Fatigue Under Wide Band Random Stresses Using the Rain-Flow Method," *Journal of Engineering Materials and Technology*, vol. 99, no. 3, pp. 205-211, 1977, doi: 10.1115/1.3443520.
- [104] S. D. Downing and D. F. Socie, "Simple rainflow counting algorithms," *International Journal of Fatigue*, vol. 4, no. 1, pp. 31-40, 1982, doi: [https://doi.org/10.1016/0142-1123\(82\)90018-4](https://doi.org/10.1016/0142-1123(82)90018-4).
- [105] G. Lindgren and I. Rychlik, "Rain flow cycle distributions for fatigue life prediction under Gaussian load progresses," *Fatigue & Fracture of Engineering Materials & Structures*, vol. 10, no. 3, pp. 251-260, 1987, doi: doi:10.1111/j.1460-2695.1987.tb00482.x.
- [106] A. K. Khosrovaneh and N. E. Dowling, "Fatigue loading history reconstruction based on the rainflow technique," *International Journal of Fatigue*, vol. 12, no. 2, pp. 99-106, 1990, doi: [https://doi.org/10.1016/0142-1123\(90\)90679-9](https://doi.org/10.1016/0142-1123(90)90679-9).
- [107] C. Amzallag, J. P. Gerey, J. L. Robert, and J. Bahuaud, "Standardization of the rainflow counting method for fatigue analysis," *International Journal of Fatigue*, vol. 16, no. 4, pp. 287-293, 1994, doi: [https://doi.org/10.1016/0142-1123\(94\)90343-3](https://doi.org/10.1016/0142-1123(94)90343-3).
- [108] Z. Li, J. W. Ringsberg, and G. Storhaug, "Time-domain fatigue assessment of ship side-shell structures," *International Journal of Fatigue*, vol. 55, pp. 276-290, 2013, doi: <https://doi.org/10.1016/j.ijfatigue.2013.07.007>.

- [109] P. H. Wirsching and M. C. Light, "Fatigue under Wide Band Random Stresses," *Journal of the Structural Division*, vol. 106, no. 7, pp. 1593-1607, 1980, doi: doi:10.1061/JSDEAG.0005477.
- [110] T. Dirlik, "Application of computers in fatigue analysis," Ph.D, University of Warwick, UK, 1985.
- [111] D. E. Newland, "Transmission of random vibration," in *An Introduction to Random Vibrations, Spectral & Wavelet Analysis*, 3 ed. United Kindom: Longman Group UK Ltd., 1994, ch. 7, sec. 2, p. 79.
- [112] D. J. Johns, "Fundamentals of Thermal Stress Analysis," in *Thermal Stress Analyses*. Oxford: Pergamon Press, 1965, pp. 1-20.
- [113] S. Timoshenko and S. Woinowsky-Krieger, *Theory of plates and shells*. New York: McGraw-Hill, 1959.
- [114] R. G. Budynas, W. C. Young, and A. M. Sadegh, "Dynamic and temperature stresses," in *Roark's Formulas for Stress and Strain*: McGraw-Hill Education, 2011, ch. 15, pp. 582-587.
- [115] K. T. Sundara Raja Iyengar and K. Chandrashekhara, "Thermal stresses in rectangular plates," *Applied Scientific Research, Section A*, journal article vol. 15, no. 1, pp. 141-160, 1966, doi: 10.1007/bf00411552.
- [116] J. Lee, "Large-Amplitude Plate Vibration in an Elevated Thermal Environment," *Applied Mechanics Reviews*, vol. 46, no. 11S, pp. S242-S254, 1993, doi: 10.1115/1.3122643.
- [117] C. Mei, J. M. Dhainaut, B. Duan, S. M. Spottswood, and H. F. Wolfe, "Nonlinear random response of composite panels in an elevated thermal environment," Old Dominion University, United States, AFRL-VA-WP-TR-2000-3049, 2000.
- [118] J. S. Mixson and L. A. Roussos, "Acoustic fatigue: overview of activities at NASA Langley," NASA TM 89143, 1987.
- [119] C. F. Ng and S. A. Clevenson, "High intensity acoustic tests of a thermally stressed aluminum plate in TAFA," NASA Langley Research Center, United States, NASA-TM-101552, 1989.
- [120] M. C. Lin and M. K. Yeh, "Buckling of elastoplastic circular cylindrical shells under axial compression," *AIAA Journal*, vol. 32, no. 11, pp. 2309-2315, 1994, doi: 10.2514/3.12291.
- [121] A. Przekop, S. A. Rizzi, and K. A. Sweitzer, "An investigation of high-cycle fatigue models for metallic structures exhibiting snap-through response," *International Journal of Fatigue*, vol. 30, no. 9, pp. 1579-1598, 2008, doi: 10.1016/j.ijfatigue.2007.11.011.
- [122] Y. D. Sha, J. Wei, Z. J. Gao, and H. J. Zhong, "Nonlinear response with snap-through and fatigue life prediction for panels to thermo-acoustic loadings," *Journal of Vibration and Control*, vol. 20, no. 5, pp. 679-697, 2014, doi: 10.1177/1077546312463751.
- [123] J. Ge, Y. Sun, J. Xu, Z. Yang, and J. Liang, "Fatigue life prediction of metal structures subjected to combined thermal-acoustic loadings using a new critical plane model," *International Journal of Fatigue*, vol. 96, pp. 89-101, 2017, doi: <https://doi.org/10.1016/j.ijfatigue.2016.11.023>.
- [124] B&K, "BAE Systems Advanced Noise and Vibration Testing Facilities at Warton and Brough," Brüel& Kjær Sound & Vibration Measurement A/S, United Kingdom, 2005.
- [125] S. A. Clevenson and E. F. Daniels, "Capabilities of the thermal acoustic fatigue apparatus," Langley Research Center, Virginia, NASA-TM-104106, 1992.
- [126] J. Pearson, "High temperature acoustic test facilities and methods," in *AGARD Conference Proceedings*, 1994, p. 549.

- [127] G. Bayerdorfer and L. Freyberg, "Design and operation of a thermoacoustic test facility," presented at the Symposium on Impact of Acoustic Loads on Aircraft Structures, Lillehammer, Norway, 1994.
- [128] Y. Y. Lee, C. F. Ng, and X. Guo, "Nonlinear Random Response of Cylindrical Panels to Acoustic Excitations Using Finite Element Modal Method," *Nonlinear Dynamics*, vol. 31, pp. 327-345, 2003.
- [129] P. R. Cunningham and R. G. White, "Dynamic response of doubly curved honeycomb sandwich panels to random acoustic excitation. Part 1: Experimental study," *Journal of Sound and Vibration*, vol. 264, no. 3, pp. 579-603, 2003, doi: 10.1016/s0022-460x(02)01210-5.
- [130] P. R. Cunningham, R. S. Langley, and R. G. White, "Dynamic response of doubly curved honeycomb sandwich panels to random acoustic excitation. Part 2: Theoretical study," *Journal of Sound and Vibration*, vol. 264, no. 3, pp. 605-637, 2003, doi: 10.1016/s0022-460x(02)01211-7.
- [131] Y. Xiao, R. G. White, and G. S. Aglietti, "Comparison of structural response and fatigue endurance of aircraft flap-like box structures subjected to acoustic loading," *The Journal of the Acoustical Society of America*, vol. 117, no. 5, pp. 2820-2834, 2005, doi: 10.1121/1.1853934.
- [132] X. Guo, Y.-Y. Lee, and C. Mei, "Non-linear random response of laminated composite shallow shells using finite element modal method," *International Journal for Numerical Methods in Engineering*, vol. 67, no. 10, pp. 1467-1489, 2006, doi: doi:10.1002/nme.1672.
- [133] M. Esmailzadeh, A. A. Lakis, M. Thomas, and L. Marcouiller, "Prediction of the response of a thin structure subjected to a turbulent boundary-layer-induced random pressure field," *Journal of Sound and Vibration*, vol. 328, no. 1, pp. 109-128, 2009. [Online]. Available: <http://www.sciencedirect.com/science/article/pii/S0022460X09006191>.
- [134] A. Wenzel, "Surface pressure correlation function for a cylinder in a diffuse reverberant sound field," Wyle laboratory, WR 66-14, 1966.
- [135] M. G. Cottis and J. G. Jasonides, "The response of a finite thin cylindrical shell to random pressure fields," in *Acoustical Fatigue in Aerospace Structures*, New York, 1965, New York: Syracuse University Press, pp. 185-212.
- [136] P. H. White, "Sound Transmission through a Finite, Closed, Cylindrical Shell," *The Journal of the Acoustical Society of America*, vol. 40, no. 5, pp. 1124-1130, 1966, doi: 10.1121/1.1910197.
- [137] D. J. Bozich and R. W. White, "A study of the vibration response of shells and plates to fluctuating pressure environments," NASA, Washington, NAS9-7484, 1970.
- [138] A. W. Leissa, *Vibration of shells*. Ohio: National Aeronautics and Space Administration, 1973.
- [139] M. Rajabi and M. Behzad, "Interaction of a plane progressive sound wave with anisotropic cylindrical shells," *Composite Structures*, vol. 116, pp. 747-760, 2014, doi: 10.1016/j.compstruct.2014.05.029.
- [140] D. Zhao, G. Squicciarini, and N. S. Ferguson, "The acoustic response of stiffened plates," *Journal of Physics: Conference Series*, vol. 1264, p. 012041, 2019, doi: 10.1088/1742-6596/1264/1/012041.
- [141] D. Zhao, G. Squicciarini, and N. Ferguson, "Vibroacoustic response of stiffened thin plates to incident sound," *Applied Acoustics*, vol. 172, p. 107578, 2021, doi: <https://doi.org/10.1016/j.apacoust.2020.107578>.
- [142] D. Zhao, G. Squicciarini, and N. S. Ferguson, "Acoustic response of thin-walled, orthogonally stiffened cylinders," *Materials Science and Engineering*, 2019. [Online]. Available: <http://dx.doi.org/10.1088/1742-6596/1264/1/012041>.

- [143] L. Meirovitch, *Analytical methods in vibrations*. New York: Macmillan, 1967.
- [144] J. W. S. B. Rayleigh, *The Theory of Sound*. Macmillan, 1896.
- [145] D. J. Thompson and P. Nelson, "Fundamentals of Acoustics," in *Fundamentals of sound and vibration*. London: CRC Press, 2015, ch. 2, p. 63.
- [146] *Acoustics module user's guide, version 5.3a*. (2017). COMSOL Inc. [Online]. Available: www.comsol.com
- [147] D. J. Ewins, "Applications," in *Modal testing: theory and practice*. UK: Research Studies Press, 1984, ch. 6, p. 225.
- [148] D. J. Thompson, P. Gardonio, and J. Rohlifing, "Can a transmission coefficient be greater than unity?," *Applied Acoustics*, vol. 70, no. 5, pp. 681-688, 2009. [Online]. Available: <https://eprints.soton.ac.uk/65271/>.
- [149] E. C. Sewell, "Transmission of reverberant sound through a single-leaf partition surrounded by an infinite rigid baffle," *Journal of Sound and Vibration*, vol. 12, no. 1, pp. 21-32, 1970, doi: [https://doi.org/10.1016/0022-460X\(70\)90046-5](https://doi.org/10.1016/0022-460X(70)90046-5).
- [150] E. Skudrzyk, "The wave equation in cylindrical coordinates and its applications," in *The Foundations of Acoustics : Basic Mathematics and Basic Acoustics*. Wien: Springer Vienna, 1971, ch. XXI, p. 446.
- [151] E. W. Weisstein. "Weyrich's Formula." Mathworld - a Wolfram Web Resource. (accessed 13-05, 2021).
- [152] D. Zhao, N. S. Ferguson, and G. Squicciarini, "Acoustic response of thin-walled, orthogonally stiffened cylinders," *IOP Conference Series: Materials Science and Engineering*, vol. 657, p. 012007, 2019, doi: 10.1088/1757-899x/657/1/012007.
- [153] F. J. Fahy and P. Gardonio, "Acoustically induced vibration of structures," in *Sound and structural vibration : radiation, transmission and response*. Oxford, UK: Academic Press, 2007, ch. 6, p. 379.
- [154] J. M. Mason, "A reciprocity technique for the characterisation of sound transmission into aircraft fuselage," Doctor of Philosophy Doctoral Dissertation, Faculty of Engineering and Applied Science, University of Southampton, Southampton, 1990.
- [155] S. S. Rao, "Transverse vibration of beam," in *Vibration of Continuous Systems*. Hoboken: Wiley, 2007, ch. 11, pp. 344-357.
- [156] <https://www.isvr.co.uk/automotive/sound-sources.htm>. "Omni-directional Sound Sources." ISVR Consulting, University of Southampton. (accessed 30-06, 2021).
- [157] F. M. Wiener, "Sound Diffraction by Rigid Spheres and Circular Cylinders," *The Journal of the Acoustical Society of America*, vol. 19, no. 3, pp. 444-451, 1947, doi: 10.1121/1.1916501.
- [158] Y. Shi and C. Mei, "A finite element time domain modal formulation for large amplitude free vibrations of beams and plates," *Journal of Sound and Vibration*, vol. 193, no. 2, pp. 453-464, 1996, doi: <https://doi.org/10.1006/jsvi.1996.0295>.
- [159] P. Tiso and E. Jansen, "A Finite Element Based Reduction Method for Nonlinear Dynamics of Structures," in *46th AIAA/ASME/ASCE/AHS/ASC Structures, Structural Dynamics and Materials Conference*. Texas, 2005.
- [160] M. Nash, "Nonlinear structural dynamics by finite element modal synthesis," Doctor of Philosophy Doctoral Dissertation, Department of Aeronautics, Imperial College, London, 1977.
- [161] A. A. Muravyov and S. A. Rizzi, "Determination of nonlinear stiffness with application to random vibration of geometrically nonlinear structures," *Computers & Structures*, vol. 81, no. 15, pp. 1513-1523, 2003, doi: [https://doi.org/10.1016/S0045-7949\(03\)00145-7](https://doi.org/10.1016/S0045-7949(03)00145-7).
- [162] J. J. Hollkamp, R. W. Gordon, and S. M. Spottswood, "Nonlinear modal models for sonic fatigue response prediction: a comparison of methods," *Journal of Sound and*

- Vibration*, vol. 284, no. 3, pp. 1145-1163, 2005, doi: <https://doi.org/10.1016/j.jsv.2004.08.036>.
- [163] A. Muravyov and S. Rizzi, "Determination of nonlinear stiffness with application to random vibration of geometrically nonlinear structures," *Computers & Structures*, vol. 81, pp. 1513-1523, 2003, doi: 10.1016/S0045-7949(03)00145-7.
 - [164] S. Rizzi and A. Muravyov, "Equivalent Linearization Analysis of Geometrically Nonlinear Random Vibrations Using Commercial Finite Element Codes," Langley Research Center, Virginia, NASA/TP-2002-211761, 2002.
 - [165] S. Rizzi and A. Przekop, "POD/MAC-Based Modal Basis Selection for a Reduced Order Nonlinear Response Analysis," in *EUROMECH Colloquium 483*, Portugal, 2007.
 - [166] S. M. Spottswood, J. J. Hollkamp, and T. G. Eason, "Reduced-Order Models for a Shallow Curved Beam Under Combined Loading," *AIAA Journal*, vol. 48, no. 1, pp. 47-55, 2010, doi: 10.2514/1.38707.
 - [167] B. Mace, "Fundamentals of vibration," in *Fundamentals of sound and vibration*. London: CRC Press, 2015, ch. 3, p. 107.
 - [168] F. J. Fahy, *Sound and structural vibration : radiation, transmission and response*. London; San Diego; New York: Academic Press, 1994.
 - [169] K. A. Sweitzer, "Random vibration response statistics for fatigue analysis of nonlinear structures," Doctor of Philosophy Doctoral Dissertation, Faculty of Engineering, Science & Mathematics, University of Southampton, Southampton, 2006.
 - [170] I. Rychlik, "A new definition of the rainflow cycle counting method," *International Journal of Fatigue*, vol. 9, no. 2, pp. 119-121, 1987, doi: [https://doi.org/10.1016/0142-1123\(87\)90054-5](https://doi.org/10.1016/0142-1123(87)90054-5).
 - [171] A. E1049-85, "Standard Practices for Cycle Counting in Fatigue Analysis," PA: ASTM International, West Conshohocken, 2017.
 - [172] S. O. Rice, "Mathematical Analysis of Random Noise," *Bell System Technical Journal*, vol. 24, no. 1, pp. 46-156, 1945, doi: 10.1002/j.1538-7305.1945.tb00453.x.
 - [173] J. S. Bendat, "Probability Functions for Random Responses: Prediction of Peaks, Fatigue Damage, and Catastrophic Failures," National Aeronautics and Space Administration, Los Angeles, California, NASA CR-33, 1964. [Online]. Available: <https://books.google.co.uk/books?id=MqKmiRbrT6AC>
 - [174] L. D. Lutes and S. Sarkani, "Chapter 11 - Failure Analysis," in *Random Vibrations*, L. D. Lutes and S. Sarkani Eds. Burlington: Butterworth-Heinemann, 2004, pp. 487-556.
 - [175] D. E. Newland, "Excitation - response relations for linear systems," in *An Introduction to Random Vibrations, Spectral & Wavelet Analysis*, 3 ed. United Kindom: Longman Group UK Ltd., 1994, ch. 6, sec. 2, p. 54.
 - [176] S. Timoshenko and S. Woinowsky-Krieger, "Pure bending of plates," in *Theory of plates and shells*. New York: McGraw-Hill, 1959, ch. 2, p. 38.
 - [177] H. M. Hilber, T. J. R. Hughes, and R. L. Taylor, "Improved numerical dissipation for time integration algorithms in structural dynamics," *Earthquake Engineering & Structural Dynamics*, vol. 5, no. 3, pp. 283-292, 1977, doi: <https://doi.org/10.1002/eqe.4290050306>.